

ÉCOLE DE TECHNOLOGIE SUPÉRIEURE  
UNIVERSITÉ DU QUÉBEC

THESIS PRESENTED TO  
ÉCOLE DE TECHNOLOGIE SUPÉRIEURE

IN PARTIAL FULFILLMENT OF THE REQUIREMENTS FOR  
THE DEGREE OF DOCTOR OF PHILOSOPHY  
Ph. D.

BY  
Ana Beatriz MARTINS AGUIAR

ELECTROMAGNETIC MODELING OF LARGE HYDRO ELECTRICAL GENERATORS  
USING 2D FINITE ELEMENT METHOD

MONTREAL, DECEMBER 17<sup>TH</sup> 2014



Ana Beatriz Martins Aguiar, 2014



This [Creative Commons](#) licence allows readers to download this work and share it with others as long as the author is credited. The content of this work can't be modified in any way or used commercially.

**BOARD OF EXAMINERS**  
**THIS THESIS HAS BEEN EVALUATED**  
**BY THE FOLLOWING BOARD OF EXAMINERS**

Prof. Kamal Al-Haddad, Thesis Supervisor  
Electrical Engineering Department at École de technologie supérieure

Dr. Arezki Merkhoul, Thesis Co-supervisor  
Institute de Recherche Hydro-Québec

Prof. Stéphane Hallé, President of the Board of Examiners  
Mechanical Engineering Department at École de technologie supérieure

Prof. Ambrish Chandra, Member of the jury  
Electrical Engineering Department at École de technologie supérieure

Prof. Aldo Boglietti, External Evaluator Independent  
Industrial Electrical Engineering Department at Politecnico di Torino

**THIS THESIS WAS PRESENTED AND DEFENDED**  
**IN THE PRESENCE OF A BOARD OF EXAMINERS AND PUBLIC**  
**NOVEMBER 28<sup>TH</sup> 2014**  
**AT ÉCOLE DE TECHNOLOGIE SUPÉRIEURE**



## ACKNOWLEDGMENTS

First and foremost I would like to thank Dr. Kamal Al-Haddad and Dr. Arezki Merkhoul for supervising my work over the last five years. Their expertise, guidance and support were fundamental for the accomplishment of this thesis.

I would also like to express my deepest gratitude to Dr. Bachir Kedjar for agreeing to be the second reader and to Dr. Raja for proof-reading and correcting the English.

My gratitude also goes to the members of my doctoral committee: Dr. Aldo Boglietti, Dr. Stéphane Hallé and Dr. Ambrish Chandra, for evaluating this thesis and providing valuable comments.

I wish to thank my colleagues at the IREQ (*Institut de Recherche Hydro Québec*), Claude Hudon, Melanie Lévesque, Federico Torriano, Samuel Cupillard, Hind Dirani and Jemimah Akiror, for the useful and pertinent discussions regarding electrical machines and core losses.

I am deeply grateful to my Canadian family that I have formed over the last few years. My special thanks go to Priscila Wakamatsu, Alvaro Tamayo, Michelle Peixoto, Luana Bezerra and Rodrigo Suguimati. I am also grateful to my close friends, Patrick Verhaar, Manuella Luiz, Stéphane Gazaille and Cecilia de la Moura. Your presence and support have allowed me to overcome many obstacles. Thank you very much.

I would like also to acknowledge my long time friends from Brazil, Livia, Sandra Paula, Merielle, Katyane and Grisangela, for their great and enduring friendship. Even when I was far away, they were always there to support me and cheer for me.

Thanks as well to my Master's thesis advisor, Dr. Joao Onofre Pereira Pinto, who guided me into the academic world and encouraged me to pursue a PhD.

Last, but definitely not least, I would like to thank my family for all their support, especially my mother Tereza Cristina, my father Marcus Sergio and my brothers Luis Felipe and Marcus Sergio, for their love and unconditional support and encouragement.



# **ELECTROMAGNETIC MODELING OF LARGE HYDRO ELECTRICAL GENERATORS USING 2D FINITE ELEMENT METHOD**

Ana Beatriz MARTINS AGUIAR

## **ABSTRACT**

With the ever increasing of the demand for electrical energy, the need for additional power has already become a reality in the energy supply market. In this context, increasing the power output of existing generators is considered as a promising and beneficial option. Unfortunately, the available methods today do not allow exploiting the full power potential of the existing generators with a precise evaluation of the impact of this increase on the residual lifetime. The challenge in uprating a large existing machine therefore is increasing the output power within the safety limits and without reducing the reliability of the system. One of the goals of Hydro-Québec is to develop new techniques which permit identification of units with potential for up rate. The understanding of the electromagnetic fields inside the generator and their implication in the losses is the first step to fulfil this goal. This thesis focuses on analyzing the electromagnetic field and establishing the magnetic core losses for different machine configurations and operating conditions. The electrical machine in question is a low-speed, salient poles synchronous generator. Initially, a literature review of the related subjects published in the last 20 years was investigated. Secondly, modelling analysis and simulation of large electrical machines using commercial software to compute the losses at the steady state was also done. Moreover, validation of this work and analysis is done using measurements of losses with emphasis on the core losses and magnetic flux density. The core loss matrix generated by FEM was also compared with the thermal calculation and measurements of the hotspots of the machine. The results from FEM simulation in comparison to the experimental measurements are presented for two machines (Manic 21 and Rapide-des-Quinze). The simulation and experimental results were in a good agreement.

**Keywords:** extrapolation of the power output, cut and bypassed stator coil, finite element model, salient pole synchronous generator.





# MODÉLISATION ÉLECTROMAGNÉTIQUE DES GRANDS GÉNÉRATEURS HYDRO ÉLECTRIQUES UTILISANT DES ÉLÉMENTS FINIS 2D

Ana Beatriz MARTINS AGUIAR

## RÉSUMÉ

Avec l'augmentation de la demande d'énergie électrique, la nécessité de la disponibilité de la puissance supplémentaire est déjà devenue une réalité du marché de l'approvisionnement en énergie. Dans ce contexte, l'augmentation de la puissance de sortie des générateurs existants est considérée comme une option prometteuse et bénéfique. Malheureusement, les méthodes d'aujourd'hui disponibles ne permettent pas exploiter le plein potentiel des générateurs existants et l'augmentation de puissance de sortie peut accroître l'impact sur la durée de vie résiduelle. L'un des objectifs d'Hydro-Québec est de développer de nouvelles techniques qui permettent d'identifier les unités avec le potentiel pour l'augmentation de puissance. La compréhension de la distribution des champs électromagnétiques à l'intérieur du générateur et son implication dans les pertes est la première étape pour atteindre cet objectif. Cette thèse consiste à analyser la distribution des champs électromagnétiques et d'établir les pertes correspondantes dans le noyau magnétique pour différentes conditions d'exploitation. Initialement, une revue de la littérature liée à ce sujet publié sur les 20 dernières années a été investiguée. Deuxièmement, la modélisation et la simulation des grandes machines électriques pour calculer les pertes à l'état d'équilibre ont également été analysées. En outre, pour des raisons de validation, les mesures portant sur les pertes fers et flux magnétique ont été effectuées. Par ailleurs, la matrice de perte dans le noyau calculée par FEM a été utilisée par le module de calcul, ainsi les températures prédites sont comparées aux mesures. Les résultats de la simulation FEM et la comparaison avec les mesures expérimentales sont présentées pour deux machines (Manic 21 et Rapide-des-Quinze). La simulation et les résultats expérimentaux sont en bon accord.

**Mots-clés:** extrapolation de la puissance de sortie, bobine de stator coupés et contournés, modèle par éléments finis, générateur synchrone à pôle saillant.



## TABLE OF CONTENTS

Page

INTRODUCTION .....	1
CHAPTER 1    LITERATURE REVIEW .....	7
1.1    Hydro-generator previous studies .....	7
1.1.1    Core loss determination .....	8
1.1.2    Damper currents and damper bar losses determination .....	10
1.2    Analytical and numerical methods used in electromagnetic simulation .....	12
1.2.1    Analytical methods .....	12
1.2.2    Numerical methods .....	13
1.3    Losses in electrical machines .....	19
1.3.1    Joule losses .....	19
1.3.2    Stray losses .....	19
1.3.3    Iron losses .....	20
1.4    Iron loss models .....	29
1.4.1    Steinmetz equation and its modifications .....	32
1.4.2    Loss separation .....	36
1.4.3    Hysteresis model .....	40
1.5    Upgrade and uprating of hydro-generators .....	41
1.6    Fault detection in electric machines .....	43
1.7    Conclusions .....	46
CHAPTER 2    COMPONENTS HYDRO-GENERATORS .....	47
2.1    Machine components .....	48
2.1.1    Stator .....	49
2.1.2    Rotor .....	57
2.1.3    Airgap .....	64
2.2    Studied machines .....	65
2.2.1    Manic 21 .....	66
2.2.2    Rapide-des-Quinze .....	69
2.3    Conclusions .....	70
CHAPTER 3    EXPERIMENTAL SET-UPS AND EXPERIMENTAL RESULTS .....	71
3.1    Magnetic material measurements .....	71
3.1.1    Magnetic resistivity .....	74
3.1.2    Magnetic material losses .....	74
3.2    Magnetic field measurements .....	75
3.3    Segregated loss .....	77
3.3.1    Open-circuit test .....	78
3.3.2    Short-circuit test .....	78
3.3.3    Calorimetric test .....	79
3.4    Experimental results .....	80

3.4.1	Magnetic material measurements .....	80
3.4.2	Manic 21 measurements .....	83
3.4.3	Rapide-des-Quinze measurements.....	93
3.5	Conclusions.....	97
CHAPTER 4 ELECTROMAGNETIC MODELING OF ELECTRICAL MACHINES....		99
4.1	Analytical method: d-q-0 model .....	101
4.2	Maxwell's equations .....	103
4.2.1	Constitutive laws.....	105
4.2.2	Boundary conditions .....	106
4.3	Different domains of electromagnetism.....	107
4.3.1	Electrostatic.....	108
4.3.2	Electrokinetics.....	108
4.3.3	Magnetostatic .....	109
4.3.4	Magnetodynamic.....	110
4.4	Potential formulations .....	110
4.4.1	Magnetic vector potential formulation ( $A, V-A$ ).....	110
4.4.2	Electric vector potential formulation ( $\vec{T} - \Omega, \Omega$ ) .....	112
4.5	Governing equations for the different parts of the machine .....	113
4.5.1	Stator core .....	114
4.5.2	Stator winding.....	115
4.5.3	Rotor core.....	116
4.5.4	Damper bars .....	117
4.5.5	Airgap .....	118
4.6	Finite element method.....	119
4.6.1	Weak formulation and it's application for magnetodynamic problems.....	120
4.6.2	Discretization of the domain and shape functions .....	122
4.6.3	Gauge conditions and source fields .....	124
4.6.4	Matrix formulation.....	126
4.6.5	Imposition of displacement constraints (movement of the machine) .....	127
4.6.6	Methods of solution of the system .....	128
4.7	Synchronous salient pole generator model .....	128
4.7.1	Mesh features .....	131
4.7.2	Choice of time step .....	133
4.7.3	External circuit.....	134
4.8	Hypothesis and simplifications .....	137
4.8.1	Geometric model.....	137
4.8.2	Equivalent model depth .....	138
4.8.3	Magnetic material characteristics .....	139
4.8.4	Types of simulation: voltage driven x current driven.....	140
4.9	Magnetic losses models .....	142
4.9.1	Solid loss model.....	142
4.9.2	Core loss model.....	144

4.9.3	Implemented model for core loss computation.....	146
4.9.3.1	Stator loss model.....	147
4.9.3.2	Rotor loss model .....	148
4.10	Conclusions.....	149
CHAPTER 5 SIMULATION RESULTS AND MODEL VALIDATION.....		151
5.1	Initial model.....	153
5.2	Model calibration.....	154
5.2.1	The influence of the mesh.....	155
5.2.2	The influence of the excitation current .....	160
5.2.3	The influence of the airgap length .....	162
5.2.4	The influence of the voltage driven simulation .....	168
5.2.5	Influence of the magnetic material characteristics.....	171
5.3	Segregated losses .....	172
5.3.1	Open circuit.....	173
5.3.1.1	Magnetic induction and its distribution .....	175
5.3.1.2	Damper bar currents.....	181
5.3.1.3	Core losses .....	182
5.3.2	Short-circuit .....	184
5.3.2.1	Magnetic flux induction and its distribution.....	185
5.3.2.2	Damper bar currents.....	187
5.3.2.3	Core losses .....	188
5.4	Core loss computation at different load operating conditions .....	190
5.4.1	Magnetic flux density and its distribution .....	191
5.4.2	Damper bar currents and its losses.....	197
5.4.3	Magnetic losses and its distribution.....	201
5.4.3.1	Core losses calculation with the implemented model.....	205
5.5	Temperature of the damper bars .....	208
5.6	Conclusions.....	212
CHAPTER 6 INDUSTRIAL APPLICATION OF THE DEVELOPED TECHNIQUE ..		213
6.1	Extrapolation of Manic 21 (>100% load).....	214
6.1.1	Extrapolation condition – 170 MVA at 14.5 kV.....	218
6.1.2	Extrapolation condition – 188 MVA at 14.5 kV.....	220
6.1.3	Discussions for the extrapolation conditions at 14.5 kV .....	221
6.2	Cut coil study of Rapide-des-Quinze.....	228
6.2.1	Circuit current calculation with one bypassed coil .....	231
6.2.2	Circuit current calculation with four bypassed coils.....	233
6.3	Conclusions.....	236
CONCLUSION.....		239
ANNEX I	Kh and Kc variable coefficients.....	243

BIBLIOGRAPHY.....	245
-------------------	-----

## LIST OF TABLES

	Page
Table 1.1	Comparison of 10 different iron loss models investigated .....30
Table 2.1	Hydro Quebec energy production.....47
Table 2.2	Winding sequence example .....56
Table 2.3	Hydro stations studied.....66
Table 2.4	Generator design and electrical parameters for Manic 21 .....67
Table 2.5	Generator design and electrical parameters for Rapide-des-Quinze.....69
Table 3.1	Magnetic flux density B (T).....86
Table 3.2	Differences between simulated and measured machine .....87
Table 3.3	Segregated losses on a similar machine (Manic 24).....88
Table 3.4	Computed losses for Manic 21 .....90
Table 3.5	Losses division on Rapide-des-Quinze.....96
Table 3.6	Computed losses for Rapide-des-Quinze.....97
Table 4.1	Basic shape functions.....124
Table 4.2	General machine parameters.....129
Table 4.3	Stator parameters .....129
Table 4.4	Rotor parameters .....130
Table 4.5	Analysis setup parameters.....130
Table 5.1	Compute magnetic core loss with different meshes (time step of 27.5 $\mu$ s) .....157
Table 5.2	Core loss and current line results for different excitation current (airgap of 15.875 mm) .....161
Table 5.3	Core loss and current line results for different airgap size ( $I_f=739$ A).....164

Table 5.4	Computed core loss with different magnetic materials.....	172
Table 5.5	Summarized simulated results .....	189
Table 5.6	Experimental values of phase current and power factor .....	191
Table 5.7	Computed magnetic core loss models.....	206
Table 5.8	Summary of the computed magnetic core loss with different models for the measured load conditions .....	207
Table 5.9	Comparison between measured and computed damper bar temperature...	210
Table 6.1	Simulated and expected values for stator phase current (14.5 kV).....	222
Table 6.2	Simulated results for machine operating over the nominal conditions.....	222
Table 6.3	Computed rotor and stator temperatures for 170 MVA and 188 MVA.....	226
Table 6.4	Computed rotor and stator temperatures for 150 MVA and 165 MVA.....	227
Table 6.5	Damper bar losses – load operation (86% and 100%).....	236
Table 6.6	Stator $K_h$ coefficient .....	243
Table 6.7	Stator $K_c$ coefficient .....	244



## LIST OF FIGURES

	Page
Figure 1.1	Physical domains and coupling between them .....43
Figure 2.1	Hydro generator .....48
Figure 2.2	Teeth dimensions – a) designed machine, b) smaller teeth dimensions .....50
Figure 2.3	Stator of a large synchronous machine .....53
Figure 2.4	Stator core geometry .....53
Figure 2.5	Stator winding geometry .....54
Figure 2.6	Stator winding .....55
Figure 2.7	Rotor Manic 21 .....58
Figure 2.8	Pole shoe shape .....59
Figure 2.9	Pole shape definition – a) 2 radii b) 3 radii .....60
Figure 2.10	Damper bars positioning .....61
Figure 2.11	Rotor poles and damper windings in a typical hydro generator .....62
Figure 2.12	Field winding .....63
Figure 2.13	Rotor, stator, coil sensor and RTD sensor during instrumentation stage .....65
Figure 2.14	Capability curve .....68
Figure 3.1	Epstein test .....75
Figure 3.2	Coil sensor placed on the stator – a) Manic 21, b) Rapide-des-Quinze .....77
Figure 3.3	Specific core loss measured at multiple frequencies (stator) .....81
Figure 3.4	BH curve (stator) .....81
Figure 3.5	Specific core loss measured at 60 Hz (rotor) .....82
Figure 3.6	BH curve (rotor) .....82
Figure 3.7	Output signal voltage of the coil sensor at open-circuit condition .....83

Figure 3.8	Airgap flux density for open-circuit operating condition (rated voltage)....	83
Figure 3.9	Airgap flux measurements for the four measurement conditions.....	85
Figure 3.10	Airgap flux measurements for the four measurement conditions.....	86
Figure 3.11	Losses separation in percent for Manic 24 .....	88
Figure 3.12	Losses separation .....	89
Figure 3.13	Open-circuit and short-circuit saturation curves – Manic 21.....	91
Figure 3.14	Temperature sensors at pole face.....	92
Figure 3.15	Measured damper bar temperature at different operating conditions .....	93
Figure 3.16	Airgap flux measurements for 86% nominal load .....	94
Figure 3.17	Open-circuit and short-circuit saturation curves – Rapide-des-Quinze .....	95
Figure 4.1	Phase diagram of a salient-pole generator .....	102
Figure 4.2	Application problems of Maxwell’s equations .....	108
Figure 4.3	FEM for electromagnetic problems .....	120
Figure 4.4	2D geometric elements .....	122
Figure 4.5	Mesh definition for each component .....	132
Figure 4.6	Stator representation .....	133
Figure 4.7	External circuit: damper winding bars circuit.....	136
Figure 4.8	External circuit at load condition.....	136
Figure 4.9	Boundary conditions .....	138
Figure 5.1	Extrapolation steps.....	152
Figure 5.2	Five poles machine model .....	153
Figure 5.3	Model calibration .....	155
Figure 5.4	Mesh density distribution in different generator parts .....	156

Figure 5.5	Current density distribution in the damper bar for: a) 23 elements per bar, b) 90 elements per bar and c) 933 elements per bar .....	158
Figure 5.6	FFT analysis of the damper bar current for different mesh configurations (nominal load).....	159
Figure 5.7	Total core loss as a function of the excitation current for nominal load.....	162
Figure 5.8	Total core loss as a function of the airgap length for nominal load.....	165
Figure 5.9	Computed magnetic flux density using the measured airgap length .....	166
Figure 5.10	Core loss distribution – a)case 11.96 mm, b) 14.93 mm .....	167
Figure 5.11	Excitation current (voltage driven simulation) a) transient current envelope, b) zoom in the last 0.1s.....	169
Figure 5.12	Phase current (voltage driven simulation) .....	170
Figure 5.13	Phase voltage (voltage driven simulation).....	170
Figure 5.14	Stator, rotor and total loss as a function of time (voltage driven simulation) .....	171
Figure 5.15	Meshing 2D of 5 poles pitch model 122.6MVA hydro-electric generator .....	173
Figure 5.16	Open-circuit curve .....	174
Figure 5.17	Open-circuit voltage x core loss curve.....	175
Figure 5.18	Magnetic flux density and flux lines at open-circuit .....	176
Figure 5.19	Magnetic flux induction B (airgap) - open-circuit (arc airgap (red) and arc rotor (blue)) – normalized distance .....	177
Figure 5.20	Spectral analysis – magnetic flux density B (airgap) – open-circuit .....	178
Figure 5.21	Spectral analysis - magnetic induction B (rotor) .....	179
Figure 5.22	Comparison between measured and simulated flux density, at rated voltage, 13.8 kV, no-load (9H sensor).....	180
Figure 5.23	FFT magnetic induction B (airgap).....	180
Figure 5.24	Damper bar current .....	181

Figure 5.25	Damper bar loss for each bar in pole 1 – open-circuit operation.....	182
Figure 5.26	Flux lines distribution and core loss distribution at open-circuit.....	183
Figure 5.27	Core loss distribution between stator and rotor on open-circuit operation .....	184
Figure 5.28	Magnetic flux density and flux lines at short-circuit .....	185
Figure 5.29	Magnetic flux induction B as a function of a normalized distance.....	186
Figure 5.30	Magnetic induction B (airgap) as a function of the time .....	187
Figure 5.31	FFT analysis of damper bar currents .....	188
Figure 5.32	Magnetic core loss and flux lines distribution .....	189
Figure 5.33	Flux lines and magnetic flux density distribution for 71% of nominal load.....	192
Figure 5.34	Flux lines and magnetic flux density distribution for 100% of nominal load.....	192
Figure 5.35	Flux lines and magnetic flux density distribution for 120% of nominal load.....	193
Figure 5.36	Magnetic flux density in the airgap and in the pole face as a function of the normalized distance for 71% of nominal load.....	194
Figure 5.37	Magnetic flux density in the airgap and in the pole face as a function of the normalized distance for 100% of nominal load.....	194
Figure 5.38	Magnetic flux density in the airgap and in the pole face as a function of the normalized distance for 120% of nominal load.....	195
Figure 5.39	Simulated and measured magnetic flux density in the airgap as a function of the time for 71% of nominal load.....	196
Figure 5.40	Simulated and measured magnetic flux density in the airgap as a function of the time for 100% of nominal load.....	196
Figure 5.41	Simulated and measured magnetic flux density in the airgap as a function of the time for 120% of nominal load.....	197
Figure 5.42	FFT of the damper bar currents for 71% of nominal load .....	198

Figure 5.43	FFT of the damper bar currents for nominal load.....	199
Figure 5.44	FFT of the damper bar currents for 120% of nominal load .....	199
Figure 5.45	Damper bar losses as a function of the line current in p.u. ....	200
Figure 5.46	Damper bar losses per bar (pole 1) .....	201
Figure 5.47	Magnetic core loss distribution and flux lines for 71% of nominal load.....	202
Figure 5.48	Magnetic core loss distribution and flux lines for nominal load .....	202
Figure 5.49	Magnetic core loss distribution and flux lines for 120% of nominal load.....	203
Figure 5.50	Comparison between rotor and stator core loss at 71%, 100% and 120% of nominal load .....	204
Figure 5.51	Division of the load core loss into hysteresis and eddy current for nominal load.....	205
Figure 5.52	Computed magnetic core loss with different models for the measured load conditions.....	208
Figure 5.53	Measured and calculated damper bar temperature for 3 different load conditions.....	211
Figure 5.54	Calculated rotor temperature.....	211
Figure 6.1	Line current versus excitation current for different load conditions.....	217
Figure 6.2	Open-circuit core loss curve and tendency curve .....	218
Figure 6.3	Flux distribution in the air gap for 170 MVA: a) as a function of time, b) as a function of the distance .....	219
Figure 6.4	Flux distribution for 170 MVA.....	219
Figure 6.5	Flux distribution in the air gap for 188 MVA: a) as a function of time, b) as a function of the distance .....	220
Figure 6.6	Flux distribution for 188 MVA at 14.5 kV .....	221
Figure 6.7	Radial flux density for 170 MVA and 188 MVA (14.5 kV) .....	221

Figure 6.8	Magnetic losses for 146.5 MVA, 170 MVA and 188 MVA .....	223
Figure 6.9	Stray load losses for 146.5 MVA, 170 MVA and 188 MVA as a function of the $I^2$ phase .....	224
Figure 6.10	Losses for 170 MVA and 188 MVA for different core loss models .....	225
Figure 6.11	Magnetic flux density distribution and the core loss distribution for 165 MVA .....	228
Figure 6.12	17 poles machine model.....	229
Figure 6.13	Meshing 2D of a 32.5 MVA hydro electrical generator a) entire machine, b) zoom of the 2D mesh .....	230
Figure 6.14	Current in p.u. per phase – load operation (86%) - 1 cut coil circuit B2.....	232
Figure 6.15	Current in p.u. per phase – load operation (100%) - 1 cut coil circuit B2.....	232
Figure 6.16	Comparison of experimental and simulation results 86% with 1 cut coil.....	233
Figure 6.17	Current in p.u. per phase – load operation (100%) - 4 cut coils circuit B2 .....	234
Figure 6.18	Current in p.u. per phase – load operation (86%) - 4 cut coils circuit B2 .....	235
Figure 6.19	Magnetic flux density and flux lines distribution for an asymmetrical machine with 4 cut coils (86% of nominal load) .....	235

## LIST OF SYMBOLS

$A$  Magnetic vector potential (Wb/m)

$B$  Magnetic flux density (T)

$D$  Electric flux density (C/m<sup>2</sup>)

$E$  Electric field intensity (V/m)

$H$  Magnetic field intensity (A/m)

$I$  Current (A)

$J$  Electric current density (A/ m<sup>2</sup>)

$L$  Inductance (H)

$M$  Magnetization (A/m)

$R$  Resistance ( $\Omega$ )

$\Phi$  Magnetic Flux (Wb)

$\varepsilon$  Electric permissively (C<sup>2</sup>/ N.m<sup>2</sup>)

$\mu$  Magnetic permeability (H/m)

$\rho$  Electric charge density (C/ m<sup>3</sup>)

$\sigma$  Conductivity ( $\Omega^{-1}\text{m}^{-1}$ )

$k_h$  Hysteresis coefficient

$k_c$  Eddy current coefficient

$k_e$  Extra-losses coefficient





## **INTRODUCTION**

Market opportunities have always lead utilities to look for different ways to maximize generating capacity, without reducing the reliability of their equipment. In liberalized market with increased competition, retooling/refurbishing an existing generator offers a good opportunity to the utilities to expand the life time of their power generation facilities with limited financial investments.

Manufacturers have failed to follow the recent developments and progress made in the field of numerical simulation due to the fact that the use of empirical models worked quite well in the past. Although, they have considerable experience in the design of generators and in the solution of associated problems, these techniques do not allow accurate evaluation of the real thermal behaviour of the generators and also they do not permit to design effective corrections.

A major challenge for all the utilities is to identify those existing generators with large potential for uprating. When such generators are identified, precaution should be taken at this stage, specifically, if certain parts of the generators are considered for refurbishment. The best candidate is the one which has the potential to achieve minimally reduced safety margin with minimal or no change of the components and at the same time without decreasing the reliability of the system.

On the other hand, over the past years, the advances of numerical models have enabled manufacturers to design generators with a better understanding of every aspect of the machine. Before, the tendency was to use larger safety margins to lower the risk. Consequently, some of the generators built a few decades ago have larger potential for uprating than newer machines.

On the rotor side, partial refurbishment can imply rewinding of the rotor poles only or substitution of the entire rotor. On the stator side, rewinding for more modern insulation class is sometimes sufficient to achieve greater output, but in some cases the stator core and a change of number of slots and winding pattern may be also necessary.

With the possibility to uprate the existing generators, the Research Institute IREQ of Hydro Québec created AUPALE project. AUPALE stands for "*AUgmentation de la Puissance des ALternateurs Existants*".

Determining the electromagnetic, mechanic, fluid and thermal limits in the stator and rotor is one of the tasks of the AUPALE project. Hence, the main objective of this thesis is to develop an accurate model and perform an exact evaluation of the rotor and stator core losses in hydro generators. For that, advanced electromagnetic numerical modeling was carried out in order to predict the exact behaviour of the modified generator before any uprating to calculate the impact of this increase on the parameters such as, flux density distribution, open circuit voltage harmonics, damper bar currents, damper bar losses, extra copper losses, open circuit and short circuit core losses, torque and force harmonics, transient and sub-transient reactances.

From the electromagnetic point of view, it is not possible to separate rotor and stator electromagnetic components. However, through simulation this separation is possible; the study of the rotor and stator core losses is another task of this thesis. Besides, the proposed research will contribute for a better understanding of the electromagnetic losses in rotating electrical machines. The obtained results will ultimately help tomorrow's engineers to design hydroelectric generators with lower losses, and therefore higher efficiency.

The analytical and numerical analysis of electromagnetic simulations for different operating conditions provides better understanding of the generator's operation. Thus, the definition of the existing operating conditions and the possible increase of energy production can be a

thorough examination of the current scenario and consequently may reduce the investments for the construction of new generating facilities to fulfil the ever increasing demand of electrical energy.

The global trend over the last twenty years is on modeling using Finite Element Method (FEM) to determine more accurately the actual capabilities and limitations of the generators. However, due to the size of the hydro machines (some over 10 meters in diameter) and the limitations of computational capacities, the FEM method was used only in the last five years for large hydro machines. Even though the FEM is the most recommended method for electromagnetic simulation, its results are not absolute and always need to be validated on site or with measurements on small-scaled laboratory prototypes.

After the electromagnetic simulation is completed, the core loss distribution results are used by the thermal experts as one of the inputs to determine hot spots of the machine. Besides, vibration and the fluid studies are added and the interactions of each study are correlated. At the end of the project (AUPALE), the decision on the suitability of the specific machine for uprating is presented. In addition, improvements necessary to increase the performance of the machine can be proposed.

Recently, another industrial application problem was introduced to the thesis, which consisted in performing an electromagnetic diagnostic of a damaged hydro generator. The studied machine is operating at 86% of its nominal power output due to one of the stator bars is cut and bypassed. In this case, the machine had to be entirely modeled and a large model was created to analyze the spatial distribution of the magnetic flux and more importantly the distribution of the stator current in each of the 4 terminals of the three phases.

Finally, the results can be complemented with the analysis on the economic viability of the uprating such as comparing the life reduction cost (if there is) of the generator with the

increased power and the increased revenue generated with the increased energy production by the machine.

### **Methodology:**

To complete the electromagnetic simulation of an existing machine, seven stages have to be performed, as following detailed:

1. Accurate data collection on existing generators. The measured data shall contain:
  - exact geometry of the generator; for that, performed measurement must be done to define unknown parameters;
  - measurement of electrical parameters of the generator (for instance: voltage, current, damper bar currents) at different operating conditions such as: load variation (69%, 100% and 120%), open circuit test and short-circuit test;
  - characterization of the magnetic material of the rotor and stator for low and higher frequencies to determinate the characteristic curves such as: peak induction - power loss (for specific frequencies) and B-H by the Epstein test.
2. Accurate electromagnetic modelling to determine the losses distribution in different parts of the machine with a focus on the rotor side;
3. Measurement of the magnetic flux on the machine, for that an induction sensor is used at some predetermined points of the airgap;
4. Simulation of the machine studying the impact of some input parameters in the simulation result, including airgap change and bypassed stator bars;
5. Study of different core loss models;
6. Extrapolation of the machine to study the possibility to increase the power output;
7. Comparison of the simulated and experimental results for validation purposes.

### **Contributions:**

The objective of this thesis is to analyze by finite element simulation the electromagnetic behaviour of a large hydro generator. The proposed research will contribute to a better understanding of the electromagnetic losses phenomena in rotating electrical machines.

Fractional machines are modeled and the results are compared with measured ones for further analysis to determine if the machine's power could be uprated. The calculation of losses, distribution of the losses and flux, phase current and voltage, damper bar currents are analyzed. The studied method based on FEM determines precisely the locations where higher magnetic fluxes are located.

Another contribution of this thesis is the calculation of the rotor and stator core losses. Before the proposed technique, the core losses were computed for the entire machine. The comprehension of how the losses are distributed in the machine will allow improvement of the machine's efficiency for a possible redesign of some of the components.

The results achieved in one generator are going to be extrapolated for others in the same power facility. Finally, the results can be extrapolated to model and perform economic analysis that could estimate the life reduction cost of the generator and compare with the increased power generation and the associated additional revenue and profit generated.

### **Engineering contributions:**

- solution to real problems for the industry;
- some work has been done in parallel with the software company to improve the software by adding some parameters that allow to study large machines;
- comparison of simulation and experimentation results in large hydro machines;
- application of methods to calculate different losses;
- separation of the iron losses from rotor and stator losses;

- separation of the core losses by simulation from hysteresis and eddy current losses;
- spatial distribution of the losses by simulation (for the experimentation only an average is achieved);
- extrapolation of the power output machine to analyze the magnetic losses by simulation and avoiding real experiments that could be harmful to the machine;
- study of the thermal dilatation of the machine pertaining to the magnetic flux density and the core loss;
- study the bypassed bars and its interference in the magnetic flux distribution;
- comparison between current driven and voltage driven simulation methods and the advantages and disadvantages of both.

### **Outline of the Thesis:**

This work is divided into an introduction to the subject of the thesis and six chapters. The first chapter presents the review of the relevant researches regarding synchronous machines during the last 20 years, where a background study of the analytical and numerical methods is provided. The second chapter consists in the description of the machine under study. The third chapter contains the experimental set-up procedures and the data obtained. Chapter 4 comprises the mathematical formulation behind the finite element method. Chapter 5 presents the simulation results of many different conditions of Manic 2, in addition, it details, the simulation results and a comparison with the experimental ones. Chapter 6 includes the two application examples of the discussed method; the first one was related to the analysis of a possible power increase of Manic 2, followed by the study of another hydro generator named Rapide-des-Quinze that operates with disconnected damage coils. Finally, the conclusions regarding the power output increase and the electromagnetic diagnostic of a damage machine are presented and also the areas for future works and thesis improvement.

## **CHAPTER 1**

### **LITERATURE REVIEW**

In this chapter, the literature review of correlated theses, master's dissertations and relevant papers are organized by topics. The focus is on worldwide works (Canada, USA, Brazil, France, Finland, etc.) from expertise areas such as numerical methods, magnetic materials, synchronous machines, hydro-generators, core loss determination and damper winding bar currents calculation. The topics were presented in more than 50 Master's and PhD thesis over the last 20 years.

#### **1.1 Hydro-generator previous studies**

In this section, previous work regarding salient pole machines is presented. The reference list concerns the core loss determination, the damper currents and damper bar losses, the eddy current and the thermal computation of hydro-generators.

In 1999, the thesis entitled “Modeling of Synchronous Machines for Systems Studies” was presented by Mohamed Labib Awad. He proposed a new method based on the machine dimensions and material properties to predict the operational inductances of the machine. The author took into consideration the linear reluctance matrix, the saturation effects, the eddy current distribution and the depth penetration for the development of his frequency-domain model. In the end, the author compared the result of his model and the measurements of a large turbo alternator concluding that the model results are essentially accurate.

For salient pole synchronous machines, a standstill frequency response test was proposed to determine the direct and quadrature axis operational impedances by (Bortoni *et al.*, 2004). The advantage of the proposed method is that the machine can be tested with the rotor at standstill and stopped at any arbitrary position. However when the research was conducted

on small machines, some errors were found when comparing the proposed theory with the standard procedure.

In 2004, Merkhouf et al. investigated the different tools and practices for large hydro-generator design used lately. The advanced electromagnetic design using time-stepping finite element methods; and the permeance model were detailed. Moreover, the use of computational fluid dynamics method allows the prediction of the fluid flow, heat transfer and mass transfer. The utilization of numerical and analytical models permits the determination of modifying design constraints and the improvement of the new machines.

In 2011, Ranlöf's thesis was entitled "Electromagnetic Analysis of Hydroelectric Generators". This thesis was the aggregation of different studies involving large hydro-power generators performed by the author. In this study, the theory of salient-pole machines, the equivalent circuit model, the finite element generator model and the coupled field-circuits are described. Besides, the permeance model was implemented to determine the effects of the damper windings on the open-circuit armature voltage waveform. Other topic presented in this thesis is the core loss estimation with comparison of the experimental and simulated results. He found that the effect of harmonics and flux rotation increase the total core loss of about 28% on an average.

### **1.1.1 Core loss determination**

A paper computing the losses in large hydro generators was published by (Traxler-Samek *et al.*, 2006). The optimization of the loss calculation of salient-pole generators in a design program using statistical methods is presented. With this improved technique, the manufacturer can estimate and guarantee machine losses (no-load iron losses). The method simplifies the decision process for special and cost-intensive design improvements.



In 2008, Znidarich studied the stator core of large hydro-generators, the physical construction features including stator core end region stepping, radial ventilation ducts, stator core clamping systems and segmented or continuously stacked stator cores. Besides, the losses in the stator core including hysteresis and eddy-current and the effects of alloying, rolling and heat treatment, grain direction, etc are presented (Znidarich, 2008a). The continuation of the last work covers the definition of the stator core loss for open-circuit and short-circuit and the way that they are segregated. The evaluation of the stator core condition is done by the stator core ring flux test; the author states that this test is the traditional and most appropriate test for assessment of the core condition. An alternative method for finding shorted lamination is called ELeCtromagnetic Core Imperfection Detector (ELCID). However, the last method does neither estimate the core loss nor the severity of the hot spot. The paper concludes with a summary of the important factors that must be considered when specifying new stator cores for hydro generator upgrades (Znidarich, 2008b).

Large hydropower generators were also investigated by Ranlöf *et al.* in 2009. It is emphasized that the total core loss prediction comparing different core loss prediction schemes with no-load measurement. Also, the authors observed that the rotational loss is closely related to the stator slot geometry. Finally, the proposed time-domain model with constant loss coefficients was found to predict the total core loss to be about 65% of the measured no-load loss in large hydro generators (Ranlöf *et al.*, 2009).

Another paper that computes the losses of a hydro-generator was presented by Bertalanic *et al.* Measurements were carried out in 12 hydro-generators onsite using the calorimetric method. It is well known that it is one of the simplest methods to determinate the losses of closed water cooling hydro-generators. The measurements were done in two different approaches: off-line and online. The authors concluded that the determination of losses based on the online tests gives more accurate results (Bertalanic *et al.*, 2010).

The core loss under no-load was calculated for a 1000 MW air cooled hydro-generator using FEM. The authors compared the simulation results of the traditional analytical method, the steady-field method (magnetostatic) and the transient field method to compute the yoke and teeth iron losses. For both numerical methods, the non-linearity of the core material and the uneven distribution of the magnetic flux density were considered and the exact value and distribution of the iron loss were obtained (Weili *et al.*, 2012).

### **1.1.2 Damper currents and damper bar losses determination**

The damper bar currents of a large salient-pole synchronous machine with skewed stator slots were measured using two Rogowski coils placed on the end ring of two different poles, the results can be found in Karmaker *et al.* (2005). Besides, a comparison between measured and calculated damper bar currents at load were presented for a 16 MVA hydro-generator.

Numerical and analytical methods were combined for the determination of the damper bar currents in large salient-pole synchronous generators under eccentricity conditions. The proposed method is based on the magneto-static FEM and on the resolution of the electrical circuit differential equations. This combined method showed faster results when compared to the transient magnetic FEM simulations with almost the same level of precision (Keller *et al.*, 2007).

The damper winding losses were calculated for large hydro-generators on open circuit and load conditions by an analytical method by Traxler-Samek *et al.* (2008b). The current distribution in the damper bars is calculated by an analytical algorithm based on the air-gap permeance function and uses a numerical integral approach for the calculation of the induced voltages in the damper bars. The proposed approach was compared with transient finite element method showing good agreement with faster results.

The computation of the current distribution and the associated power losses in damper-winding, The damper-winding bars of salient-pole synchronous machines due to the tooth-ripple pulsations and the stator-winding armature-reaction harmonics on open-circuit and load conditions are detailed in Traxler-Samek *et al.* (2010a). The calculations were based on the air-gap permeance model, and a numerical integration for the calculation of the induced damper-bar voltages was used. This integration allows the consideration of the local variation of the air-gap. The method is based on an equivalent network of the damper bar winding containing all the bars of a section of the machine. This investigation didn't take into consideration real test measurements. Instead, for validation purpose, the authors compared the proposed analytical algorithm with the traditional 2D finite element method for calculation of current and corresponding losses of damper windings.

Ranlöf *et al.* (2010) developed a semi-analytic permeance model to predict the open-circuit voltage harmonics and the damper winding losses. The authors considered integral slot armature winding generators and the centralization of the damper windings around the pole axis. Compared with the previously permeance model, two modifications have been suggested concerning the model of the damper bar reaction. First, the MMF of a damper loop was based on the observations of the actual radial flux paths in the airgap; and, the coupling between adjacent damper loops was included in the model. In general, the agreement between measured and calculated model was considered reasonable by the authors.

The additional losses on the rotor pole surface and the damper windings of 250 MW hydro-generator were calculated by time stepping finite element model. Besides, a 3D temperature field model was done and the temperature distribution was analyzed under rated voltage and no-load conditions. The authors concluded for this specific generator that the temperature distribution of the damper winding and end ring damp rises from end to axial centre (Feiyang *et al.*, 2010).

## **1.2 Analytical and numerical methods used in electromagnetic simulation**

The electromagnetic simulation is the first stage of any study on uprating of an existing machine. This has been the subject of many publications (Zhan, 2010; Karneva, 2005; Zhong, 2010). However, the methods of calculation and measurement of the flow of electromagnetic energy have been studied since 1800's. An interesting review of the progress of the electromagnetic study is presented by Guedes, (1983).

The electromagnetic theory developed by Maxwell in 1873 was able to embrace electromagnetic phenomena such as Faraday's law, Ampere's law, Gauss' law in a series of differential (or integral form) equations. The application of the time-dependent Maxwell's equations and the boundary conditions allows the calculation of the electric and magnetic fields in a closed surface.

The Maxwell equations can be solved either by analytical, numerical or even the combination of both methods. For simple geometrical shapes, analytical method is still a good option, but due to the boundary and interface conditions, the numerical methods are usually applied for more complex structures.

### **1.2.1 Analytical methods**

The range of possible problems which can be solved by using analytical methods are very restricted, because these methods only allow the determination of linear and simple geometric structures (mostly in 1D or 2D).

One of the models widely used to study the synchronous machine comes from Park Theory where the stator's three-phase quantities are transformed and transferred to a new reference system, orthogonal and fixed to the rotor, known as direct and quadrature (d-q) axes. In 2004, another thesis was completed in Helsinki University of Technology regarding electric

machines and electromagnetic simulation. Entitled “*Analytical Prediction of the Electromagnetic Torques in Single-Phase and Two-Phase AC Motors*” Mircea Popescu discussed about the two axis d-q theory to the prediction of the electromagnetic torque. The developed models take into account the most important asymmetries of the motor configuration such as: different distribution, conductor dimensions and effective turns in the stator point of view and asymmetrical rotor cage, variable reluctance and permanent magnetic effects on the rotor side. The author stated that the developed mathematical models have been successfully used for education purposes (Popescu, 2004).

Galbraith, in his master's dissertation, presented a technique for the estimation of the synchronous generator parameters using time-domain responses (Galbraith, 2005). For the determination of machine parameters, some measurements were done such as: generator terminal voltages; generator terminal currents; field current; speed and gate position. Using Matlab software, the author searched for a way to facilitate the transfer from the field measurements to the simulation environment with respect to data conditioning by developing an analytical tool for processing of the field measurement data and estimating specific parameters using measured machine responses.

A revision of the electromagnetic transient simulation techniques for synchronous machine is presented in 2007. In this work, the d-q model, phase-domain model and voltage-behind-reactance (VBR) model were detailed. The study shows that the three models are equivalent in the continuous time domain when the time step is sufficiently small. For large time-steps, the VBR model shows better stability property and provides the most accurate results (Wang *et al.*, 2007).

### **1.2.2 Numerical methods**

In 1983, Guedes (1983) performed an extensive survey on the numerical methods for analysis of the magnetic field of electrical machines. Finite difference method and the finite

element method were explained and the advantages and disadvantages of each were detailed through a comparative study. This thesis is a good reference to identify the differences between the different methods and the suitability of each to a specific application.

In 1994, Jin G. Zhu presented his PhD thesis entitled “Numerical Modelling of Magnetic Materials for Computer Aided Design on Electromagnetic Devices” at the University of Technology in Sydney, Australia. The focus of his work was on modelling of hysteresis loops with alternating magnetic fields. A new dynamic circuit model taking into account the hysteresis, eddy current, and anomalous losses was included to simulate the performance of magnetic cores with non-sinusoidal alternating flux and also with rotational flux (Zhu, 1994). As a continuation of his work, in 1998, he published a paper presenting improved formulations for rotational core losses in rotating machines (Zhu, Ramsden, 1998). Besides, in 2008, the author (with others) presented a revision of the measurement and modeling of rotational core losses techniques of soft magnetic materials used in electrical machines (Guo et al., 2008). This last paper presents an extensive survey on the measurement and modelling of rotational core losses. These publications focus on the practical applications to engineering.

In 1996, Jonathan Hill presented the master's dissertation entitled “Efficient implementation of mesh generation and FDTD simulation of electromagnetic fields”. In this study, the finite difference time domain (FDTD) was implemented in a parallel computer system for the analysis of the electromagnetic phenomenon. Moreover, an algorithm was used to produce the parallel implementation of the mesh generator. This dissertation detailed the steps regarding the generation of mesh in electromagnetic waves devices (Hill, 1996).

Besides, FDTD methods were also investigated by Chow et al. The authors used parallel computation for a high performance electromagnetic solution. (Chow *et al.*, 2007).

In 2001, the thesis “Magnetic Field Analysis of Electric Machines Taking Ferromagnetic Hysteresis into Account” was presented by Július Saitz at Helsinki University of Technology. The author incorporated the vector hysteresis model into a 2D time-stepping solution through the fixed-point iterative technique. This method was applied to the magnetic field simulation and the computation of the core loss of three cage induction motors. The author concluded that even though the technique is rather slow, it is robust, reliable and it always converges (Saitz, 2001).

The 2D FEM was used to calculate the stator coil flux linkages taking into account the rotor motion by moving band technique. Kim *et al.* implemented a method to analyse the harmonic distortion factor of output voltage waveform of a synchronous generator using the discrete Fourier transform. Calculated and experimental results were compared for a 150 kW machine. The authors highlighted that the proposed technique can be useful for pole shape design optimization to satisfy the specification for maximum acceptable waveform distortion factor (Kim, Sykulski, 2002).

In 2002, Merkhoul presented a transient model based on 2-D time-stepping finite element method of a salient-pole synchronous machine. The simulation model took into account the saturation effects, the eddy current losses and the end effects for open-circuit and sudden three-phase short-circuit. The results obtained from simulation (voltage waveform, telephone influence factor and dynamic reactances) were compared with measurements in a large hydro-generator. The simulation leads to a better understanding of the complex physical phenomena occurring during sudden short circuits and therefore leads to more accurate prediction of machine model parameters at the design stage (Merkhoul, 2002).

A comparative analysis of different theoretical iron losses evaluations techniques coupled with finite element calculations and material modeling has been presented by (Bottauscio *et al.*, 2002). Two different aspects were considered in this study: the model of the electromagnetic device and the model of the ferromagnetic material, which took into account

the eddy current and the hysteresis losses. The analysis was performed in a discrete space with a two-dimensional finite-element code using a voltage driven formulation. All the predictions of the developed models were in the same order; however the results were not compared to any test data.

In addition, time domain dynamic core loss model was proposed (Lin *et al.*, 2004) to estimate core loss in both ferromagnetic and power ferrite materials with arbitrary flux waveforms. The model was applied to compute instantaneous core losses in small electromagnetic devices in both two-dimensional and three-dimensional transient finite element analysis. The authors concluded that their method is practical for industrial applications because it provides reasonable accuracy and all the necessary parameters are obtained directly or by the loss curves provided by the manufacturer.

Numerical methods can also be used for transient field-circuit coupled simulation analysis. Using finite integration technique to discretize the field part of the field-circuit model and external circuits that are treated as lumped parameters, a strong coupling was implemented by (Benderskaya, 2007).

A simulation of a 2D solid rotor synchronous machine was solved by finite element method by (Petite, 2008). In this master's dissertation, the steady-state solution behaviour in the presence of voltage inputs is solved using shooting-Newton method.

Zhan (Zhan, 2010) developed a finite element model for AC machine systems and also an efficient numerical solution for the system equations. The author analyzed the stray losses in AC machines under a variety of operations, design and manufacturing conditions.

The determination of equivalent circuit parameters based on FEM was investigated for synchronous machines (Chmelicek, 2010). Steady state and transient operation simulations were performed using FEM for the estimation of the generator reactance. For the steady state



operation, the reactance profile estimation was obtained from the magneto-static field solution. The estimation of transient and sub-transient reactances were obtained by sudden short-circuit method; and an automated Matlab script was developed in order to achieve precise curve fitting and more accurate results. The author states that software packages using FEM allow precise computation of field problems even with nonlinear material properties or time variance.

A 3D time-harmonic finite element analysis of the end-region of large-sized three-phase induction machines was studied by Lin (2010). In it, the electromagnetic and mechanical phenomena were carefully analyzed regarding the end-magnetic field, the stator end-winding leakage inductance, the eddy currents in the end shield and end frame and the end-winding forces and vibrations.

A combination of finite-element and analytical modeling technique (permeance model) was developed by Knight *et al.* (2001) to predict the damper winding effects and the force due to harmonic components. The combination of both the techniques reduces the computation time when compared to a full time-stepping finite element solution. Measured results from two different machines were presented and compared with the simulation ones. The combination of numerical and analytical methods for the determination of the power loss was also presented by (Keller *et al.*, 2006) and (Knight *et al.*, 2009 a, b).

Analytical methods were used in the past, but now are studied much less with the development of the numerical method. However, the analytical method still plays an important role when providing qualitative ideas about the data that would be calculated numerically. Besides, they are always used as a fast tool to validate the results of computational methods. For instance, analytical and numerical models were compared and validated by Traxler-Samek *et al.* (2010a); in it, the authors calculated the additional losses and the currents in the damper winding on open-circuit and load conditions.

The investigation and simulation of fields in large salient pole synchronous machine with skewed stator slots was the paper's target by Karmaker and Knight. (2005). The authors developed a computational model combining finite element and analytical formulation based on the permeance model and analyzed the electromagnetic field distribution, the damper bar currents and the pole face iron losses on fractional stator slots per pole of the machine. Measured data show that skewing introduces a phase shift on the machine and a progressive increase in the magnitude of the flux density. The authors concluded that their simulation technique offered rapid simulation time and accurate prediction that can help the designers to better understand the impact that design changes may have on stray load losses.

An overview of the interfacing rotating machine models in transient simulation programs was presented by Wang *et al.* (2010). The authors studied the electromagnetic transient programs (EMTP) and also the state-variable-based simulation programs (SV). The EMTP based on the nodal equations enabled an efficient numerical solution. One of the well-known simulation programs is MATLAB/Simulink that is used to study the dynamics of the electrical systems.

Another thesis (Iamamura, 2011) dealing with turbo alternators was presented in 2011 where the aim was to develop methods to detect, locate and recognize faults. A combination of an analytical approach with a numerical model based on FEM was done and the simulation results were compared with other available methods to detect and locate the rotor faults. Both results are in a good agreement even at different operating points showing a good reliability of the method (Iamamura, 2011).

Finite element methods are widely used today by commercial organizations (Alstom, Andritz, GE, etc.) and also by the academy as an optimal tool to study the behaviour of the electromagnetic field distribution in an electrical machine (Traxler-Samek *et al.*, 2006, 2008a, 2008b, 2010a, 2010b; Merkhoulf *et al.*, 2004, Karmaker *et al.*, 2005; Wallin *et al.*, 2010).

### 1.3 Losses in electrical machines

Losses in electrical machines can be divided as: joule loss, mechanical loss, stray loss and iron losses. In this section, the joule losses, stray losses and iron losses will be highlighted.

#### 1.3.1 Joule losses

Joule loss, also known as  $I^2R$  losses, is the ohmic heating loss that occurs in windings (stator, rotor and field windings) of a synchronous machine. The conductor resistance is temperature dependent; hence the Joule losses are also dependent on the operating temperature of the machine.

In the stator and field windings the Joule losses are computed using lumped resistance multiplied by the square of the currents; however in solid conductors like the ones in the damper bars, the losses cannot be computed in this way as the density of induced currents are not uniformly distributed in the cross section due to skin effect. Using a FEM technique the induced current density can be computed locally and consequently the Joule loss.

Joule losses are commonly used to describe the losses at fundamental frequency. However, harmonic currents and harmonic fields cause another component of Joule loss, which also can be treated as portion of the stray losses (Zhan, 2010).

#### 1.3.2 Stray losses

Stray losses are related to Joule and iron losses for all harmonic currents and fields except the fundamental frequency. The stray losses are the remaining losses obtained when subtracting the friction loss, the windage loss, the stator  $I^2R$  losses, the rotor  $I^2R$  losses and the iron losses from the total loss (IEEE-115, 2010).

According to Merkhouf *et al.* (2008), the most relevant causes for harmonics in electric machines are:

- “space harmonics in the airgap permeance due to stator slotting;
- space harmonics in the stator MMF due to winding in discrete slots;
- space and time harmonics in the airgap permeance due to rotor slotting;
- space and time harmonics in the rotor MMF due to winding in discrete slot.”

The stray loss in AC machines (induction, synchronous and permanent magnetic synchronous machines) was determined using time-stepped finite element technique by Zhan (2010). The traditional 2D FEM was modified to take into account the variations of the electromagnetic field along the machine’s axis. Simulation and test results under different load conditions were compared and the additional harmonic stray loss was investigated.

Another work including stray loss and induction machines was presented by Aoulkadi (2011). In it, different tests to lower the stray load losses due to the skin effect in the stator winding in generators for 1.5 MW wind turbines were implemented during the manufacturing process. The estimation of the stator load losses as result of the skin effect was performed through analytical models and the results were compared with those measured.

### **1.3.3 Iron losses**

Iron losses are also known as open circuit core losses. According to IEEE- Std 115, the open circuit core losses are the sum of: losses in the stator core, teeth losses, end loss in cores and surface loss. These losses are explained as follows:

## 1. Losses in the stator core

The losses in the stator core happen in the annulus between the bottom of the slots and the outside diameter of the core.

## 2. Tooth-ripple losses

A very good definition of tooth-ripple losses was provided by Karmaker (1982, p.1122) as follow:

*“Tooth-ripple losses are caused by the permeance variation along the airgap of a rotating machine due to the slotted structure of the armature so that the pole surface flux density in the airgap, instead of being uniform over the main part of the pole arc, has superimposed on it a ripple. This flux pulsation gives rise to parasitic eddy currents of diverse frequencies in the machine parts of which are in relative motion with respect to the ripple flux.”*

The tooth ripple losses in practical poles with amortisseur windings have been measured by a calorimetric and a Poynting vector method (Karmaker, 1982).

In the calculation of tooth-ripple eddy-current losses in laminated poles, there are four important factors which should be considered (Sen 1971):

- the harmonics in the flux density distribution over the pole face;
- the effect of eddy currents on the inducing or applied field;
- the nature of the disturbance travel in pole-shoe material;
- the skin effect phenomena.

In the problem of tooth-ripple losses, the pulsating flux is superimposed on a polarizing or unidirectional flux, and the resulting hysteresis loop is displaced from the origin of the magnetization curve by an amount depending on the mean flux density. The alternating

hysteresis loss due to this displaced loop is usually higher than the loss due to symmetrical loops having the same magnitude of flux pulsation (Fam, 1971).

Ueda, Ohta and Uenosono studied in real time the behaviour of the airgap flux distribution at the point where a synchronous generator actually supplies electric power to various loads for that; they developed a microprocessor-based instrument. The instrument, the principle and method of measuring the airgap flux distribution are described by the authors in (Ueda, Ohta, Uenosono, 1987).

### **3. End losses in cores**

The leakage flux from the rotor pole shoe to the end of the stator core is alternating at generated frequency and therefore produces losses in the end faces of the stator core (Walker, 1981).

### **4. Surface losses (pole face losses)**

Surface losses are basically functions of the flux density, the frequency pulsation, the quality and quantity of material and main dimensions and shape of slot and pole shoe.

Another type of classification of the iron losses was presented by Traxler-Samek *et al.* (2010b, p.174) where they were enumerated as:

- 1) “iron losses in the stator core including the effects of harmonics and rotating fields;
- 2) eddy current losses on the pole shoe due to tooth-ripple pulsation and stator winding armature reaction MMF;
- 3) eddy current losses in the stator clamping plates;
- 4) eddy current losses in the stator clamping fingers;
- 5) eddy current losses in the stator core end laminations;
- 6) eddy current losses in external metallic air guides.”

The variation of the magnetic flux in the core of an electric machine produces the iron losses, they can be classified as: hysteresis loss, eddy current loss and excess loss.

Hysteresis losses are associated with the magnetizing and re-magnetizing of the magnetic material. Hysteresis loss also depends on the volume and quality of the used magnetic material, maximum value of the flux density and frequency of electric current (Atallah *et al. apud* Troitskaia, 2008), (Wakileh, 2003).

Otherwise, eddy current losses are the power associated with varying magnetic fluxes that induces EMFs in iron. Finally, the eddy current excess loss occurs due to microscopic eddy currents induced on the walls of moving domains. (Atallah *et al. apud* Troitskaia, 2008).

*“Eddy-current loss is the power loss associated with the flow of eddy currents induced in the armature core of a rotating machine as a result of its rotation in the magnetic field or in the core of a transformer as a result of ac excitation”* (Wakileh, 2003, p.32).

In the calculation of eddy current losses in solid pole face, two important factors should be considered. First, the harmonics in the flux density distribution over the pole face; the losses due to these harmonics form a very considerable part of total losses. The second factor is the effect of the eddy currents on the inducting or applied field due to slotting (Fam, 1971).

Eddy current loss is proportional to the square of the lamination material thickness and inversely proportional to the magnetic material resistivity.

The prediction of core loss in electrical machines and steel lamination sheets is a challenging task and many improvements of the existing calculation methods are reported over and over. For instance, the effects of the steel lamination core loss on transient magnetic fields were

presented by (Lin *et al.*, 2008) based on core loss separation (hysteresis losses, classical eddy current losses and excess loss) in frequency domain.

Besides, the core loss calculation in laminated sheets was also subject of study by (Chen and Pillay, 2002), in this paper, the authors compared three different methods to compute the core loss of steel laminations. The first method was the using the Steinmetz equation considering that the maximum magnetic flux density does not overcome 1Tesla. The second method is a small modification of the first method and uses the domain wall theory to compute the core loss. In it, the component of the hysteresis loss is supposed to vary linearly with the flux density. The third method compared related hysteresis losses, classical eddy current losses and excess loss or also called anomalous loss for the computation of core loss. The authors concluded that the third method provide results that were closer to the measured ones.

*“Hysteresis, eddy current and excess losses due to rotational flux in parts of a magnetic circuit where flux changes direction, have been found to comprise about 50% of iron losses in an induction motor”* (Findlay *et al. apud* Troitskaia, 2008, ).

Another example of the improvement of the existing models for the calculation of the power loss is the addition of the rotational field reported by Ranlof *et al.* (2009), Zhu and Ramsden (1998), Guo *et al.* (2008)

The calculation of rotor surface losses in small to medium cylindrical synchronous machine was carried out by Hiramatsu *et al.* (2007). The authors proposed an estimation method to calculate the induced slot ripple loss on the rotor surface. Further, they compared different kinds of damper system using the finite-element method. The authors concluded that the conventional estimation of rotor pole loss was overestimated, due to overlooking the effects of slot pitch and damping effect of the flux ripple density.



In 2008, Guo et al. presented a revision about the measurement and modeling techniques of rotational core losses of soft magnetic materials used in electrical machines. The rotational hysteresis loss is explained and then, the total rotational loss which is the addition of the hysteresis rotational loss, the classical eddy-current loss and the anomalous loss is detailed. Four methods for measuring the core loss are presented: torque-metric, thermometric, field-metric and wall-metric. Besides, four different techniques for measuring B and H are presented: magnetization current, sensing coil, hall elements and B tips. Finally, the authors concluded that the mechanisms of rotational core loss were still far from being fully understood and that it was not practical to develop a model with a strong physical background at the current stage due to these very complicated mechanisms (Guo *et al.*, 2008).

In 2011, the core losses in the stator and the rotor of a caged induction machine were predicted by circuit models. The authors concluded that the rotor core losses were largely dependent on the airgap voltage and the effect of fundamental frequency was negligible and the segregated stator and rotor loss were inaccurate. They stated that segregated losses allowed for a more detailed investigation of the machine physics, therefore, developing segregated circuit models would lead to improvements in the prediction of losses (Laldin *et al.*, 2011).

The open and short circuit core losses in large hydro electrical generators are major components in the efficiency and temperature rise calculations for any considered uprating. Therefore the determination of synchronous machine losses has been the subject for many investigators (Alger, 1970), (Karmaker, 1982), (Bottauscio, 2002) for many years. The synchronous losses are segregated into iron loss (core and stray load losses), copper loss (armature and field winding losses), and mechanical loss (friction and windage losses) (Karmaker, 1982) and (IEEE Std.115). A comparative analysis for the estimation of iron losses was proposed by Bottauscio (2002) using different theoretical evaluation techniques coupled with finite element calculations and material modeling.

Traditionally, open circuit core losses are termed as fixed or load independent losses, with short circuit core losses termed as variable or load dependant losses. The core loss in any electrical machine represents one of the highest losses and must be calculated for accurate prediction of machine efficiency and core temperature rise (Znidarich, 2008b).

Some authors (Merkhouf, 2002), (Weeber, 1997), (Tsukerman *et al.*, 1992), presented the equations to model the field, the rotor motion and the windings and loads. The simulation of machine short circuits for the purpose of power system analysis as well as machine design is a difficult task due to the complexity introduced by the interaction of several individual windings, rotor motion, non-linearity of magnetic materials, and eddy-current effects (Merkhouf, 2002).

Merkhouf et al showed modern tools developed by GE Hydro to allow engineers to explore a large number of design possibilities in a short time. These tools include advanced electromagnetic analysis software that helps on the prediction of electromagnetic parameters with more accuracy. Techniques such as time-stepping finite element and permeance model are used for this purpose. For air-cooled hydro generators, GE Hydro uses ventilation network calculations and finite element thermal calculations for thermal design of company's conventional air-cooled generators. The use of advance techniques such as computational fluid dynamics (CFD) have become an important tool in the field of hydroelectric generator design (Merkhouf *et al.*, 2004).

TSTEP (time-stepping) formulation models have been proved to be more accurate and reliable than those obtained by conventional analytical tools, such as MMF-permeance or equivalent circuit models. The present capability of the software package includes the following analysis: open circuit analysis at rated terminal voltage or at any other point on the saturation curve; load analysis in the generator mode or motor mode; and steady-state short circuit analysis; or under pre-fault conditions of the load (Merkhouf et al, 2004).

Owing to the progress of the computers and the electromagnetic (EM)-field analysis, two-dimensional (2-D) or three-dimensional (3-D) finite-element methods considering the harmonics and magnetic saturation are often applied to calculate the characteristics of the induction motors. However, we frequently face the problem that the accuracies are not sufficient, especially, in the calculation of the losses and efficiency. One reason is that the most of the analysis neglect the interbar currents, which flow from the rotor bars into the rotor core. The losses produced by the interbar currents are relatively large, especially in the case of the skewed rotor (Yamazaki, Watanabe, 2006).

Two numerical models to model the electrical machine are: eddy current and coupled circuit. Eddy current model uses simultaneous solution of the rotor circuit equations, stator circuit equations and magnetic field equations for each region in a 2D FEM. However, the coupled circuit method applies time-steps the stator and the rotor circuit equations and uses finite element analysis to update the circuit parameters at each step (Troitskaia, 2008).

A combined finite element and analytical formulation based on permeance and MMF wave was developed by (Knight, 2001) and extended to predict the field distribution and the damper bar currents in (Karmaker, 2005). In parallel, the permeance model combined with the inter-bar current model was proposed in (Troitskaia, 2009a) and (Troitskaia, 2009b); the model in (Troitskaia, 2009a) was used to predict the inter-bar currents and pole face iron losses. It has to be noted that the spatial losses distribution were not achieved in this last model, only average pole face losses were computed.

The recent time domain dynamic core loss model proposed in (Lin *et al.*, 2004) was initially applied to compute instantaneous core losses in small electromagnetic devices in both two-dimensional and three-dimensional finite element analysis. The proposed model in (Lin *et al.*, 2004) is extended by the authors in this present document to compute the magnetic core losses and there corresponding spatial distribution in large hydro electrical generators. The obtained core loss matrix is then transferred to the thermal model to compute the temperature

rise in different parts of the generator. The challenge of the integration of electromagnetic results with thermal and fluid flow models are well described in (Hudon *et al.*, 2010b).

Airgap flux density can be obtained by permeance model as a product of airgap permeance and magneto motive force (MMF) waves. Permeance model can also be used to evaluate the performance of salient pole generators. A semi-analytic permeance model was developed for the prediction of the open-circuit voltage harmonic and damper winding losses in large hydro-generators (Ranlöf *et al.*, 2010). The major differences between this model and the previous ones are simplified characterizations of the damper MMF and the mutual damper loop inductance matrix. This study was performed only on hydro-generators with integral slot armature windings. The authors compared the new method with the 2D finite element and they found that the results were in a very good agreement in terms of the voltage harmonic and damper bar current prediction.

Over the past ten years, many advanced electromagnetic analysis simulation tools have been developed and used in the industry and academic. Automatic finite element mesh generators for both integral and fractional slot machines have been developed and used to model single and multiple pole pitches electrical machines as reported elsewhere (Bottauscio *et al.*, 2002), (Traxler-Samek *et al.*, 2010). Also, a permeance model has emerged in the last few years with the development of fast simulation tool for open voltage evaluation of large hydro electrical machines. The latter is based on using combined analytical and magneto-static finite element solutions (Knight *et al.*, 2001), (Keller, 2006). Recently, the usefulness of the permeance modeling technique for voltage harmonics prediction of machine with axially skewed stator slots was demonstrated (Troitskaia *et al.*, 2009 a,b), where the authors combined the permeance model and the inter-bar current model to predict the inter-bar currents and pole face iron losses. The proposed model was mostly validated on machines with integral slots.

The mathematical formulation for the transient finite element analysis of synchronous machines including the external circuits and rotor motion has been previously described in (Lin *et al.*, 2004, Zhou *et al.*, 2002). The present result was a software application that had been used for the evaluation of the different electrical parameters of large hydro electrical generators. The analysis was performed based on two-dimensional finite element code using current driven simulation mode. The effects of the end region fringing and leakage flux were included in the formulation through circuit elements, such as end winding resistance and end leakage inductance.

Steady-state and transient electromagnetic field problems with balanced and unbalanced loads have been solved using time-stepping formulations with actual winding topology load conditions and kinematic equations of rotor motion. Also, permeance model had been developed by using combined analytical and magneto-static finite element solutions with a one pole pitch model. This method made the computational algorithm very fast compared to time-stepping solutions (Merkhouf *et al.*, 2004).

#### **1.4 Iron loss models**

In a magnetic material, the core loss occurs when the material is exposed to a time varying magnetic flux. An overview of the iron loss models for electrical machine was presented by (Krings *et al.*, 2010 and Krings *et al.*, 2012, and Yamazaki *et al.*, 2004). The aim of the authors was to provide machine designers ideas for integrating appropriate iron loss models into the design process of the machine. Ten different models with different complexity were compared and the results are presented in Table 1.1 taking into account prior knowledge of the material; the presence of complex waveforms and rotating fields and the accuracy of the methods (Krings *et al.*, 2010).

Table 1.1 Comparison of 10 different iron loss models investigated  
 Extracted from Krings and Soulard (2010, p.167)

<b>Iron loss models</b>	<b>Complex waveforms</b>	<b>Rotating fields</b>	<b>Material prior knowledge</b>	<b>Accuracy</b>
Steinmetz equation (SE)	-	-	Small	Low
Modified Steinmetz equation (MSE)	+	-	Small	Low-Medium
Improved generalized Steinmetz equation	+	-	Small	Low-Medium
Loss separation model after Bertotti	+	-	Medium	Medium
Dynamic hysteresis model	+	-	High	Good
Loss surface model	+	-	High	Good
Magneto dynamic viscosity based model	+	-	High	Good
Friction like hysteresis model	+	+	High	Good
Energy based hysteresis model	+	+	High	Good
Loss separation after magnetizing process	+	+	Model dependent	Model dependent

Dunlop investigated in his master's project, different models to compute the core loss; this work also evaluated several of the core loss models using experimental data. His thesis not only provides us a good literature review of the most used models and the magnetic materials characteristics but also the existing experimentation methods (Dunlop, 2008).

Experience shows that the actual core loss in an assembled rotating machine can be as much as 1.5 to 2.5 times higher when compared to the results obtained from the Epstein test

(Nailen *apud* Znidarich, 2008b). For any machine, the losses must be accurately determined to evaluate accurately the machine's efficiency and the correct requirement for the cooling system capacity (Znidarich, 2008b).

In the work presented by Krings *et al.* (2010 and 2012), the iron loss models were divided into three groups: Steinmetz equation (and its modifications); loss separation (into eddy current, hysteresis and excess loss) and mathematical hysteresis models. The description of each group is detailed in sections 1.4.1 to 1.4.3.

Steinmetz equation and its modification state that there would be interdependence between hysteresis loss and eddy current loss, thereby implying that the loss separation into components could not be justified. However, the justification of the separation of losses comes from the fact that it helps to design, optimize use of magnetic material and predict the losses in electrical machines for instance (Pluta, 2011).

A comparison of models for estimating magnetic core losses in electrical machines was performed by Dlala (2009). In his work, the accuracy, efficiency and stability of certain models were investigated and implemented using the finite element method. The author compared three different techniques. The traditional one where the losses are calculated by post processing of the magnetic field using empirical equations; and using the advanced technique that computes the core loss by modelling the vector hysteresis relation; and also with the hybrid technique that omits the numerical procedure of the nonlinear penetration equations (presented in the advanced technique) that determine three magnetic field strength components. The results obtained from these three techniques were compared with the experimental core loss results. The traditional technique showed relatively accurate results at lower voltage levels but bigger discrepancies were seen at higher voltage levels. For the advanced and hybrid techniques, the results were relatively accurate over the whole range of voltage, but the hybrid model showed a better correlation with the results obtained from

measurements. In addition, the convergence speed of the hybrid method is superior to the advanced model.

The core losses of salient-pole synchronous machines were investigated by Rasilo (2012). In this work, a numerical iron-loss model which combined existing models for eddy-current losses, magnetic hysteresis and excess eddy-current losses for ferromagnetic core laminations was implemented and coupled with a 2D FEM. Besides, measurements using the calorimetric method were performed in three different prototypes. In the end, the numerical simulation and the experimentation results were compared in order to validate the proposed methods. This thesis is another great example of the partnership between the academia and the industry.

#### 1.4.1 Steinmetz equation and its modifications

One of the earliest publications regarding iron loss model was presented in 1892 by Steinmetz (Steinmetz, republished 1984). On this paper titled “On the law of hysteresis”, Steinmetz presented an extensive experimental work of many magnetic materials and a simple way to compute the hysteresis loss as:

$$P_v = k f B^\beta \quad (1.1)$$

Where  $f$  is the frequency of the magnetic field;  $B$  is the maximum flux density;  $k$  is the hysteresis loss coefficient and  $\beta$  is the exponent of the flux density.

Nearly all the magnetic materials studied, had the exponent of the flux density equal to 1.6. Besides, the model presented some limitations as almost all the magnetic materials used on the experiment had a maximum permeability lower than 5000; the magnetic flux density was sinusoidal with magnetic frequency limited to the range between 30 and 100 Hz and the magnetic flux had limited range between 0.2T to 1.5T (Pluta, 2011). These assumptions are



not practical in electrical machines (for instance for hydro electrical generators) where, in reality, sometimes the flux density exceeds these limits, especially in certain areas of these large electrical machines such as, the pole face or the stator teeth.

However, the original Steinmetz equation was modified to include all the electromagnetic losses. The total re-magnetization losses including static and dynamic eddy-current losses in ferromagnetic materials can be computed using a modified Steinmetz equation and it is presented as follows (Reinert *et al.*, 2001):

$$P_v = k f^\alpha B^\beta \quad (1.2)$$

Where  $\alpha$  is the exponent of the magnetizing frequency and  $k$  is the material coefficient. However, this model given by Eq. (1.2) is applicable under the assumption that the re-magnetization is sinusoidal. This assumption is not a reality for some electrical devices that have PWM power supplies.

To extend the equation 1.2 to non-sinusoidal problems for ferro-magnetic and ferri-magnetic materials, the Modified Steinmetz Equation (MSE) was proposed by (Reinert *et al.*, 2001). MSE considers an equivalent frequency ( $f_{eq}$ ) which is calculated from the average re-magnetization rate that is directly related to the core losses. The power losses can be calculated by:

$$P_v = (k f_{eq}^{\alpha-1} \hat{B}^\beta) f_r \quad (1.3)$$

Where  $f_{eq}$  is the equivalent frequency,  $f_r$  is the operating frequency and  $\hat{B}$  is the average remagnetization rate  $\hat{B} = \frac{\Delta B}{2} = \frac{B_{\max} - B_{\min}}{2}$ .

The equivalent frequency  $f_{eq}$  can be defined as in function of  $B_{pp}$  (peak-to-peak induction value) and the operating period  $T$ :

$$f_{eq} = \frac{2}{\left(2\pi \frac{B_{pp}}{2}\right)^2} \int_0^T \left(\frac{dB}{dt}\right)^2 dt \quad (1.4)$$

The model given in Eq. (1.3) was extended to take into account the magnetic core loss with non-sinusoidal flux waveforms in MnZn ferrite. The proposed approach, called Generalized Steinmetz Equation (GSE), is a function of the flux density  $B(t)$  and the rate of change of the flux density ( $dB/dt$ ); this formulation is given in equation (1.5) (Li, Abdallah, Sullivan, 2001):

$$P_v = \frac{1}{T} \int_0^T k_s \left| \frac{dB}{dt} \right|^\alpha |B(t)|^{\beta-\alpha} dt \quad (1.5)$$

The above equation is consistent with SE if  $k_s$  is equal to:

$$k_s = \frac{k}{(2\pi)^{\alpha-1} \int_0^{2\pi} |\cos \theta|^\alpha |\sin \theta|^{\beta-\alpha} d\theta} \quad (1.6)$$

The GSE formulation shows to avoid anomalies presented in MSE for the calculation of the losses for nonsinusoidal waveforms for a MnZn ferrite sheets. According to (Li, Abdallah, Sullivan, 2001) the advantage of GSE over MSE is that the GSE has dc-bias sensitivity without the need of additional coefficients and measurements. Besides, particularly for waveforms with small fundamental frequency amplitudes experiments show that GSE is often more accurate than MSE method. The dc sensitivity of the GSE appears to be greater than the actual material (Venkatachalam *et al.*, 2002).

A disadvantage of the GSE is the accuracy limitation if the third or any higher harmonic becomes significant. In the improved generalized Steinmetz equation (iGSE), the flux trajectory is divided into major and minor loops and the iron loss for each loop is determined by Venkatachalam *et al.* (2002):

$$P_v = \frac{1}{T} \int_0^T k_i \left| \frac{dB}{dt} \right|^\alpha |\Delta B|^{\beta-\alpha} dt \quad (1.7)$$

Where  $\Delta B$  is peak-to-peak flux density and  $k_i$  is determine by:

$$k_i = \frac{k}{(2\pi)^{\alpha-1} \int_0^{2\pi} |\cos \theta|^\alpha 2^{\beta-\alpha} d\theta} \quad (1.8)$$

To take into account the minor loops of the hysteresis loops the iGSE was developed and the results of the calculated iGSE method core loss were comparable to the measured values for toroidal core of 3C85 MnZn power ferrite. Even then ferrite core loss varies with the dc bias; the iGSE predicts loss independently of it (Venkatachalam *et al.*, 2002).

The Natural Steinmetz Extension (NSE) proposed by Bossche *et al.* (2004) is quite straightforward and the experiments showed that this model is comparable to those obtained using the MSE and the results were in agreement with measurements on two different ferrite grades. NSE is a similar approach to the iGSE where the peak to peak value of the flux density is taken into account. In this strategy the minor loops of the hysteresis loop are neglected. Equation 1.9 describes NSE method as:

$$P_v = \left( \frac{\Delta B}{2} \right)^{\beta-\alpha} \frac{k_N}{T} \int_0^T \left| \frac{dB}{dt} \right|^\alpha dt \quad (1.9)$$

The above equation is consistent with SE if  $k_n$  is equal to:

$$k_N = \frac{k}{(2\pi)^{\alpha-1} \int_0^{2\pi} |\cos \theta|^\alpha d\theta} \quad (1.10)$$

Knowing  $k$  and  $\alpha$  from SE,  $k_n$  can be obtained by a curve presented in (Bossche *et al.*, 2004)

Recently, a new core loss model called improved-improved generalized Steinmetz equation (i<sup>2</sup>GSE) was introduced for the magnetic materials employed in power electronic systems. The method i<sup>2</sup>GSE considers relaxation process when calculating core loss. The equation (1.9) was extended by an additional term that describes the loss behavior for a transient to constant flux  $P_{rl}$  (Mühlethaler *et al.*, 2012).

$$P_v = \frac{1}{T} \int_0^T k_s \left| \frac{dB}{dt} \right|^\alpha |\Delta B|^{\beta-\alpha} dt + \sum_{r=1}^n P_{rl} \quad (1.11)$$

$P_{rl}$  represents the time-average power loss density due to the  $l^{\text{th}}$  of  $n$  transients to zero voltage.

Most of the described methods were designed for ferrites at higher frequencies. However in electrical hydro generators; the core is usually built with SiFe alloys. The only method that investigated lamination sheets of electrical machines was the modified Steinmetz Equation (MSE) (Krings, Soulrad, 2011).

#### 1.4.2 Loss separation

The discrepancy between measured and calculated losses was one of the main reasons in the development of three components loss model.

In the original Steinmetz work of 1892, one of the experiments was built up with 17 layers of soft kind of sheet-iron and in it, the induction of the eddy-current iron and consequently its losses were found. Steinmetz expressed that the losses for that particular material were the sum of the hysteresis and the eddy-current losses.

An extension of the Steinmetz work was presented in 1956 by Jordan (*apud* Krings, Soulrad, 2011) and the iron losses are separated into static hysteresis loss and dynamic eddy current loss, as seen in Eq.1.12:

$$P_v = P_h + P_c = k_h f B^\alpha + k_c f^2 B^2 \quad (1.12)$$

In this work, the hysteresis loss is considered proportional to the hysteresis loop at low frequencies and the eddy current losses is computed by Maxwell's equation. The coefficient  $k_c$  is equal to  $d^2/12\rho\gamma$  where  $d$  is the thickness of the electric sheet;  $\rho$  is the specific resistivity and  $\gamma$  is the material density.

The model proposed by Bertotti *et al.* (1987, 1992, and 1993) was more complex than all other models discussed above. The physical justification for separation of losses into hysteresis, classical eddy current and excess loss contributions were provided in theses references. It was assumed that the excess loss component is specially governed by the statistical distribution of the local threshold fields at which different magnetic object become magnetically active. Accordingly, the magnetic core losses under sinusoidal flux condition are then given by the Eq. (1.13) as follows:

$$\begin{aligned} P_v &= P_h + P_c + P_e \\ &= k_h f B^\alpha + k_c f^2 B^2 + k_e (fB)^{3/2} \end{aligned} \quad (1.13)$$

Where  $P_h$  is the hysteresis loss,  $P_c$  is the eddy current loss and  $P_e$  is referred to the excess loss. The loss coefficients  $k_h$ ,  $\alpha$ ,  $k_c$ ,  $k_e$  are mostly related to the magnetic material lamination characteristics and can be determined from the measured loss curve function of the flux density.

The separation of the Steinmetz model for hot rolled silicon steel sheets under sinusoidal waveform was also applied by Lee *et al.* (2011). Basically, in electrical machinery equipments, the soft magnetic material operates under 400 Hz and the magnetic flux density inferior to 1.5 T.

The model proposed by Bertotti *et al.* (1987, 1992) was extended to include the impact of the pulsating magnetic flux at multiples frequencies. The last two terms in Eq.1.14 related respectively to the eddy current and excess losses were modified. The losses are computed then taking into account all the present harmonics in the magnetic flux spectrum. The general equation, function of multiples harmonics of the pulsating flux is then given as follows:

$$P_v = P_h + k_c f^2 \sum (n^2 B_n^2) + k_e \int_0^T \left| \sum 2\pi f B_n \cdot \cos(2\pi n f B_n t + \varphi_n) \right|^{1.5} dt \quad (1.14)$$

Another work including the presence of non-sinusoidal magnetic field is presented by Han *et al.* (2010). The proposed method takes into account the minor loops on the hysteresis losses and the time harmonics on the eddy-current losses. The focus of the paper is to compute the rotor losses during high-speed constant power under flux-weakening conditions of Interior Permanent Magnetic synchronous machines (IPM). Generally, the eddy-current losses dominate the hysteresis losses in the IPM's rotor.

The first two terms of the equations are hysteresis loss and eddy-current losses under sinusoidal magnetic field, as discussed earlier; the third term is related to the hysteresis loss

due to the effect of minor loops and the fourth term takes into account the time harmonics on the eddy-current losses.

$$\begin{aligned}
 P_v &= P_{hyst\_sin} + P_{eddy-sin} + P_{hyst\_nonsyn} + P_{eddy\_nonsyn} \\
 &= k_h f^a B^b + k_c f^2 B^2 + k_h f^a B^b \left( \frac{k}{B} \sum_{i=1}^N \Delta B_i \right) + k_c f^2 \sum_{h>1} |h B_h|^2
 \end{aligned} \tag{1.15}$$

where  $k$  is a constant in the range of 0.6–0.7,  $\Delta B_i$  is the flux reversal associated with a minor loop,  $N$  is the number of minor loops and  $B_h$  is the amplitude of the  $h^{th}$  flux harmonic.

The time-domain dynamic core loss model proposed in (Lin *et al.*, 2004) was also used in this study to compute the core losses. This last model was initially applied to compute instantaneous core losses in small electromagnetic devices in both two-dimensional and three-dimensional finite element analysis.

The general equation for this proposed dynamic model is given as follow:

$$P_v(t) = H_{irr} \left( \frac{dB}{dt} \right) + k_c \left( \frac{dB}{dt} \right)^2 + k_e \left| \frac{dB}{dt} \right|^{3/2} \tag{1.16}$$

The three terms in (1.15) are respectively representing the hysteresis, eddy and excess losses given in the time domain.

The procedure for determining the irreversible component of the magnetic field in a static hysteresis loop  $H_{irr}$  is the key to computing the hysteresis loss. The expression of the irreversible component  $H_{irr}$  as proposed in Bottauscio, Cavano (2002) and Lin *et al.* (2004) is given as follows:

$$H_{irr} = \frac{1}{\pi} k_h \cdot B_m \cos(\theta) \quad (1.17)$$

where  $B_m$  is obtained directly from the historical record of the flux density and  $\theta$  is equal to  $2\pi ft$ .

In equation (1.15) the coefficient  $k_c$  of the classical loss (eddy-current) is given as:

$$k_c = \frac{\sigma \cdot d^2}{12} \quad (1.18)$$

The loss coefficients for the hysteresis and excess-loss components  $k_h$  and  $k_e$  respectively, are derived using the curve regression algorithm based on the measured specific core loss curve at different frequencies. Usually, the parameters  $\alpha$  is between 0.8 and 2.3,  $k_e$  and  $k_h$  are calculated from measured core loss data. The parameter  $d$  is the lamination thickness;  $\sigma$  is the material conductivity. More details about the derivation of these different coefficients such as: hysteresis and excess-loss coefficients can be found in these references (Lin *et al.*, 2004) and (Bottauscio *et al.*, 2002).

### 1.4.3 Hysteresis model

The inner area of BH hysteresis loop is proportional to the iron loss; that is why mathematical hysteresis model tries to simulate the shape of the BH curve of a magnetic material. Krings *et al.* (2012) classified the mathematical hysteresis models into: loss surface model (LSM); viscosity-based magneto-dynamic model; energy based vector hysteresis model and friction like hysteresis model.

Other common classification is to separate the hysteresis models into two branches: Preisach model and its modifications and Jiles-Atherton model and its extensions. Preisach develop some hypotheses concerning the physical mechanism of magnetization (Preisach *apud*



Mayergoyz, 1986). Besides, Preisach model considers hysteresis as a superposition of fundamental hysteresis loops.

A variation of the static Preisach model was presented by Dlala (2008) where a magnetodynamic vector hysteresis model was developed. This model produces an accurate overall prediction of the iron loss under alternating and rotational flux excitations in the core laminations of rotating electrical machines.

On the other hand, Jiles-Atherton model (Jiles-Atherton, 1983) considers the mean field approximation theory to describe the initial magnetization curve and the hysteresis loops of the magnetic material; Jiles-Atherton model was further extended in (Jiles *et al.*, 1992).

According to Dlala (2008), it is stated that the attractive features of the Preisach model are its accuracy and generality whereas the Jiles-Atherton model are its speed and simplicity.

## **1.5 Upgrade and uprating of hydro-generators**

According to CERI (Canadian Energy Research Institute) Report, in many areas of the world, notably Europe and North America, there is no room for expansion of hydroelectric power; nearly all of the available sites are in use already [CERI, 2008].

The life expectancy of a hydro-generator depends basically on the mechanical, electrical and thermal stress levels and the maintenance standards.

According to Blecken, the common upgrading procedures in hydro-generators can be summarized as:

- “installation of a new stator winding;
- re-insulation of field coils or installation of new ones;

- installation of static exciter equipment;
- improving the cooling air circuit;
- replacement of stator winding shrouds and
- improving the field pole area and rotor surface” (Blecken, 1997).

Basically, hydropower plant refurbishment can be done as a result of wearing out and obsolescence of equipments or to increase the efficiency of the machine.

According to Koncar company, the refurbishment of a hydro-power plant is a profitable investment that would be refunded and many other benefits effects could be achieved such as:

- “increased reliability;
- reduced production costs;
- increased power and generation of electric energy;
- increased static and dynamic stability;
- extended service life;
- increased efficiency;
- extension of operation area –operating diagram” (Koncar, 2014).

The experience acquired by Manitoba Hydro with hydro-generator core resting, repair and uprated were detailed by Gamblin and Solomon (2002). The 115 MVA machines have been uprated to 132 MVA in a work that includes replacing the turbines, re-insulating field poles, replacing the stator coil windings for an epoxy mica bar type and also converting the stator frame sole plates from rigid anchored type to radial key design. The results of the core loop test are also presented and it was helpful to locate a hidden are of core damage.

When a machine is considered for upgrade, a multi dynamic study (electromagnetic, thermal, mechanical) should be done to take into account the coupling between the different physical

domains. In Figure 1.1, it can be seen the interconnections between electromagnetic field analysis and the mechanics (acoustic, thermal and fluid dynamics) and also the electric grid.

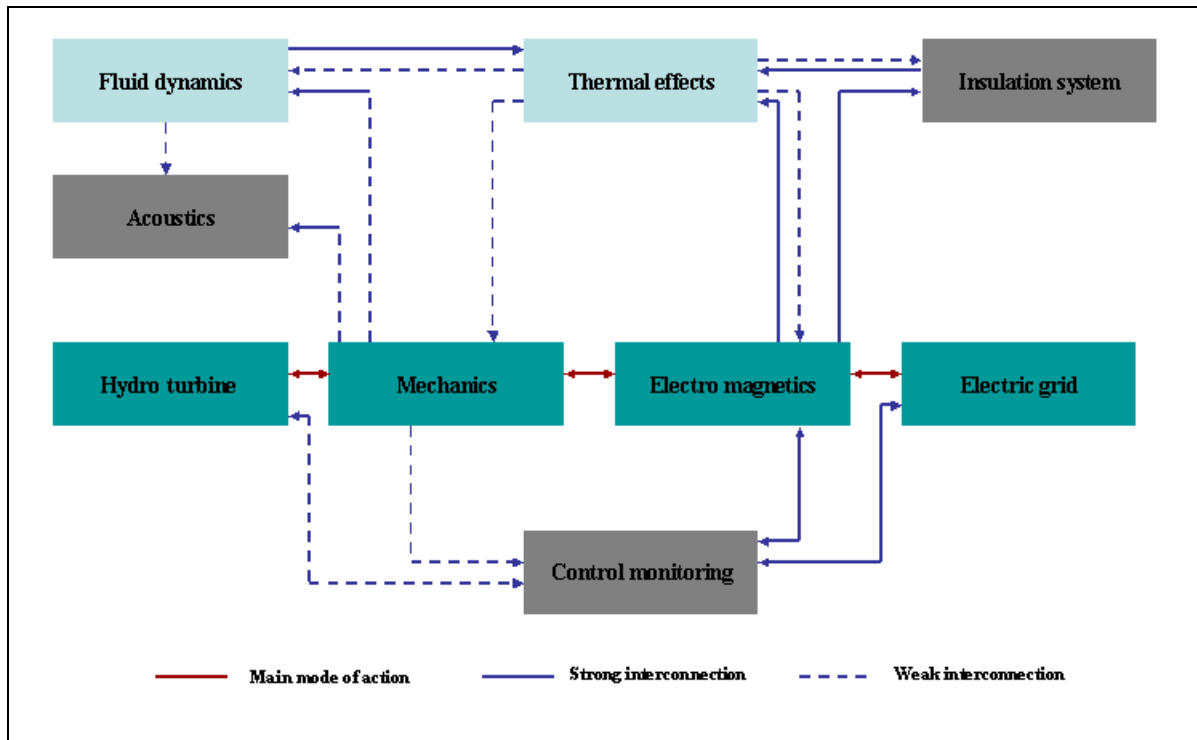


Figure 1.1 Physical domains and coupling between them  
Extracted from Lahres (2007, p.14)

In AUPALE project of Hydro-Quebec, three fields of science were combined: electrical, for the determination of the electromagnetic field and loss distribution; mechanical, for determination of the fluid motion and also for the determination of the vibration components and thermal for the determination of the hot spots in the machine. This thesis focuses on the problematic of determination of the electromagnetic domain.

## 1.6 Fault detection in electric machines

The electrical faults in electrical machines are classified as stator and rotor faults. Examples of stator faults include: stator faults resulting in the opening or shorting of the stator phase

windings; abnormal connection of the stator windings. Examples of current problems on the rotor are faults due to, broken rotor bar; cracked rotor end-rings and shorted rotor field winding (Vas, 1993; Agrawal *et al.*, 2011; Siddiqui *et al.*, 2014).

The detection, location and analysis of faults play a vital role in the safe and reliable operation of electrical machines. In order to correlate troubleshoot symptoms and determine the course of action to identify the failures, several fields of science must be combined whenever it is possible (Negrea, 2006).

The recent problems experienced with motor and generator windings were investigated by Clyde *et al.* (2004); Stone *et al.* (2009). In the stator, problems such as electric stress control problems; loose coils in slots; vibration sparking; end winding partial discharge and end winding vibrations have led to failures in as short as 5 years of operation (Stone *et al.*, 2009). In the rotor, the most common causes of failure in salient pole generators are the continuous centrifugal forces imposed on them by rotation and the cyclic centrifugal forces induced by starting and stopping the machine (Stone *et al.*, 2009). Besides, the static and the dynamic eccentricity were analyzed in a three phase induction motor (Nandi *et al.*, 2001). The papers (Vas, 1993; Nandi *et al.*, 2001; Clyde *et al.*, 2004; Negrea, 2006; Stone *et al.*, 2009; Agrawal *et al.*, 2011; Siddiqui *et al.*, 2014) present monitoring techniques for detection of the mechanical and electrical faults.

When a stator winding failure occurs in large electrical machines it is possible to make a temporary repair by cutting out and bypassing the failed coils, keeping the safety operation of the machine, and permitting a quick return to service of the machine (Brighty *et al.*, 1987).

However, a machine with parallel windings, the removal of stator coils has the following effects on the phase where the coils are removed:

- imbalance voltages across the parallel circuits in the phase;
- introduction of a phase shift between parallel circuits of one phase;

- reduction in leakage inductance of the circuits.

Since all parallel circuits are connected together in one phase and the voltage across each parallel must be equal within the phase, removing a coil creates circulating currents between parallel circuits in amounts that will depend on the particular coil which is removed. In addition, the average phase voltage will be reduced, and a phase shift in the net phase voltage from the ideal value may be introduced. In turn, this results in imbalance in phase voltages for the machine and negative sequence currents.

In fact, a few publications regarding cut out coils are presented in the literature. Reference (Brune, Seinsch, 2006) analyzed the performance of 3-phase motors after disconnecting some of its damaged coils. The constant and pulsating torques, the losses, the current distribution and the magnetic pull were computed using an analytical method with certain comparison with the experimental results. In addition, the performance of synchronous machines operating with imbalance in stator coils was analyzed by Rhudy *et al.* (1988) and the electrical and mechanical effects concerning the mechanical forces associated with the circulating current were presented.

A hydroelectric generator with bypassed stator coils was studied in DeHaan (1999) and the imbalance split-phase stator winding currents and the stator and rotor temperature were measured. Comparing the current measured and calculated in Brighty *et al.* (1987), it was concluded that an overestimation of 0.2 p.u. was observed. Reference (Brighty *et al.*, 1987) provides a conservative calculation method to predict the magnitude of circulating current. Actual measurements of current in each parallel circuit of the winding may be necessary when higher accuracy is required.

Depending on the number of bypassed coils and their positions in the winding, the machine can be operated even at full load when the winding temperature limits of different circuit do not exceed the values recommended by different standards. However, in certain cases, the

machine needs to be de-rated to keep the level of the current within the acceptable range and at the same time maintain at the corresponding temperatures.

With the advance in powerful computation, finite element method is now widely used to determine many characteristics of large rotating electrical machines such as: the core loss distribution in different parts of the machine (Aguiar *et al.*, 2013c, 2014; Ionel *et al.*, 2007) at different operating conditions including in partly damaged machines. Recently, complete models of large machines were simulated to investigate the effects of the cut-coil bar using FEM (Aguiar *et al.*, 2013c).

In this thesis, an investigation of the performance characteristics of a large hydro-electric machine with bypassed stator winding coils is presented using finite element analysis. The simulation results thus obtained for this configuration are discussed in Chapter 6, session 6.2.

## **1.7 Conclusions**

In the first chapter an extensive literature review was performed on the subjects of hydro-generators, analytical and numerical methods used in electromagnetic field simulations, the types of losses in electrical machines and finally the existing models to compute the core loss of magnetic materials. Previous studies on the calculation of core loss, damper bar currents and losses, eddy current and thermal effects in large hydro-generators were highlighted. Besides, the iron loss models were classified into: Steinmetz equation and its modifications, loss separation and hysteresis model and each of these topics were detailed. It was also shown that the joint effort of the academia and the industry will be beneficial for a better understanding of the complex phenomena of electromagnetism in order to improve the future designs or to upgrade the existing machines.

## CHAPTER 2

### COMPONENTS HYDRO-GENERATORS

This chapter starts with a brief introduction to the Quebec's electricity production, followed by the causes and consequences of the uprating and upgrading hydro-generators. Further, the components of a hydro-generator are detailed and the two machines under study are presented. Finally, the conclusion is discussed.

The electricity produced by Canada is based on hydro power generation. According to 2013 Hydro-Québec Annual Report, the installed Hydro-Quebec power capacity is 36 068 MW, where 35 364 MW (98.05%) was produced by hydroelectric generating stations, as showed in Table 2.1.

Table 2.1 Hydro Quebec energy production

<b>Generating facilities</b>	
Hydroelectric generation stations (60)	35 364 MW
Thermal stations (26)	704 MW

Hydro-Quebec generates, transmits and distributes electricity and it uses mostly hydro-power as generating option. Hydro-Quebec also supports the development of other technologies to generate power using energy sources such as wind, solar and biomass. Four other hydroelectric generating stations are planned or under construction that will add 1550 MW of power in the next couple of years (Annual Report, 2013).

Hydro Quebec has 61 hydroelectric generating stations. Robert-Bourassa, La Grande-4, La Grande-3 and La Grande-2A are the four hydroelectric stations with higher installed capacity, 5 616 MW, 2 779 MW, 2 417 MW and 2106 MW respectively.

## 2.1 Machine components

The synchronous machine is based on two structures made of ferromagnetic material: stator and rotor. The rotor is the part that rotates and is composed also of two windings: field and damper. The stator is the fixed part, also known as armature, and it has slots and stator windings.

Figure 2.1 presents the model of the electrical hydro generator. In this thesis, the studied electrical generators consist of low-speed synchronous machines with salient poles. Synchronous generators can generate active power and also of generate or absorb reactive power.

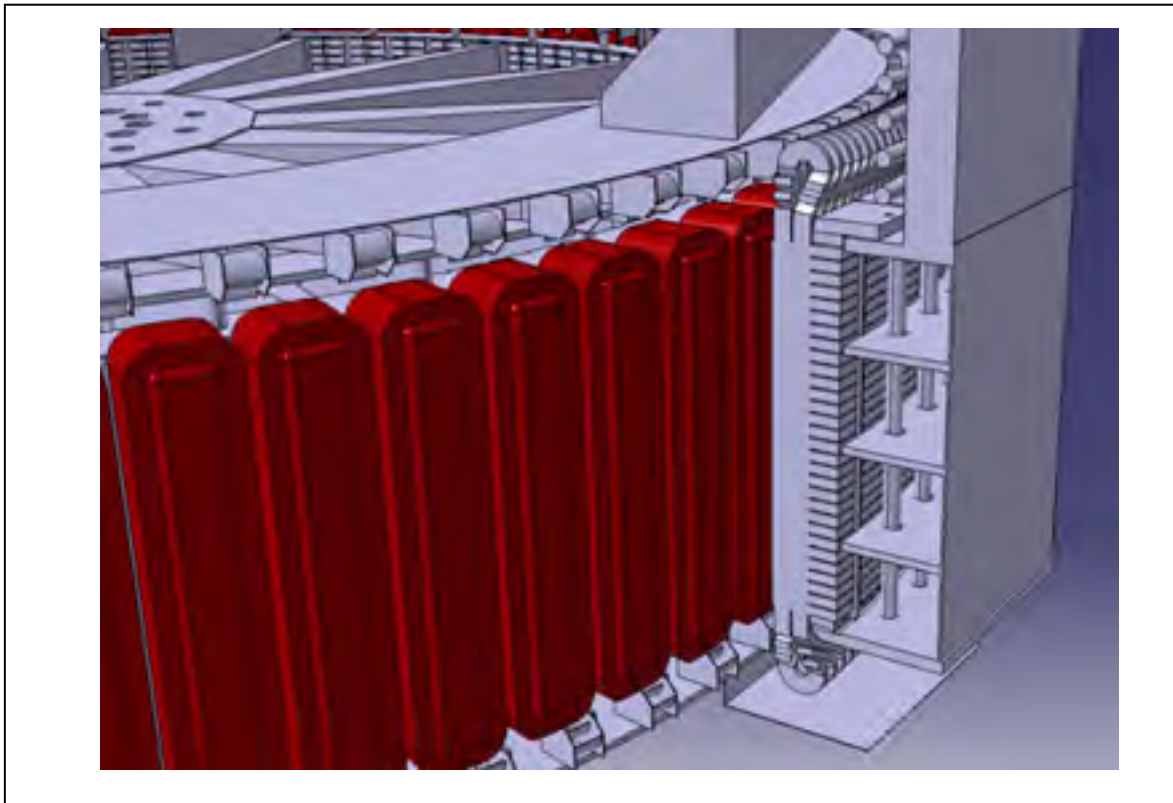


Figure 2.1 Hydro generator  
Extracted from Hudon presentation (2012)



In the following subsections the most important parts of the generator are described: stator core, stator windings, rotor core, damper bars, field windings and the airgap.

### 2.1.1 Stator

The main functions of hydro generator stator core are to conduct magnetic flux, transmit machine torques, provide space and support for stator winding, serve as a part of machine cooling circuit, and provide grounding plane for stator winding slot sections (Znidarich, 2008a).

The stator winding of a generator (also known as armature winding) delivers active power to the electrical system. In synchronous salient pole machines the stator windings are distributed and arranged in fractional pitch-coils. Besides, it is also in two layers called, double-layer windings.

In large hydro electrical machine, the number of slots per pole per phase is usually fractional. This fraction can be determined as:

$$q = \frac{N_s}{2p.n} \quad (2.1)$$

where  $q$  is the number of slots per pole per phase,  $N_s$  is the number of stator slots,  $p$  is the number of pole pair and  $n$  is the number of phases.

In the initial stage of the design of a machine, the number of slots, the type of winding, and the coil-pitch have to be specified.

Some combinations of number of slots per pole could lead to low fundamental winding factor. These combinations have to be avoided during the machine design stage. A fractional

$q$  also avoids sub-harmonics and leads to the production of a sinusoidal (or close to sinusoidal) Electro-Magnetic Force (EMF).

Certain harmonics can also be reduced by the proper selection of the coil-pitch. Besides, short coil pitches reduces the amount of copper and consequently the copper losses in the end-connections of the windings.

Increasing the number of stator slots improves the sinusoidal distribution of windings; however, the number of slots cannot be extremely large because it can result in narrow teeth and consequently in more chances of saturation in this region. Moreover, the maximum allowable current density in the stator windings has a great impact on the slot dimensions. Besides, the slot dimension is directly related to the eddy current losses. Figure 2.2 shows two different teeth dimensions for the same machine.

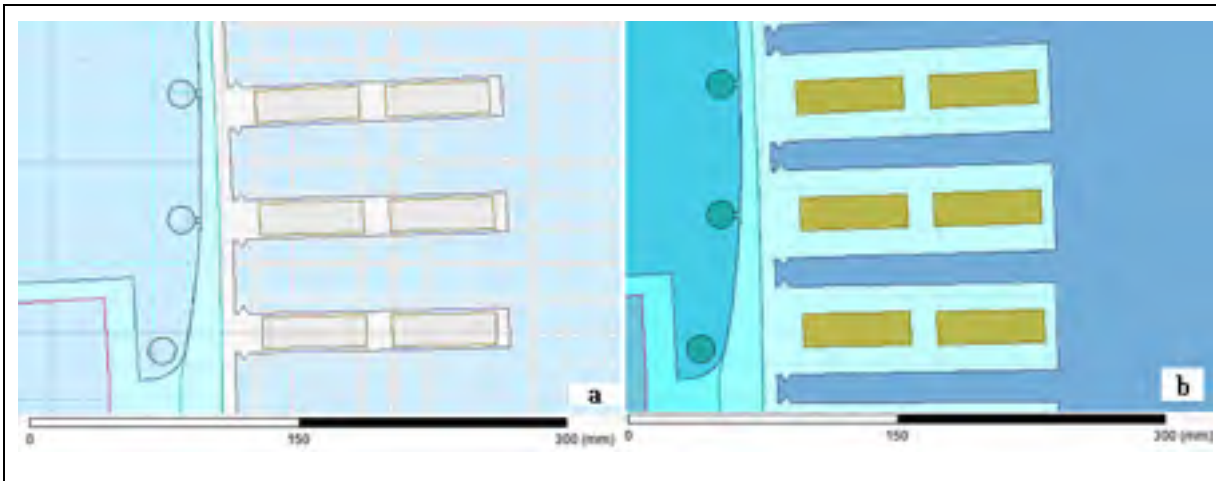


Figure 2.2 Teeth dimensions – a) designed machine, b) smaller teeth dimensions

In the end, the teeth size is always a combination of multiple factors. It cannot be too big; to avoid high core loss but also cannot be too small, because of the concentration of the flux in a small region, leads to possible saturation areas and later on to problems regarding insulation and thermal losses.

In addition, one way to improve the quality of the voltage wave of electrical machine is to skew the stator slot and the rotor.

The stator slots cause oscillations in the airgap flux that induce currents in the damper bars. The fractional slot winding induces magneto-motive force harmonics of pitches greater than two field poles as well as shorter ones (Calvert, 1938).

Certain harmonics can be reduced by the proper selection of the coil-pitch. Besides, short coil pitches reduce the amount of copper and consequently the copper losses in the end-connections of the windings.

Besides the number of windings in parallel branches ( $n_p$ ), the number of stator slots is determined by the eq. (2.2) (Walker, 1981):

$$n_p = \frac{N_s T_c}{3T_{ph}} \quad (2.2)$$

Where  $T_c$  is the number of turns per coil,  $T_{ph}$  is the number of turns per phase and  $N_s$  is the number of stator slots.

A hydro-generator stator core is axially and radial segmented, and separated by radial vents for passage of cooling air. The main function of radial ventilation ducts is to maximize the surface contact area between the cooling air and stator core surfaces for more efficient cooling and heat removal (Nailen *apud* Znidarich, 2008a).

In the stator, the armature winding is assigned in the slots. The latter consists in three windings with magnetic axis whose phases are shifted by  $120^\circ$  between them. The windings produce a magnetic field that spins in the same mechanical speed of the rotor. The

distribution of the windings on the slots has the objective to produce a Magneto-Motive Force (MMF) a waveform as close as possible to a sinusoidal shape.

The stator slots openings produce variation of the permeance in the airgap; these variations are displayed as ripples in the airgap flux density. Due to the MMF frequencies and the tooth ripple harmonics, losses will occur in the damper windings and the pole shoes. The MMF harmonics cause induced voltage and current, and consequently, Joule losses ( $I^2R$ ).

According to Znidarich, the 0.50 mm thick core is almost universally selected for hydro-generator stator cores because it is the best combination for low loss at low costs (Znidarich, 2008b).

Figure 2.3 shows the stator of a large hydro electrical machine. This machine has an external diameter over 10 meters.

The fact that the stator windings are embedded in the slots causes flux lines to gather above the teeth, inducing ripples in the distribution of magnetic flux density in the airgap. By selecting coil pitch of the windings certain harmonics in the phase EMF can be reduced or even suppressed.



Figure 2.3 Stator of a large synchronous machine

On the stator side, as shown in Fig. 2.4, the outer ( $DeCM$ ) and inner diameter ( $Do$ ), the number of slots, the stacking factor and slot type and sizes ( $Ws$  and  $Ls$ ) are some of the general parameters necessities for the construction of the geometric model.

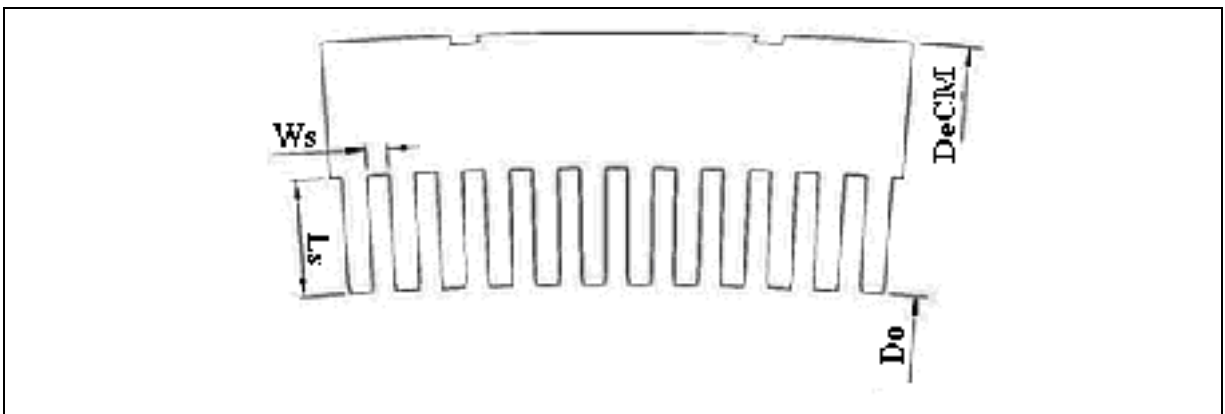


Figure 2.4 Stator core geometry

Besides, some parameters of the stator winding must be added such as number of winding layers, winding type, coil pitch and stator insulation.

In electrical machines, the field windings and the stator windings can be considered as stranded conductors. In the stator winding AC current is induced. Fig 2.5 shows the stator side of a large hydro machine, in it the stator core and the stator's winding can be seen. In the drawing, the geometry of the winding is observed, with the stranded conductors and the insulation between them.

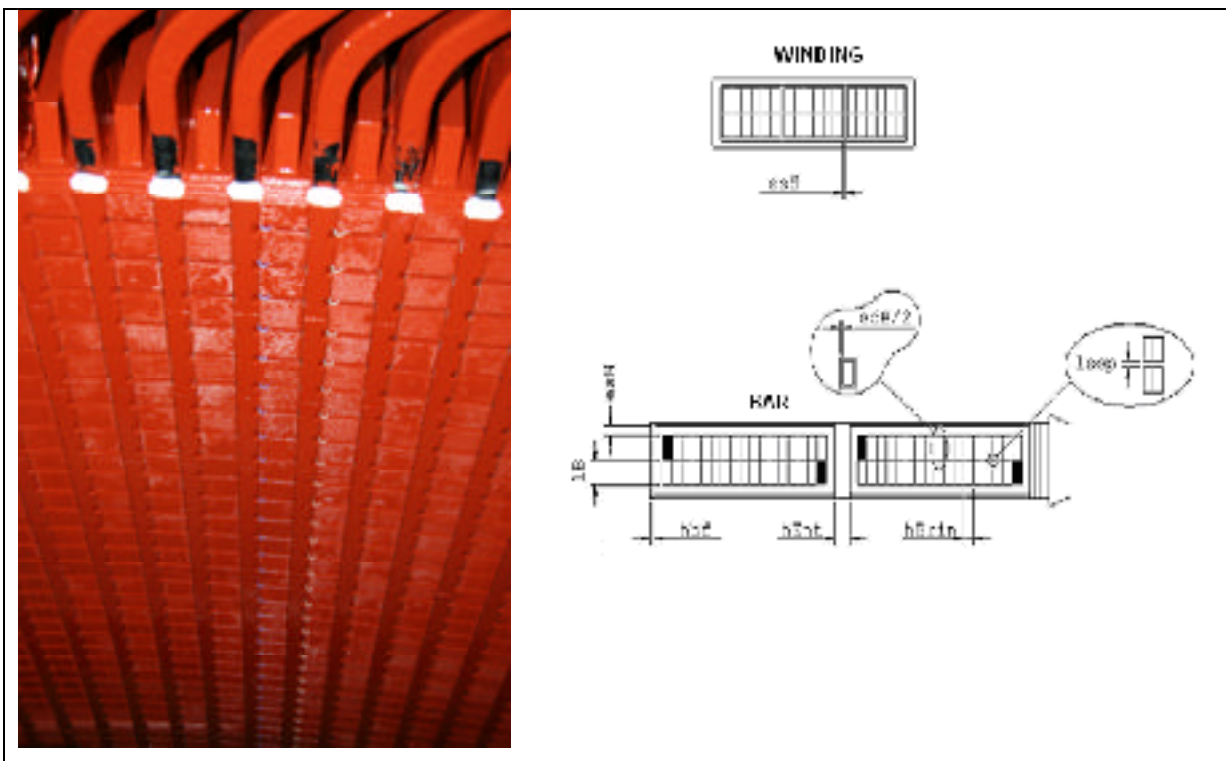


Figure 2.5 Stator winding geometry

When in an electrical machine, the ratio of slots per pole is not an integral number, this machine is called fractional slot machine. In this type of machine, the presence of MMF wave varies from pole to pole. This is the reason why, it is necessary to model more than one pole to have a correct representation of the machine's electromagnetic fields.

Besides, fractional winding has shorter end windings and this gives additional space and also gives a possibility in cost saving while manufacturing (Salminen, 2004).

Several winding possibilities of a fractional winding can be selected. The best choice should take into account the amplitude of the MMF harmonics.

The actual stator winding sequence of Manic 21 is presented in Fig. 2.6. This sequence is repeated 12 times in the machine.

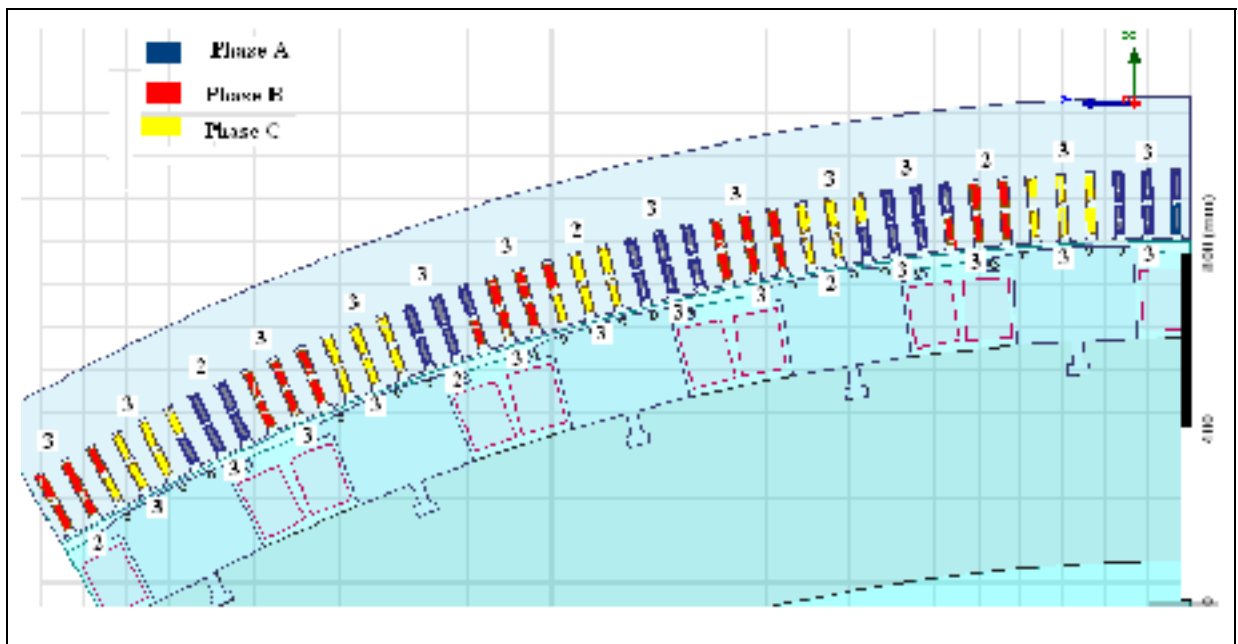


Figure 2.6 Stator winding

For Manic 21, the 3-phase, 2-layer winding can be arranged in 42 slots ( $504/12$ ) as presented at Table 2.2:

Table 2.2 Winding sequence example

Air Gap Side Stator Coils				Back Stator Coils			
3	Coil 1	A+	PhA 1	3	CoilRe 9	A-	PhARe 9
	Coil 2	A+	PhA 2		CoilRe 10	A-	PhARe 10
	Coil 3	A+	PhA 3		CoilRe 11	A-	PhARe 11
3	Coil 4	C-	PhC 4	3	CoilRe 12	C+	PhCRe 12
	Coil 5	C-	PhC 5		CoilRe 13	C+	PhCRe 13
	Coil 6	C-	PhC 6		CoilRe 14	C+	PhCRe 14
3	Coil 7	B+	PhB 7	3	CoilRe 15	B-	PhBRe 15
	Coil 8	B+	PhB 8		CoilRe 16	B-	PhBRe 16
	Coil 9	B+	PhB 9		CoilRe 17	B-	PhBRe 17
3	Coil 10	A-	PhA 10	3	CoilRe 18	A+	PhARe 18
	Coil 11	A-	PhA 11		CoilRe 19	A+	PhARe 19
	Coil 12	A-	PhA 12		CoilRe 20	A+	PhARe 20
2	Coil 13	C+	PhC 13	2	CoilRe 21	C-	PhCRe 21
	Coil 14	C+	PhC 14		CoilRe 22	C-	PhCRe 22
3	Coil 15	B-	PhB 15	3	CoilRe 23	B+	PhBRe 23
	Coil 16	B-	PhB 16		CoilRe 24	B+	PhBRe 24
	Coil 17	B-	PhB 17		CoilRe 25	B+	PhBRe 25
3	Coil 18	A+	PhA 18	3	CoilRe 26	A-	PhARe 26
	Coil 19	A+	PhA 19		CoilRe 27	A-	PhARe 27
	Coil 20	A+	PhA 20		CoilRe 28	A-	PhARe 28
3	Coil 21	C-	PhC21	3	CoilRe 29	C+	PhCRe 29
	Coil 22	C-	PhC22		CoilRe 30	C+	PhCRe 30
	Coil 23	C-	PhC23		CoilRe 31	C+	PhCRe 31
3	Coil 24	B+	PhB 24	3	CoilRe 32	B-	PhBRe 32
	Coil 25	B+	PhB 25		CoilRe 33	B-	PhBRe 33
	Coil 26	B+	PhB 26		CoilRe 34	B-	PhBRe 34
2	Coil 27	A-	PhA 27	2	CoilRe 35	A+	PhARe 35
	Coil 28	A-	PhA 28		CoilRe 36	A+	PhARe 36
3	Coil 29	C+	PhC 29	3	CoilRe 37	C-	PhCRe 37
	Coil 30	C+	PhC 30		CoilRe 38	C-	PhCRe 38
	Coil 31	C+	PhC 31		CoilRe 39	C-	PhCRe 39



Air Gap Side Stator Coils					Back Stator Coils			
3	Coil 32	B-	PhB 32	3	CoilRe 40	B+	PhBRe 40	
	Coil 33	B-	PhB 33		CoilRe 41	B+	PhBRe 41	
	Coil 34	B-	PhB 34		CoilRe 42	B+	PhBRe 42	
3	Coil 35	A+	PhA 35	3	CoilRe 43	A-	PhARe 43	
	Coil 36	A+	PhA 36		CoilRe 44	A-	PhARe 44	
	Coil 37	A+	PhA 37		CoilRe 45	A-	PhARe 45	
3	Coil 38	C-	PhC 38	3	CoilRe 46	C+	PhCRe 46	
	Coil 39	C-	PhC 39		CoilRe 47	C+	PhCRe 47	
	Coil 40	C-	PhC 40		CoilRe 48	C+	PhCRe 48	
2	Coil 41	B+	PhB 41	2	CoilRe 49	B-	PhBRe 49	
	Coil 42	B+	PhB 42		CoilRe 50	B-	PhBRe 50	

The choice of the slot combination and slot pitch has to be carefully made and in many cases it should be possible to avoid (or minimize) the objectionable harmonics. MMF harmonics produce losses, additional reactance, torques, radial forces and noise (Calvert, 1938).

### 2.1.2 Rotor

The rotor of a salient-pole synchronous machine consists of the pole shoes, pole shaft, rotor spider, field winding and the damper bars.

The pole shoes are built as laminated iron stack. The pole shoe is laminated to suppress the eddy currents induced by the slot ripple in the airgap magnetic field and consequently to reduce the eddy current losses in the area.

In a synchronous machine, the rotor, together with the magnetic field generated by DC current of the rotor field rotates at the same speed (timing) with respect to the rotating magnetic field produced by the currents in the stator winding resulting in a constant torque.

In the case of salient poles, examination of the magnetic circuit of the stator MMF reveals that the permeance of this circuit changes with the rotor position due to the variations of the airgap.

Figure 2.7 presents the rotor of a large synchronous machine where 7 poles are observed.



Figure 2.7 Rotor Manic 21

The salient poles have field winding surrounding pole bodies. With a proper pole shape face, non uniform airgap is obtained and it produces the distribution of the radial airgap flux density closer to a sinusoidal waveform.

In the pole face, three radii can be observed, as seen in Fig. 2.8. The first radius is the curvature and the distances to the second and third radii must be introduced. The shape

salient pole is chosen to keep the harmonic content in the air gap flux wave within reasonable limits.

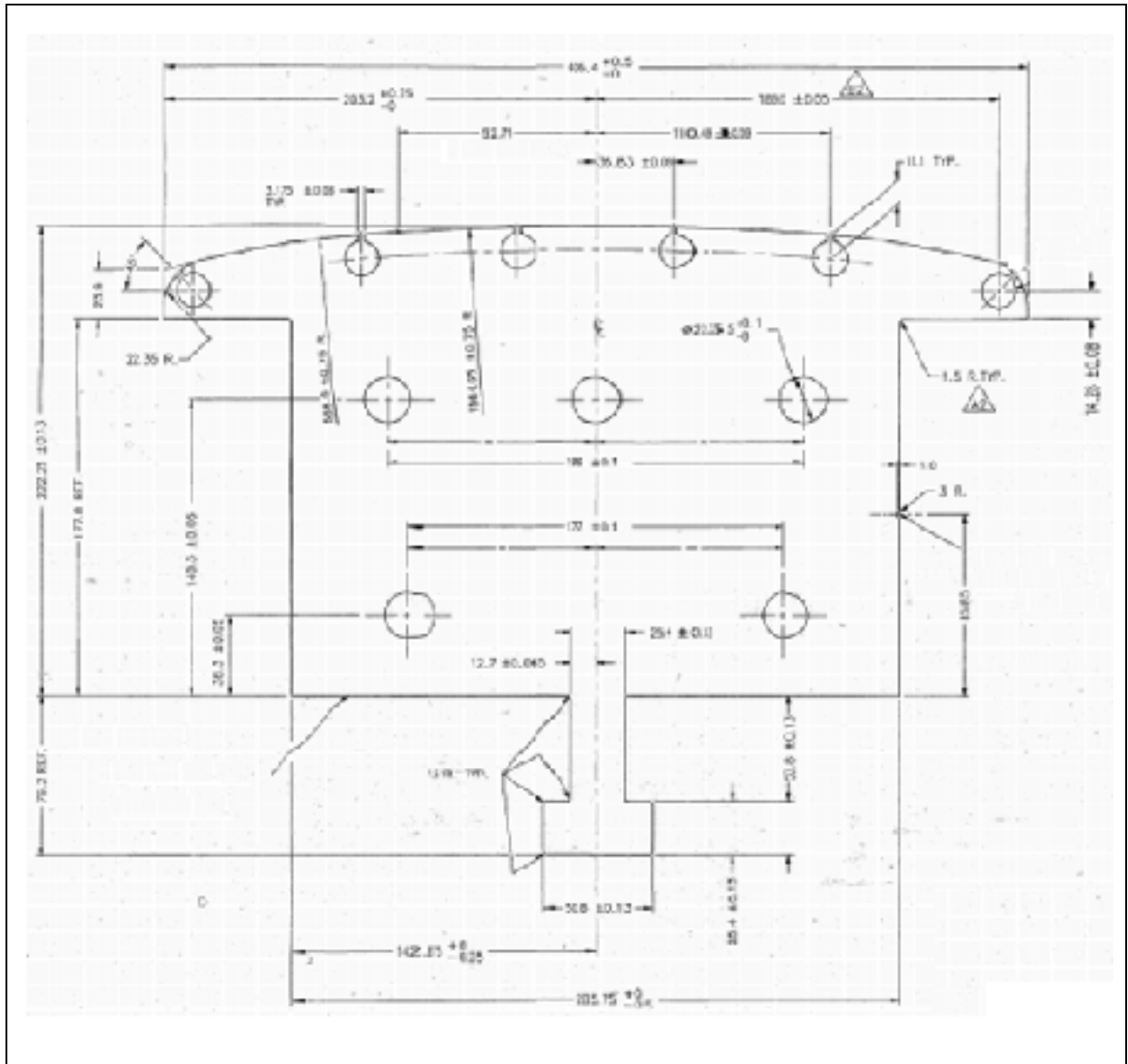


Figure 2.8 Pole shoe shape  
Extracted from Alstom drawings (HQ files)

The pole shape plays an important role in the determination of total core loss. In Fig. 2.9, the first machine considered has a rotor with two radii and in the second one the rotor has three radii.

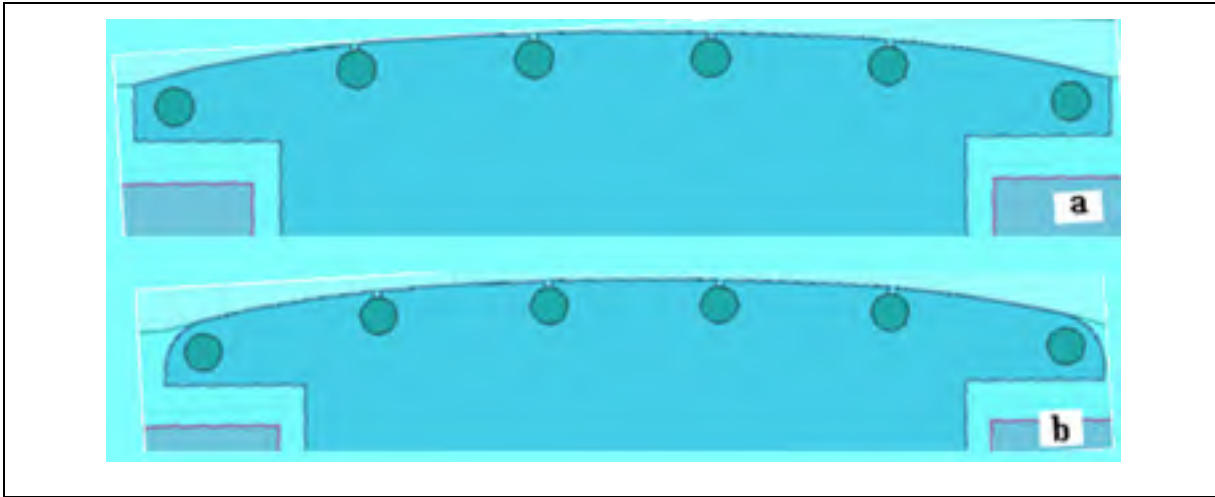


Figure 2.9 Pole shape definition – a) 2 radii b) 3 radii

The geometry of the shape of the pole face in large hydro-generator affects many parameters or aspects of the electromagnetic design, such as: voltage waveform; voltage distortion and interference with telephone lines (telephone interference factor); reactance; airgap stiffness; magnetic noise; vibration and electromagnetic losses (Merkhouf, 2003).

In order to reduce the additional rotor losses, the rotor magnetic material can be laminated. As the rotor rotates, centrifugal forces are observed in the poles and the field winding, so the thickness of the rotor laminations is usually larger than the stator ones.

Moreover, many parameters must be added to complete the model of the rotor such as the number of damper bars, their type and the distance between one and the other, as shown in Fig. 2.10.

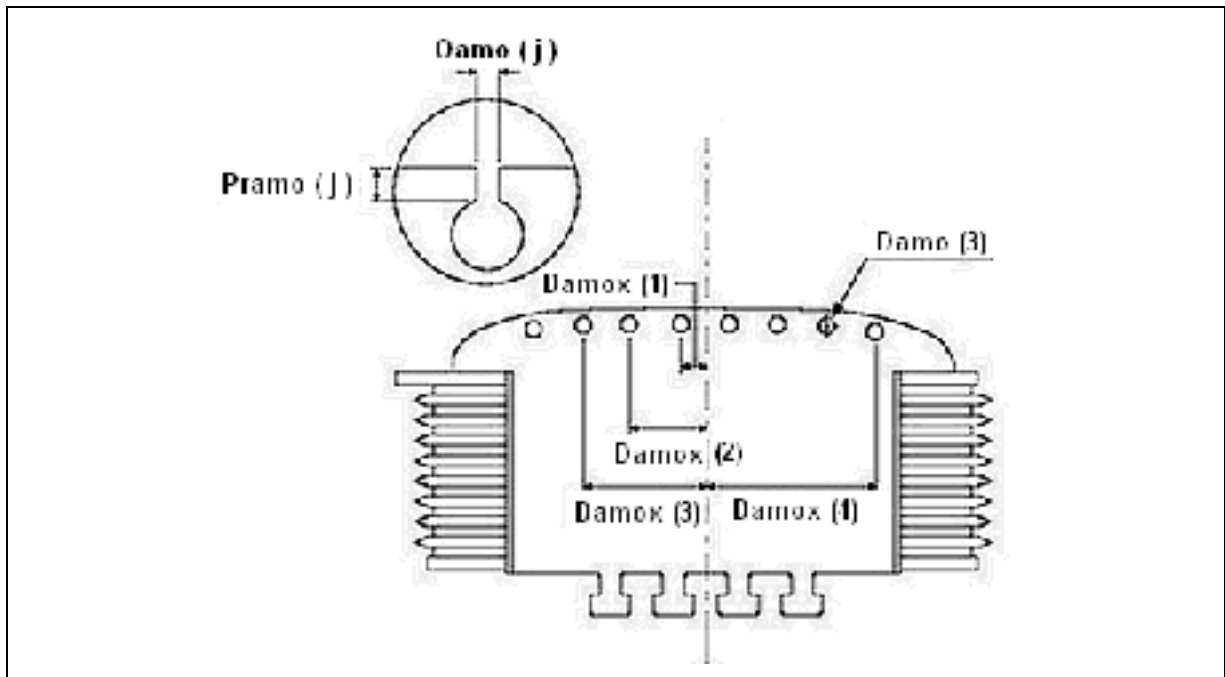


Figure 2.10 Damper bars positioning

Where:  $Oamo$  is the tangential width opening in the pole face;  $Pramo$  is radial depth of the bar relative to the pole face;  $Damo$  is the damper bar diameter and  $Damox$  is the distance in x-axis between the center of the pole and the center of the damper bars.

The damper bars can be classified into two types. It can either be complete (with damper ring) or be of the pole-grid type (without pole connection). The damper winding is disposed on the slots on the rotor pole shoe, as shown in Fig. 2.11. The damper winding of salient pole synchronous machine is usually short-circuited cage winding and its material used is generally copper. Damper windings are also called amortisseur windings.

The main purpose of the amortisseur winding is to dampen oscillations that result from mechanical or electrical disturbances. Besides, it is also employed to speed-up the machine during the start-up (Zhan, 2010).

The damper windings are effective in reducing peak voltages during short-circuits and also in improving system stability (Karmaker, 1982).

The damper winding performs the following tasks (Traxler-Samek *et al.*, 2010):

- “damping of torque oscillations;
- reduction of parasitic airgap magnetic-field harmonics;
- suppression of the negative sequence field at unbalanced-load operation;
- protection of the excitation winding at transient faults;
- transient stability.”

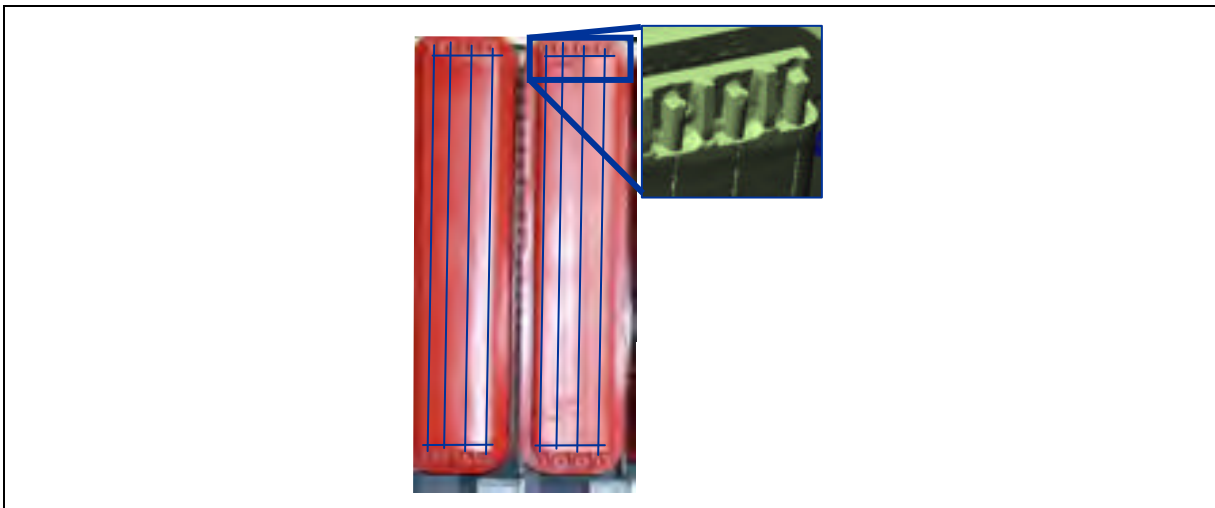


Figure 2.11 Rotor poles and damper windings in a typical hydro generator

At steady-state condition, the airgap magnetic field harmonics induce voltages in the damper bars and lead to compensating currents resulting in power losses. The field harmonics are caused by: tooth ripple harmonics and armature reaction (Traxler-Samek *et al.*, 2008b).

In general, the stator and rotor slot pitches are not the same, in this way, a phase difference between EMFs in the successive bars on the same salient pole is obtained. Thus, an unequal current distribution between the bars is produced. Usually, the outer bar currents are greater than the inner bars (Walker, 1947). Besides, the slot pole of the rotor has to be selected in

order to deviate about 10 to 15% from the stator slot pitch to avoid the harmful effects of the flux harmonics, such as noise (Pyrhönen *et al.*, 2009).

To damp counter-rotating fields produced by unbalanced load currents a small resistance is select to the damper windings. Besides, the cross-sectional area of it is often chosen to be 20 to 30% of the cross-sectional area of the armature winding (Pyrhönen *et al.*, 2009).

In salient pole synchronous machines, the rotor contains a field winding (shown in Fig 2.12) which is excited by a DC current.

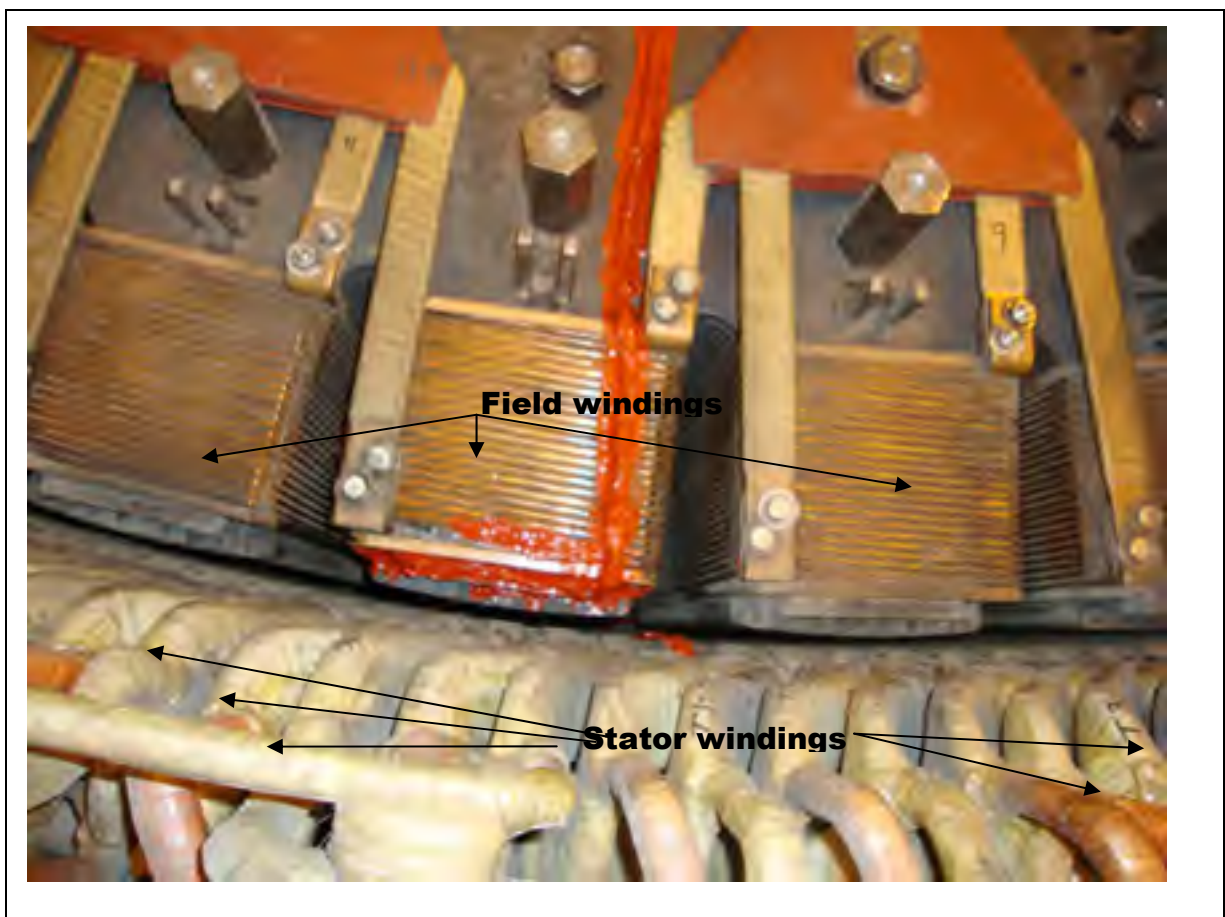


Figure 2.12 Field winding

The field coils are wound on an iron magnetic core which guides the magnetic field lines. In salient pole generators, the field windings are placed in the rotor, which rotate within it. The field winding behaves as an electromagnet producing a magnetic field of strength proportional to the applied field current. The field windings generate the magnetic field requested for the energy conversion.

### **2.1.3 Airgap**

The area between rotor and stator in a synchronous machine is called airgap. The airgap in a hydro machine is eccentric, non-uniform and it presents a small length size.

The eccentricity means that the rotor and the stator are not concentric. The non-uniformity of the airgap is observed because of the configuration of the salient poles. In this type of machine, the airgap length measures some millimetres, which is a small value when compared to the diameter of the machine. For instance the air gap of one of the studied machines in this thesis is of 15.875 mm for a stator external diameter of 11m.

The size of the air gap influences many parameters. For instance, an increase in the airgap length results as an increase in the reluctance. Besides, the length of the air gap impacts the airgap magnetic flux which consequently influences the damper bar currents.

The non-uniformity of the air gap of the salient pole machines result that the reluctance path of the airgap varies according to the position of the machine's rotor (Szabados, 2014).

The airgap offers the possibility for the direct measurement of individual harmonic loss on the stator and on the rotor region. Figure 2.13 shows the rotor, the stator and the air gap of a hydro generator.



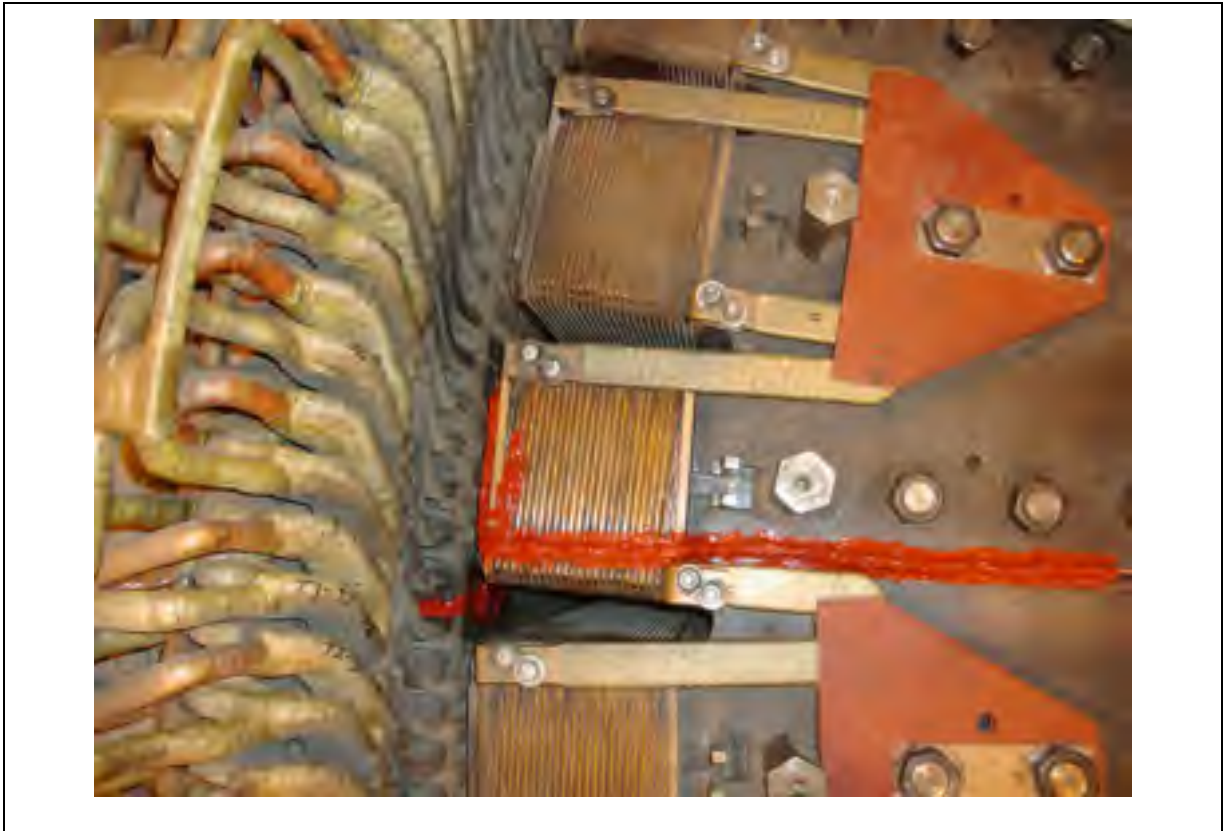


Figure 2.13 Rotor, stator, coil sensor and RTD sensor during instrumentation stage

The pulsation of the airgap flux is due to the slot openings in the airgap region. The fundamental tooth harmonic frequency  $F$  is given by equation 2.3:

$$F = (2s \pm 1)f \quad (2.3)$$

Where  $s$  is the number of stator slots per pole and  $f$  is the generator frequency.

## 2.2 Studied machines

Two machines were simulated (Manic 21 and Rapide-des-Quinze) using 2D finite-element method. Manic 21 was studied with the purpose of increasing its power output and Rapide-

des-Quinze was investigated to understand the operating behaviour of a hydro-generator operating with damaged coils.

The simulation results of Manic 21 are detailed in Chapter 5 and 6, and those of the other machine in Rapide-des-Quinze are also presented in Chapter 6.

Table 2.3 presents the hydro stations under investigation during the course of this research work with their installed capacities; the number of units; the type of the generating facility and when they were constructed.

Table 2.3 Hydro stations studied  
Adapted from: HQ website

<b>Name</b>	<b>Watersheds</b>	<b>Type</b>	<b>Installed Capacity (MW)</b>	<b>Number of Units</b>	<b>Head (m)</b>	<b>Commissioning Date</b>
Manic-2	Minicouagan	Run-of-river	1,145	8	70.11	1965-1967
Rapide-des-15	Ottawa	Run-of-river	103	6	25.9	1923-1955

### 2.2.1 Manic 21

Manic 2 Station was constructed in 1967 and the generator's stator was refurbished in 2009. The investigated generator has the rating of 122.6 MVA, 60 poles, 504 slots, 13.8 kV, 120 rpm, 60 Hz with 6 damper bars per pole. Table 2.4 presents the manufacture parameters of Manic 2.

Table 2.4 Generator design and electrical parameters for Manic 21

Parameter		Value	Units
General	Power (summer/winter)	122.6 / 150.7	MVA
	Rated speed	120	rpm
	Rated frequency	60	Hz
	Power factor	0.9	
	Machine active length	1626	mm
	Airgap length (cold)	15.875	mm
	Cooling system: water (summer / winter)	15 / 5	°C
Stator	Number of phases	3	
	Type of connection	Y	
	Number of slots	504	
	Number of bars per slot	2	
	Number of slots/ pole/ phase	2 4/5	
	Number of parallel circuits	3	
	Phase winding resistance (25 °C)	0.00232	Ω
	Slot width	23.24	mm
	Slot height	159	mm
	Stator outer diameter	11277.6	mm
	Stator inner diameter	10617.2	mm
	Insulation class	F	
	Maximum temperature	110	°C
	Winding sequence	3 3 3 3 2	
Rotor	Number of poles	60	
	Pole body height	177.8	mm
	Rotor outer diameter	10585.5	mm
	Rotor inner diameter	9099.6	mm
	Field conductor section	402.6	mm <sup>2</sup>
	Number of turn	30	
	Field winding resistance (25 °C)	0.3369	Ω

The capability curve of the studied generator is presented at Fig. 2.14. The capability curve provides the boundaries within the generator can operate safely. In the x-axis, the active power in p.u. and in the y-axis, the lagging reactive power also in p.u., so, when the active power and voltage are fixed, the reactive power loading is limited by the field winding heating.

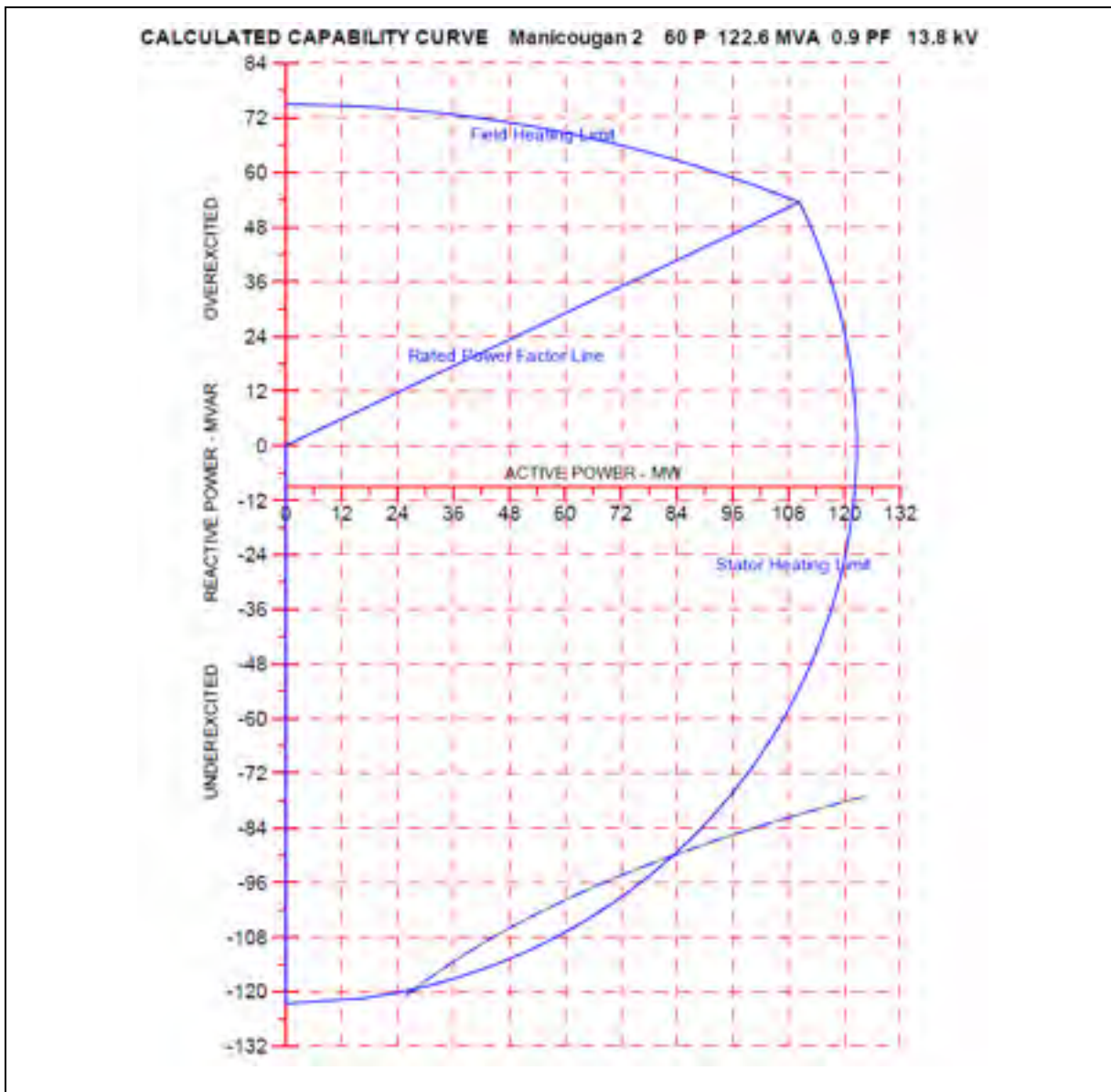


Figure 2.14 Capability curve  
Provided by Andritz Company (2014)

The armature winding has a heating limit depending on its insulation class. This heating limit is directly related to the active power. The curve produced relating the active power, the reactive power and the armature winding heating limit is called ‘stator heating limit’

Another curve that establishes the heating limit is the “field heating limit”. This limit is caused by the heating limit of the conductor in the field winding.

The rated power factor line determines the maximum active power that the machine is able to generate under the rated operating conditions.

### 2.2.2 Rapide-des-Quinze

Rapide-des-Quinze Station was constructed in 1955 to operate at 25 Hz and in 1989 the generator was refurbished to operate at 60 Hz.

Presently, the investigated generator has the rating of 32.5 MVA, 68 poles, 432 slots, 13.2 kV, 105.9 rpm, 60 Hz with 6 damper bars per pole. Table 2.5 presents the manufacture parameters of the machine.

Table 2.5 Generator design and electrical parameters for Rapide-des-Quinze

Parameter		Value	Units
<b>General</b>	Power	32.5	MVA
	Rated speed	105.9	rpm
	Rated frequency	60	Hz
	Power factor	0.8	
	Airgap length	11.9	mm
<b>Stator</b>	Number of phases	3	
	Type of connection	Y	
	Number of slots	432	

Parameter		Value	Units
	Number of bars per slot	2	
	Number of slots/ pole/ phase	2+2/17	
	Number of parallel circuits	4	
	Stator outer diameter	8229.6	mm
	Stator inner diameter	7518.4	mm
	Winding sequence	3 2 2 2 2 2 2 2 2 2 3 2 2 2 2 2 2	
<b>Rotor</b>	Number of poles	68	
	Pole body height	228.6	mm
	Rotor outer diameter	7495	mm
	Rotor inner diameter	6968	mm

### 2.3 Conclusions

This chapter had the aim of presenting the hydro-generator components of two hydro power stations. The details pertaining to the construction of the stator core and stator windings are given. Then, and on the rotor side, the details of the poles, the damper bars and the field winding were described. Besides, some more characteristics pertaining to the dimensions, the number of poles, the number of stator slots of the two machines was presented. These two machines are objects of study in the present thesis.

## **CHAPTER 3**

### **EXPERIMENTAL SET-UPS AND EXPERIMENTAL RESULTS**

In order to validate the simulation model, experimental measurements are required. Some of the experimental data serves as inputs of the model, for instance the magnetic material characteristics and the machine geometry. Besides, during post-processing stage, the experimental data such as core loss and magnetic flux density allow the comparison with the simulated results resulting in a confidence of the model for further analysis.

In this chapter, the experimental measurements performed on the two studied generators are described. The first section explains the tests on the magnetic material; the tests determined the magnetic resistivity, the magnetic material losses and the BH curve. The next section presents the magnetic field measurement method. The third section considers the segregation method concerning the open-circuit and the short-circuit tests and also the calorimetric test. The last section investigates the experimental results for different operating conditions and finally this chapter is closed by the conclusions.

#### **3.1 Magnetic material measurements**

The magnetic materials are classified into 5 different groups: diamagnetic, paramagnetic, ferromagnetic, ferrimagnetic and anti-ferromagnetic. The material used in the hydro-electric machines is ferromagnetic. In ferromagnetic materials, the atoms of a paramagnetic material have a permanent magnetic dipole moment. The permanent magnetic dipoles are strongly aligned in the presence of an external magnetic field. Ferromagnetic materials present a large relative permeability.

In addition, ferromagnetic materials can be also divided into: “soft” and “hard” steels. In (Bertotti, 1988) the general properties of the power losses in soft materials are presented

which are usually used in hydro-electric machines in the rotor and stator cores. The connection between dynamic losses and micro-structure of the soft materials is established and the nonlinearity in the behaviour of the loss per cycle was also observed for soft ferromagnetic materials.

It is important to note that when the ferromagnetic material is heated and its temperature overpass the critical value (Curie temperature), then the ferromagnetic material changes its behaviour to that of a paramagnetic one.

For the core loss determination, the magnetic material characteristics curves are an important input in the core loss model. Basically two curves of the iron-core material must be studied: B-H curve (magnetization characteristics) and B-P curve (loss characteristics), which can be determinate for 60 Hz and multiple frequencies. With the B-P curve, and some parameters as thickness, conductivity, the coefficients  $k_h$ ,  $k_c$  and  $k_e$  related to the hysteresis phenomenon, classical eddy current and additional losses respectively can be obtained.

In ferromagnetic materials, the ratio between flux density and field strength is not constant. Looking the BH curve, the non linearity of the magnetic material and the saturation point of the material can be observed.

According to the standards BS EN 10106, ASTM A677-05 (American Society for Testing Materials) and the old AISI (American Iron and Steel Institute), the core plates are divided into fully-processed non-oriented electrical steels and semi-processed electrical steels (Znidarich, 2008b).

The BS EN 10106 standard specifies the measurement in the metric system for 50 Hz applications for fully-processed non-oriented electrical steels and it is used in most European countries. This standard dictates the maximum core loss limits for different alloy grades and lamination thickness (0.35 mm; 0.50 mm; 0.65 mm and 1.00 mm). Its designation starts with



a letter followed by three digits and two digits. For instance, M250-50A refers M for magnetic, 250 represent the maximum core loss in W/kg at 1.5 T and 50 Hz, meaning 2.5 W/kg, and 50 stands for the lamination thickness of 0.50 mm (BS EN 10106 *apud* Znidarich, 2008b).

The ASTM A677-05 standard defines the requirements for fully-processed non-oriented electrical steels in the imperial system of measurement for 60 Hz applications. This standard dictates the maximum core loss limits for different alloy grades and lamination thickness (0.36 mm; 0.47 mm; and 0.635 mm). The material designation starts with two digits followed by a letter and three digits. For example, 47F165 refers to the material thickness (0.47 mm); F for fully-processed property of the material and 165 is the maximum core loss in W/lb at 1.5 T and 60 Hz, meaning 1.65 W/lb (ASTM A677-05 *apud* Znidarich, 2008b).

The old AISI standard is not current anymore; however some end users still refer to it. It was designated for fully-processed non-oriented electrical steels in the imperial system of measurement for 60 Hz applications. The materials are designated by a letter followed by two numbers, i.e. M-15 refers to M for magnetic and 15 for the maximum core loss in W/lb at 1.5 T and 60 Hz, meaning 1.5 W/lb (AISI *apud* Znidarich, 2008b).

To minimize the core loss in electrical machines, the stator core is made of laminated steel. The lamination of the magnetic material core is the usual procedure in the salient pole machine not only for the stator, but also for the rotor. By laminating the magnetic material the losses caused by the magnetic flux flowing in a radial direction are reduced.

The magnetic materials are subjected to some manufacturing steps as: guillotine, laser-cutting, welding, pressing and punching. These processes were studied by (Arshad *et al.*, 2007) where 5 Hz to 10 kHz tests were done on Epstein strips, on L-shaped segments and on standard stator laminations for two different steel grades. The authors showed that the lamination techniques are sensitive to the cutting method and the variations in losses and in

permeability can be up to 10% and up to 20% due to the cutting method (laser cutting or guillotine or punching). Besides, the pressing (stacked stator and rotor laminations) and the welding processes alter the magnetic properties of the laminations by increasing the iron losses for all flux density levels. Concluding the authors cited some important guidelines for design tools regarding the anisotropy, the cutting length and the cutting technique of magnetic materials.

For instance, magnetic materials used on hydro generators are: M-13, M-15 and M-5114. For these materials, the tests used to characterize the magnetic resistivity, the magnetic material losses and the BH curve are described in the following subsections.

### 3.1.1 Magnetic resistivity

In order to provide accurate results for the simulation, the magnetic material resistivity was calculated. Firstly, the material sample was measured (length, width and thickness ( $th$ )), and the micro-ohmmeter was used to compute the resistance ( $R$ ). The following equation was used to determinate the resistivity ( $\rho$ ):

$$\rho = R * th * (\pi / \ln(2)) \quad (3.1)$$

### 3.1.2 Magnetic material losses

The measurements of the ferromagnetic material magnetic losses were performed with the device AMH- 25 form the company Walker Scientific, shown in Figure 3.1. Strips of 3 cm by 28 cm were installed in the Epstein test frame. According to the standard ASTM A 343-97, the amount of sheets to use is one kilogram equally divided in the four branches of the module Epstein Test Frame. To the stator material, a kilogram corresponds to 8 metal layers of sheet in each branch, for a total of 32 sheets.

The apparatus measures a frequency scan allows up to 1000 Hz and a maximum magnetic polarisation  $B$  of about 1.75 T. In fact, the limit of the device is rather affected by the current density  $J$  maximum which is limited to 15000 A/m. In this case, a sweep from 0.1 to 1.7 T with a 0.1 T progression for frequencies ranging from 60 Hz to 960 Hz in multiples of 60 Hz. In order to achieve a high field and a high frequency, the number of sheets in the module Epstein Test Frame is reduced, allowing a higher density of current in the sheets. Thus, measurements at low-field and low frequencies are all made with 8 layers of sheets (32 strips). When the equipment is not able to provide the required current density, it is necessary to reduce the number of layers to 7, then 6 down to a single layer. It should be noticed that measurements with a reduced number of plates can lead to error in the results.



Figure 3.1 Epstein test

### 3.2 Magnetic field measurements

In the cores of rotating electrical machines, the magnetic flux varies as a function of time in terms of magnitude and direction.

Induction coil sensors have an output voltage  $V$  directly related to the number of turns  $n$  and the area  $A$  of the coil sensor and the rate of the change of magnetic flux density  $B$ .

The typical frequency range of this sensor is from 1 HZ to 1 MHz. The coil sensor was developed by Hydro Quebec with ten turns of wire of size No. 40 copper which has an area of 654.16 mm<sup>2</sup>. More information about search coil and other magnetic sensors such as flux-gate, optically pumped, nuclear precision, Hall Effect, etc. can be found at (Lenz, 1990).

The induction coil sensor was used to calculate the voltage using Faraday's law. Equation 3.2 relates the measured voltage with the variation of the magnetic flux as a function of time.

$$V = -n \cdot \frac{d\Phi}{dt} = -n \cdot A \cdot \frac{dB}{dt} = -n \cdot A \cdot \mu_0 \frac{dH}{dt} \quad (3.2)$$

Where  $\Phi$  is the magnetic flux passing through a coil;  $A$  is the area and  $n$  is the number of turns.

To obtain the flux, the voltage waveform must be integrated and a coefficient factor (1/NA) has to be calculated.

Four induction coil sensors were installed in the airgap at 90 degrees to each other. Fig.3.2 shows the coil sensor installed on the stator teeth for Manic 2 and Rapide-des-Quinze.

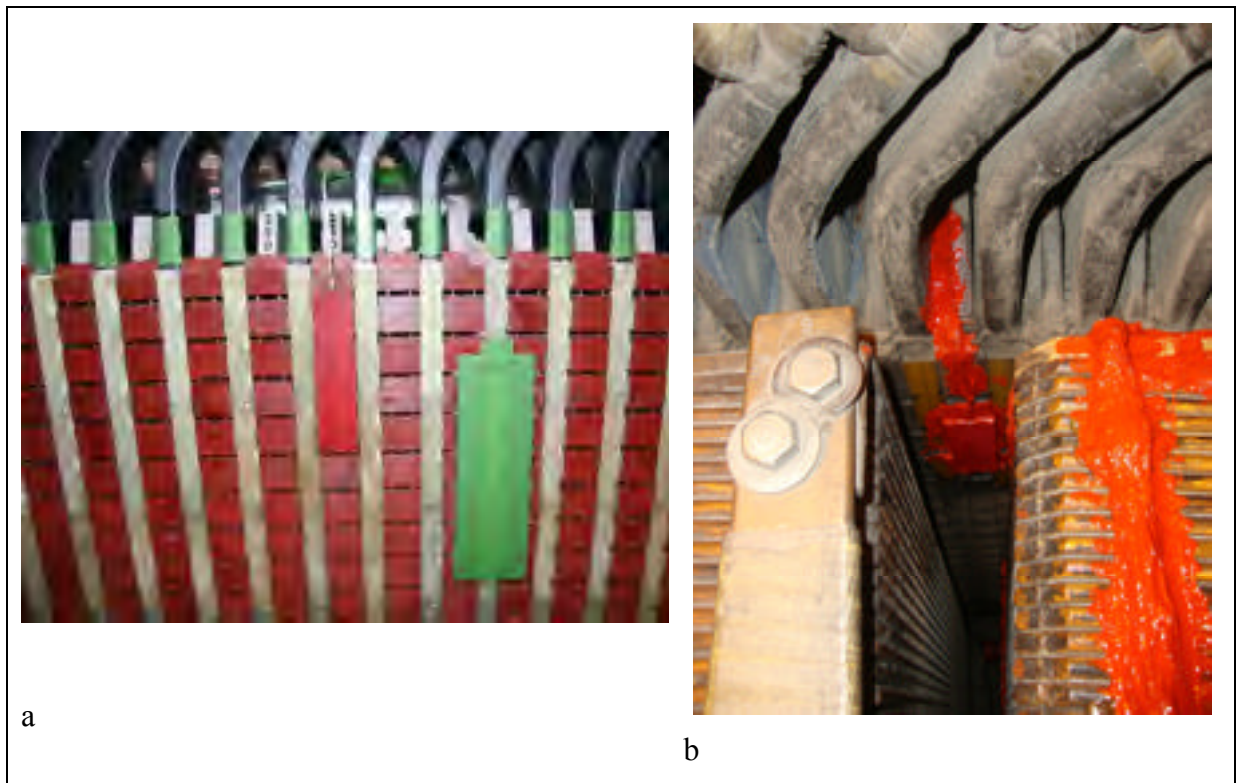


Figure 3.2 Coil sensor placed on the stator – a) Manic 21, b) Rapide-des-Quinze.

### 3.3 Segregated loss

According to the IEEE Std- 115, the losses of a synchronous machine can be divided into (Std- 115, 2010):

- friction and windage loss;
- core loss (on an open circuit);
- stray-load loss (on a short circuit);
- armature  $I^2 R_a$  loss;
- field  $I^2 R_f$  loss.

For the determination of the losses, four methods can be used: separate drive, electric input, retardation and heat transfer. For the first three-methods, the data for the open-circuit and

short-circuit saturation curves obtained during tests are used. For the heat transfer method, the machine operates with load during the test (Std-115, 2010). In this thesis, only the core losses are investigated.

The method used to segregate the losses was heat transfer method (Std-115, 2010) (also known as calorimetric test by (IEC 60034-2-1, 2010)).

### **3.3.1 Open-circuit test**

In the open-circuit test, the machine is driven at rated speed, with open-circuited stator and the armature terminal voltage, field current and terminal speed data are recorded. For loss measurement, when the armature terminals are open-circuited, the total loss includes friction and windage of all mechanically connected apparatus (IEEE Std.115, 2010).

Besides, on open-circuit test, the total open-circuit loss and the open-circuit saturation curves can be obtained.

### **3.3.2 Short-circuit test**

In the short-circuit test, the machine is driven at rated speed, with the stator winding terminals short-circuited and the armature fields and currents are recorded. For loss measurement, when the stator terminals are short-circuited, the total loss includes friction and windage of all mechanically connected apparatus and the stator copper loss and stray-load losses corresponding to the armature current and frequency (IEEE Std.115, 2010).

In the short-circuit test, the short-circuit saturation curve and the short-circuit loss (sum of the  $I^2 R_a$  and stray-load losses) can be determined.

### 3.3.3 Calorimetric test

The calorimetric method is quite straightforward since it relies on the fact that the loss is equal to the sum of the heat added to the water  $P_{ref}$  and by convection  $P_{conv}$ . The calorimetric method is based on the measurement of the water flow  $Q$  in each of the cooling circuits and the water temperatures at the inlet  $T_i$  and at the output  $T_o$  of the same circuits. Knowing the water specific heat  $C_p$  and the density of the cooling water  $\rho$ , the losses evacuated through the cooling circuit of the alternator for a given operating condition can be obtained as follows:

$$P_{rad}(kW) = C_p \times \rho \times Q \times \Delta T \quad (3.3)$$

where  $C_p$  is the water specific heat (kJ/kg°C),  $\rho$  is the water density (kg/m<sup>3</sup>),  $Q$  is the water flow (m<sup>3</sup>/s) and  $\Delta T$  is the water temperature variation (°C).

Besides, the vertical walls of the generator and all the access doors to the turbine should be covered with a reflecting heat insulating material. A coefficient of heat transfer  $c$  is used for measuring losses across the surface that is not covered until the vicinity of the collector compartment. These losses can be calculated by:

$$P_{conv}(kW) = \frac{S \times \Delta T \times c}{1000} \quad (3.4)$$

Where  $S$  is the considered exchange surface (m<sup>2</sup>) and  $c$  is the heat transmission coefficient (m<sup>2</sup>°C). More details about the calorimetric method can be found in (IEC 60034-2-1, 1972).

The core loss measurement was done during open-circuit, not-synchronized, at nominal speed and under rated voltage. The measured loss in these conditions is the sum of the iron losses, ventilation losses, rotor joule losses and also exciter loss.

The stray losses were obtained when the generator operates at nominal speed with a three phase short circuit at its terminals. The excitation current is adjusted in order to obtain the short-circuit currents corresponding to 60, 80 and 100% of the nominal current. The measured losses in these conditions are the sum of the ventilation losses, rotor and stator joule losses, stray losses and also the exciter losses.

### **3.4 Experimental results**

In this section the experimental measurements that were done for the magnetic materials and the two studied machines are presented.

#### **3.4.1 Magnetic material measurements**

Manic 21 was refurbished in 2002. The magnetic material of the stator was replaced and the rotor material was kept. A sample of the stator material was analyzed and the BP and the BH curves were obtained during the Epstein test. For the rotor material, the characteristics (BP and BH) curves were informed by the machine manufacturer.

For Rapide-des-Quinze, no information regarding the magnetic material was obtained. So for simulation purposes, the magnetic material used in the rotor and the stator were the same ones of Manic 21.

Fig.3.3 presents the  $B \times \text{Core Loss}$  curve of stator material used in Manic 21 powerhouse. And Fig. 3.4 presents the  $BH$  curve of the stator material of Manic 21.



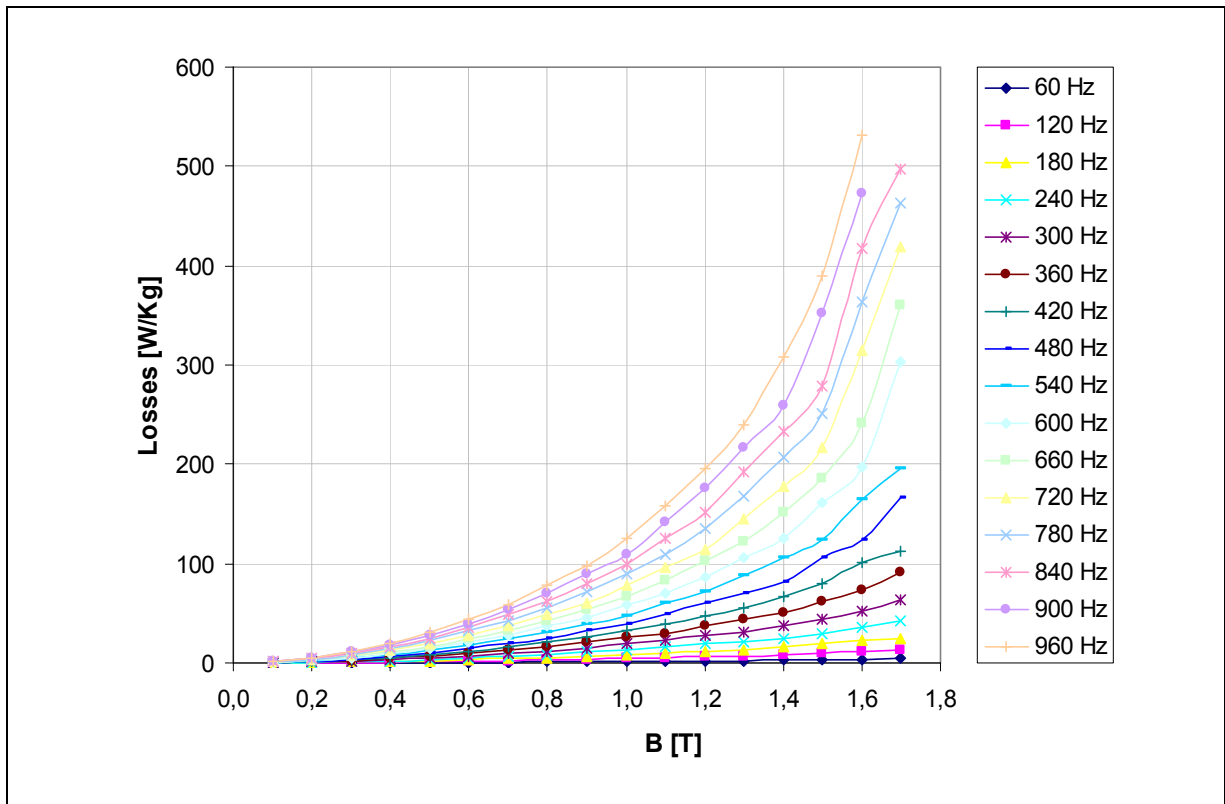


Figure 3.3 Specific core loss measured at multiple frequencies (stator)

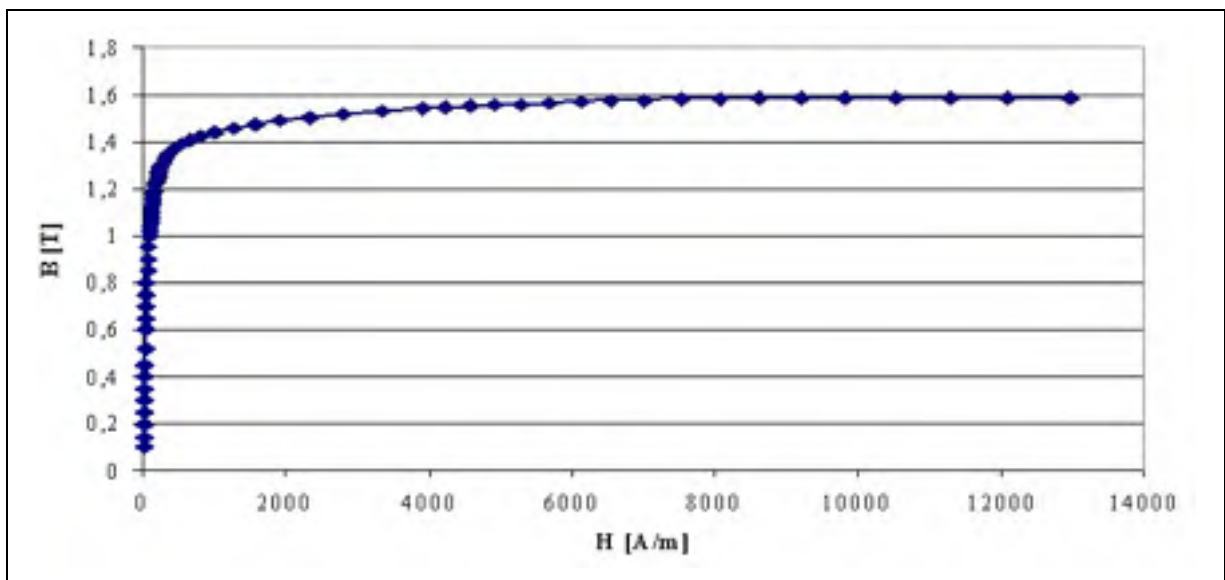


Figure 3.4 BH curve (stator)

The stator material is called M15 and it has a conductivity of 1960000 S/m, the mass density of 7650 kg/m<sup>3</sup> and the thickness of 0.5 mm.

Fig.3.5 presents the  $B \times \text{Core Loss}$  curve of rotor material used in Manic 21 powerhouse. And Fig. 3.6 presents the  $BH$  curve of the rotor material of Manic 21.

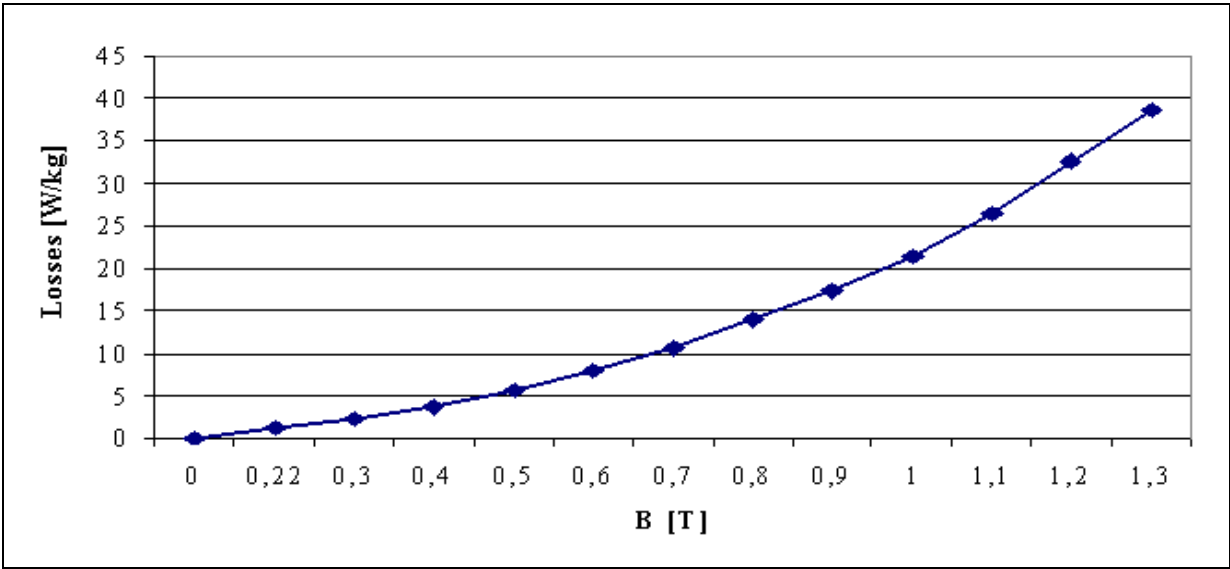


Figure 3.5 Specific core loss measured at 60 Hz (rotor)

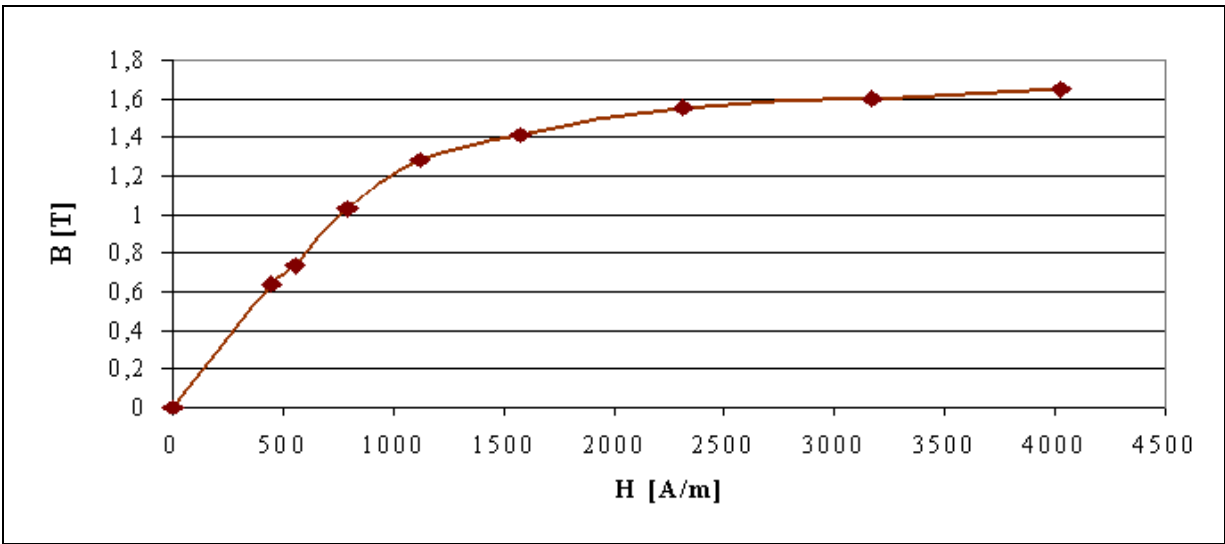


Figure 3.6 BH curve (rotor)

The rotor material is called GE71 (M5114) and it has a conductivity of 6864000 S/m, the mass density of 7850 kg/m<sup>3</sup> and the thickness of 0.071 in (1.8 mm).

### 3.4.2 Manic 21 measurements

Fig. 3.7 shows the output signal  $V$  of the coil sensor for Manic 21 for no load at 9 hours position. In addition, a post-processing was done (using equation 3.2) and the integral of the signal was calculated; the magnetic flux density result for three cycles is shown in Fig.3.8.

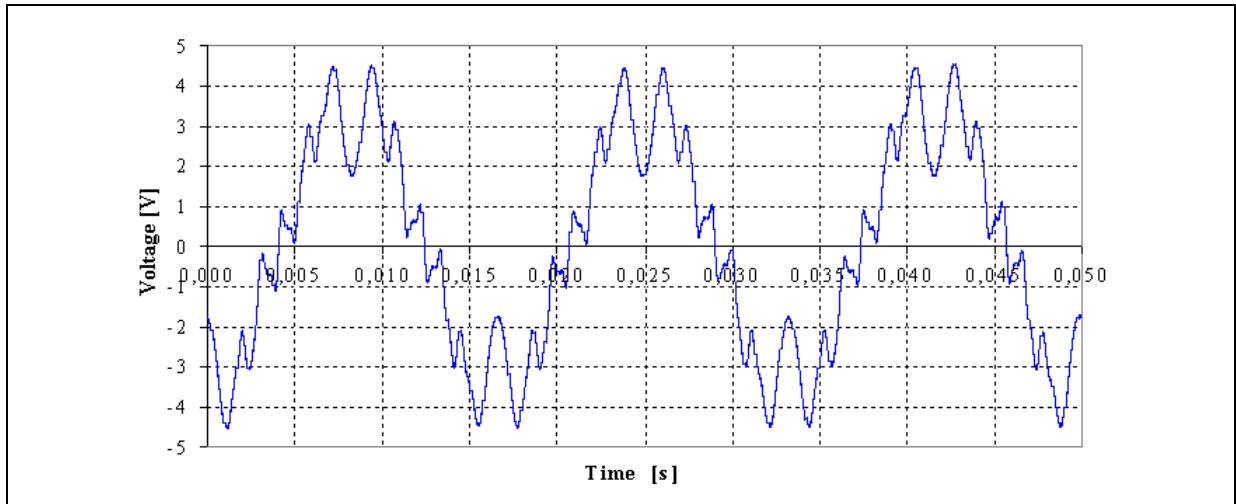


Figure 3.7 Output signal voltage of the coil sensor at open-circuit condition

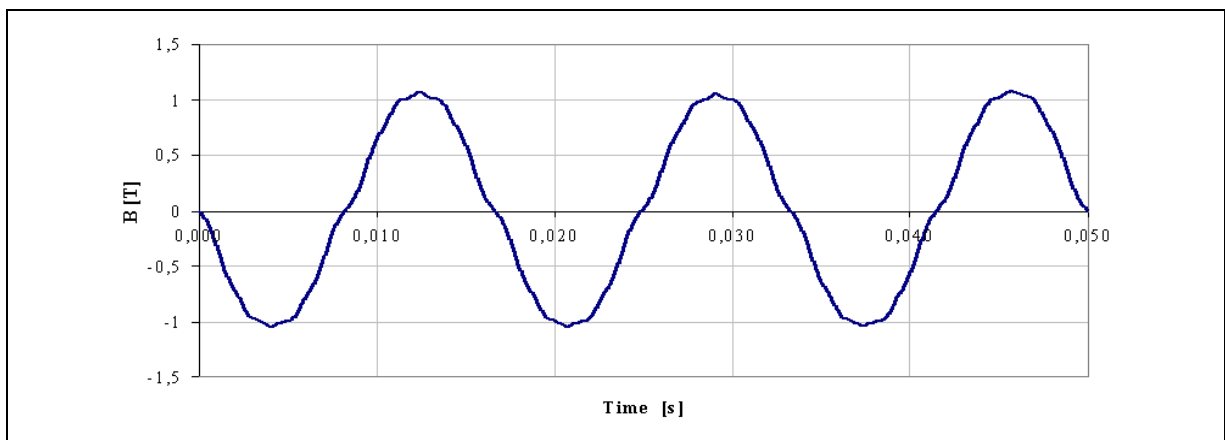
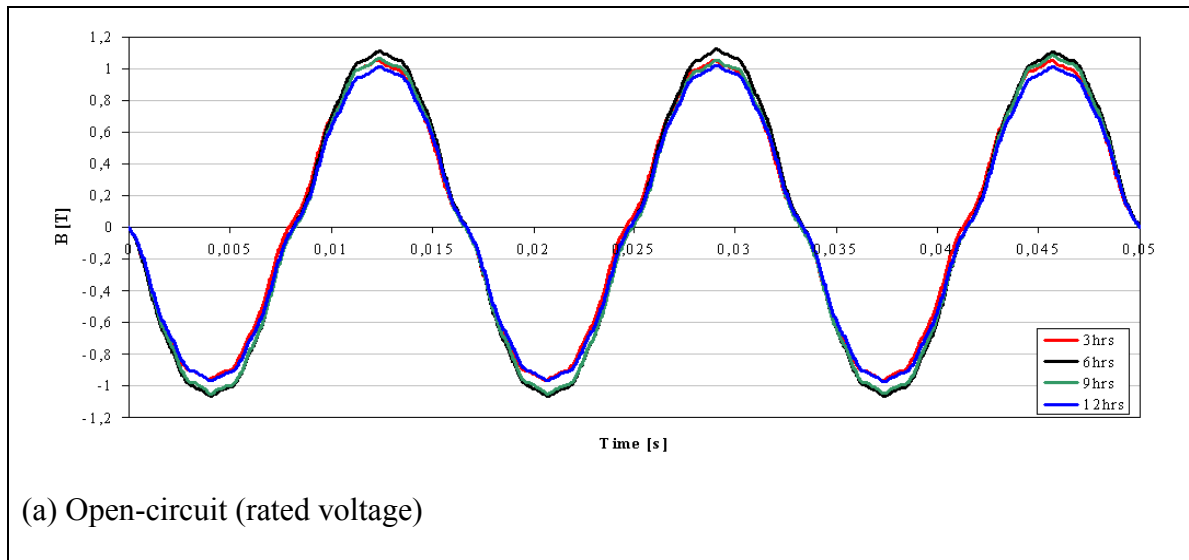


Figure 3.8 Airgap flux density for open-circuit operating condition (rated voltage)

Figure 3.9 displays the time variations of the magnetic flux for the four points. Actually, this result is an indirect value, the result of the integration of the curve of the measured voltage. The airgap magnetic flux was measured for open-circuit condition, as seen in Fig. 3.9a and it varies between  $\pm 1.00$  T (peak value) for 12 hours position and  $\pm 1.10$  T for 6 hours position. The waveform is almost sinusoidal. However, for 71%, Fig. 3.9b, the magnetic flux varies between  $\pm 1.19$  T for 12 hours position and  $\pm 1.34$  T for 6 hours position; and some harmonics can be seen in the waveform. Besides, for 100% load and 120% load, not much difference can be found (Fig. 3.9c and 3.9d, respectively) between the two waveforms; the magnetic flux varies from  $\pm 1.21$  T for 12 hours position and  $\pm 1.39$  T for 6 hours position. The same results are presented in a histogram graphic shown in Fig 3.10.



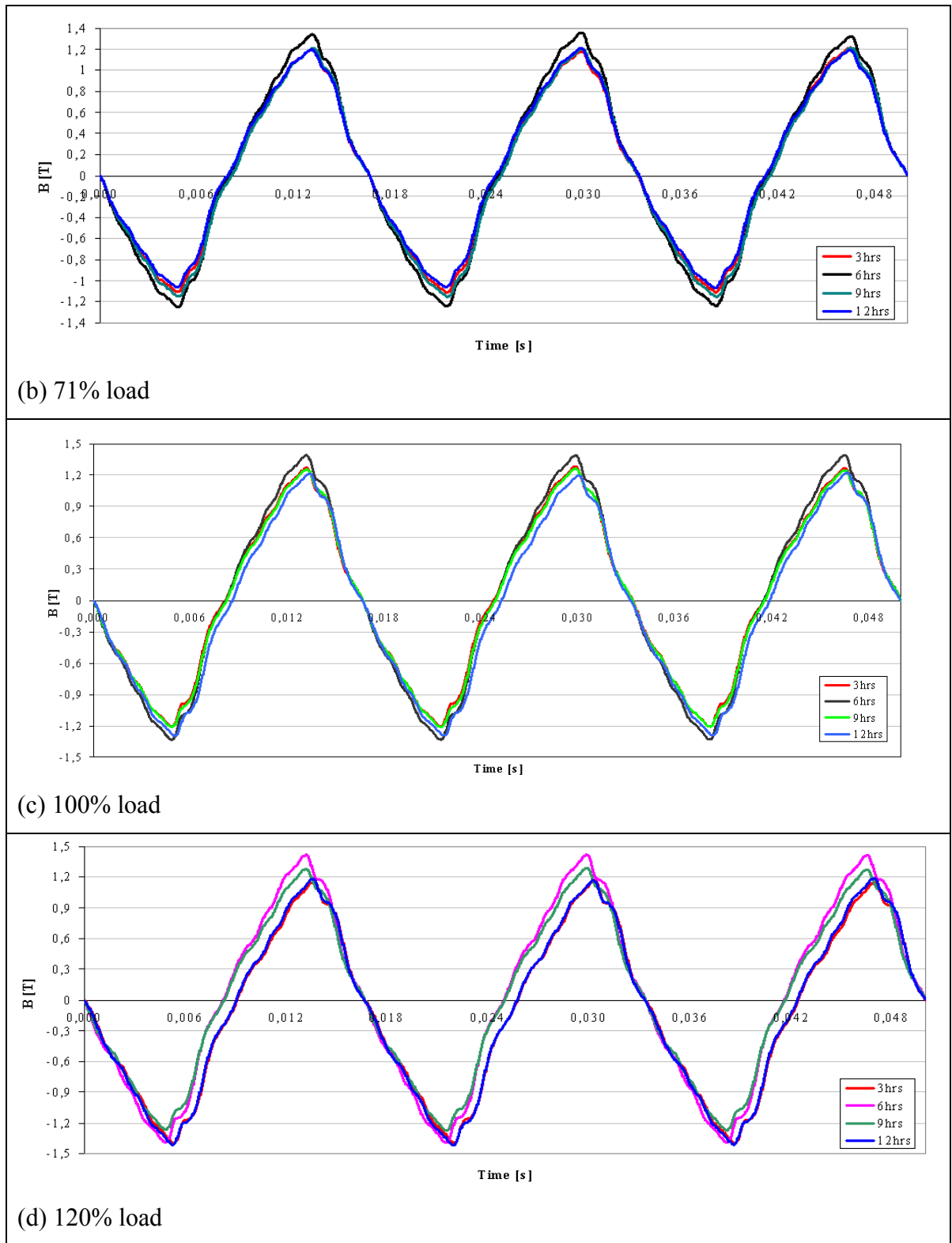


Figure 3.9 Airgap flux measurements for the four measurement conditions

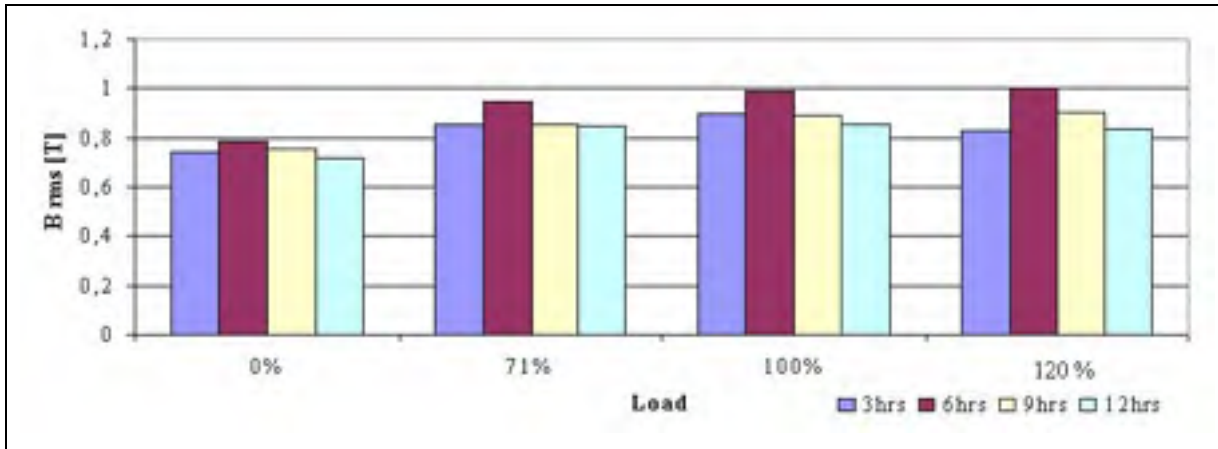


Figure 3.10 Airgap flux measurements for the four measurement conditions

Table 3.1 presents the average of the measured magnetic flux density in RMS for the four different load conditions. The magnitudes of the flux density vary as a function of the flux coil position, which could be related to the operating airgap shape.

Table 3.1 Magnetic flux density B (T)

Load condition	Average B (T)
0%	0,748
71%	0,873
100%	0,905
120%	0,891

It should be noted that the measurements of the magnetic flux density were done for 0%, 71% and 100% at rated voltage (13.8 kV). The measurement for 120% was performed at a higher voltage rate (14.5 kV) and for this reason; the magnetic flux density is lower than the one at 100% nominal voltage.

The machine under study did not have a segregation loss test done. However another unit of the same powerhouse with the same design was measured by calorimetric test.

The two biggest differences between both the machines (presented in Table 3.2) are the stator material and their thickness. In the similar machine, the old stator laminations (0.4 mm) were re-stacked and re-insulated. On the other hand, in the studied machine, the stator magnetic material (0.5 mm) and the stator windings were replaced. Besides, other differences between the measured machine and the simulated machine need to be highlighted.

Table 3.2 Differences between simulated and measured machine

<b>Machine Details</b>	<b>Manic 21 (simulated machine)</b>	<b>Manic 24 (measured machine)</b>
Vent width stator (38 vents)	6 mm	6.85 mm
Useful iron length of the magnetic circuit (stator)	1621.1 mm	1609.3 mm
Type stator sheet	M15	Original
Thickness of one stator sheet	0.5 mm	0.4 mm
Stator staking factor	0.97	0.96
Length of winding heads	1226 mm	1122 mm
Average length of one bar (half turn)	2902 mm	2799 mm
Rotor staking factor	0.97	0.96

Because of the change in stator magnetic material, lamination thickness and the stacking factor, it is expected that the machine under study has higher hysteresis losses and lower eddy current losses than the measured one.

After segregating the losses, the total magnetic loss measured at no load was calculated as 547.6 kW. Besides, the stray loss were measured during short-circuit test as 216.3 kW. The magnetic core loss at load was deduced from the measured results and the analytical and numerical simulation methods and its results are presented in Table 3.3 in kW and in Fig. 3.11 as percentage of the total loss.

Table 3.3 Segregated losses on a similar machine (Manic 24)

Method	Description	Losses (kW)
Experimental	Windage loss	462.1
	Core loss at open-circuit	547.6
	Stray loss	216.3
	Joule (rotor) loss	244.3
	Joule (stator) loss	228.1
	Exciter loss	43.1
	Friction loss	185.5
	Total Losses	1927.0

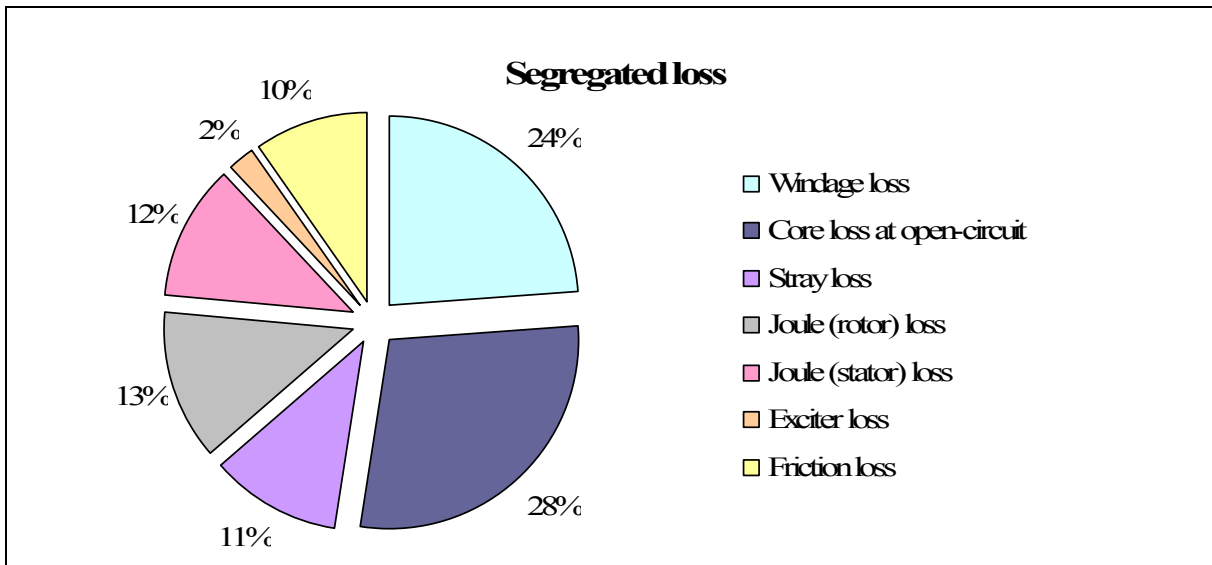


Figure 3.11 Losses separation in percent for Manic 24  
Adapted from report Centrale Manic 2 – Essais de réception de l’alternateur  
24 après réfection, (2002)

The losses type that it is studied in this thesis represents more than 28% of the total losses in the machine Manic 24, as observed in Fig. 3.12. The core losses at load include the core loss at open-circuit and also the core losses part of the stray load losses.



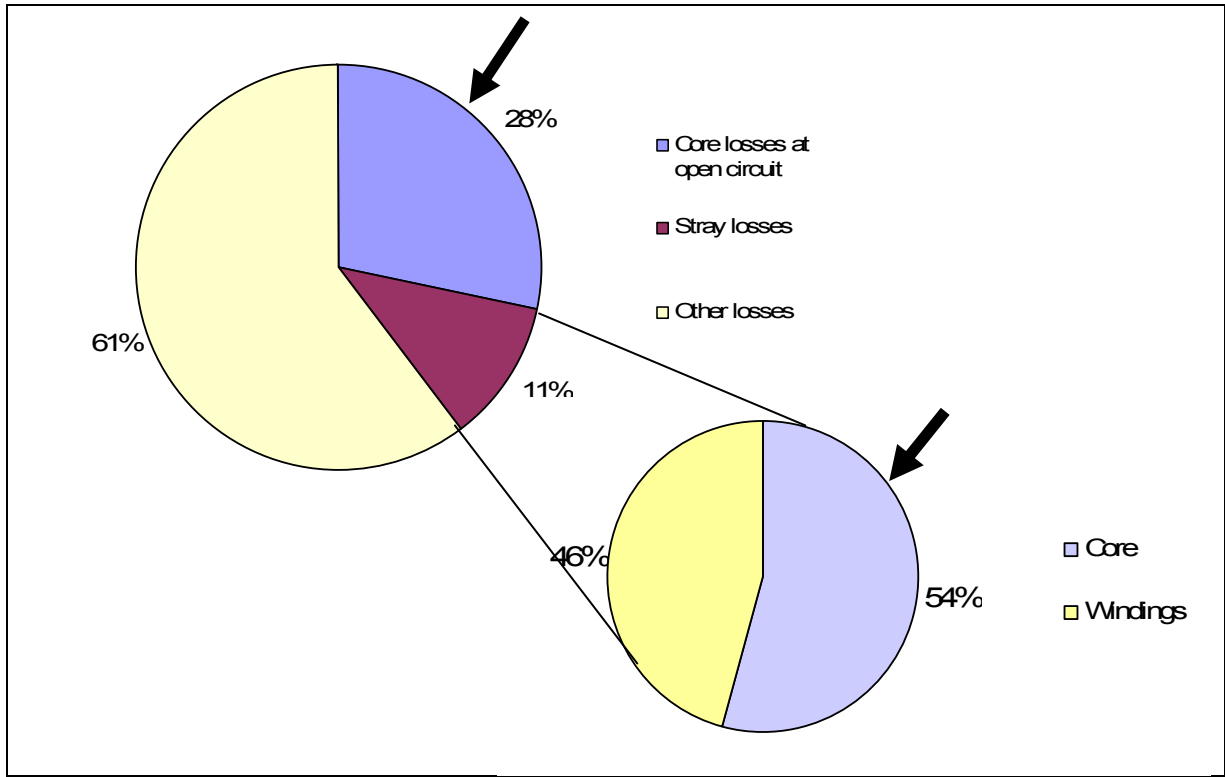


Figure 3.12 Losses separation

The magnetic core loss at nominal load was computed as given by the equation (3.5):

$$P_{mag-load} = P_{occl} + (P_{sccl} - P_{copper-stray} - P_{damper}) \quad (3.5)$$

Where  $P_{mag-load}$  is the magnetic core loss at nominal load,  $P_{occl}$  is the open-circuit core loss measured (547.6 kW) at rated voltage,  $P_{sccl}$  represents the short circuit core losses or also known as stray losses (216.3 kW) measured under short-circuit test at rated current. These losses ( $P_{sccl}$ ) include the damper bar losses  $P_{damper}$  and copper stray load losses in the field and stator windings  $P_{copper-stray}$ . These two losses ( $P_{damper}$  and  $P_{copper-stray}$ ) will be subtracted from  $P_{sccl}$  and the result corresponds to the stray-load loss that happens on the stator and rotor core during load.

The magnetic core losses at load  $P_{\text{mag-load}}$  were deduced from the measured results combined with the analytical (copper stray load loss) and numerical results (damper bar losses). The deduced magnetic core losses in this case include the hysteresis and eddy current losses in the stator core and in rotor pole face. Finally, these results in this case are summarized in Table 3.4.

Table 3.4 Computed losses for Manic 21

Method	Description	Losses (kW)
Experimental	Open-circuit + short circuit test (core loss)	763.9
Analytical	Extra-cooper losses	66.0
Numerical	Damper bar losses	32.9
Experimental + Analytical + Numerical	Core loss at load	665.0

For Manic 21, open-circuit and short circuit tests were performed in the year 2010. Figure 3.13 represents the open-circuit saturation curve and the short-circuit saturation curve.

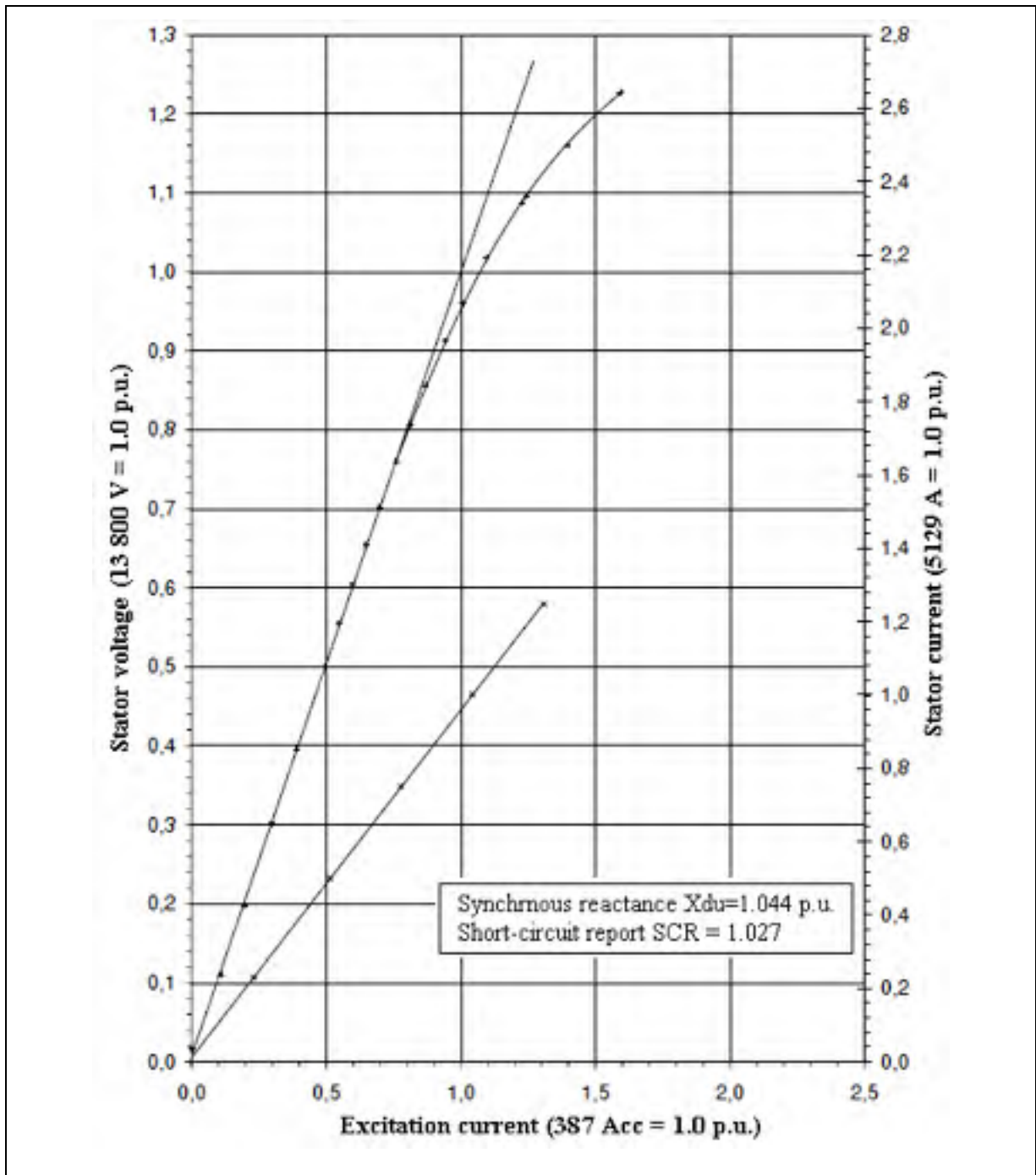


Figure 3.13 Open-circuit and short-circuit saturation curves – Manic 21  
Extracted from HQ internal Report (2010, p.17).

In Manic 21, site tests were performed to determine the pole face and the damper bars temperature under different operating conditions (0%, 71%, 100% and 120%). Even if in some cases the temperature could vary from one pole to the next on the generator tested, only one pole was instrumented for this study with several thermistors; there were connected to a data logger to store data under various operating conditions, as shown in Fig.3.14. The data were stored in the data logger for more than 10 hours.

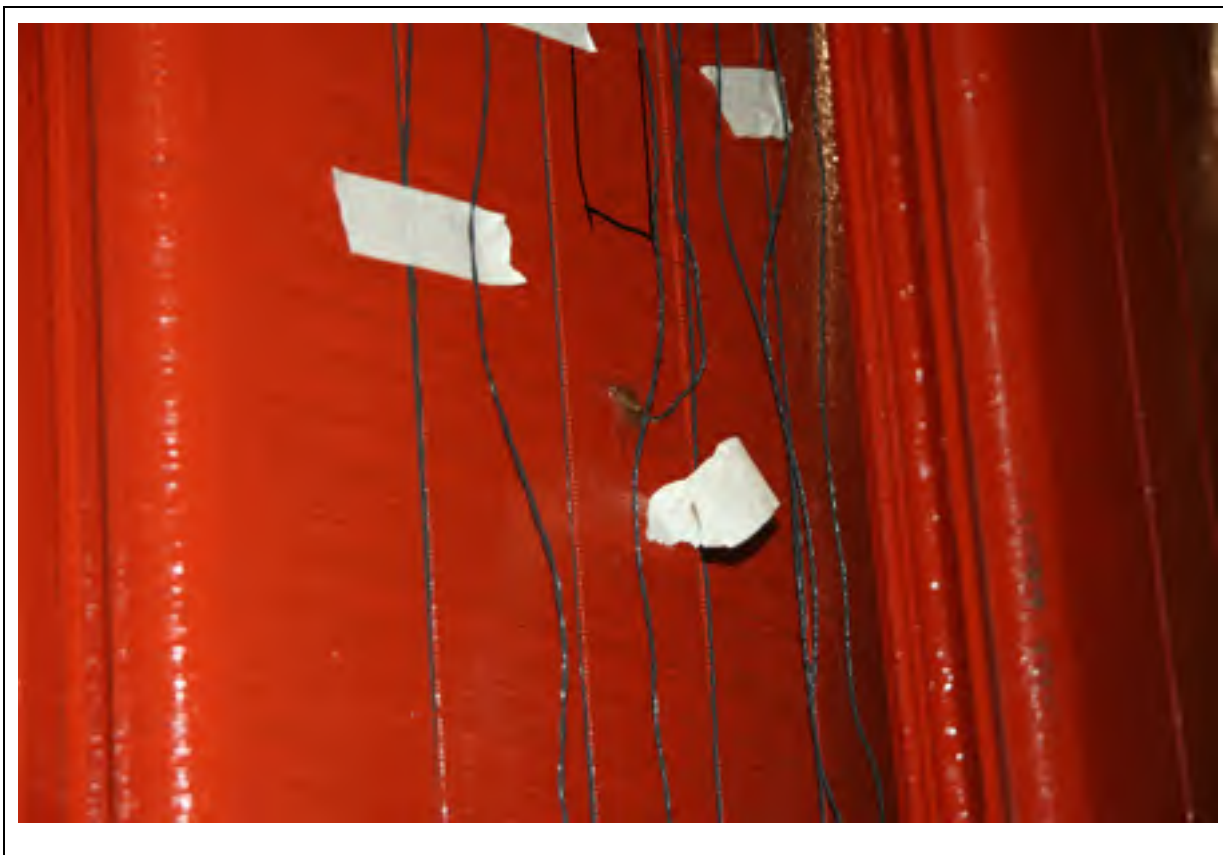


Figure 3.14 Temperature sensors at pole face

The temperature distribution in the damper bars is not only a function of load but also it is a function of the fluid dynamics phenomena and corresponding heat transfer coefficient in the airgap and the pole face area. Figure 3.15 shows the measured temperature on different damper bars at different load conditions (rated voltage no-load, 71%, 100% and at 120%),

where it can be observed that the damper temperature are load dependent and they are also not uniformly distributed across the pole face area.

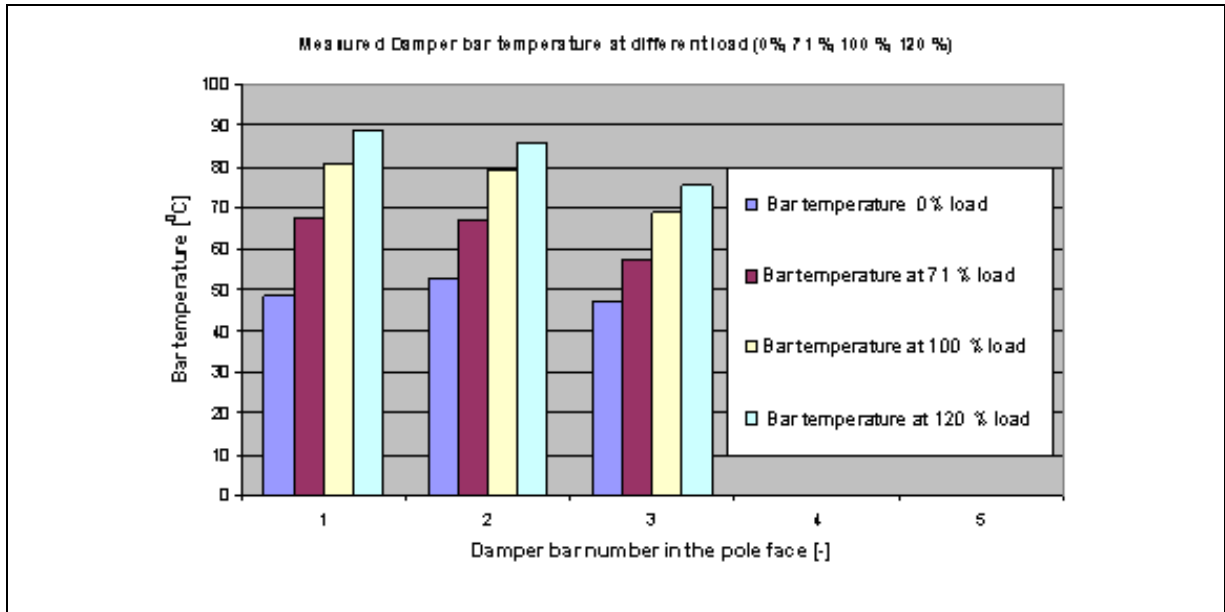


Figure 3.15 Measured damper bar temperature at different operating conditions  
Extracted from Merkhoul *et al.*, (2013)

In this particular case it was not possible to measure the damper bar current because of the inaccessibility of the damper windings (all damper windings are embedded in the pole face).

### 3.4.3 Rapide-des-Quinze measurements

Four coil sensors were placed at 3h, 6h, 9h and 12h positions in the machine under study. The results for 86% of nominal load are presented in Fig 3.16.

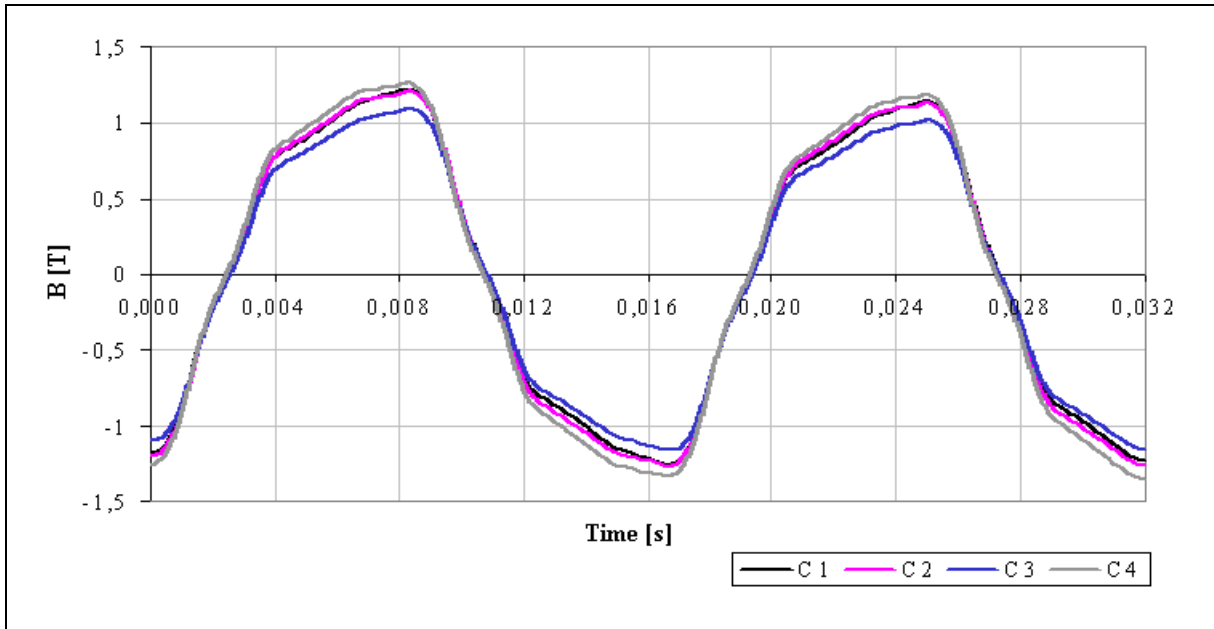


Figure 3.16 Airgap flux measurements for 86% nominal load

For Rapide-des-Quinze, the open-circuit and short circuit tests were performed a long time ago (1989). Open-circuit and short-circuit saturation curves are combined at Fig. 3.17.

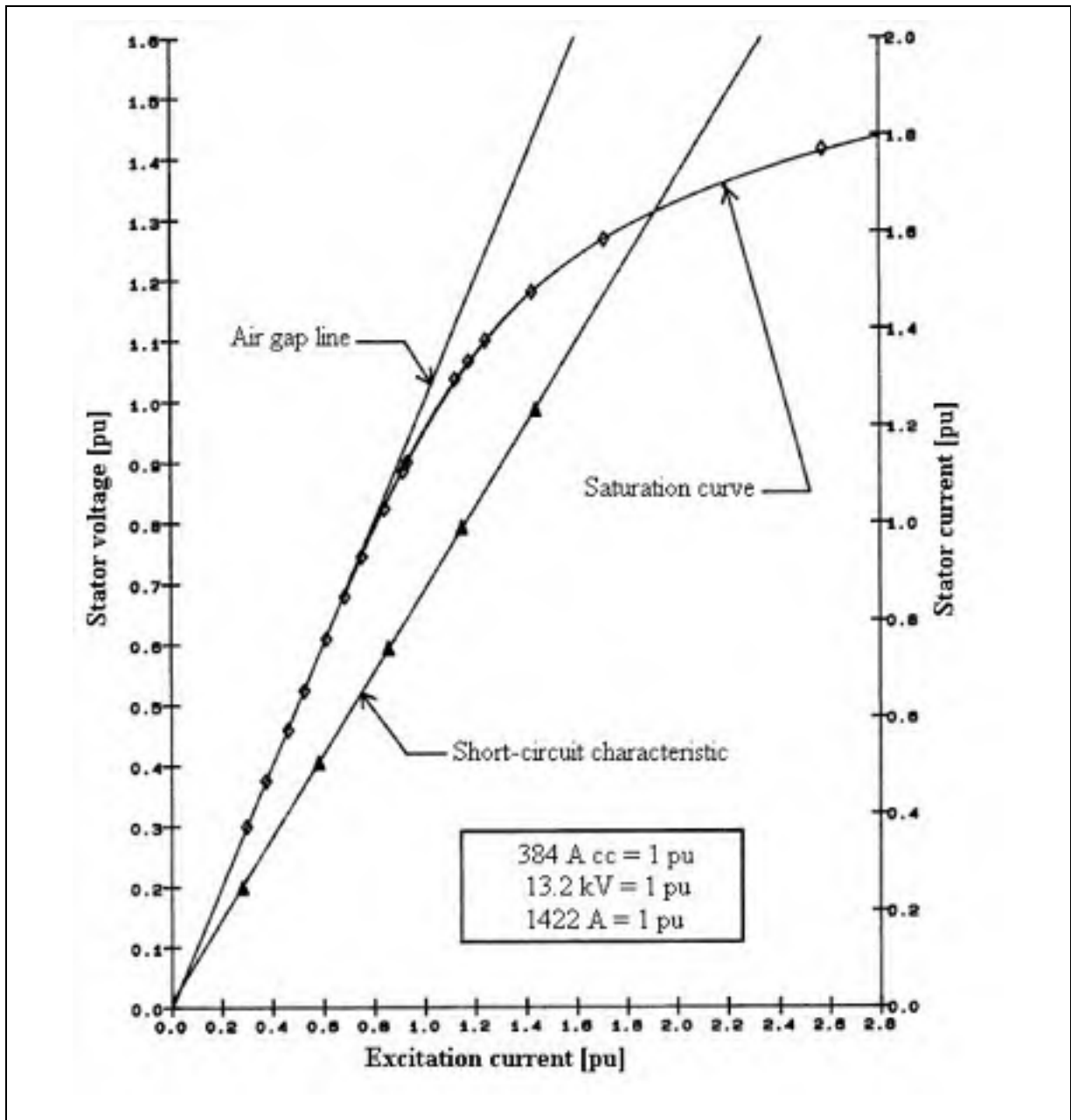


Figure 3.17 Open-circuit and short-circuit saturation curves – Rapide-des-Quinze  
Source: HQ internal Report, (1989, p.4).

It must be emphasized that when the experimental measurements were done (1989) the machine was working well without any stator bar cut.

In the machine studied at Rapide-des-Quinze the calorimetric method was performed during the summer of 2012. The total magnetic losses measured at no-load were 176 kW. During short-circuit test, the fluctuations of the rotor current have resulted in significant fluctuations in the stator current. This instability was so important that it was difficult to derive a reliable value for the stray losses. However, during the test conducted in 1989, the segregation method was done and the results are summarized in Table 3.5 for 1989 and 2012.

Table 3.5 Losses division on Rapide-des-Quinze

Method	Description	Losses (kW)	
		1989	2012
Experimental	Windage loss	60.0	84.5
	Core loss at open-circuit	137.0	176.0
	Stray loss	86.0	-
	Joule (rotor) loss	175.0	188.5
	Joule (stator) loss	157.88	181.0
	Exciter loss	-	18.6
	Friction loss	-	5.0

Using equation 3.5, the magnetic core losses at load were also computed. These losses were 176 kW for the open-circuit core loss measured at rated voltage; 86 kW for the stray-load losses measured under short-circuit test at rated current. Further, the damper bar losses were 20 kW as determined by numerical simulation and 14 kW for the extra-cooper losses was determined analytically. Table 3.6 summarizes the different losses either measured or computed.



Table 3.6 Computed losses for Rapide-des-Quinze

<b>Method</b>	<b>Description</b>	<b>Losses (kW)</b>
Experimental	Open-circuit + short circuit test (core loss)	262
Analytical	Extra-cooper losses	14
Numerical	Damper bar losses	20
Experimental + Analytical + Numerical	Core loss at nominal load	228

### 3.5 Conclusions

In this chapter, the experimental data necessary to perform the electromagnetic simulation were highlighted. Manic 21 was studied with the aim of uprating and the simulation results are presented in Chapters 5 and 6. Rapide-des-Quinze was studied in order to analyze the performance of a hydro-generator with damaged coils and the simulation results are presented in Chapter 6. The experimental results will be compared with the simulations in Chapters 5 and 6.



## CHAPTER 4

### ELECTROMAGNETIC MODELING OF ELECTRICAL MACHINES

Machine modeling is usually the representation of the machine behaviour by mathematical equations and implemented by a numerical or analytical model. For instance, when the model of a hydro-generator is created, the approach used, depends on what outputs you need to obtain, the precision of the model and also the available simulation time.

In this chapter, the machine modeling is presented starting with the traditional d-q model and ending with the finite element method and the electromagnetic equations that will be solved in each part of the hydro-electric machine.

One of the requirements of the Hydro-Quebec AUPALE project is to obtain a spatial distribution of the magnetic field, the iron losses and the thermal data of existing hydro-generators. Through experimentation, the average of the core loss and some points of the magnetic field and temperature can be obtained. However, the existing experimental techniques do not provide either the spatial distribution of the magnetic field or the spatial distribution of the core losses or the hot spots of the machine. Besides, sometimes the description of the physical behaviour by experimentation of a machine may not be feasible due to high cost of experimentation or inaccessible inputs and outputs. Hence, the utilization of a numerical simulation method allows a better understanding of the behaviour of the machine in order to obtain the spatial distribution of these three variables.

The simulation of the machine is performed in order to represent a real system via mathematical models. Numerical methods for analyzing the magnetic field depend on partial differential equations that govern the magnetic field. The most applied numerical method is called the Finite Element Method (FEM). The FEM allows the determination of the electromagnetic magnitude of the devices and power systems. The use of FEM is an alternative way to calculate the magnetic field distribution of a complex structure. With

numerical method it is also possible to solve the problems relating to the determination of magnetic field in a medium with no linear properties.

The electromagnetic simulation using finite element method for large existing hydro machines re-emerged with the development of powerful computer work-stations. As a result, now it is viable to use time-stepping (TSTEP) finite element (FE) methods for many design applications. Nowadays, it is possible to simulate a large fractional machine (5 to 19 poles) with a refined mesh or even a complete machine (60 to 68 poles) with a good mesh resolution using numerical methods.

The power induced in the polar faces depends on several factors namely the polar forms, the size of the airgap, the number of slots, the number of poles and the winding sequence. To take into account all these parameters, a complex numerical model must be developed. This presents a major challenge in science and engineering.

The combination of the number of slot per pole and per phase, which is fractional in major existing hydro-electric generators, leads to use a finite element model for multiple pole pitches. The number of poles required for finite element model is obtained from the design information for the armature winding, and it is given by the lowest denominator of the fraction resulting from the calculation of number of stator slots per pole per phase.

Further, the external circuit was created for each type of simulation (open circuit, short circuit or load); also the mesh and the time-step were defined. The electromagnetic simulations were performed, and the core losses, damper bar current, voltage waveform, flux density and core loss density were calculated.

Advanced electromagnetic numerical models must be carried out in order to estimate various quantities for the machine, such as, open circuit core losses, short circuit core losses, and at loads higher than nominal level. An accurate electromagnetic modelling was done to

determine the distribution of the losses in different parts of the machine. The analysis is performed based on two-dimensional finite element code using current driven simulation mode. The effects of the end region fringing and leakage flux are included in the formulation through circuit elements, such as end winding resistance and end leakage inductance. The numerical models must be validated with different measurements on the generator during several standard heat run and calorimetric test.

Even though commercial software is used to perform the finite element simulation it is important to understand the idea behind this method and the equations that are hidden in it. For that, this chapter was structured in the following subsections: d-q model; electromagnetic equations; governing equations for each part of the machine; finite element method, synchronous machine model, hypothesis and simplifications and finally the conclusions.

#### **4.1 Analytical method: d-q-0 model**

The concept of the direct-quadrature and zero axis (d-q-0 model) has been widely adopted as a way to represent electrical machines. The three-phase circuits (abc) can be transformed into a three-phase system (dq0) and in the case of balanced three phase circuits, the three phase quantities can be modeled into corresponding two-axis (dq).

The two-phase (d-q model, also known as Park model) is commonly used for its simplicity and the idea behind this model consists in defining the magnetic axes of the machine as the direct axis and an orthogonal quadrature axis located  $90^\circ$  ahead (Kaukonen, 1999; Awad, 1999).

In the d-q model, the stator and rotor fluxes are indicated by first-order equations and the machine terminal voltage can be associated with the phase displacement  $\delta$ .

The phasor diagram of the salient-pole machine is presented in Fig. 4.1, where  $I_a$ ,  $I_d$  and  $I_q$  represent respectively the armature current, the direct-axis current and quadrature-axis current;  $E_a$  is machine terminal voltage;  $E_{GU}$  is the generated voltage back of  $X_{du}$ ;  $E_{QD}$  is the location of the phasor relative to  $E_a$ ;  $R_l$  is the positive sequence resistance and  $X_{qu}$  and  $X_{du}$  are the quadrature-axis unsaturated synchronous reactance and the direct-axis unsaturated synchronous reactance respectively (IEEE Std-115, 2010).

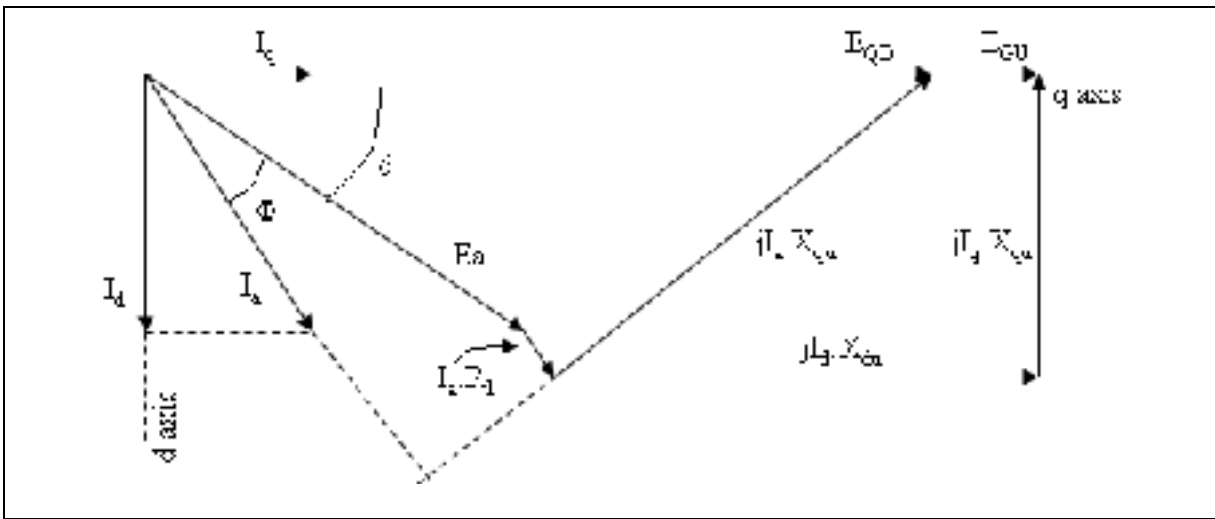


Figure 4.1 Phase diagram of a salient-pole generator  
Available at IEEE-115 (2010, p.55).

The phase displacement  $\delta$  between  $E_{GU}$  and  $E_a$  is the power angle that can be determined by the relation of the positive sequence resistance  $R_l$ , the power-factor angle  $\phi$ , the quadrature-axis unsaturated synchronous reactance  $X_{qu}$  and the machine terminal voltage  $E_a$  (IEEE-115, 2010).

$$\delta = \tan^{-1} \left\{ \frac{|I_a| R_l \sin \phi + |I_a| X_{qu} \cos \phi}{|E_a| + |I_a| R_l \cos \phi - |I_a| X_{qu} \sin \phi} \right\} \quad (4.1)$$

The generated voltage back of  $X_{du}$  ( $E_{GU}$ ) can be computed as:

$$E_{GU} = E_a + I_a R_1 + jI_q X_{qu} + jI_d X_{du} \quad (4.2)$$

Analytically, the excitation current of a synchronous machine can be found by varying the active power; the reactive power; the terminal voltage of the machine and some machine parameters: direct-axis synchronous reactance  $X_d$ , quadrature-axis synchronous reactance  $X_q$ . To compute the excitation current properly, many measurements have to be done on the machine such as: open circuit and short circuit characteristics curves; armature resistance; unsaturated quadrature reactance and leakage reactance (Hawa, 2003).

## 4.2 Maxwell's equations

Between 1861 and 1862 Maxwell composed a unified field theory that connects electricity with magnetism. His theory is based on four partial differential equations known as: Gauss' law, Gauss' law for magnetism, Ampere-Maxwell law and Faraday law.

Gauss's Law also known as the first Maxwell equation states that the electric field going through a closed surface is the closed surface integral of  $E$  dot  $dA$  which is equal to the sum of all charges  $Q$  that are inside the closed surface divided by dielectric of free space ( $\epsilon_0$ ). Integral and differential equations are used to represent Gauss's Law, as:

$$\phi = \oint \vec{E} \cdot d\vec{A} = \frac{\sum Q_{inside}}{\epsilon_0} \text{ or } \nabla \cdot \vec{E} = \frac{\rho}{\epsilon_0} \quad (4.3)$$

For Macroscopic scale Gauss's Law can be seen as:

$$\nabla \cdot \vec{D} = \rho \text{ or } \oint_{\delta_V} D dS = Q_f \quad (4.4)$$

Where  $D$  and  $\rho$  represent the electric flux density ( $C/m^2$ ) and the volumetric charge density ( $C/m^3$ ) respectively.

Gauss's Law for magnetism states that the divergence of magnetic flux density is null. Equation 4.5 is also known as magnetic flux continuity equation.

$$\oint \vec{B} \cdot d\vec{A} = 0 \text{ or } \nabla \cdot \vec{B} = 0 \quad (4.5)$$

The Ampere's Law relates the magnetic field strength  $H(t)$  to the winding current  $i(t)$ . Maxwell was the responsible of adding the displacement current to the original Ampere's Law. So, Ampere-Maxwell Law can be expressed as: the curl of the magnetic field strength minus the derivate of the electric flux density over time (displacement current) is equal to the static electric current density  $J$  ( $A/m^2$ ).

$$\nabla \times \vec{H} - \frac{\partial D}{\partial t} = J \quad (4.6)$$

For rotating machines, the field excited by the coils are considered quasi-stationary, i.e. the variation of the field is slow and the periodic fields are up to 10 kHz (Zhong, 2010). So, inside these coils the displacement current can be considered negligible and the magnetic field  $H$  is excited only by the free current density  $J$ . So, the Ampere-Maxwell's equation can be simplified, as (that is basically the Ampere's Law):

$$\nabla \times \vec{H} = J \quad (4.7)$$

Applying the divergent into both sides of equation 4.8 ( $\nabla \cdot (\nabla \times H) = \nabla \cdot J$ ), equation 4.8 can be achieved:



$$\nabla \cdot J = 0 \quad (4.8)$$

The Faraday's Law relates the magnetic flux density  $B$  (T) with the electric field  $E$  (V/m). The induced electromotive force (EMF) in a closed circuit is equal to the time rate of the variation of the magnetic flux over the circuit.

$$\nabla \times \vec{E} = -\frac{\partial \vec{B}}{\partial t} \quad (4.9)$$

#### 4.2.1 Constitutive laws

Besides the four Maxwell's equations, three equations also known as constitutive laws are used to solve the electromagnetic problem. The three equations relate the current density ( $J$ ) to the electric field ( $E$ ); the magnetic induction ( $B$ ) to the magnetic field ( $H$ ) and the electric displacement ( $D$ ) to the electric field ( $E$ ).

$$J = \sigma(\vec{E} + v \times \vec{B}) + J_s \quad (4.10)$$

$$\vec{B} = \mu_0(\vec{H} + \vec{M}) \quad (4.11)$$

$$\vec{D} = \epsilon_0 \vec{E} + \vec{P} \quad (4.12)$$

Where  $\sigma$  is the electric conductivity (S/m);  $v$  is the speed of the moving conductor {m/s};  $J_0$  is the source current density (A/m<sup>2</sup>) that can be considered imposed in the case of generators;  $\mu_0$  is the magnetic permeability of vacuum ( $4\pi 10^{-7}$  H/m);  $M$  is the magnetization induced by the applied external magnetic field strength  $H$  (A/m);  $D$  is the electric flux density (C/m<sup>2</sup>);  $\epsilon_0$  is

the vacuum electric permittivity (F/m) and  $E$  is the electric field (V/m) and  $P$  is the electric polarization (C/m<sup>2</sup>).

For isotropic medium the constitutive laws can be simplified as:

$$\vec{J} = \sigma \vec{E} \quad (4.13)$$

$$\vec{B} = \mu \vec{H} \quad (4.14)$$

$$\vec{D} = \epsilon \vec{E} \quad (4.15)$$

With  $\mu$  equal to magnetic permeability of the medium (H/m) and  $\epsilon$  is the electric permittivity of the medium (F/m).

#### 4.2.2 Boundary conditions

Homogeneous boundary condition can be applied to the magnetic fields.

For the electric field  $E$  and the magnetic field  $H$ , these boundary conditions can take the form of:

$$E \times n|_{\Gamma_e} = 0 \quad (4.16)$$

$$H \times n|_{\Gamma_h} = 0 \quad (4.17)$$

With  $\Gamma_e$  and  $\Gamma_h$  are the parts of the boundary  $\Gamma$  where the corresponding field ( $E$  and  $H$ ) is imposed and  $n$  is the unit normal to  $\Gamma$ .

When the vector product of the field and the normal is imposed to be zero in the boundary, it means that the corresponding field is normal at the surface defined by the normal  $n$ .

For the fields  $B$ ,  $D$  and  $J$ , the boundary condition can be applied:

$$B.n|_{\Gamma_b} = 0 \quad (4.18)$$

$$D.n|_{\Gamma_d} = 0 \quad (4.19)$$

$$J.n|_{\Gamma_j} = 0 \quad (4.20)$$

$\Gamma_b$ ,  $\Gamma_d$  and  $\Gamma_j$  are the parts of the boundary  $\Gamma$  where the corresponding field ( $B$ ,  $D$  and  $J$ ) respectively.

When the scalar product of the field and the normal is imposed to be zero in the boundary, it means that the corresponding field is tangent at the surface defined by the normal  $n$ .

### 4.3 Different domains of electromagnetism

For low frequency phenomena, electromagnetic field equations (Maxwell's equations) can be decoupled into three different applications cases: electrostatic, magnetostatic and magnetodynamic, as presented in Fig. 4.2.

---

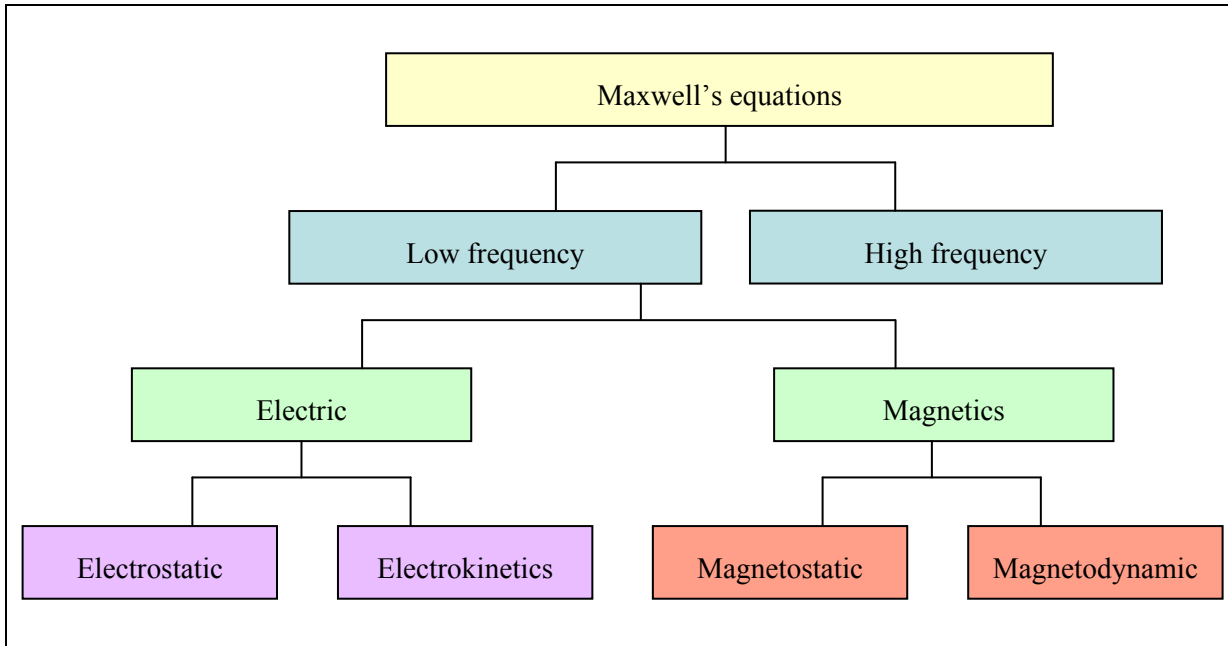


Figure 4.2 Application problems of Maxwell's equations

### 4.3.1 Electrostatic

In electrostatic problems the Maxwell's equations to be solved can be written as ( $\nabla \times \vec{E} = 0$  and  $\nabla \cdot \vec{D} = \rho$ ) and the behaviour law is also necessary ( $\vec{D} = \epsilon \vec{E}$ ). And two boundaries conditions can be applied  $E \times n|_{\Gamma_e} = 0$  and  $D.n|_{\Gamma_d} = 0$ .

In this type of problem, the electric field can be expressed as the form of an electric scalar potential ( $\vec{E} = -\nabla V$ ) and the electric vector potential  $P$  is related to ( $\vec{D} = \vec{D}_s + \nabla \times \vec{P}$ ).

### 4.3.2 Electrokinetics

In electrokinetics problems, the charges  $\rho_m$  are in movement in a conductor and the current density can be written as:  $\vec{J} = \rho_m \vec{v}$ . The Maxwell's equations to be solved are ( $\nabla \times \vec{E} = 0$

and  $\nabla \cdot \vec{J} = 0$  ) and the behaviour law is also necessary ( $\vec{J} = \sigma \vec{E}$  ). And three boundaries conditions can be applied:  $E \times n|_{\Gamma_{ek}} = 0$  ,  $J.n|_{\Gamma_j} = 0$  and  $\int_{\Gamma_{ek}} J \cdot ds = \pm i$  .

In this type of problem, the electric field can be expressed as the form of an electric scalar potential ( $\vec{E} = -\nabla V$  ).

### 4.3.3 Magnetostatic

Magnetostatic formulations are related to the equations ( $\nabla \cdot \vec{B} = 0$  and  $\nabla \times \vec{H} = \vec{J}_s$  ) that describe the behaviour of the static magnetic field. The behaviour law of the medium is also used ( $\vec{B} = \mu \vec{H}$  ). Besides, two boundaries conditions can be applied  $H \times n|_{\Gamma_h} = 0$  and  $B.n|_{\Gamma_b} = 0$  .

Using vector potential formulation, the magnetic flux vector with a divergence free can be expressed from the magnetic vector potential ( $A$ ) as:  $\vec{B} = \nabla \times \vec{A}$  . Besides, the scalar potential formulation can be used and the magnetic scalar potential ( $\Omega$ ) is introduced as:  $\vec{H} = \vec{H}_s - \nabla \Omega$  .

With this type of magnetostatic problem, it is possible to study the machine for each position as static and later add all the results for a dynamic behaviour of the machine.

#### 4.3.4 Magnetodynamic

The solution of the magnetodynamic formulation allows the temporal characterization of the evolution of the electromagnetic field in the space, and in particular induced currents in conductive materials in the presence of certain sources.

In magnetodynamic problems, the Maxwell's equations to be solved are:  $\nabla \times \vec{E} = -\frac{\partial \vec{B}}{\partial t}$ ,  $\nabla \times \vec{H} = \vec{J}$  and  $\nabla \cdot \vec{B} = 0$ . The behaviour laws applicable are:  $\vec{B} = \mu \vec{H}$  and  $\vec{J} = \sigma \vec{E}$ .

In this type of problem, two different formulation types can be used:

- formulation ( $A$ - $V$ ), where the magnetic vector potential  $A$  and the electric scalar potential  $V$  are applied;
- formulation ( $T$ - $\Omega$ ), where the electric vector potential  $T$  and magnetic scalar potential  $\Omega$  are applied.

### 4.4 Potential formulations

Formulating the problems in terms of potentials is a way to reduce the mathematical complexity of the first order coupled differential equations. There are several potential formulations applicable to compute the electromagnetic field. These formulations are based on the scalar (electric scalar potential  $V$  and magnetic scalar potential  $\Omega$ ) or vector (magnetic vector potential  $A$ ; electric vector potential  $T$ ) potentials.

#### 4.4.1 Magnetic vector potential formulation (A, V-A)

The application of potential is frequently used when solving electromagnetic problems, especially for the magnetic vector potential  $A$ .  $A$ ,  $V$ - $A$  formulation uses the magnetic vector potential  $\vec{A}$  both in  $\Omega_1$  and  $\Omega_2$ , and the electric scalar potential  $V$  in  $\Omega_1$ .

Its relationship with the magnetic field  $B$  can be obtained from the following equation:

$$\vec{B} = \nabla \times \vec{A} \quad (4.21)$$

The advantage of using the vector potential  $A$  is that all the conditions of the other equations to be satisfied are now combined into only one equation, thereby reducing the mathematical complexity of the problem.

Besides, the electric scalar potential  $V$  is usually used to calculate the field and it is obtained by the following equation (substituting the magnetic vector potential into Faraday's law):

$$\vec{E} + \frac{\partial \vec{A}}{\partial t} = -\nabla V \quad (4.22)$$

The magnetic vector potential  $A$  can be coupled with the electric scalar potential  $V$ .

Testoni in this thesis described the electromagnetic field formulation including the equations of the A, V-A formulation and summarized on page 14 of his thesis the differential equations, the boundary conditions and the interface conditions (Testoni, 2003).

$$\nabla \times \nu \nabla \times \vec{A} - \nabla \nu \nabla \cdot \vec{A} + \sigma \left\{ \frac{\partial \vec{A}}{\partial t} + \nabla V \right\} = 0 \quad \text{in } \Omega_1 \quad (4.23)$$

$$\nabla \times \nu \nabla \times \vec{A} - \nabla \nu \nabla \cdot \vec{A} = \vec{J}_s \quad \text{in } \Omega_2 \quad (4.24)$$

$$\nabla \cdot \left\{ -\sigma \frac{\partial \vec{A}}{\partial t} - \sigma \nabla V \right\} = 0 \quad \text{in } \Omega_1 \quad (4.25)$$

Boundary conditions:

$$\nu \nabla \cdot \vec{A} = 0 \quad \text{on } S_B \quad (4.26)$$

$$\hat{n} \times \vec{A} = 0 \quad \text{on } S_B \quad (4.27)$$

$$\frac{\partial}{\partial n}(\nu \nabla \cdot \vec{A}) = 0 \quad \text{on } S_H \quad (4.28)$$

$$\hat{n} \cdot \vec{A} = 0 \quad \text{on } S_H \quad (4.29)$$

Interface conditions:

$$\hat{n}_1 \cdot \nabla \times \vec{A}_1 + \hat{n}_2 \cdot \nabla \times \vec{A}_2 = 0 \quad \text{on } S_{12} \quad (4.30)$$

$$\nu \nabla \times \vec{A}_1 \times \hat{n}_1 + \nu \nabla \times \vec{A}_2 \times \hat{n}_2 = 0 \quad \text{on } S_{12} \quad (4.31)$$

$$n \cdot \left\{ -\sigma \frac{\partial \vec{A}}{\partial t} - \sigma \nabla V \right\} = 0 \quad \text{on } S_{12} \quad (4.32)$$

The equations for  $A$ ,  $V$ - $\emptyset$  formulation is also presented in Testoni's work and are summarized on pages 18 and 19 of his thesis (Testoni, 2003).

#### 4.4.2 Electric vector potential formulation ( $\vec{T} - \Omega, \Omega$ )

Another type of formulation is called electric vector potential,  $\vec{T} - \Omega, \Omega$  formulation.

When the frequencies are low enough so that the displacement current term can be neglected,  $\nabla \cdot \vec{J} = 0$ , the formulation  $\vec{T} - \Omega, \Omega$  can be used. In this type of formulation, the current distribution and the voltage calculation can be obtained directly.

The software Maxwell uses the  $T$ - $\Omega$  method on transient magnetic field simulations (Lin, *et al.*, 2008).

The  $\vec{T} - \Omega, \Omega$  formulation decreases the degrees of freedom from three to one in all-non conduction region, hence, reducing the computation cost (Testoni, 2003).



In this formulation, the electric vector potential  $\vec{T}$  is introduced, where:

$$\vec{J} = \nabla \times \vec{T} \quad (4.33)$$

The differential equations of this formulation are:

$$\nabla \cdot \mu(\vec{T} - \nabla \Omega) = 0 \quad \text{in } \Omega_2 \quad (4.34)$$

$$-\nabla \cdot \mu \nabla \Omega = 0 \quad \text{in } \Omega_2 \quad (4.35)$$

$$\nabla \times \frac{1}{\sigma} \nabla \times \vec{T} - \nabla \times \frac{1}{\sigma} \nabla \cdot \vec{T} + \mu \frac{\partial}{\partial t} (\vec{T} - \nabla \Omega) = 0 \quad \text{in } \Omega_1 \quad (4.36)$$

Boundary conditions:

$$\mu \cdot (\vec{T} - \nabla \Omega) \cdot \hat{n} = 0 \quad \text{on } S_B \text{ and } \sigma \neq 0 \quad (4.37)$$

$$\mu \cdot (-\nabla \Omega) \cdot \hat{n} = 0 \quad \text{on } S_B \text{ and } \sigma = 0 \quad (4.38)$$

$$(\vec{T} - \nabla \Omega) \times \hat{n} = 0 \quad \text{on } S_H \text{ and } \sigma \neq 0 \quad (4.39)$$

$$(-\nabla \Omega) \times \hat{n} = 0 \quad \text{on } S_H \text{ and } \sigma = 0 \quad (4.40)$$

Interface conditions:

$$\mu \cdot (\vec{T}_1 - \nabla \Omega_1) \cdot \hat{n}_1 + \mu \cdot (-\nabla \Omega_1) \cdot \hat{n}_2 = 0 \quad \text{on } S_{12} \quad (4.41)$$

$$(\vec{T}_1 - \nabla \Omega_1) \times \hat{n}_1 + (-\nabla \Omega_1) \times \hat{n}_2 = 0 \quad \text{on } S_{12} \quad (4.42)$$

## 4.5 Governing equations for the different parts of the machine

With Maxwell equations, the continuity equations, the constitutive laws and the potential equations (magnetic vector potential and electric scalar potential) the equations for each part of the machine can be obtained.

Electrical machines consist of ferromagnetic material (stator core and rotor core), nonmagnetic areas filled with conductors (stator windings) and nonmagnetic areas without conductors (airgap).

For each part, a specific formulation needs to be applied in order to solve the governing equation.

#### 4.5.1 Stator core

For the stator core of a synchronous generator, three important laws should be applied:

- Ampere's law ( $\nabla \times \vec{H} = \vec{J}$ );
- magnetic flux continuity ( $\nabla \cdot \vec{B} = 0$ );
- constitutive equation ( $\vec{B} = \mu \vec{H}$ ).

Substituting the magnetic vector potential ( $\vec{B} = \nabla \times \vec{A}$ ) into the constitutive law, we have:

$$\vec{H} = \frac{1}{\mu} \vec{B} = \frac{1}{\mu} (\nabla \times \vec{A}) \quad (4.43)$$

In the stator core, the current density  $\vec{J}$  corresponds to the equivalent magnetization current density  $\vec{J}_m$  in Ampere's law:

$$\nabla \times \vec{H} = \vec{J}_m \quad (4.44)$$

Substituting 4.43 into 4.44:

$$\nabla \times \left( \frac{1}{\mu} (\nabla \times \vec{A}) \right) = \vec{J}_m \quad (4.45)$$

Applying the vector identity ( $\nabla \times \nabla \times A = \nabla(\nabla \cdot A) - \nabla^2 A$ ) and the Coulomb gauge condition ( $\nabla \cdot A = 0$ ) we have:

$$-\frac{1}{\mu} \nabla^2 A_z = J_m \quad (4.46)$$

#### 4.5.2 Stator winding

For the stator winding of a synchronous generator, three important laws should be applied:

- Ampere's law ( $\nabla \times \vec{H} = \vec{J}$ );
- magnetic flux continuity ( $\nabla \cdot \vec{B} = 0$ );
- constitutive equation ( $\vec{B} = \mu \vec{H}$ ).

Substituting the magnetic vector potential ( $\vec{B} = \nabla \times \vec{A}$ ) into the constitutive law, we have:

$$\vec{H} = \frac{1}{\mu} \vec{B} = \frac{1}{\mu} (\nabla \times \vec{A}) \quad (4.47)$$

In the stator winding, the current density  $J$  corresponds to the source term  $J_s$  in Ampere's Law:

$$\nabla \times \vec{H} = J_s \quad (4.48)$$

Substituting 4.47 into 4.48:

$$\nabla \times \left( \frac{1}{\mu} (\nabla \times \vec{A}) \right) = J_s \quad (4.49)$$

Applying the vector identity  $(\nabla \times \nabla \times A = \nabla(\nabla \cdot A) - \nabla^2 A)$  and the Coulomb gauge condition  $(\nabla \cdot A = 0)$  we have:

$$-\frac{1}{\mu} \nabla^2 A = J_s \quad (4.50)$$

The stator phase windings are generally modeled as stranded conductors.

### 4.5.3 Rotor core

In the rotor core, low frequency quasi-stationary fields are presented and 5 important equations should be applied:

- Ampere's law  $(\nabla \times \vec{H} = \vec{J})$ ;
- Faraday's Law  $(\nabla \times \vec{E} = -\frac{\partial \vec{B}}{\partial t})$ ;
- magnetic flux continuity  $(\nabla \cdot \vec{B} = 0)$ ;
- constitutive equations  $(\vec{B} = \mu \vec{H} \text{ and } \vec{J} = \sigma \vec{E})$ .

Substituting the magnetic vector potential  $A$  into Faraday's law, we get:

$$\begin{aligned} \nabla \times E + \frac{\partial B}{\partial t} &= 0 \\ \nabla \times (E + \frac{\partial A}{\partial t}) &= 0 \therefore E + \frac{\partial A}{\partial t} = -\nabla V \end{aligned} \quad (4.51)$$

Using the potentials  $A$  and  $V$  (electric scalar potential) the electric field  $E$  can be rewritten as:

$$E = -\frac{\partial A}{\partial t} - \nabla V \quad (4.52)$$

Then the constitutive law ( $\vec{J} = \sigma \vec{E}$ ) is employed to calculate the current density  $J$ :

$$J = \sigma \cdot E = -\sigma \left( \frac{\partial A}{\partial t} + \nabla V \right) \quad (4.53)$$

Ampere's law ( $\nabla \times \vec{H} = \vec{J}$ ) can be rewritten using equations (4.47) and (4.53):

$$\nabla \times \left( \frac{1}{\mu} \cdot \nabla \times A \right) = -\sigma \left( \frac{\partial A}{\partial t} + \nabla V \right) \quad (4.54)$$

Applying the vector identity ( $\nabla \times \nabla \times A = \nabla(\nabla \cdot A) - \nabla^2 A$ ) and assuming Coulomb gauge condition in (4.54) is yielding the  $A$ - $\Phi$  formulation for quasi-stationary magnetic field in the time domain:

$$\frac{1}{\mu} \nabla^2 A = \sigma \left( \frac{\partial A}{\partial t} + \nabla V \right) \quad (4.55)$$

#### 4.5.4 Damper bars

The time-domain quasi-stationary magnetic fields in the damper bars follows the same line of thinking as for the rotor core. It can be expressed by:

$$\frac{1}{\mu} \nabla^2 A = \sigma \left( \frac{\partial A}{\partial t} + \nabla V \right) \quad (4.56)$$

The damper bars are generally modeled as solid conductors with eddy currents.

#### 4.5.5 Airgap

Basically, in the airgap, the laws to be followed are:

- Ampere's law ( $\nabla \times \vec{H} = \vec{J}$ );
- magnetic flux continuity ( $\nabla \cdot \vec{B} = 0$ );
- constitutive equation ( $\vec{B} = \mu_0 \vec{H}$ ).

Substituting the magnetic vector potential ( $\vec{B} = \nabla \times \vec{A}$ ) into the constitutive law, we have:

$$\vec{H} = \frac{1}{\mu_0} \vec{B} = \frac{1}{\mu_0} (\nabla \times \vec{A}) \quad (4.57)$$

Substituting 4.57 into 4.7 (Ampere's law):

$$\nabla \times \left( \frac{1}{\mu_0} (\nabla \times \vec{A}) \right) = \vec{J} \quad (4.58)$$

Applying the vector identity ( $\nabla \times \nabla \times \vec{A} = \nabla(\nabla \cdot \vec{A}) - \nabla^2 \vec{A}$ ) and the Coulomb gauge condition ( $\nabla \cdot \vec{A} = 0$ ) we have:

$$-\frac{1}{\mu_0} \nabla^2 \vec{A} = \vec{J} \quad (4.59)$$

As  $\vec{J}=0$  in the airgap equation (4.59) becomes Laplace's equation:

$$\nabla^2 \vec{A} = 0 \quad (4.60)$$

## 4.6 Finite element method

This numerical method consists in dividing complex geometries into smaller and simpler ones for which Maxwell's equations can be applied to compute the distributed magnetic flux. By using an integral formulation, the FEM allows a discrete representation of the system converts a set of spatial partial differential equations into a set of algebraic equations (Amaya *et al.*, 2003).

The software Maxwell uses the finite element method to compute the flux density distribution and consequently the core loss. In the transient magnetic analysis, the magnetic fields due to time varying currents are studied.

Basically, the steps used for the analysis based on finite element method are detailed in the following subsections, as presented in Fig. 4.3: weak formulation; domain discretization and shape function; gauge conditions (physical laws and boundary conditions); matrix formulation; imposition of displacement constraints and system resolution. In this session, the reference material is basically (Pirou *et al.*, 2014).

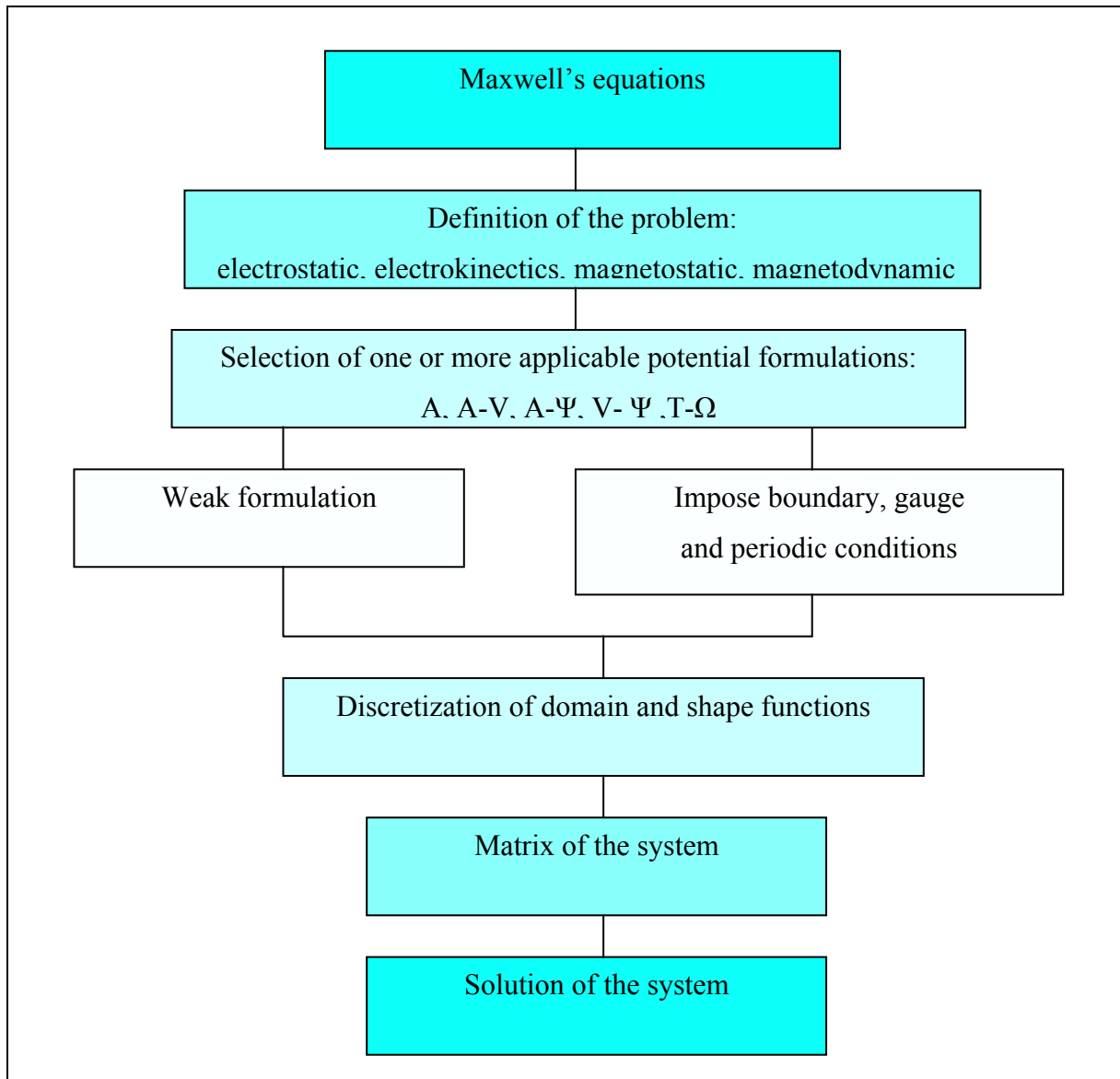


Figure 4.3 FEM for electromagnetic problems

#### 4.6.1 Weak formulation and it's application for magnetodynamic problems

Before the development of the finite element method, an approximation technique was used for solving differential equations. This technique is called Method of Weighted Residuals, also called of Weak Formulation.



The weighted residual method is based on the integration of the studied domain  $D$  of the equilibrium equation multiplied by a test function  $\psi$  (also known as weighting function) that:

$$\iiint_D (L(u) - f_s) \cdot \psi \, d\tau = 0 \quad \forall \psi \in V(D) \quad (4.61)$$

In time domain simulations, Maxwell software solver uses the  $\vec{T}-\Omega$  formulation. In it, the motion is allowed; the excitations currents and/or voltages can assume arbitrary shapes and the nonlinear BH material dependencies are also allowed (Maxwell Online Help, 2014).

For the application of magnetodynamic problems using  $\vec{T}-\Omega$  formulation, some equations must be solved:

$$\left( \nabla \times \frac{1}{\sigma} \right) (\nabla \times T) = - \frac{\partial}{\partial t} \mu (H_s + T - \nabla \Omega) \quad (4.62)$$

$$\nabla \cdot (\mu (H_s + T - \nabla \Omega)) = 0 \quad (4.63)$$

With:  $H_s \in H_{Rot,h}$ ,  $T \in H_{Rot,h}$  and  $\Omega \in H_{grad,h}$ . Also having  $J_s$  imposed as source, then:

$$\nabla \times H_s = J_s$$

Using the weighted residual method, equations 4.62 and 4.63 take form of:

$$\iiint_{D_{nc} \cup D_s} \mu (H_s - \nabla \Omega) \cdot \nabla \alpha \, d\tau = 0 \quad (4.64)$$

$$\iiint_{D_c} \mu (H_s + T - \nabla \Omega) \cdot \nabla \alpha \, d\tau = 0 \quad (4.65)$$

$$\iiint_{D_c} \sigma^{-1} (\nabla \times T) (\nabla \times \psi) \, d\tau + \iiint_{D_c} \frac{\partial}{\partial t} (\mu (H_s + T - \nabla \Omega)) \psi \, d\tau = 0 \quad (4.66)$$

With:  $\forall \alpha \in H_{grad,h}$  and  $\forall \psi \in H_{Rot,h}$ .

#### 4.6.2 Discretization of the domain and shape functions

The first step of the finite element method involves the discretization of the geometry (domain) into smaller and simpler sub-domains (elements) without overlapping. The elements can be in one, two or three dimensions. Triangles and quadrilaterals are the most commonly shapes used in this method. Besides, the number of the degrees of freedom has to be decided: increasing this number is required to analyse more complex system geometry and also to obtain a higher accuracy. For instance, in a triangular element, a 1<sup>st</sup> order equation has 3 nodes (one in each vertex) and a 2<sup>nd</sup> order equation has 6 nodes (one in each vertex and in the middle of each edge), as shown in Fig. 4.4. Once the sub-domains are defined and interconnected, the complex partial differential equations (Maxwell's equations) are reduced to a finite number of either linear or non-linear simultaneous algebraic equations.

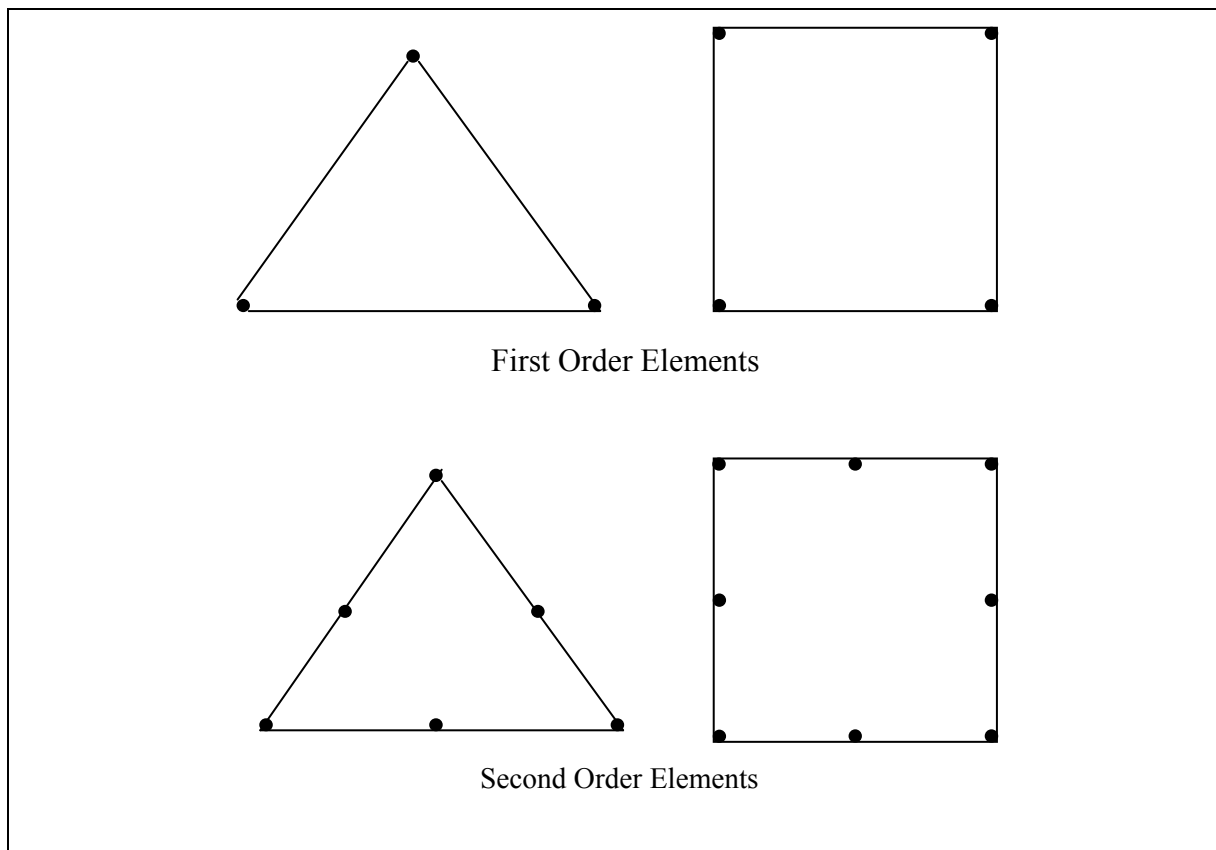


Figure 4.4 2D geometric elements

If the function  $u(x)$  interpolate on  $\kappa$ , it can be written:

$$u_h(x) = \sum_{i=1}^{n_\kappa} \omega_i \phi_i \cong u(x) \quad (4.67)$$

Where:  $n_\kappa$  is the number of degree of freedom on the geometric element  $\kappa$ ;  $\omega_i$  is the shape function and  $\phi_i$  is the discrete form of  $u(x)$ .

Inside each element, the physical properties are constants. The magnetic field of each element can be obtained through an interpolation function of all element nodes. The interpolation functions can be discretized on the nodes, on the edges, on the facets and on the volume (for 3 D).

The shape functions are usually polynomial forms of independent variables. A finite element is called “iso-parametric” when the shape functions are identical to the interpolation function. “Iso-parametric” elements are the most commonly used elements in Finite Element (FE) codes. Although, “sub-parametric” and “over-parametric” elements can also be implemented when the mapping functions have lower or higher order than the interpolation function, respectively (Bastos, Sadowski, 2003).

Then, the finite element methodology must be selected with the definition of the shape function; for instance, linear shape functions (interpolation function). For more details, about the equations, their simplifications and assumptions are presented in (Zhong, 2010) and in many others finite element theory books (Zienkiewicz, 2000; Bastos *et al.*, 2003).

For instance the node element, the interpolation function is discretized at the nodes of the elements and the basic functions are noted  $\omega_{ni}$ . The set of nodal functions create the space of mode elements of dimension  $N$  and noted  $\mathcal{W}^0$ . With,  $\omega_{n_i}(x_j) = \delta(i, j)$  and  $\sum_{i=1}^n \omega_{n_i} = 1$ . Then:

$$u_h(x) \in W^0 \therefore u_h(x) = \sum_{i=1}^n \omega_i u_{ni} \quad (4.68)$$

For 2D models, a space of edge elements  $W^1$  and a space of facet elements  $W^2$  should also be created and the properties for each space also need to be defined, Table 4.1 summarizes the basic shape functions, its properties and its spaces.

Table 4.1 Basic shape functions  
Extracted from Piriou *et al. apud* Meunier, 2010, (2014)

Functions	Properties	Continuity	Spaces
$\omega_n$	$\omega_{n_i}(x_j) = \delta_{ij}$	continuous	$W^0$
$\omega_e$	$\int_e \omega_b \cdot dl = \delta_{eb}$	$\omega_e \times n$	$W^1$
$\omega_f$	$\int_f \omega_g \cdot dS = \delta_{fg}$	$\omega_f \cdot n$	$W^2$

Whitney's complex describes the properties of discrete spaces. As in continuous domain, the discrete subspaces can be defined as:

$$W_u^0 = \{u \in W^0, u = 0|_{\Gamma_u}\} \quad (4.69)$$

$$W_u^1 = \{u \in W^1, u \times n|_{\Gamma_u} = 0\} \quad (4.70)$$

$$W_u^2 = \{u \in W^2, u \cdot n|_{\Gamma_u} = 0\} \quad (4.71)$$

### 4.6.3 Gauge conditions and source fields

If the domain is simply connected with a connected boundary, the vector field solution needs to be unique and for that it is necessary to impose constraint conditions (gauge conditions)

and also the boundary conditions. In the case of the scalar potentials ( $\Omega$  and  $V$ ), the potential is imposed at the node of the mesh and no gauge condition is necessary. However, for the vector potentials ( $A$  and  $T$ ) it is necessary to impose a gauge condition.

So, if a vector field is defined in a single way, it becomes necessary to know its rotational, divergence and boundary conditions. “If one of the operators is not fixed, it is necessary to impose a gauge condition” (Meunier, 2010). One example of the well-known gauge condition is Coulomb gauge that it was applied in section 4.5.

Dirichlet boundary conditions and Neumann boundary conditions can be applied depending upon the unknowns. On the set of linear equations obtained from the weak formulation of the differential equation, boundary conditions are imposed. Two types of boundary conditions are well-known: Dirichlet boundary condition, also called as essential boundary condition and Neumann boundary condition, also called mixed boundary condition.

Dirichlet boundary conditions define an exact value for a field in a boundary region. For instance for the magnetic vector potential  $A$ , when  $A=0$  is established along the boundary, this means that the magnetic flux is kept inside the closed surface thus avoiding it to cross the boundary. Neumann boundary conditions specify the normal derivative of potential along it,  $\partial A/\partial n = 0$ .

Besides, in an electric machine, the magnetic field is periodical; therefore, the machine does not need to be modeled in its entirety. For instance, in the case of Manic 21 it is only required to model 1/12 of the full geometry. This periodic condition states that the magnetic vector potential along the radial line must be exactly the negative at an angular displacement of period ( $\pi/6$  in Manic).

$$A(r, \theta) = -A\left(r, \theta + \frac{2\pi}{p}\right) \quad (4.72)$$

Where  $p$  is the number of times that the symmetry is repeated in a full geometry model.

After the gauge, boundary conditions and periodic conditions are applied; the problem consists in finding the solution of the magnetic vector on the nodes  $A_z$ .

#### 4.6.4 Matrix formulation

The matrix formulation is assembling local elements into a global matrix for each part of the machine.

After the weak formulation is obtained, the discrete form of  $T$ ,  $\Omega$  and  $H_s$  is:

$$T_h(x) = \sum_{i=1}^{E'} \omega_{e_i} T_{he_i} \quad (4.73)$$

$$\Omega_h(x) = \sum_{i=1}^{N'} \omega_{n_i} \Omega_{n_i} \quad (4.74)$$

$$H_{sh}(x) = \sum_{i=1}^{E'} \omega_{e_i} H_{se_i} \quad (4.75)$$

For the formulation  $T$ -  $\Omega$  with  $J_s$  imposed as source terms, Eq. (4.64 – 4.66) can be written in a matrix system as:

$$\begin{bmatrix} [S] & [0] \\ [0] & [M] \end{bmatrix} \begin{bmatrix} T_h \\ \Omega_h \end{bmatrix} + \begin{bmatrix} [Q] & [P] \\ [P]^t & [0] \end{bmatrix} \frac{d}{dt} \begin{bmatrix} T_h \\ \Omega_h \end{bmatrix} = \begin{bmatrix} [0] & [0] \\ [F] & [0] \end{bmatrix} \begin{bmatrix} H_h \\ [0] \end{bmatrix} - \begin{bmatrix} [Q] & [0] \\ [0] & [0] \end{bmatrix} \frac{d}{dt} \begin{bmatrix} H_h \\ [0] \end{bmatrix} \quad (4.76)$$

With:

$$s_{i,j} = \iiint_{D_c} \sigma^{-1} (\nabla \times \omega_{e_i}) (\nabla \times \omega_{e_j}) d\tau \quad (4.77)$$

$$q_{i,j} = \iiint_{D_c} \mu \omega_{e_i} \omega_{e_j} d\tau \quad (4.78)$$

$$p_{j,k} = \iiint_{D_c} \mu \omega_{e_k} \nabla \omega_{n_j} d\tau \quad (4.79)$$

$$m_{i,j} = \iiint_D \mu \nabla \omega_{n_i} \nabla \omega_{n_j} d\tau \quad (4.80)$$

$$f_{j,k} = \iiint_D \omega_{f_k} \omega_{e_j} d\tau \quad (4.81)$$

The resulting matrix to solve is:

$$\begin{bmatrix} [S] + \Delta t^{-1}[Q] & \Delta t^{-1}[P] \\ \Delta t^{-1}[P] & [M] \end{bmatrix} \begin{bmatrix} T_h \\ \Omega_h \end{bmatrix}_{n+1} = \begin{bmatrix} -\Delta t^{-1}[Q] & [0] \\ [F] & [0] \end{bmatrix} \begin{bmatrix} H_h \\ [0] \end{bmatrix}_{n+1} \quad (4.82)$$

$$+ \begin{bmatrix} \Delta t^{-1}[Q] & [0] \\ [0] & [0] \end{bmatrix} \begin{bmatrix} H_{sh} \\ 0 \end{bmatrix}_n + \begin{bmatrix} \Delta t^{-1}[Q] & \Delta t^{-1}[P] \\ \Delta t^{-1}[P] & [0] \end{bmatrix} \begin{bmatrix} T_h \\ \Omega_h \end{bmatrix}_n$$

Some of the classic iterative matrix methods are included in Maxwell software, such as: Jacob method, Gauss-Seidel method and successive over-relaxation method (Maxwell Online Help, 2014). Further information about those methods can be found in (Van der Vorst, 2003).

#### 4.6.5 Imposition of displacement constraints (movement of the machine)

The machine is rotating with respect to time and this movement has to be accounted in a way that the mesh also moves with the speed  $w$ . For that, a fixed coordinate system for Maxwell's equations in the moving and stationary part of the model is used in Maxwell software. With that, the motion term is eliminated for the translational type of the motion and the rotational type of motion is obtained by using a cylindrical coordinate system with z axis aligned with the rotational axis.

#### **4.6.6 Methods of solution of the system**

The solution of the matrix can be performed by any linear solving technique (for instance, Gauss elimination) after inserting the boundary conditions into the global system. For implementation purposes a program like Fortran or C++ can be used.

Automated multi-level sub-structuring methods are implemented for frequency response and real mode computations in some commercial codes as ANSYS (Roches, 2011).

Using FEM and the formulation of the approximation method, the problem is transferred from a system of differential equations to a system of algebraic equations. The solution of the algebraic equations can be obtained by the Newton-Raphson method.

Newton-Raphson method is the technique used by Maxwell software to solve interactively the nonlinear problem.

#### **4.7 Synchronous salient pole generator model**

Maxwell software is used to solve static and also time-varying electromagnetic fields. This software utilizes a CAD tool called RMXpert for the generation of the geometric model of the electrical machine.

The electrical machine studied in this thesis consists in a synchronous generator, low-speed with salient poles. The first step to build the model is to measure the electrical and geometric parameters of the machine. After that, the obtained results are therefore introduced in the software for simulation purposes. Tables 4.2 to 4.5 show the inputs related to the stator, rotor, winding, ventilation, insulation and setup analysis. More than 70 data must be introduced for the completion of the model.



Table 4.2 General machine parameters

<b>Machine</b>
Number of poles
Frictional loss
Windage loss
Reference speed

Table 4.3 Stator parameters

<b>Stator</b>
Outer diameter
Inner diameter
Length
Stacking factor
Steel type
Number of slot
Slot type
Lamination sector
Press board thickness
Skew width

<b>Stator / winding</b>
Number winding layers
Winding type
Conductors per slot
Coil pitch
Number of strands
Wire Wrap thickness
Wire width
Wire thickness

<b>Stator / insulation</b>
Input half-turn length
End extension
Base inner radius
Tip inner diameter
End clearance
Coil wrap
Slot liner
Wedge thickness
Layer insulation
Bottom insulation

<b>Stator / vent</b>
Number vent duct (radial)
Duct Width (radial)
Duct pitch
Magnetic Spacer width

Table 4.4 Rotor parameters

<b>Rotor</b>	<b>Rotor / pole</b>	<b>Rotor / winding</b>
Outer Diameter	Pole arc offset	Winding type
Inner Diameter	Pole shoe width	Conductors per pole
Length	Pole shoe height	Number of strand
Stacking factor	Pole body width	Wire wrap thickness
Steel type	Pole body height	Inter turn insulation
	Press board thickness	Wire size

<b>Rotor/damper</b>	<b>Rotor/insulation</b>
Damper slot per pole	Shoe insulation thickness
Slot type	Pole insulation thickness
Bar conductor type	
End length	
End ring width	
End ring height	
End ring conductor type	
Slot pitch	
Center slot pitch	
End ring type	

Table 4.5 Analysis setup parameters

<b>Analysis setup</b>
Rated apparent power
Rated power factor
Rated voltage
Winding connection
Load type
Rated speed
Operating temperature
Exciter efficiency
Exciting current

After the model is completed, the mesh and the time step have to be carefully selected. Besides, the external circuit has to be coupled at the model. These three parameters are well explained in the following subsections.

#### 4.7.1 Mesh features

The finite element method has been applied to various electromagnetic problems. In this method, the field region is divided into sub regions where a vector potential can be represented by an interpolation function that contains the value of the potential at the respective node of each element. The elements in this method can have various shapes, and can be adapted to any shape of boundary and interface geometries. Each element consists of nodes, edges and facets.

In the software Maxwell 2D, the element shape is a triangle, with 6 nodes per element, resulting in a quadratic function of second order.

The mesh size is mostly related to the skin depth and function of the frequency of different harmonics involved in different parts of the generator at different operating conditions.

Higher harmonics are in general induced in the damper bars especially at slot passing frequency, and also at other frequencies related to the stator magneto electromotive forces. Hence, the mesh density in these areas has to be refined according to the skin depth ( $\delta$ ) which can be calculated from eq. 4.83:

$$\delta = \sqrt{\frac{1}{\pi \cdot \mu_0 \cdot \sigma \cdot f}} \quad (4.83)$$

Where  $\mu_0$  is the permeability of free space ( $4\pi 10^{-7}$  H/m),  $\sigma$  is the electrical conductivity and  $f$  is the excitation frequency.

Rotating electrical machines can be analyzed as a function of the time for various positions of the rotor. For coupling of the model parts (relative movement between the rotor and the stator), three approaches of mesh can be used: movement band (Davat *et al.*, 1985); locked step, (Preston, 1988) and overlapping (Tsukerman, 1995).

The magnetic material characteristics and the mesh definition will influence the total magnetic loss. After the magnetic material is chosen, the mesh has to be defined taking into account the needed results. If the analysis requires the calculation of the magnetic losses, the selected mesh has to be denser at the important parts of the machine where higher losses occur. On the other hand, if the defined mesh very dense, the total simulation time is higher. The challenge consists in choosing the properly sized mesh that can capture the important information and at the same would not take too much time for the simulation.

The sizes of the meshes are chosen making use of the best available experience in this area. For example, even in the case of the smallest meshes containing a number of elements, they were denser at the pole face and in the stator teeth, as shown in Figure 4.5.

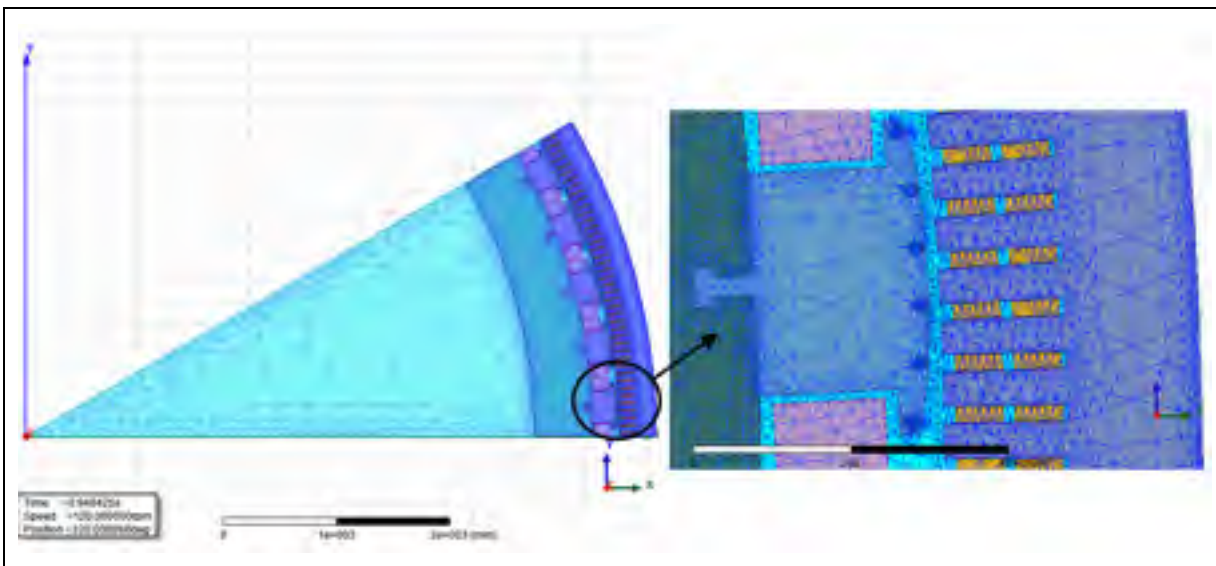


Figure 4.5 Mesh definition for each component

#### 4.7.2 Choice of time step

The time step in a frequency-domain simulation should always be calculated as a function of the characteristics of the machine (number of poles and rotational speed). In a synchronous machine, the duration of one electric cycle can be computed as:

$$\text{Time of 1 electric cycle} = \frac{60}{p \cdot \Omega} \quad (4.84)$$

Where  $p$  is the number of pole pairs and  $\Omega$  is the speed rotation of the machine in rpm.

The time-step is a ratio of the electric cycle time and a pair number (integer). Larger this integer, smaller will be the time step and consequently more harmonics will be observed in the voltage, current and induced field waveforms. For instance, if the integer number is 32, the number of the harmonic order will be 16<sup>th</sup>.

An alternate way to compute the time step is also studied. This method is usually applied for time-domain simulations and the variables to compute the time step; take into account the number of stator slots (Figure 4.6).

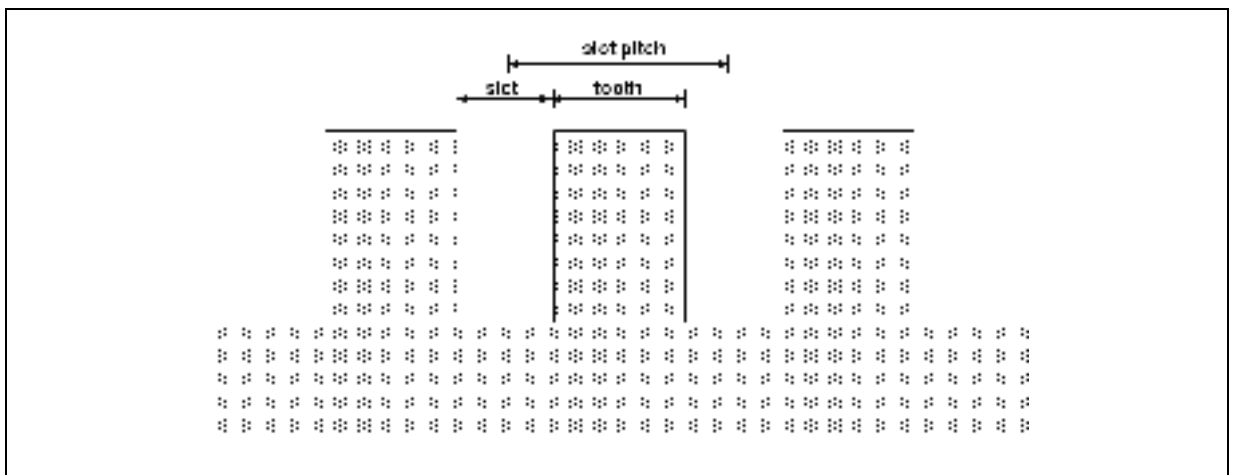


Figure 4.6 Stator representation

The computation equation required for time step for transient simulation is given as follows:

$$Time\ step = \frac{f \cdot \tau}{2 \cdot \pi \cdot R \cdot \Omega \cdot N_{samp}} = \frac{f}{N_s \cdot \Omega \cdot N_{samp}} \quad (4.85)$$

Where  $f$  is the network frequency,  $\tau$  is the slot pitch,  $N_s$  is the number of slots,  $R$  is the stator radius,  $\Omega$  is the rotation speed in rpm and  $N_{samp}$  is the number of samples.

To make a critical analysis, a low time step is required; according to the Nyquist criteria, the simulation time-step used was to allow computation of higher harmonics. With an appropriate time-step, it is therefore possible to capture all the existing harmonics in the machine, such as slot passing frequencies.

The total simulation time can be fixed at one full revolution of the machine. Longer simulation time is always desirable to cover at least three full revolutions of the rotor, but in practice this is limited to keep the computing time reasonable.

#### 4.7.3 External circuit

The Maxwell's partial differential equations of the magnetic field are coupled with the electric circuits equations obtained from Kirchhoff's laws. External circuit takes into account the effects of the end region fringing and leakage flux and also the damper bars connections.

The terminals of the rotor field windings and the armature windings are connected through external circuits. The field and the circuit equations are solved simultaneously to predict the behaviour of the machine. More details about the coupled circuit with electromagnetic solution can be found in (Zhou *et al.*, 2002).

In the case of field-circuit coupled models, the electrical circuit is described in terms of the lumped elements, while the spatial discretization is employed for the field part of a model (Benderskaya, 2007).

The coupling equations that are needed to associate a set of conductor subdomains to a winding are given by (Ranlöf, 2011):

$$\sigma \int_{S_c} \frac{dA_z}{dt} dS - \sigma \psi_c = 0 \quad (4.86)$$

$$\sigma \psi_c + S_c \sigma \frac{\partial V_c}{\partial z} + I = 0 \quad (4.87)$$

where  $S_c$  denotes the conductor area,  $V_c$  the applied conductor voltage,  $I$  is the current in the conductor and  $\psi_c$  is the induced conductor EMF integrated over the conductor surface.

For voltage driven and current driven simulations, the damper bar connection is added to the system as external circuit. Each damper bar is represented by an inductance  $L_{bar}$  and all bars of one pole are connected in parallel through resistance  $R_{end}$  and inductance  $L_{end}$  in series, as shown in Fig.4.7. The damper bars of each pole are connected, but there is no connection between the bars from one pole to another pole, that is why a large resistance of 10 M $\Omega$  is added to the scheme.

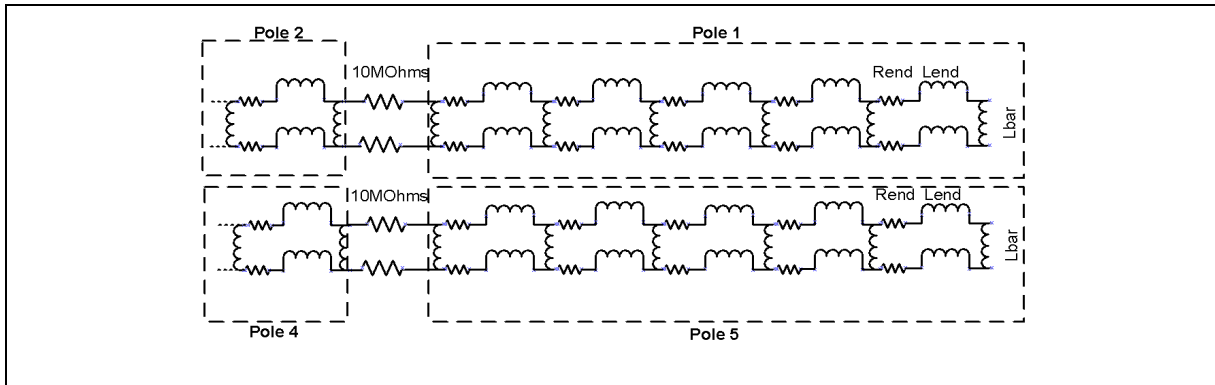


Figure 4.7 External circuit: damper winding bars circuit

For current driven simulations, the three phases; load and the end connections are also coupled to the 2D model by an external circuit. Figure 4.9 presents the load represented by resistance and inductance  $R_{load}$  and  $L_{load}$  respectively and the end bar impedance  $Z_{end}$  consisting of  $R_{end}$  and  $L_{end}$ .

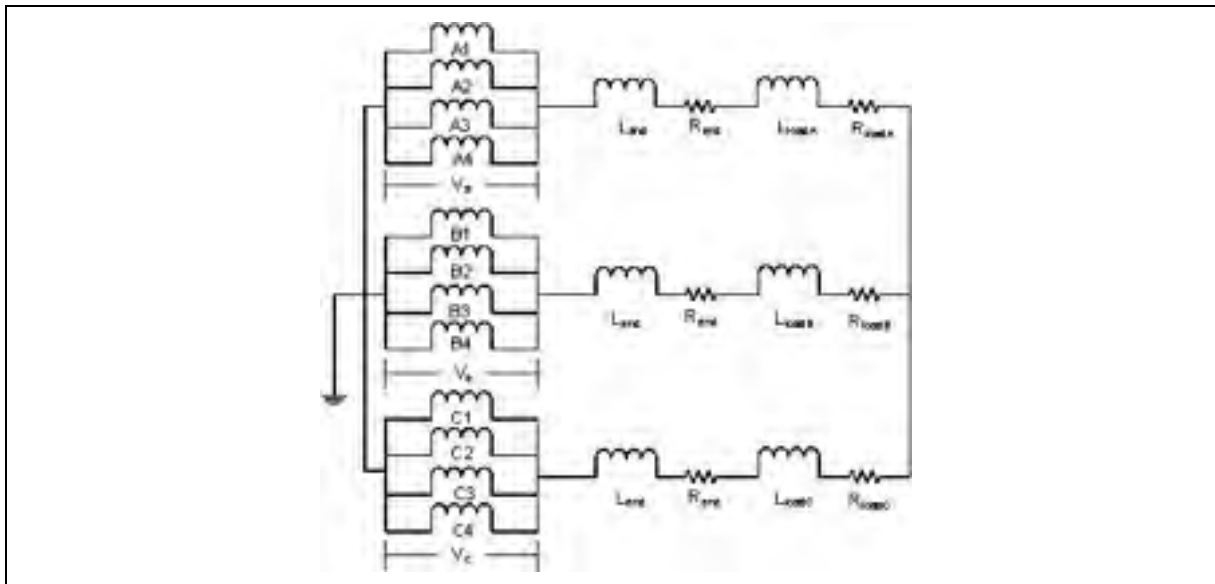


Figure 4.8 External circuit at load condition

For balanced loads, the circuit equations can be determined from Kirchhoff's circuit laws as:



$$\begin{aligned}
V_a - R_{end}i_a - L_{end} \frac{di_a}{dt} - R_{LoadA}i_a - L_{LoadA} \frac{di_a}{dt} - \\
-V_b + R_{end}i_b + L_{end} \frac{di_b}{dt} + R_{LoadB}i_b + L_{LoadB} \frac{di_b}{dt} = 0
\end{aligned} \tag{4.88}$$

$$\begin{aligned}
V_b - R_{end}i_b - L_{end} \frac{di_b}{dt} - R_{LoadB}i_b - L_{LoadB} \frac{di_b}{dt} - \\
-V_c + R_{end}i_c + L_{end} \frac{di_c}{dt} + R_{LoadC}i_c + L_{LoadC} \frac{di_c}{dt} = 0
\end{aligned} \tag{4.89}$$

$$i_a + i_b + i_c = 0 \tag{4.90}$$

## 4.8 Hypothesis and simplifications

### 4.8.1 Geometric model

Hydro-electric generators are usually fractional machines because of its magnetic symmetry. Magnetic symmetry conditions can be determined by the number of slots/pole/phase and the winding sequence. In hydro-electric machines, this number is composed of an integral part and a fractional part where the denominator will serve as the number of modeled poles.

Figure 4.9 presents an example of a fractional machine and its boundary conditions. Originally this three phase machine had 60 poles and 504 stator slots, according to the condition of magnetic symmetry; this machine is a  $2+4/5$ , resulting in 5 poles that had to be modeled.

Besides, the winding sequence had also to be observed to see if an integer number of sequence repetitions is present in the modeled part (in this example 1/12 of the machine, 42 stator slots). In this machine, the winding sequence is 3 3 3 3 2, representing a sequence of

14 parallel windings; hence, the winding sequence is repetitive thrice ( $42/14$ ) in the 5 pole model. As this machine satisfies both the conditions, 5 pole-pitch model is the smallest fraction that can be modeled.

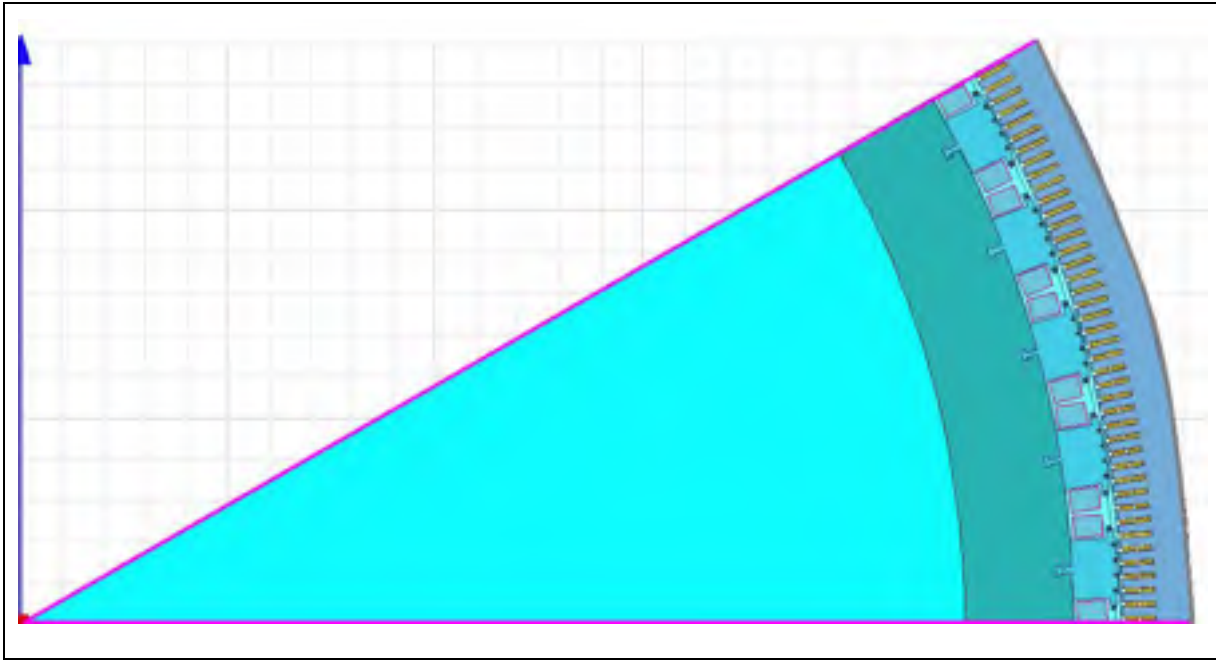


Figure 4.9 Boundary conditions

In Fig. 4.9, the grey line represents the boundary condition of Dirichlet meaning that the magnetic flux is inside the machine and nothing exceeds the boundary. The two pink highlighted lines relate to the master and slave vectors where the field on the master boundary is mapped to the slave boundary. If the machine needs to be entirely simulated, there will be no master/slave vectors.

#### 4.8.2 Equivalent model depth

Simulation of a complex 3D structure usually requires large computation time and powerful computers. So if it is possible, some models could be simplified in 2D models. For that, some assumptions are necessary including the computation of an equivalent model depth for the

rotor and the stator. Simulations were carried out under the assumption that the machine axial length is infinite and the machine geometry is invariant along the axial length. This assumption simplified the problem but neglected the three dimensional effects, such as end-winding leakage. End winding reactance was added to the model by analytical equation based on calculation of effective end-winding length as reported in the section entitled External circuit.

The model depth ( $L_m$ ) in Maxwell software is an input and it constitutes the length of the rotor and the stator considering the staking factor, the duct widths of the rotor and the stator. Basically the model depth can be calculated according to the following formula:

$$L_m = \min(L_r, L_s) - n_v \cdot b_v \cdot k_{bv} \quad (4.91)$$

Where  $L_r$  and  $L_s$  are related to the rotor and stator lengths respectively,  $n_v$  is the number of aligned radial ducts;  $b_v$  is the duct width and  $k_{bv}$  is the duct-loss-width coefficient related to. Unfortunately this equation considers the same model depth for the entire machine.

In Maxwell 2D the model depth is used in the post-processing of the core loss. After the core loss for each element in each instant of time is calculated, this value is multiplied by 3 different parameters: the area of each element, the model depth and the fractions (that in case of Manic 21, this number is equal to 12). However, as the model depth could not be the same for the rotor and the stator, a global value that we considered introduced an error in the result of post processing analysis result.

### 4.8.3 Magnetic material characteristics

For the core loss determination, the magnetic material characteristic curves are important inputs in the core loss model. Basically two curves of the iron-core material must be studied: The B-H curve (magnetization characteristics) and the (Flux density-Permeance) B-P curve

(loss characteristics) can then be determined for 60 Hz and multiple frequencies. With the B-P curve, and considering some parameters such as thickness, conductivity, the coefficients  $k_h$ ,  $k_c$  and  $k_e$  related to the hysteresis phenomenon, classical eddy current and additional losses respectively can also be obtained.

To take into account the non-linearity of the magnetic material different models can be used: analytical curve method and also Marrocco method. Marrocco method performs the approximation of the reluctivity.

Maxwell software takes into account the non-linearity of the magnetic material. This model is an alternative way of specifying anisotropic behaviour when using laminations. The nonlinear behaviour for the material lamination is defined by a user specified B-H curve, while the global anisotropy is modeled by specifying a stacking factor and the stacking direction. In this way, Maxwell software can consider a global anisotropy with two orientations - one in the plane of the lamination, and the other in the corresponding orthogonal direction.

#### **4.8.4 Types of simulation: voltage driven x current driven**

In this subsection, two types of simulations are described: voltage-driven and current-driven.

For voltage-driven problems, the voltage is a known value and it is specified as boundary conditions to the FE problem. The voltage for the time-harmonic problem has real and imaginary components.

In voltage driven simulation, the machine is connected to an infinite grid and there is no necessity of an external circuit. This type of simulation is extremely sensible to the power angle  $\delta$  used in the simulation. As already explained in session 4.1, the procedure to get the power-factor angle  $\delta$  is difficult and its calculation method is presented in the Std. IEEE-115.

A small error in the calculation of the load angle  $\phi$  can lead to large errors in the final result of the power-factor angle and the power output. There is a direct proportional relation between the power output and the power-factor angle.

Voltage driven simulation demands the calculation for many electric cycles resulting in more simulation time for the solution to converge to a stable value and reach the steady-state. For voltage driven simulation, the phase voltages are computed and added into the circuit as inputs. In this type of simulation, the generator is connected to an infinite grid.

For current-driven problems, the prior knowledge of the current waveform can be used as input of the finite-element process. In finite element simulations, the most commonly applied method is the current driven especially because the convergence of the results are faster, resulting in a smaller computing simulation time. However, the voltage driven method has one greater advantage, the excitation current is an output of the system and can be calculated when the system is stable.

The current driven method is usually the most commonly used in finite element formulations and therefore it is chosen for the most part of the simulations in this thesis. In current driven simulation mode, the excitation current is considered as a fixed input (the measured excitation value during test is used as reference). Besides, the simulation can be performed on load, open-circuit and short-circuit conditions by simply adjusting the external circuit for each configuration. In this method, the simulation time is shorter when compared to the case when simulation is based on voltage driven input, and at the same time providing acceptable results.

In finite element simulations, the most applied method is the current driven especially because the results converge faster, resulting in a smaller simulation time. However, the voltage driven method has one greater advantage, the excitation current is an output the system and it can be determined when the system is stable.

## 4.9 Magnetic losses models

The precise characterization of magnetic material is crucial for the determination of the magnetic losses. These losses are determined after the fields ( $A$ ,  $B$ ,  $J$ ) are computed by FEM and then the post-processing is completed.

In the two following subsections the models of the losses in the damper bars and the core losses are investigated.

### 4.9.1 Solid loss model

Solid loss represents the resistive loss in the machine. It is also known as damper bar loss or Joule losses in the damper bars. The solid loss is related to the current density  $J$  and it can be obtained through the magnetic potential vector as given by eq. 4.92:

$$J = -\sigma \frac{\partial A_z}{\partial t} \quad (4.92)$$

Where  $J$  is the electric current density which is not uniform over the damper bar surface,  $\sigma$  is the material conductivity and  $A_z$  is the magnetic potential vector on z-axis.

Consequently, the solid losses can be computed by the integration over the volume of the square of the current density:

$$P_d = \frac{1}{\sigma} \int_{vol} J^2 dV \quad (4.93)$$

The current density  $J$  is simply the current  $I$  per unit of area. Once  $J$  is computed,  $I$  is easily obtained.

The computation of the induced currents in various damper bar windings is a fairly complex problem in an electrical machine while in operation, especially with fractional slot machines which is almost always the case with large hydro-electric machines. The frequencies, magnitude of these currents and their distribution, are significantly affected by the following parameters:

- the number of bars per pole; the distribution of these bars across the pole face; the bar permeance, determined primarily by the dimension of the slots above the bars. And the connection of the amortisseur windings between poles, or the lack of such connection;
- the shape of the airgap (ratio of maximum to minimum airgap, pole face geometry, second pole face radius, etc.); number of slots, slot pitch and slot dimensions in the stator core; the amplitude and frequencies of the armature reaction MMF waves.

A number of other design variables are not listed above, which may have a second order effect but their interactions are not necessarily negligible. The computation of the temperature of the damper winding during operation at rated load condition or during any asymmetrical fault requires an accurate prediction of the induced current distribution in the damper circuits.

The damper current distribution for steady-state operation has been traditionally calculated with d- and q-axis synchronous machine equivalent circuits (Vögele *et al.*, 1998). The accuracy of the solution for the bar currents is, however, limited by the accuracy with which the d- and q-axis circuit parameters could be determined.

Due to the recent advent of powerful workstations, the analysis of synchronous machines has become feasible for performing simulation studies using electromagnetic transient FEA. The finite element analysis was already used to compute the eddy current in the damper winding during start-up (Kladas and Razeq, 1988). The simulation of unbalanced operating condition of an electrical machine and specifically for the design of the damper bars of single-phase synchronous generators was also reported in (Weeber, 1998); this work was extended in

(Karmaker and Mi, 2004) to evaluate damper bar performance during start-up of large salient pole synchronous machines; however, the damper bar temperature in this last case was computed only based on adiabatic heating without considering any heat transfer in airgap and in the pole face area. Recently additional losses in the damper bars were also computed analytically and numerically (Traxler-Samek *et al.*, 2010) but without any test validation or any consideration for the thermal capability of the damper bars.

Based on the calculated solid losses and the damper bar currents, both computed by the software, a constant damper bar resistance is calculated. The FFT of the current was performed and the amplitudes of each harmonic were established. With this resistance, the losses were then recomputed for each damper bar of each pole.

#### 4.9.2 Core loss model

The time-domain dynamic core loss model proposed in (Lin *et al.*, 2004) was also used in this study to compute the core losses. This last model was initially applied to compute instantaneous core losses in small electromagnetic devices in both two-dimensional and three-dimensional finite element analysis.

The general equation for this proposed dynamic model is given by eq. 4.94:

$$P_v(t) = H_{irr} \left( \frac{dB}{dt} \right) + k_c \left( \frac{dB}{dt} \right)^2 + k_e \left| \frac{dB}{dt} \right|^{3/2} \quad (4.94)$$

The three terms in (4.94) are respectively the hysteresis, eddy and excess losses given in the time domain.



The procedure for the determination of the irreversible component of the magnetic field in a static hysteresis loop  $H_{irr}$  is the key to computing the hysteresis loss. The expression of the irreversible component  $H_{irr}$  as proposed in (Bottauscio, Cavano, 2002) and (Lin *et al.*, 2004) is given by eq. 4.95:

$$H_{irr} = \frac{1}{\pi} k_h \cdot B_m \cos(\theta) \quad (4.95)$$

Where  $B_m$  is obtained directly from the historical record of the flux density.

In equation (4.94) the coefficient  $k_c$  of the classical loss is given as:

$$k_c = \frac{\sigma \cdot d^2}{12} \quad (4.96)$$

The loss coefficients for the hysteresis and excess-loss components  $k_h$  and  $k_e$  respectively, are derived using the regression curve algorithm based on the measured specific core loss curve at different frequencies. Usually, the parameters  $\alpha$  (between 0.8 and 2.3),  $k_e$  and  $k_h$  are calculated from measured loss data. The parameter  $d$  is the lamination thickness and  $\sigma$  is the material conductivity.

Equation 4.94 can be extended in for 3D coordinates xyz as shown by eq. 4.97-4.99:

$$P_h(t) = \left\{ \left| H_x \frac{dB_x}{dt} \right|^{\frac{2}{\beta}} + \left| H_y \frac{dB_y}{dt} \right|^{\frac{2}{\beta}} + \left| H_z \frac{dB_z}{dt} \right|^{\frac{2}{\beta}} \right\}^{\frac{\beta}{2}} \quad (4.97)$$

$$P_c(t) = \frac{1}{2\pi^2} k_c \left\{ \left( \frac{dB_x}{dt} \right)^2 + \left( \frac{dB_y}{dt} \right)^2 + \left( \frac{dB_z}{dt} \right)^2 \right\} \quad (4.98)$$

$$P_e(t) = \frac{1}{C_e} k_e \left\{ \left( \frac{dB_x}{dt} \right)^2 + \left( \frac{dB_y}{dt} \right)^2 + \left( \frac{dB_z}{dt} \right)^2 \right\}^{0.75} \quad (4.99)$$

And  $C_e$  is equal to 8.763363 and it is obtained from the numerical integration of:

$$C_e = (2\pi)^{1.5} \frac{2}{\pi} \int_0^{\pi/2} \cos^{1.5} \theta d\theta \quad (4.100)$$

### 4.9.3 Implemented model for core loss computation

The choice of the magnetic material has a significant impact on the magnetic core losses. However, the magnetic material characteristic curves are not always available for older generators selected for the study of uprating.

The studied machine was refurbished and the stator material was replaced. The new stator magnetic material was characterized regarding the losses at multiple frequencies. On the other hand, the rotor material was still as the original one. The iron losses of the rotor material were characterized by the manufacturer only at 60 Hz.

The losses in the stator and in the rotor were calculated by different methods. In order to provide a core loss method that could take into account variable coefficients for (4.94), the stator losses were determined by the method presented in section 4.9.3.1. Besides, in the rotor, a general equation was used to determine the additional losses; this method is shown in section 4.9.3.2.

#### 4.9.3.1 Stator loss model

The model proposed by Bertotti *et al.* (1987, 1992, and 1993) separated the core loss into three components. The physical justification for separation of losses into hysteresis, classical eddy current and excess loss contributions was provided in these references. It was assumed that the excess loss component is specially governed by the statistical distribution of the local threshold fields at which different magnetic objects become magnetically active. Accordingly, the magnetic core losses under sinusoidal flux condition are then given by the Eq. (4.101)

$$\begin{aligned} P_v &= P_h + P_c + P_e \\ &= k_h f B^\alpha + k_c f^2 B^2 + k_e (fB)^{3/2} \end{aligned} \quad (4.101)$$

Where  $P_h$  is the hysteresis loss,  $P_c$  is the eddy current loss and  $P_e$  is referred to the excess loss. The loss coefficients  $k_h$ ,  $\alpha$ ,  $k_c$ ,  $k_e$  are mostly related to the magnetic material lamination characteristics and can be determined from the measured loss curve function of the flux density.

The coefficients in (4.101) are always assumed to be constant and invariable with the frequency  $f$  and magnetic induction  $B$ . However, (Ionel *et al.*, 2006 and Chen and Pillay, 2002) proposed a new method that takes into account the non-uniformity of these two parameters. The first step of this method is to determine the losses in the magnetic material. Then, in order to determine the  $k_h$ ,  $n$ ,  $k_c$ ,  $k_e$ , the total loss is divided by the frequency as:

$$\frac{P_v}{f} = a + b\sqrt{f} + c(\sqrt{f})^2 \quad (4.102)$$

Where  $a$ ,  $b$  and  $c$  are defined by eq. 4.103

$$a = k_h B^n \quad b = k_e B^{1.5} \quad c = k_c B^2 \quad (4.103)$$

The core loss measurements on the magnetic material varied with frequency from 60 Hz to 960 Hz were used to determinate the coefficients  $a$ ,  $b$  and  $c$  of the magnetic material. The eddy-current and excess loss coefficients are readily identifiable. However, the hysteresis loss coefficient and the exponent  $\alpha$  are obtained by the eq. 4.104 (Ionel *et al.*, 2006):

$$\log a = \log k_h + (\alpha_0 + \alpha_1 B + \alpha_2 B^2 + \alpha_3 B^3) \log B \quad (4.104)$$

An algorithm that describes the steps procedures necessary for solving the equations 4.101 to 4.104 is presented in (Ionel *et al.*, 2006).

This core loss method can be simplified as:

$$P_v = \sum_{n=1}^N \left( K_h(B_n) (nf) B_n^2 + K_c(nf, B_n) (nfB)^2 \right) \quad (4.105)$$

The biggest advantage of this method is that  $K_h$  and  $K_c$  are not constants anymore;  $K_h$  is a function of the magnetic flux and  $K_c$  is a function of the frequency and the magnetic flux.  $K_h$  and  $K_c$  can be tabulated in a look-up table presented in Annex 1.

#### 4.9.3.2 Rotor loss model

The electromagnetic rotor loss of large hydro-generators consists of two parts: damper bar copper loss and additional loss in the damper bars and the pole surface. The additional losses caused by harmonic fields associated with the space non sinusoidal distribution is computed in this thesis.

The additional loss of the magnetic pole surface under no-load and rated voltage is given by (Zhang Dong *et al.*, 2002), (Weili *et al.*, 2011), (Fan *et al.*, 2008) and (Feiyang *et al.*, 2010):

$$P_{fe,p} = k_0 (B_0 \tau_1)^2 (Z_1 n_N)^{1.5} \quad (4.106)$$

Where  $k_0$  is the coefficient for calculating surface loss relating to the magnetic material properties;  $B_0$  is the maximum harmonic flux density of the tooth;  $\tau_1$  is the stator teeth pitch;  $Z_1$  is the number of stator slot and  $n_N$  is the synchronous speed.

In this thesis, the same equation (eq. 4.106) was extended to calculate the additional loss of the magnetic pole surface for the load condition; however, a small change was made,  $B_0$  was considered as the flux density at the pole face during loaded condition.

$$P_{fe,p} = k_0 (B \tau_1)^2 (Z_1 n_N)^{1.5} \quad (4.107)$$

Where  $B$  is the maximum harmonic flux density of the pole shoes.

In the equations 4.106 and 4.107, the flux density is raised to an exponential two and the machine characteristics (speed and number of slots) are related to the exponential of 1.5.

The rotor core losses under load calculation were computed using the equation 4.107 only for the pole shoes area; in the rest of the pole body the losses were neglected.

## 4.10 Conclusions

Simulating an electrical machine by finite element method requires a large number of variables that need to be analyzed in order to obtain a proper model for the machine.

In this chapter, the mathematical model to compute the electromagnetic flux density and the model to compute the core loss of a synchronous salient pole generator were detailed. This chapter started with the traditional d-q model and then highlighted the Maxwell's equations, boundary conditions, governing vector potential  $A$  equations and the applied equations that are used in the finite element model for each part of the machine. This part had the aim of explaining the equations that are presented in some of the commercial finite element software.

Then, in order to construct the generator model, some hypothesis and simplifications have to be made on the mesh features, external circuit and time step. All these variables were detailed and showed how important they are for getting an accurate model.

More equations are detailed to explain the models used for the evaluation of solid loss and the core loss. Besides, a core loss model is proposed. For that, the software is used to compute the magnetic flux  $B$  and, the core loss model is chosen according to the available information on the magnetic material characteristics. The idea behind using a proposed model was to compare the results with those obtained from the various other available models, discuss which one of these models is suitable for a specific case; in addition the proposed model was to compare the results obtained from time domain model (presented already in the software) with those obtained from frequency domain. The results obtained from the existing core loss model available in Maxwell software and the proposed model will be presented in the following chapters.

## CHAPTER 5

### SIMULATION RESULTS AND MODEL VALIDATION

A first set of simulations were performed in Manic 21 with the intention of validating the model described at Chapter 4. The machine model was built with some parameters obtained from the experimental tests and other tests regarding the machine's magnetic material. The first step to validate the model is by checking if the simulation results are comparable to those obtained from experiment and if not, a calibration of the model must be done.

The simulated results depend on the operating condition (open-circuit, short circuit or load conditions) and the available experimental data for each of these measurements. Basically, the phase voltages and currents, the average core loss, the damper bar currents and the solid loss are analyzed. Besides, simulation by FEM allows the determination of the magnetic flux and the core losses distributions.

Figure 5.1 presents the steps that were done to extrapolate the machine for a higher operating point. For all simulations, a matrix of core losses and a matrix of magnetic flux density were generated.

The determination of the matrix loss distribution for different operating conditions is the major contribution of this thesis and an important key parameter for the multi-disciplinary team to determine any hot spot temperature in the generator under study. These hot spots are used later to determine the power limit of the same generator.

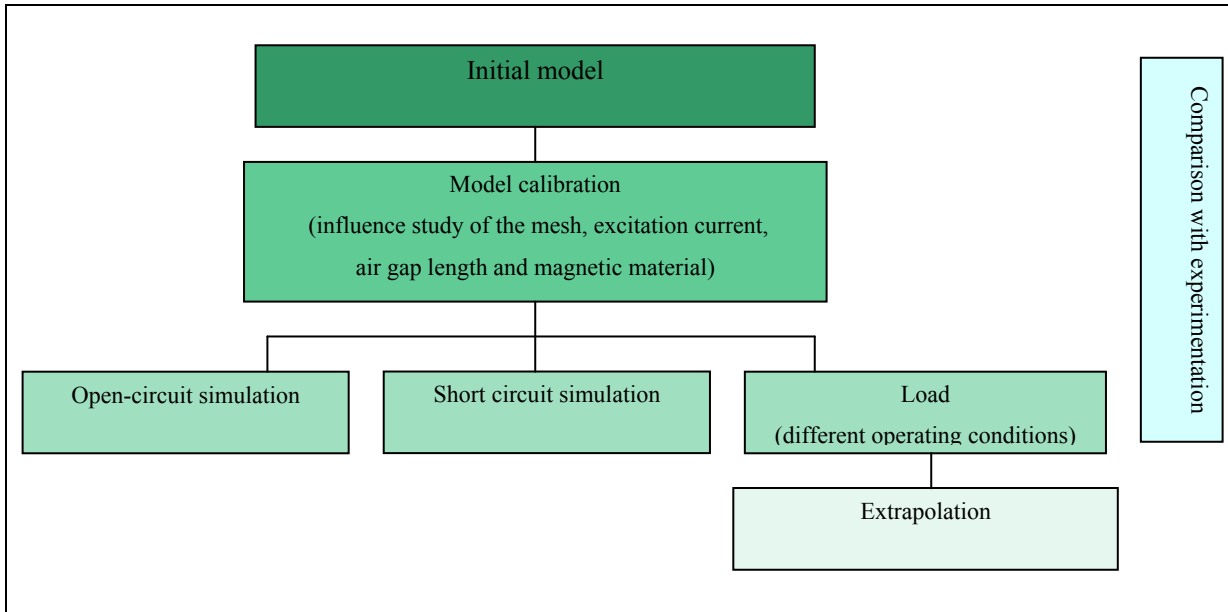


Figure 5.1 Extrapolation steps

The simulation presented in this chapter has the aim to first validate the model for different operating conditions for which experimental tests are available and later for further extrapolation of extending the operation of the machine. Chapter 5 was divided into 6 sections. The first one introduces the initial model of Manic 2. Section 5.2 presents the calibration of the model and those aspects that are considered necessary to get an accurate model. Section 5.3 details the simulation results on open-circuit and short-circuit conditions. Section 5.4 presents the results of computation of the core losses for different percentage of loads. In section 5.5, the results for a different core loss model is presented for the stator and for the rotor under the same operating load conditions as before. Finally from these results the conclusions are detailed.

Some of the results presented in this chapter have been already published and appear at (Aguilar *et al.*, 2011a, 2011b, 2012a, 2012b, 2013a, 2013b, 2014; Merkhoulf *et al.*, 2011, 2012, 2013).



## 5.1 Initial model

The armature winding of Manic 2 is fractional with  $2\frac{4}{5}$  slots per pole per phase. This allows 5 poles pitch model to be used for the electromagnetic transient simulation, as shown in Fig.5.2.

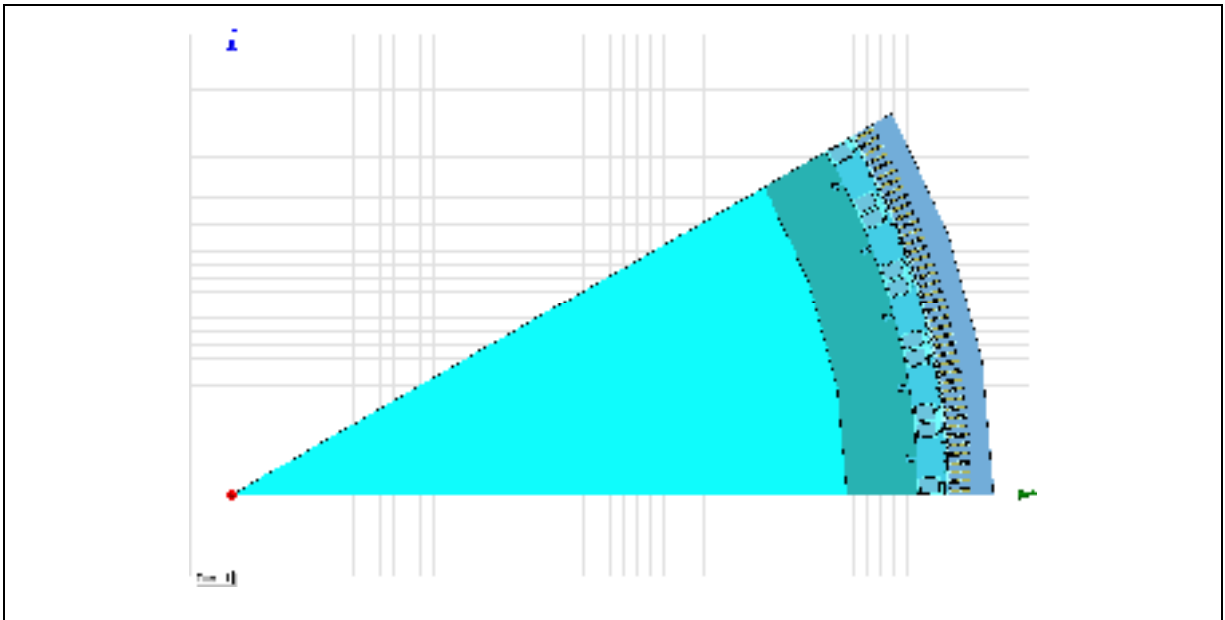


Figure 5.2 Five poles machine model

Electromagnetic simulation of Manic-generator 21 is performed by finite elements analysis using a refined mesh and a time step of the order of a few microseconds. This allows to calculate all the higher harmonics and sub-harmonics present, as well as, transient electromagnetic forces, transient torque, tension, slot passing frequencies, induced currents in different parts of the machine and the corresponding induced electromagnetic losses.

To allow critical analysis, a low time step is required, according to the Nyquist criteria; the simulation time-step of  $2.75 \times 10^{-5}$  seconds (computed by equation 4.87 of chapter 4) was selected for the machine in Manic 2 that allows computing higher harmonics up to 300<sup>th</sup>.

## 5.2 Model calibration

There are modeling difficulties: one of them being that the operational airgap being different from the designed one; another, the load excitation current can deviate from the actual load excitation measurement, and so forth. These are true for both types of machines, new and existing. However, when the generators are considered for uprating the core loss distribution has to be carefully studied to guaranty that the short term benefits are not detrimental to the equipment's life expectancy.

Modeling a large machine is a process with many uncertainties, particularly when some of the parameters are unknown and presumed, is a difficult one. It requires several iterations to extract the several required parameters. For instance, the magnetic material of existing machines is sometimes unknown. Besides, some of the questions could be: how many elements one must have to get a good mesh for the Finite Element Analysis? What is the purpose of the simulation? If it is only for the calculation of the average loss or if it is necessary to computer the loss distribution to determine the hot spots of the machine? Further, if the simulation time is important, how long a simulation run could take? Other important parameters and considerations are: the size of the airgap, should the airgap be considered as designed for nominal operation, if the value of the airgap is available. Finally, the last input parameter studied is the excitation current and its importance. Does the measured excitation current provide a good core loss output or this value must be changed in order to be closer to the measured core loss value? All these questions are answered in the next subsections and they are organized according to the diagram presented at Fig. 5.3.

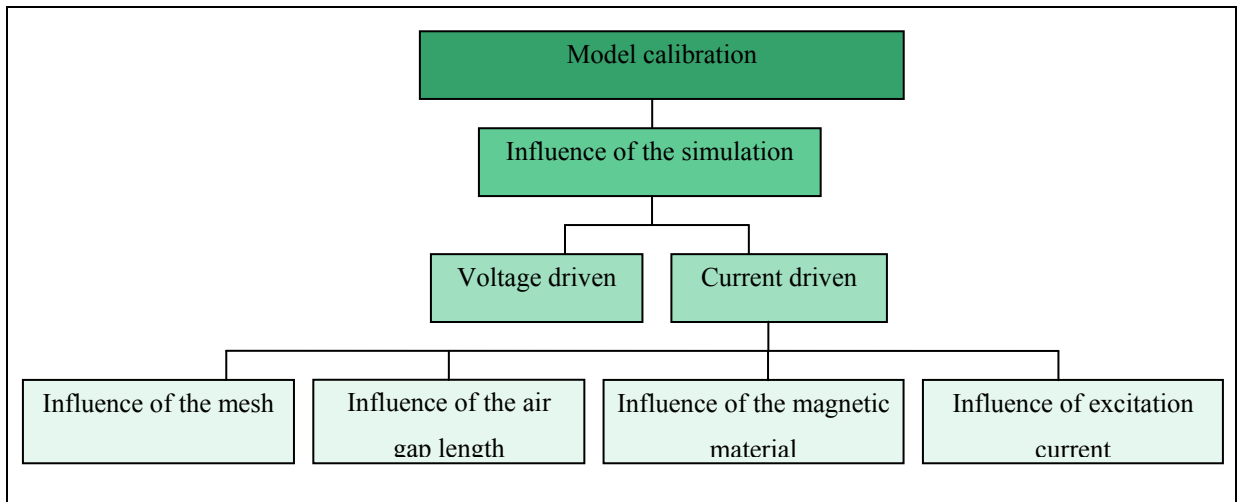


Figure 5.3 Model calibration

### 5.2.1 The influence of the mesh

The large diameter of hydro-electric generators (ten meters or more) leads to a model with a very large number of elements. The mesh size is related to the skin depth involved in different sections of the machine, and this is a function of the frequency of various harmonics that are involved during the different operating conditions of the generator.

In general, higher the mesh is refined, the solution will be more accurate, but more time to calculate will be needed for obtaining different electromagnetic solutions.

The mesh density defined during simulations can have a direct impact on the calculated voltage and current waveforms, induced current in the damper bars and on the different induced magnetic core losses in different parts of the generator. Magnetic losses are not uniformly distributed in the generator; thus the mesh density cannot be uniformly distributed in all sections of the generator. In order to capture all the electromagnetic phenomena, the mesh density has to be more refined in sections where higher magnetic losses are expected, such as: pole shoes, damper bars, the airgap, teeth, notches and the crown portion of the stator.

It is a challenge to choose the mesh size that can capture all important phenomena while giving reasonable simulation time. Fig.5.4 shows a typical mesh density distribution in a model. Electromagnetic simulations were carried out with three different meshes at rated conditions (123.1 MVA, 0.8956 p.f., and excitation current of 739 A). In the initial mesh of 35471 elements, higher mesh density was used at the pole face and in the stator teeth. In the other two cases, the mesh size was increased to 125473 and 224227 number of elements respectively.

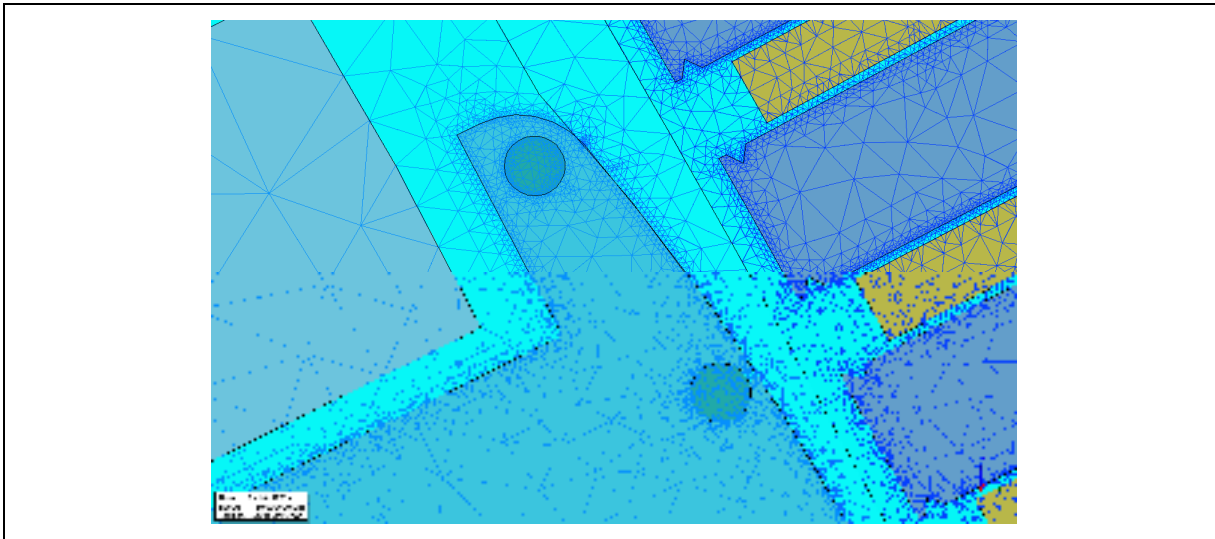


Figure 5.4 Mesh density distribution in different generator parts

To capture the effect of the induced current in the damper bar at the slot ripple frequency, the selected mesh size was the same for all the three cases and it was based on the calculated skin depth at 3 kHz (3 times slot ripple frequency for this generator) for a specific number of layers. In addition, a time step of 27.5  $\mu$ s was used during these simulations in order to evaluate the impact of the mesh size on the computed magnetic losses and computational time.

Table 5.1 summarizes the obtained results of these three cases at rated operating conditions. The computed total magnetic core losses at rated operating conditions are all reasonably

close. But, the simulation time increases drastically when the number of elements chosen for the mesh size gets reduced.

Table 5.1 Compute magnetic core loss with different meshes (time step of 27.5  $\mu$ s)

<b>Mesh Size (number of elements)</b>	<b>Core Loss (kW)</b>	<b>Simulation Time</b>
35 471	617	33h 29min
125 473	629	122h 45min
224 277	631	188h 49min

It can be concluded from this short study that the variation on the total computed magnetic core losses is not significant, within our test range. Therefore, the following simulations were performed using a mesh density of 35,471 elements. It is expected that using higher mesh density will lead to a better prediction of the spatial distribution of the losses, which could improve the prediction of the localization of hot spot temperature during the thermal analysis.

The current density distribution in the damper bar as functions of mesh size was also studied. Fig 5.5 shows the distribution of the induced damper current (current density) obtained with three different mesh sizes in the damper bars for given specific time step. The damper bar losses were calculated for one bar, as 71.87 W, 83.59 W and 85.18 W for the meshing with 23, 90 and 933 elements, respectively. It can be inferred from the Fig. 5.5 that the mesh density affects directly the distribution of the damper bar losses.

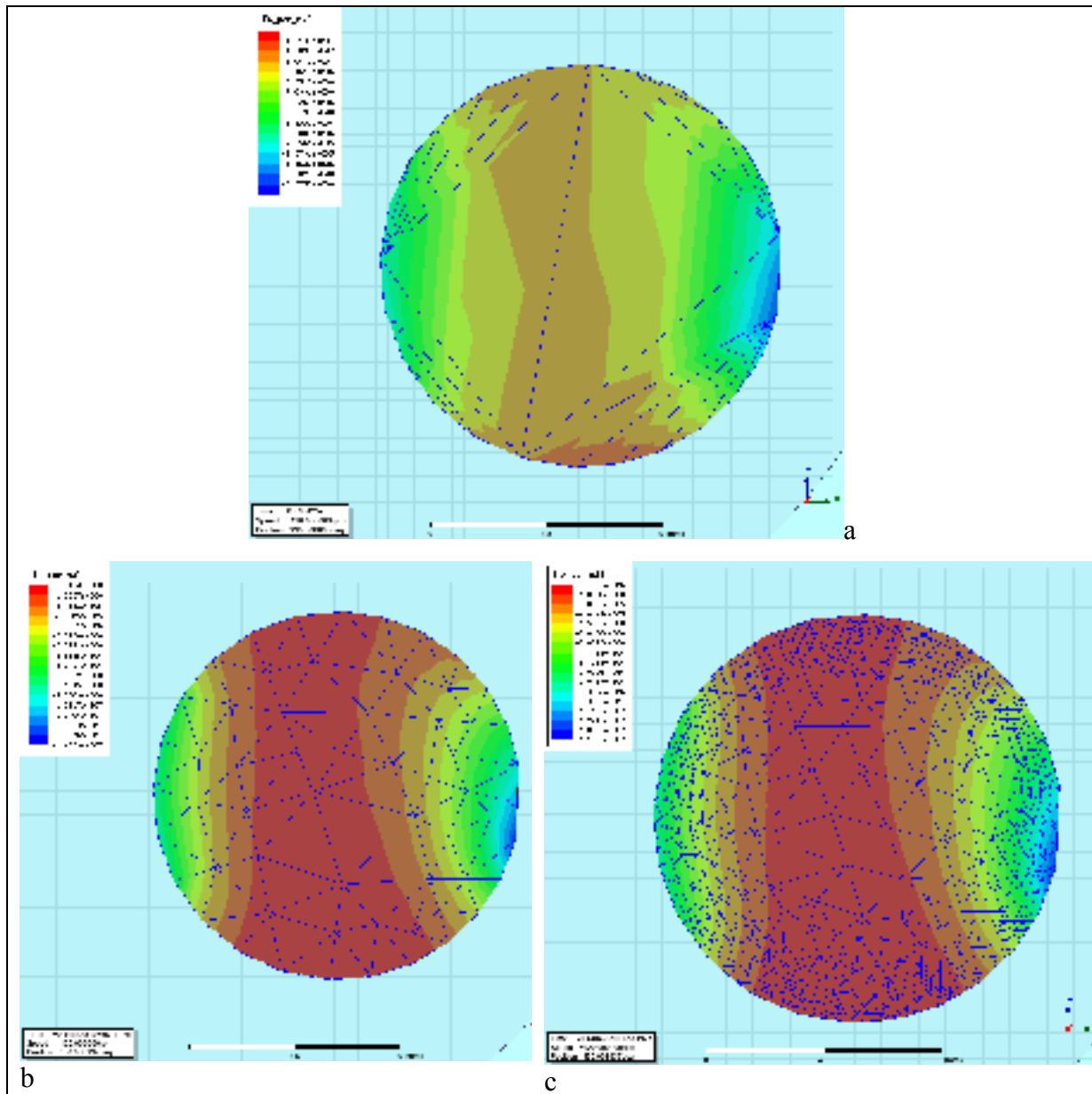


Figure 5.5 Current density distribution in the damper bar for: a) 23 elements per bar, b) 90 elements per bar and c) 933 elements per bar

The variation of the total computed magnetic core losses is almost negligible when a mesh density is chosen as a function of the area or the cross section of the generator where higher power densities are caused at the pole face and the stator teeth. Therefore, if the aim of the

simulation is the prediction of the loss distribution profile, the mesh has to be carefully selected.

Another brief study took into consideration the spectral analysis of the damper bar currents of pole 1 bar 1 for the three different number of mesh elements (23, 90 and 939 elements), as presented in Fig. 5.6. It is observed that the currents do not present any significant variation when the mesh is denser or not. For all the other studies, the mesh for the damper bars contains 90 elements per bar.

However, it must be highlighted that the minimum number of elements defined by the software was 23 for each damper bar of this machine. If the number was smaller than this, the obtained conclusions could be different.

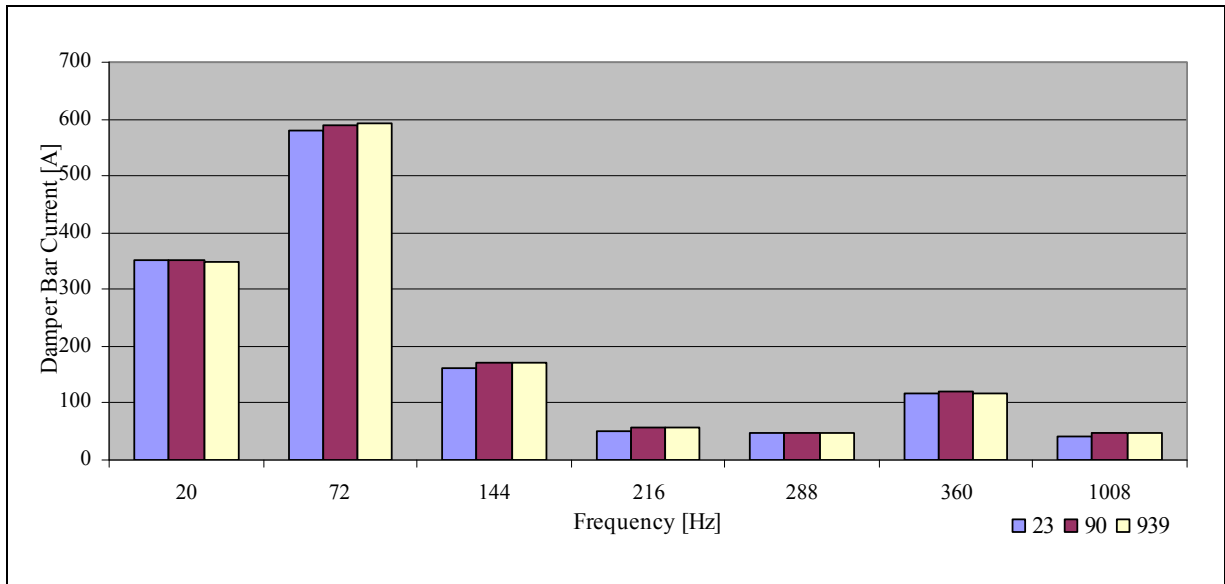


Figure 5.6 FFT analysis of the damper bar current for different mesh configurations (nominal load)

### 5.2.2 The influence of the excitation current

The impact of the excitation current on the simulation results is also studied. In the current driven simulation mode, the excitation current is considered as a fixed input (the measured excitation value during test is used as reference). The measured excitation current can be as much as 15% different from the design value. This difference can be related to the operating point, the airgap average size or airgap shape due to the eccentricity or ellipticity of the stator or of the rotor. It is difficult to predict the effective airgap that can be used during the numerical simulations without measurements. In many cases, for a given airgap size and operating conditions, the excitation current needs to be adjusted consequently in order to obtain the expected voltage and line current during electromagnetic simulations. However, the adjustment on the excitation current for a given airgap size is not without consequences on other electrical parameters as the lines currents, internal voltage and magnetic losses.

The impact of the adjustment of the excitation current on other different electrical parameters is evaluated and thoroughly discussed. The pole face shape, stator slots and the armature windings affect the airgap flux waveform and consequently the losses in the pole face and in the stator teeth. The geometry of the poles with different radii produces a non-uniform airgap and the stator slots and the armature windings cause the flux lines to crowd above the teeth, leading to ripple in the airgap radial flux density distribution. Saturation effects in the pole face and stator teeth are noted even when operating below rated conditions (Gordon and Barton, 1994). These regions need to be studied in order to better understand the physical phenomena behind the flux density and the core loss distributions.

The simulations were performed at load condition (123.08 MVA, 0.8956 p.f.) with three different excitation currents: 739 A, 759 A and 779 A and with design airgap of 15.875 mm. The simulation results confirm established results that can be found in some advanced textbooks on electrical machine design; for instance, higher excitation current results in higher airgap flux density and consequently higher core losses as seen in Table 15; however



the main objective is not only to confirm these facts listed above, but also to determine the loss distribution or the matrix loss density that can be used later in the thermal model to predict temperature field distribution in the generator.

It can be observed that the line current (1 p.u.) was reached for an excitation current of 779 A. Besides, it can be also concluded from these three simulations that the increase of excitation current by 3% (a variation by 20 A) leads to increase of magnetic core losses in the stator and rotor by 3 and 4% respectively.

For an excitation current of 779 A, the total computed magnetic losses at load were around 657 kW. It has to be noted for instance that for 2D model simulation does not include the induced losses in the end plates (3D effect). The end plate losses were analytically computed as 10 kW for this generator; the total magnetic losses are then around 667 kW. This value is close to the measured value of 665 kW calculated as reported in the previous section. However, the excitation current of 739 A produced smaller error regarding the calculation of the magnetic flux density (0.22% when compared to 0.898 T of the experimental value).

Table 5.2 Core loss and current line results for different excitation current  
(airgap of 15.875 mm)

<b>Excitation Current (A)</b>	<b>Results</b>				
	<b>Line Current (p.u.)</b>	<b>Magnetic Flux Density Rms (T)</b>	<b>Induced Voltage (p.u.)</b>	<b>Rotor Loss (kW)</b>	<b>Stator Loss (kW)</b>
739	0.97	0.90	1.06	174	443
759	0.99	0.92	1.07	181	456
779	1.00	0.93	1.09	187	470

The increase of the measured excitation current during the simulation for this machine is reflected as a linear increase of the magnetic core losses in the stator and the rotor. The total

core loss (rotor core loss plus stator core loss) is plotted as a function of the excitation current in Figure 5.7.

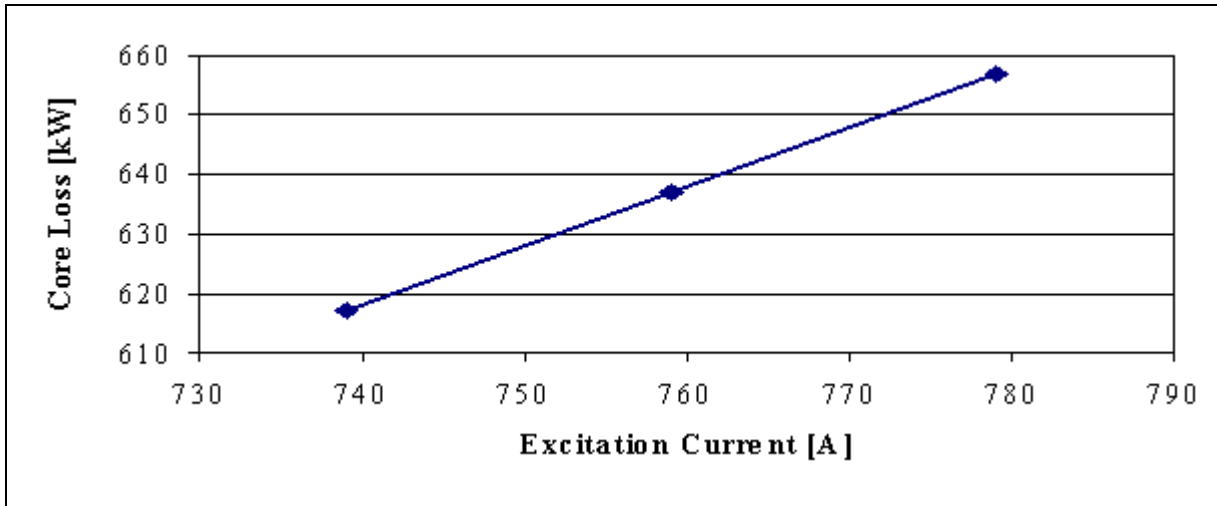


Figure 5.7 Total core loss as a function of the excitation current for nominal load

### 5.2.3 The influence of the airgap length

In order to analyze the influence of the airgap length on the magnetic flux density and core loss distribution on the selected hydro-electric generator, finite element analysis was done for three different values of airgap.

The airgap size varies as a function of the operating conditions. The airgap is affected simultaneously by thermal expansion of the rotor and the stator, the centrifugal forces and the magnetic pull. To determine the actual airgap during operation, online measurements were performed using eight airgap sensors on the machine studied. The airgap measured at full load varied from 11.96 mm (minimum airgap) to 14.93 mm (maximum airgap), with an average of 13.4 mm.

The length of the airgap is always dimensioned at the design stage to produce a minimum magnetizing current; in addition, to get an optimal efficiency design, subject to direct axis

synchronous reactance constraints. The designed airgap is not the same as its value while in operation and it can change substantially with load and temperatures in large hydro-electric machines. In addition, the airgap is non-uniform and usually can be eccentric or elliptical, which results in an asymmetric or non-uniform airgap flux distribution.

The airgap size varies as a function of the operating conditions. This airgap is affected simultaneously by thermal expansion of the rotor and the stator, the centrifugal forces and the magnetic pull distribution.

In a multi-disciplinary project such as generator uprate study, the electromagnetic and thermal teams play an important role in the decision of the initial model conditions regarding the geometry of the machine. In this project, the thermal group believed that the airgap used for the simulation should be the measured one at nominal condition; however, others considered that the designed airgap should be used. To analyze which assumption was accurate; simulations were carried out with measured and designed values of the airgap.

To determine the actual airgap during operation, on-site measurements were performed using eight airgap sensors installed on the machine under study. The airgap measured at rated load varied from 11.96 mm (minimum airgap) to 14.93 mm (maximum airgap), with an average airgap of 13.4 mm.

Electromagnetic simulations were performed with three models having an uniform airgap size of: 11.96 mm, 13.40 mm, 14.93 mm and at the designed value of 15.875 mm. Simulations were performed under measured load condition of: 123.1 MVA, with 0.8956 p.f., and excitation current of 739 A.

The line current, flux density, induced internal voltage, and induced magnetic core losses were computed under these simulations. All the results are summarized in Table 5.3, where it can be observed that the line current varied from 0.97 p.u. (with the maximum airgap length)

to 1.05 p.u. (with the minimum measured airgap). Also a variation of 7.7% of the internal winding induced voltage was found between these two cases. However, considering the core losses at load condition, it can be noted that the magnitude of the computed magnetic core losses; especially the rotor core losses are highly dependent of the airgap size length. As reported in Table 5.3, the variation of the magnetic stator core losses was in the order of 15%, the results are quite different from the variation of the rotor losses for the same cases where 157% variation are observed. A smaller airgap leads to the increase of induced eddy current losses surfacing the pole face area (Phhönen *et al.*, 2008).

Table 5.3 Core loss and current line results for different airgap size ( $I_f=739$  A)

<b>Airgap Length (mm)</b>	<b>Results</b>				
	<b>Line Current (p.u.)</b>	<b>Magnetic Flux Density RMS (T)</b>	<b>Induced Voltage (p.u.)</b>	<b>Rotor Loss (kW)</b>	<b>Stator Loss (kW)</b>
11.96	1.05	1.00	1.13	447	510
13.4	1.02	0.96	1.11	317	485
14.93	0.99	0.93	1.08	219	459
15.875	0.97	0.90	1.06	174	443

The values of total core loss, the rotor core loss and the stator core loss are plotted in Fig. 5.8, as a function of the airgap length. These results show the high impact of value of the airgap length especially on the rotor core losses. When the measured airgap is considered in the model, the excitation current has to be recalculated to achieve the adequate measured line current and line voltage.

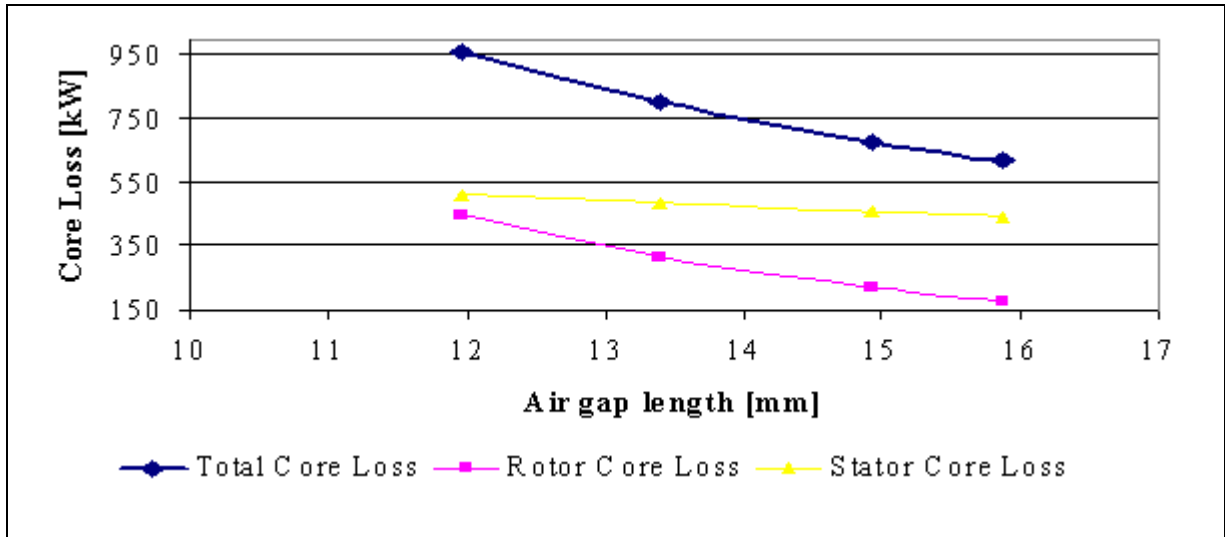


Figure 5.8 Total core loss as a function of the airgap length for nominal load

Fig 5.9 shows the computed spatial magnetic flux density distribution in the airgap obtained with the models considering three different airgap sizes. The impact of the slot ripple frequency on the flux density distribution is clearly observed. As expected, the flux density is higher with smaller airgap. For instance, a flux density of 1 Tesla (RMS) was obtained with an airgap size of 11.96 mm. For an airgap of 14.93 mm the magnetic flux density was 0.93 T presenting an error of 3.56% when compared with the measured value as reported in Table 3.1.

The calculated magnetic core losses are extremely high with smaller air values of the gap size; the proportion of the pole face losses compared to stator losses increases with decreasing airgap sizes. Even if the calculated line current was closer to 1 p.u. when the machine presents an airgap of 14.93 mm, the total computed magnetic core loss (678 kW) in this condition was 2% higher than the experimental value (665 kW).

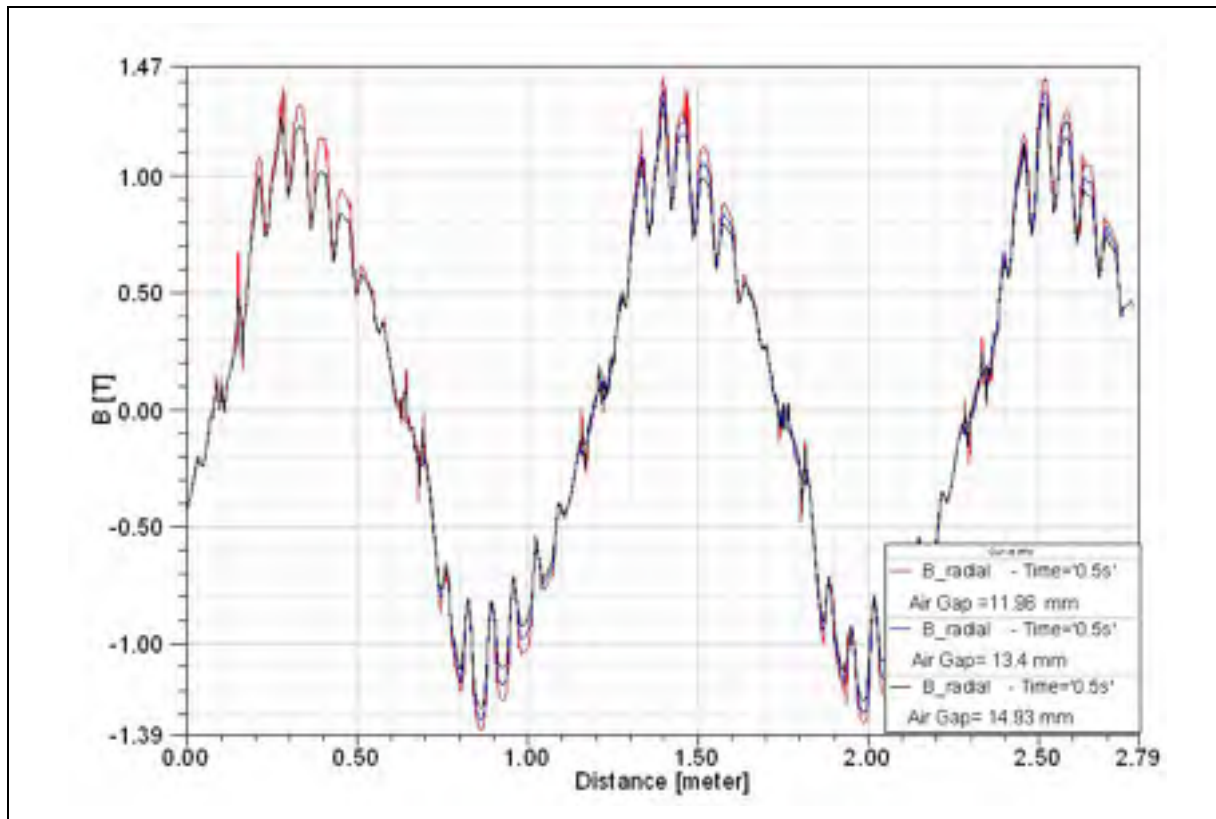


Figure 5.9 Computed magnetic flux density using the measured airgap length

Figures 5.10a and 5.10b show the computed magnetic core loss density distribution obtained respectively with airgap size of 11.96 mm and 14.93 m with the same excitation current of 739 A. It can be observed that the magnetic loss densities are not uniform and are more pronounced in the middle of the pole face and around the damper bars areas.

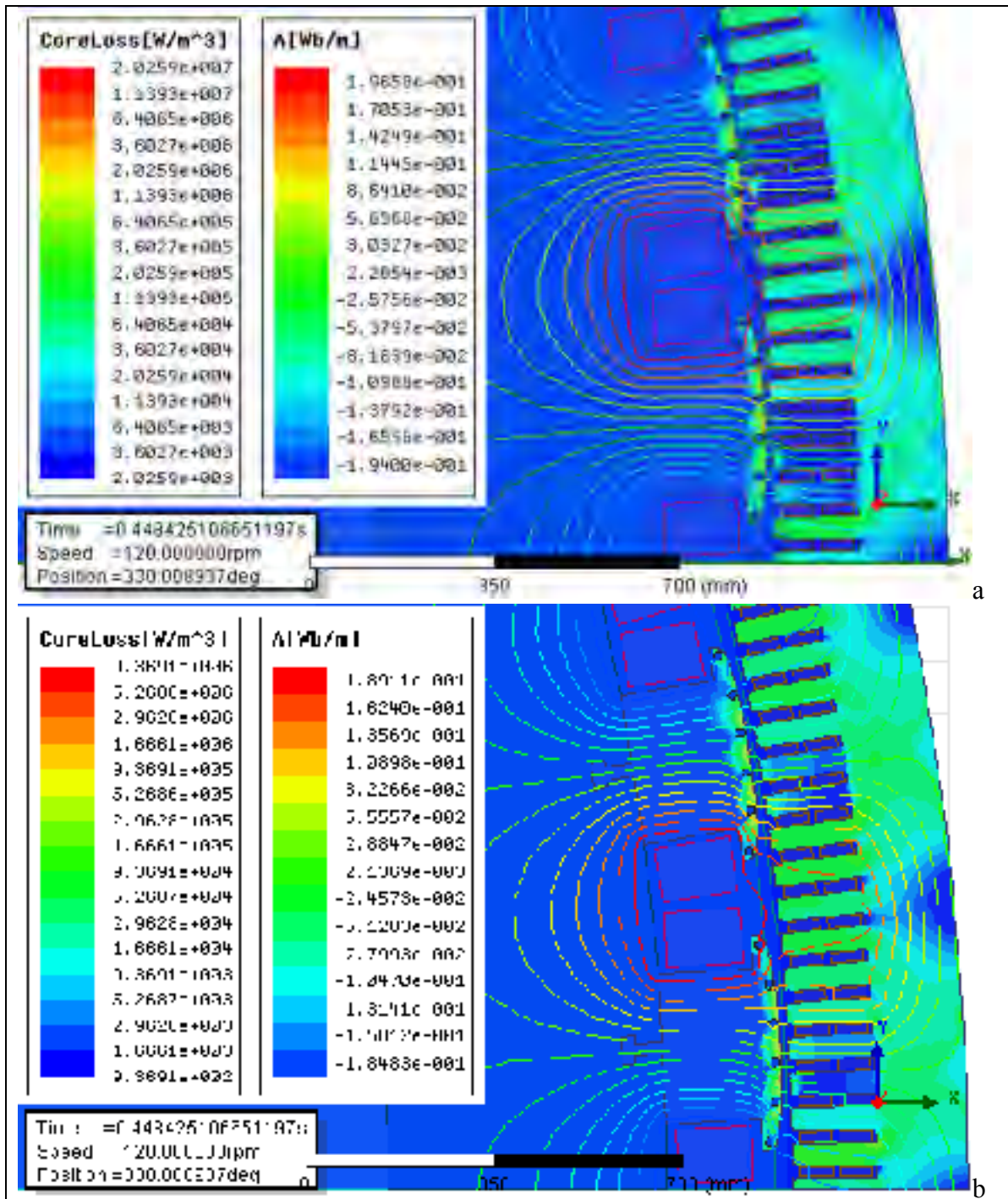


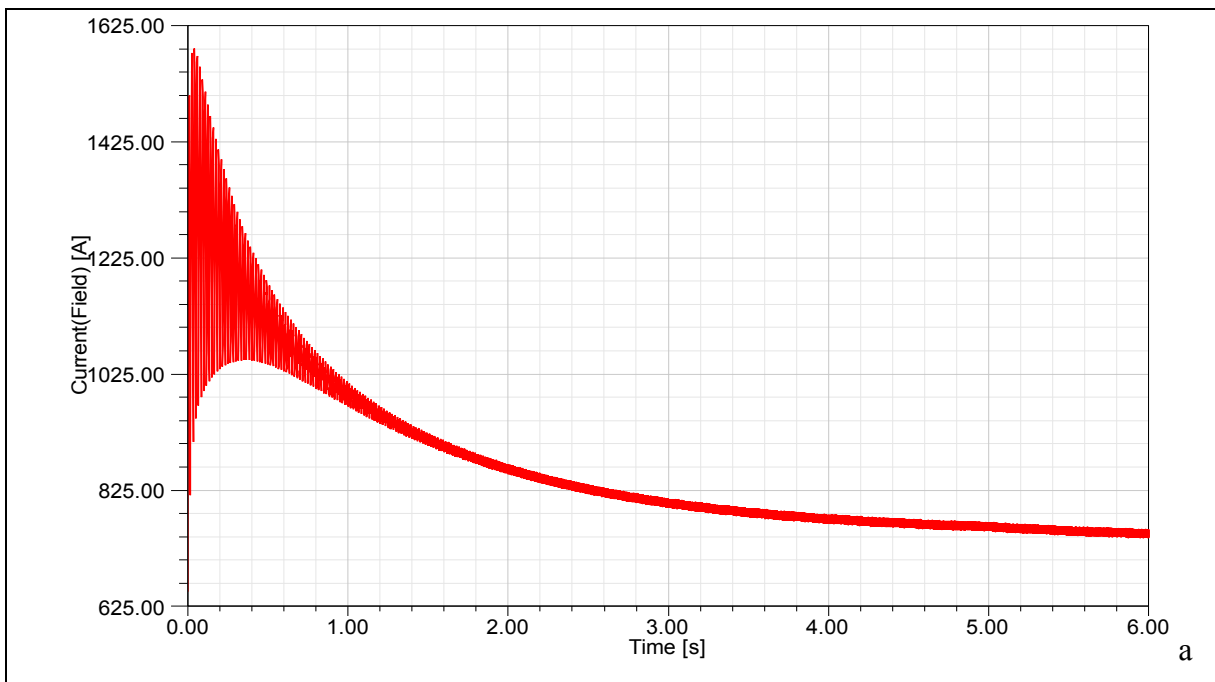
Figure 5.10 Core loss distribution – a) case 11.96 mm, b) 14.93 mm

The accurate prediction of the local core loss is really dependent on the shape and size of the airgap. However, a complete model taking into account the effect of the shape of the airgap such as ellipticity and eccentricity has to be developed in the future. For the estimation of the magnetic losses

#### 5.2.4 The influence of the voltage driven simulation

For a voltage-driven problem, the voltage is a known quantity specified by the user and it is used as boundary conditions for the analysis by finite elements method.

In this simulation, the designed airgap of 15.875 mm was used. The simulation results concerning the core losses and the damper bar currents were almost the same as the values obtained from current driven case. In this subsection, the excitation current is shown in Fig. 5.11a and b.





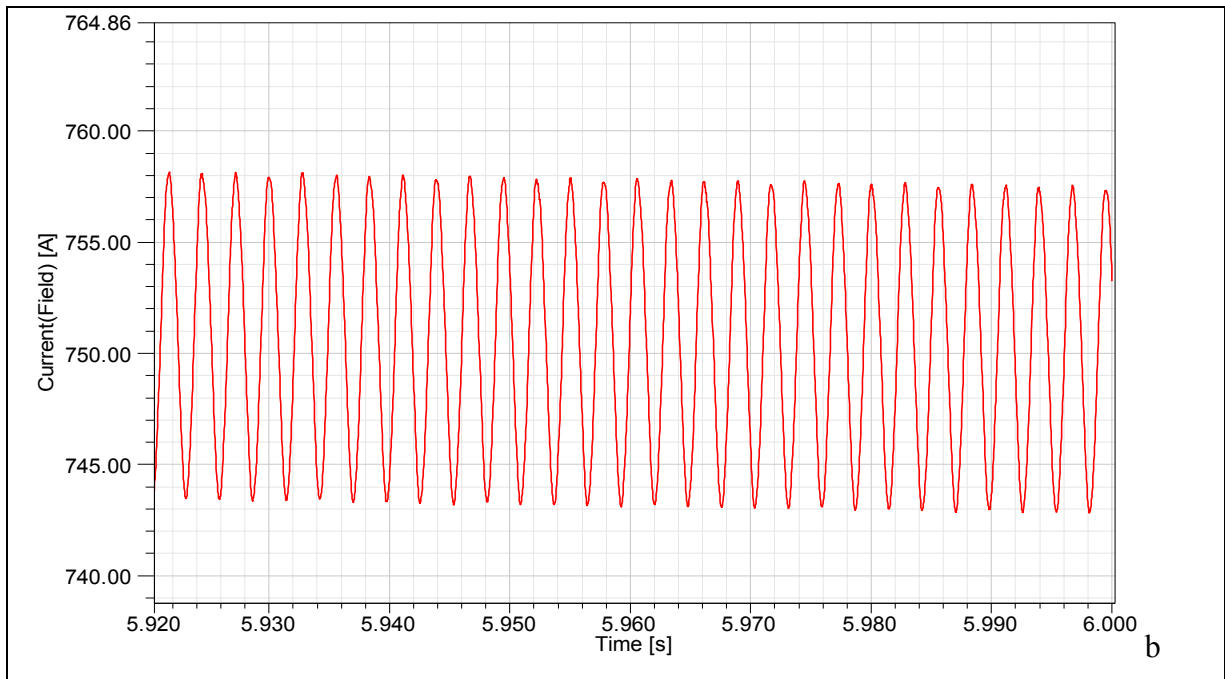


Figure 5.11 Excitation current (voltage driven simulation) a) transient current envelope, b) zoom in the last 0.1s

To provide the proper line current and consequently power output, the average of 748 A was calculated. In the voltage driven, the simulation time took at least 3 times more with a larger time step than the current driven mode summarizing more than 150 hours to completion. This type of simulation is very useful when the value of the excitation current is unknown.

When the phase current is analyzed in the voltage driven simulation, the third harmonic is observed. Figure 5.12a presents the current per phase waveform and 5.12b, the spectral analysis. When the same model is simulated using current driven mode, only the fundamental frequency (60 Hz) is observed.

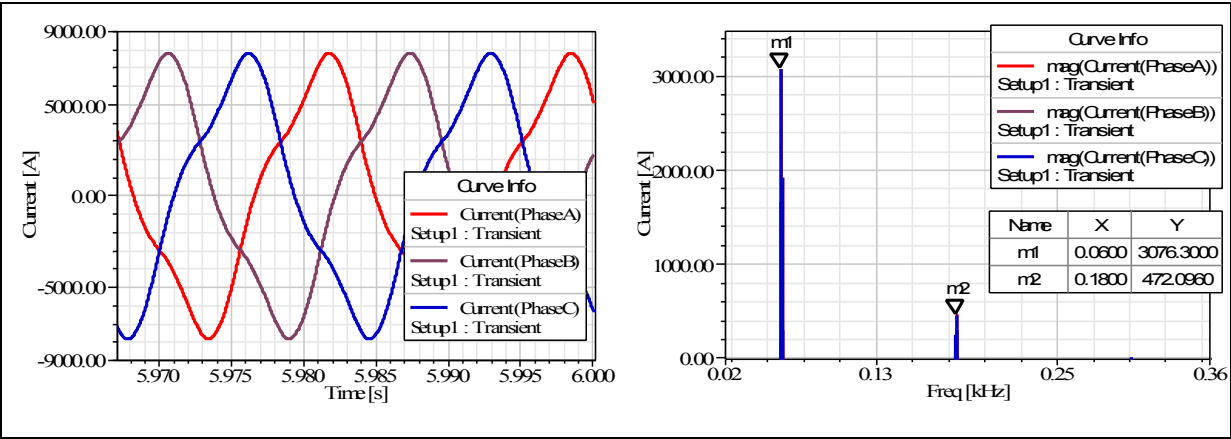


Figure 5.12 Phase current (voltage driven simulation)

Another plot that can be obtained is the voltage per phase at nominal load as shown in Figure 5.13. The voltage waveform is perfectly sinusoidal for all the three phases at nominal load.

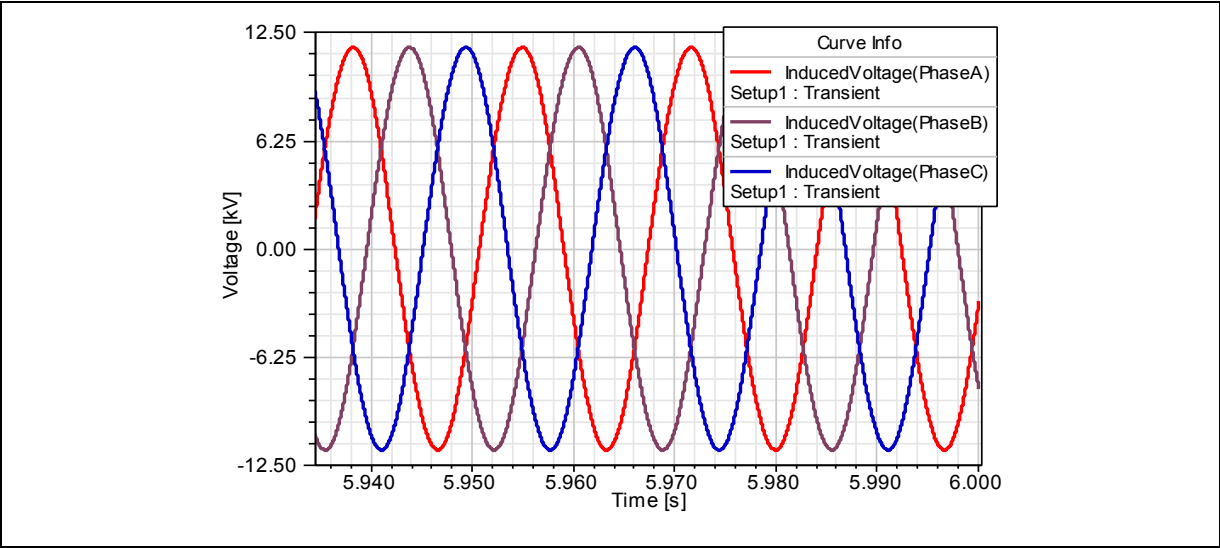


Figure 5.13 Phase voltage (voltage driven simulation)

Besides, the core loss can also be plotted as a function of the time. In figure 5.14, the rotor and stator core loss were obtained during a post-processing stage. The losses in the stator at nominal load using voltage driven simulation mode represents 72% of the total core losses.

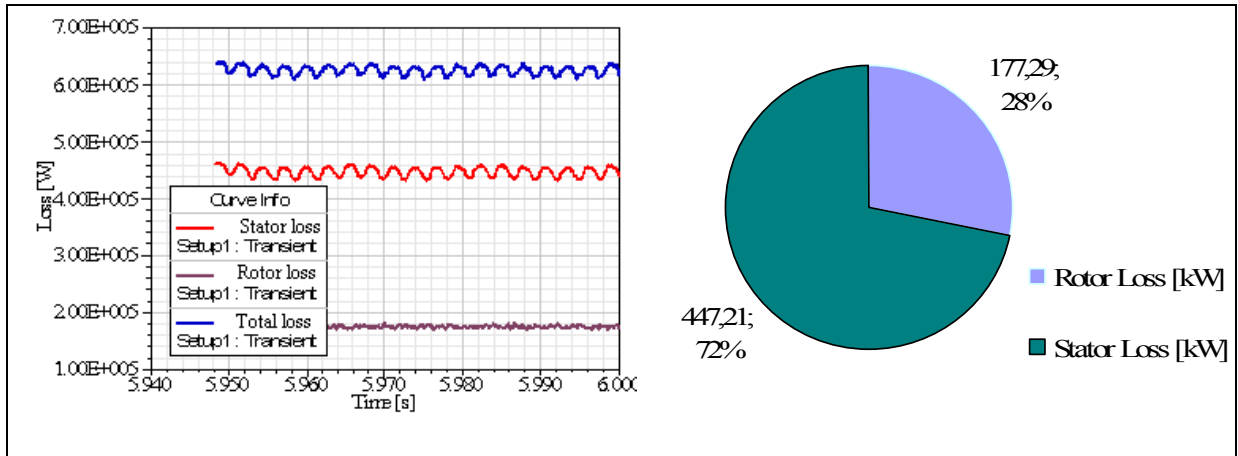


Figure 5.14 Stator, rotor and total loss as a function of time (voltage driven simulation)

### 5.2.5 Influence of the magnetic material characteristics

It is very common to have unknown magnetic material characteristics for old hydro-electric generators. The uncertainties of imposing certain magnetic material characteristics during simulation can sometimes lead to incorrect prediction of magnetic core losses. The challenging task in determining the magnetic properties of the rotor and stator material, where the manufacturer data are invaluable, is well known as reported previously by (Zarko et al., 2008).

The choice of the magnetic material can have a significant impact on the calculated magnetic losses. To study this effect, simulations were performed with three different configurations for the magnetic material in the stator and the rotor.

The simulations were performed under a load condition (122.6 MVA, 0.9 p.f.) with an excitation current of 726 A. In these three cases, the model considered only the designed value for the airgap of 15.875 mm. It can be observed in Table 5.4 that the derived total magnetic core losses at rated load varies from 441 to 594 kW depending on the chosen magnetic material in the stator and rotor respectively. The magnetic losses computed in the first and second cases present a difference of 4.3% (460 and 441 kW respectively); showing

that the change of the magnetic material in the rotor did not have a significant impact on total computed magnetic core losses. It should be pointed out that in both the cases, the magnetic core losses in the models were only computed at a frequency of 60 Hz, and the pole faces losses are known to be mainly caused by high frequency harmonics. The influence of considering the harmonic content or its absence not is highlighted in the third case. It can be observed that the derived value of magnetic core losses (where the specific losses are functions of all frequencies) is comparable and it is about the same order with the test data given previously in Table 3.4.

Table 5.4 Computed core loss with different magnetic materials

<b>Cases</b>	<b>Material</b>		<b>Core Losses at Nominal Load (kW)</b>
	<b>Stator</b>	<b>Rotor</b>	
Case 1	M15 - 60 Hz	M5114 - 60 Hz	460
Case 2	M15 - 60 Hz	Manufacturer A - 60 Hz	441
Case 3	M15 - All Hz	M5114 - 60 Hz	594

Even when the right magnetic material is used in the simulation, the deterioration of the insulation between laminations can change the magnetic characteristics of the material. This information adds to another uncertainty in the total computed losses.

Moreover, it was found that the derived total magnetic core losses at rated load conditions vary by at least 25% depending on the selected magnetic material for the stator and rotor.

### 5.3 Segregated losses

Simulations were done for two operating conditions, namely, open circuit and short-circuit. The simulation results of core losses and magnetic field from these conditions were compared with the measured data presented in the previous chapter.

The mesh chosen for open-circuit and short-circuit simulation studies consisted of more than 35000 elements. The armature winding is fractional with  $2\frac{4}{5}$  slots per pole per phase, which means that a 5-pole pitch model needs to be used for the electromagnetic transient simulation. Fig.5.15 shows the meshes used for the 2D model for the specific machine.

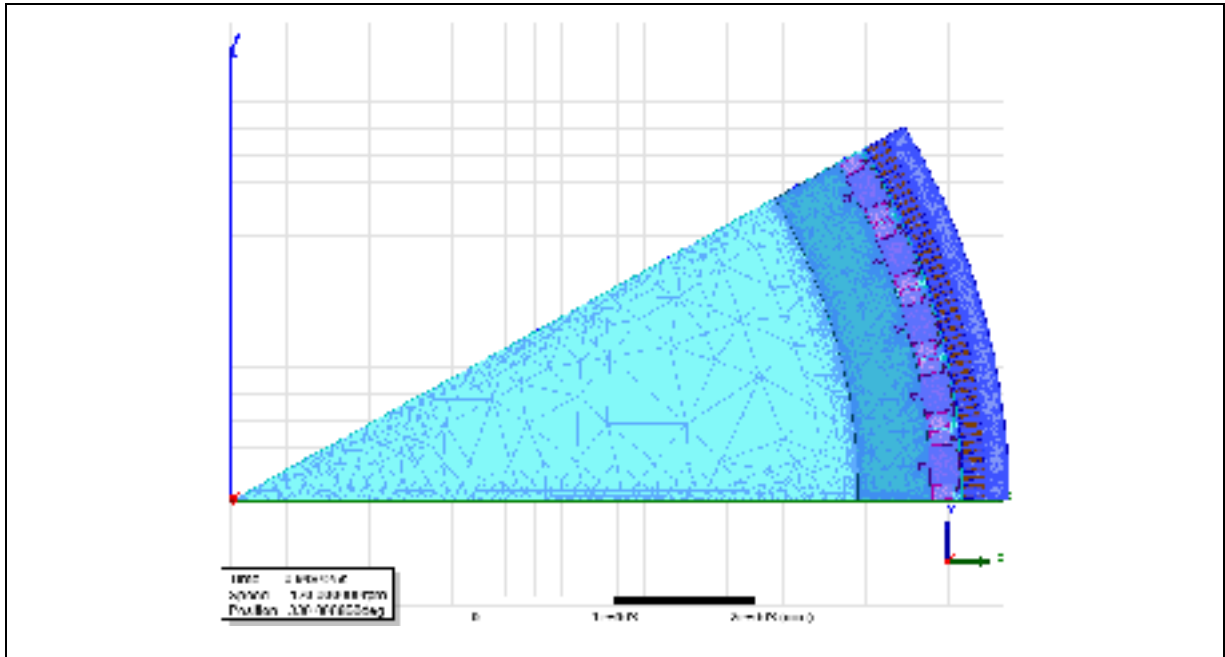


Figure 5.15 Meshing 2D of 5 poles pitch model 122.6MVA hydro-electric generator

### 5.3.1 Open circuit

The open-circuit characteristic curve and airgap line are shown in Fig. 5.16. In it, it can be observed that the open-circuit voltage characteristic corresponding to unsaturated operation represented by the airgap line; the deviation from this curve corresponding to the saturated operation of the machine is the open-circuit characteristic (OCC) curve. Six simulation studies were performed with the excitation current varying from 0 to 600 A. The open circuit characteristic (Fig. 5.16) curve shows three parts: the first part (four points) is a linear comportment of the voltage from 0 A to 300 A, and the second (two points) is from 300 A to 500 A with a small deviation from linearly varying airgap curve, and finally the third and

final one (two pints) from 500A to 600 A, showing pronounced deviation from the airgap line due to the saturation of the magnetic circuit.

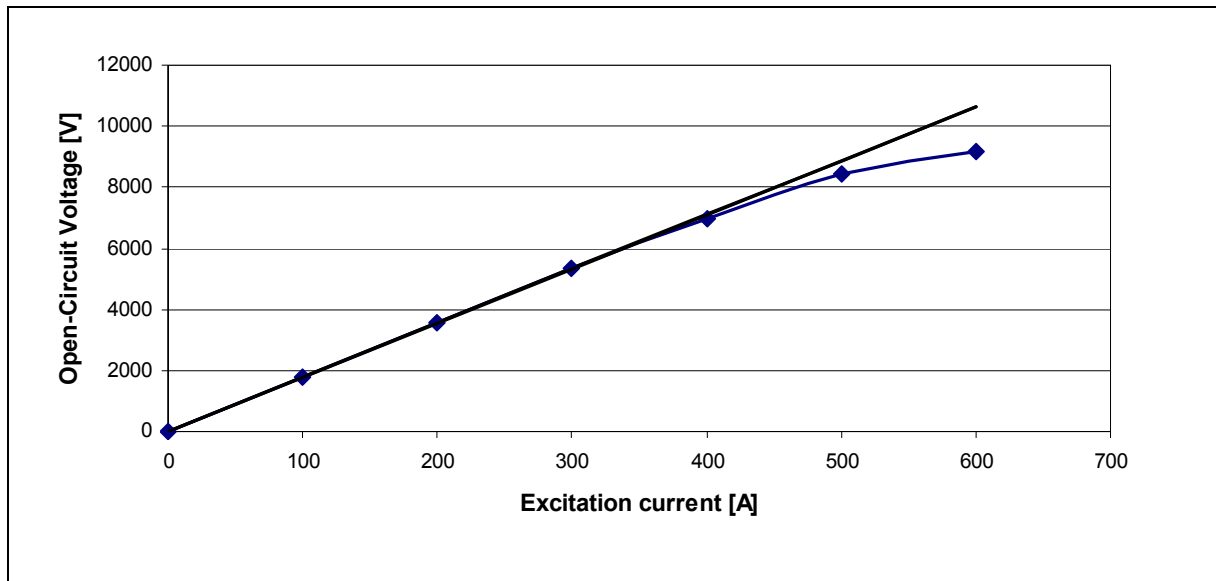


Figure 5.16 Open-circuit curve

The open-circuit core loss is a function of the flux (which is proportional to the open-circuit voltage). Figure 5.17 shows the simulated results obtained for the open circuit voltage and the respective no-load core loss on open-circuit for the same six values of excitation currents. The black point in the graphic represents the experimental test at nominal voltage.

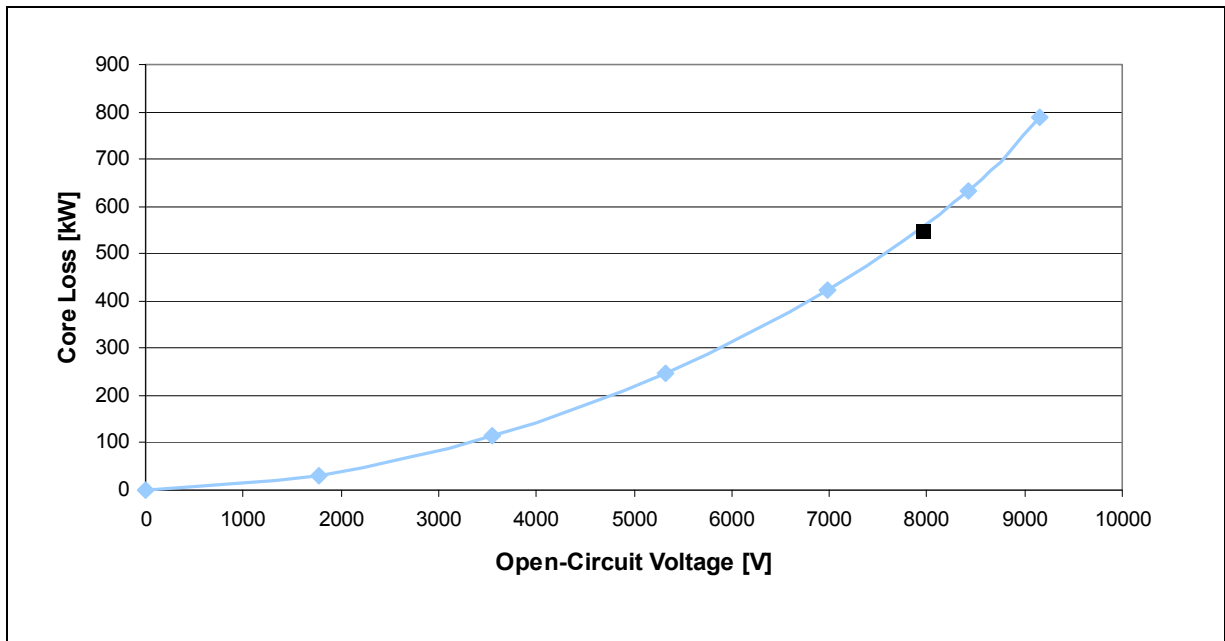


Figure 5.17 Open-circuit voltage x core loss curve

After the computation of the two last characteristics (Fig.5.16 and Fig.5.17), the simulation results for an excitation current of 467 A (the same one used during experimentation) were basically focused on three items, which will be presented in the following subsections:

- magnetic flux density, electromagnetic induction and its harmonics;
- induced damper bar currents its harmonics and losses;
- magnetic losses in the stator and in the rotor.

### 5.3.1.1 Magnetic induction and its distribution

The magnetic flux density distribution and flux lines were plotted for open-circuit operation. Figure 5.18 shows the distribution of the magnetic flux density  $B$  in the poles and in the stator of Manic 2.

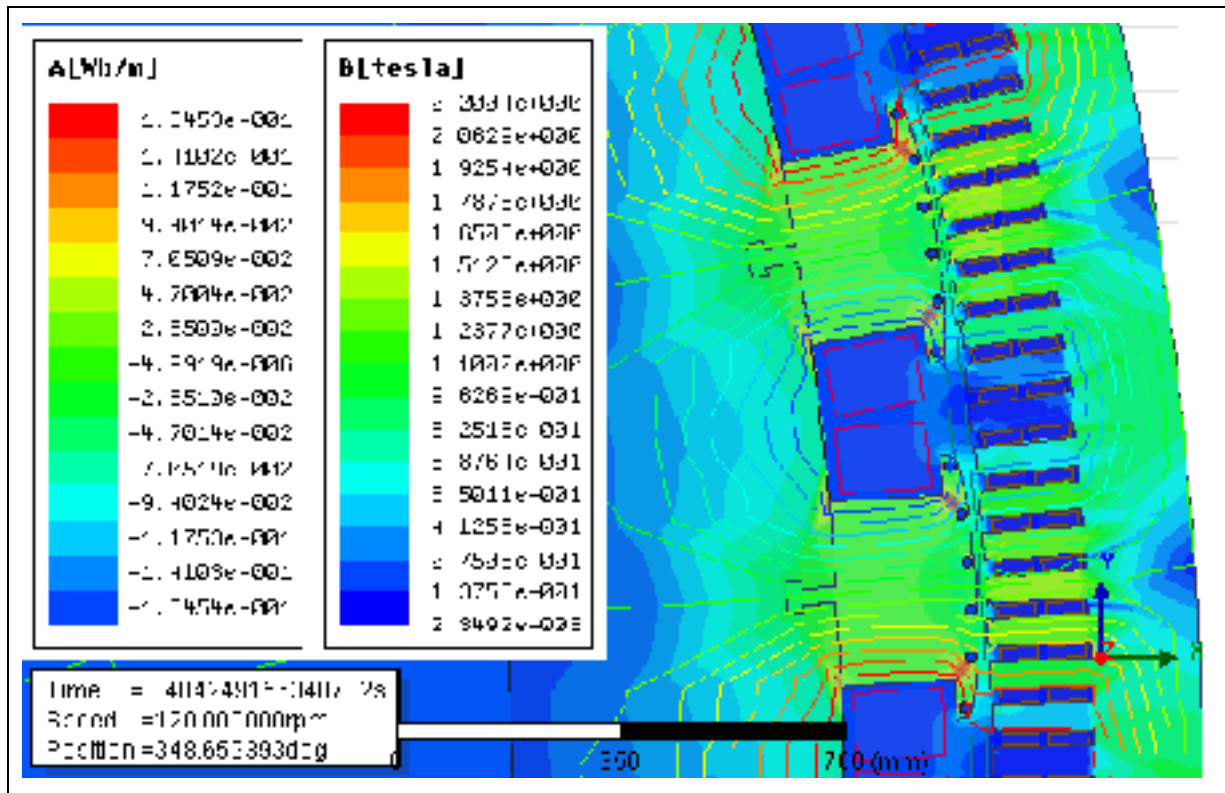


Figure 5.18 Magnetic flux density and flux lines at open-circuit

The computed radial flux density distribution in the airgap at no-load and at rated voltage is shown in Fig. 5.19, where the stator slotting effect on the magnetic-flux density pulsation in the airgap is clearly observed. Besides, the waveform was analyzed by (Fast Fourier Transform) FFT, which indicate the presence of the 5th, 7th, 9th harmonics with maximum amplitude of 0.03 Tesla. Other harmonics at multiples of 60 Hz are also observed but at much lower amplitude levels.

The computed radial flux density distribution in the rotor arc (located at the middle of the rotor) at no-load and rated voltage is also shown in Fig. 5.19. The waveform of the radial flux density in this arc resembles a rectangular shape and the maximum magnetic flux density (peak value) is in the range of 1.4 T.



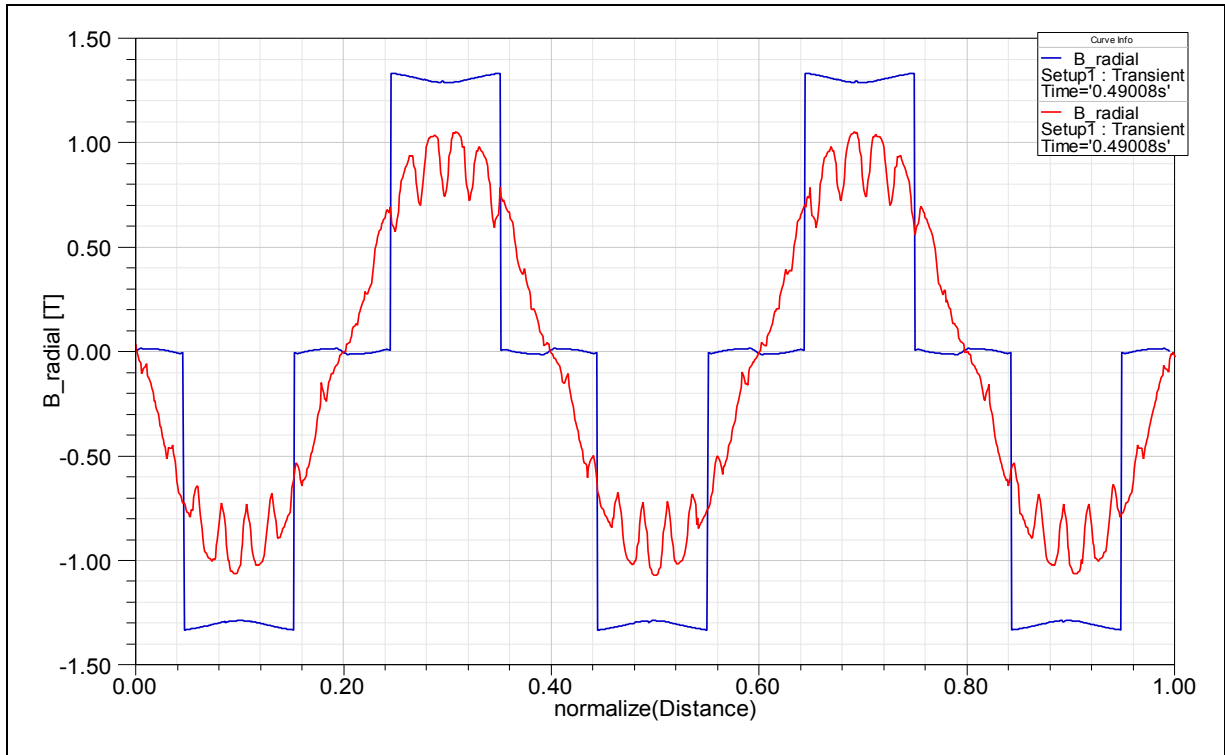


Figure 5.19 Magnetic flux induction B (airgap) - open-circuit (arc airgap (red) and arc rotor (blue)) – normalized distance

Using equation 2.3, the pulsation of the airgap flux due to the slot openings in the airgap region was calculated for Manic 21. The machine has 504 stator slots and 60 poles.

$$F = \left(2 \cdot \frac{504}{60} \pm 1\right) \cdot 60$$

$$F_1 = 948 \text{ Hz and } F_2 = 1068 \text{ Hz}$$

When the harmonics of the magnetic flux density in the airgap is calculated, the dominant slot harmonic frequencies are 16 and 18 for this specific generator. In Fig 5.20 the results of the spectral analysis of the airgap flux are presented, that show the amplitudes of all the dominant harmonics.

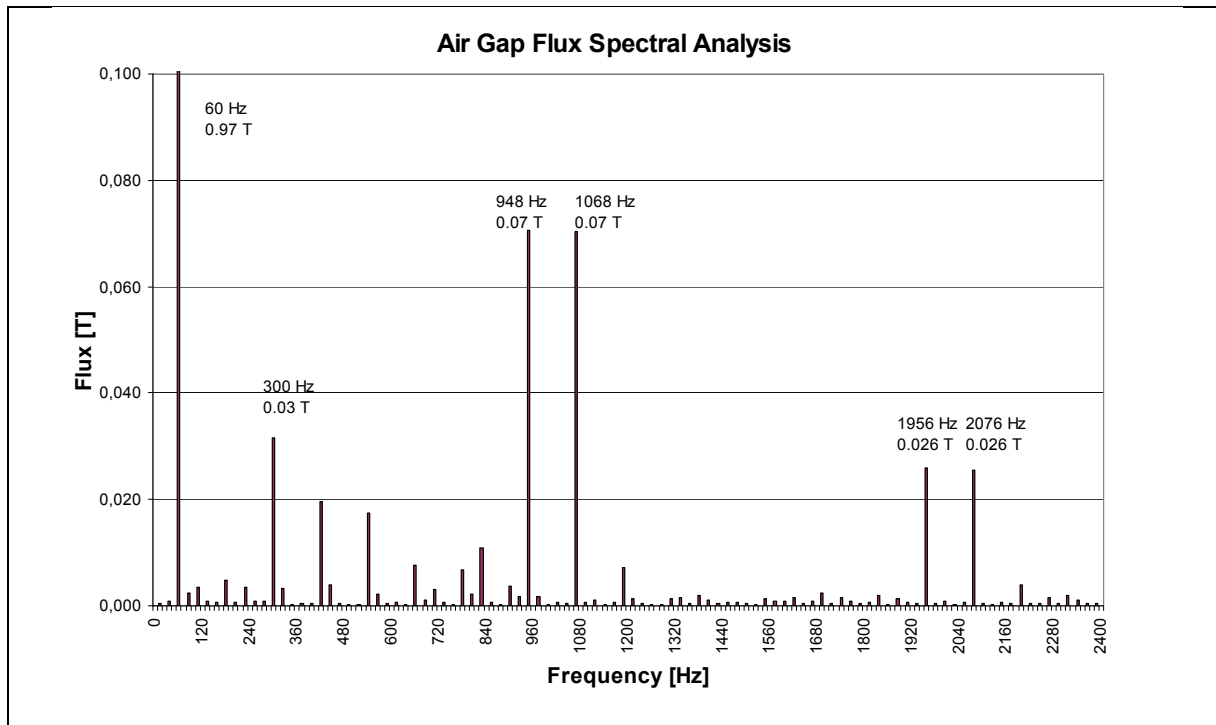


Figure 5.20 Spectral analysis – magnetic flux density B (airgap) – open-circuit

The FFT analysis of the magnetic flux density can also be done for the rotor arc and the frequency spectral from this analysis is shown in Fig. 5.21. The third and the fifth order harmonics are presented in the spatial magnetic flux density on the rotor.

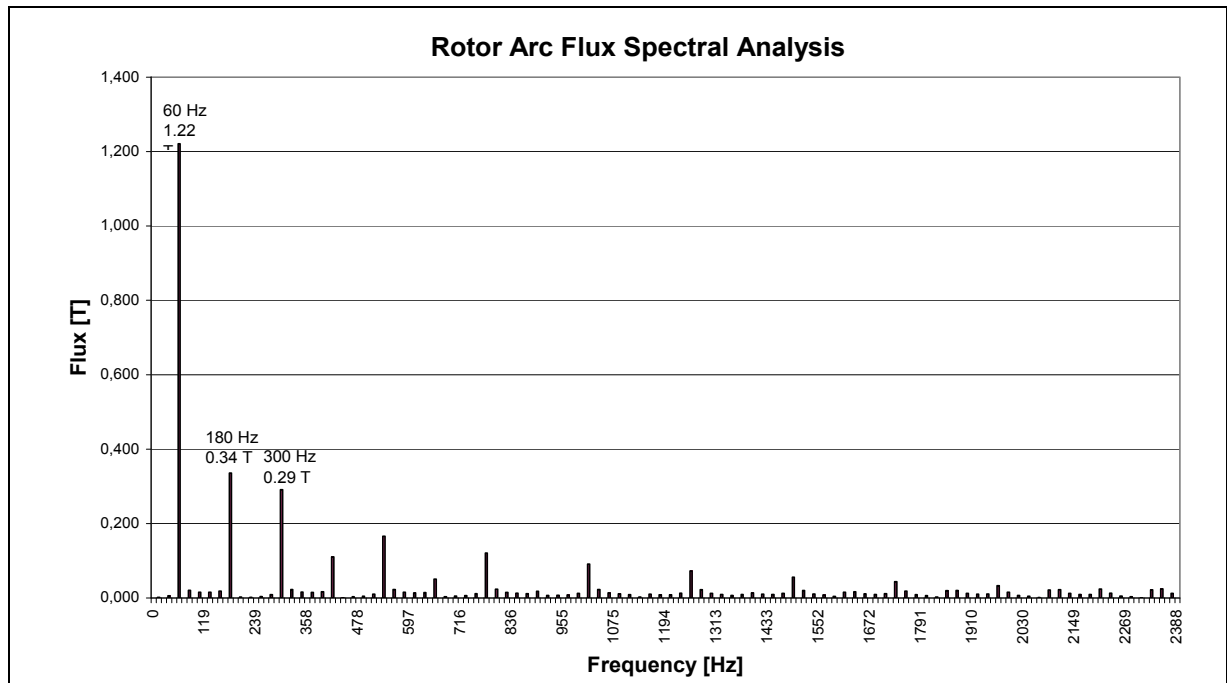


Figure 5.21 Spectral analysis - magnetic induction B (rotor)

The magnetic flux density as a function of time for a specific point can be obtained by placing a point in the model and doing the post-processing of the magnetic field for this point for all the instants of saved time. This approach was used in order to recreate the coil sensor measurement and compare the measured value of the magnetic flux for the specific position with the one obtained by simulation. Since the coil sensor is located on the stator tooth in the experiment, for the purpose of simulations the same point was chosen to place the simulated sensor. The magnetic flux on the stator tooth as obtained by simulation varies between  $\pm 0.98$  T (peak value) while and the experimentally obtained value varies between  $\pm 1.05$  T at the same position. This result is shown in Fig. 5.22. It also shows that there is a small difference between the values obtained from simulation and those from test data and that the maximum deviation is 6.88%.

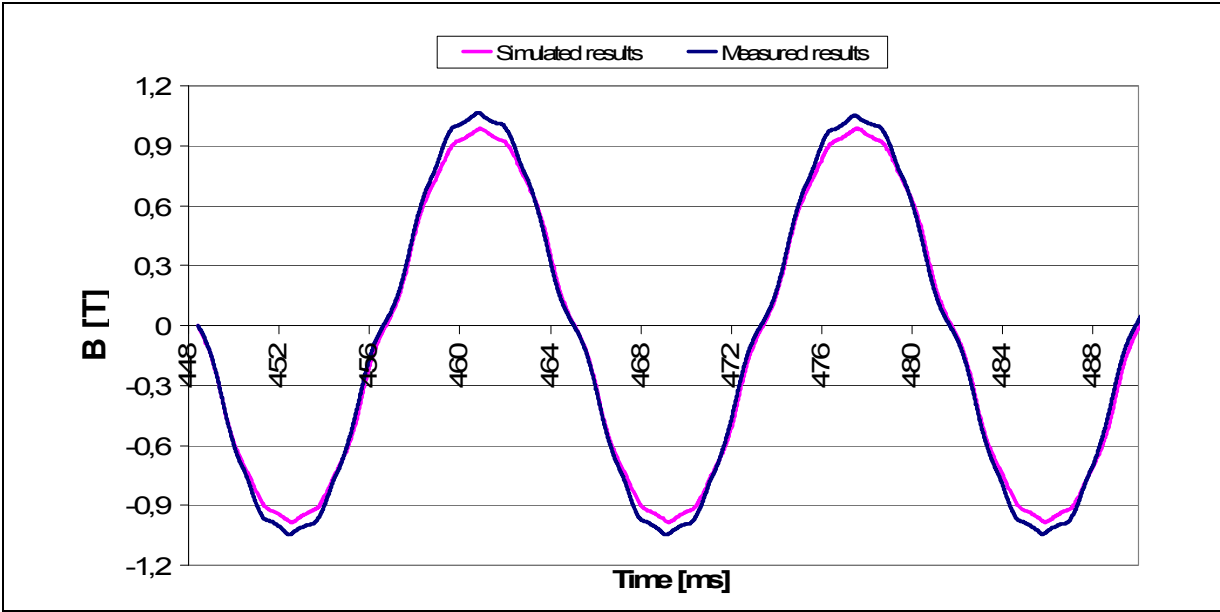


Figure 5.22 Comparison between measured and simulated flux density, at rated voltage, 13.8 kV, no-load (9H sensor)

For the magnetic flux waveform as a function of time, the FFT was performed and the window used analysis was Blackman. The FFT spectrum analysis is presented at Fig. 5.23 for open-circuit condition. In the spectral analysis, the frequency of 72 Hz presents a higher value (0.962 T).

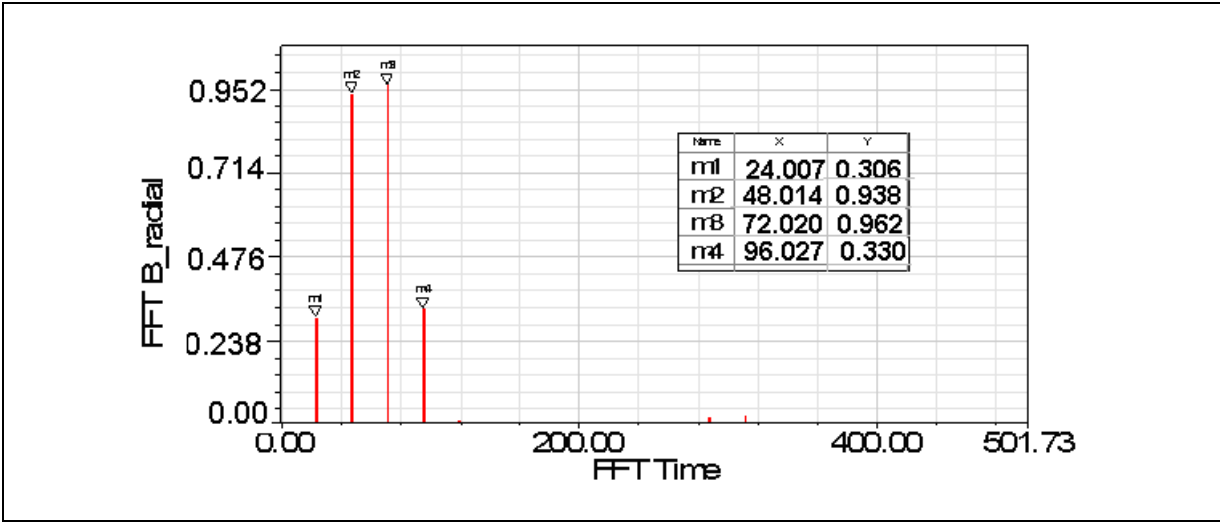


Figure 5.23 FFT magnetic induction B (airgap)

### 5.3.1.2 Damper bar currents

Fig. 5.24 shows the damper bar currents for a pole. As it can be noted, the damper bar current for open-circuit presents a sinusoidal waveform varying according to the position of the bar.

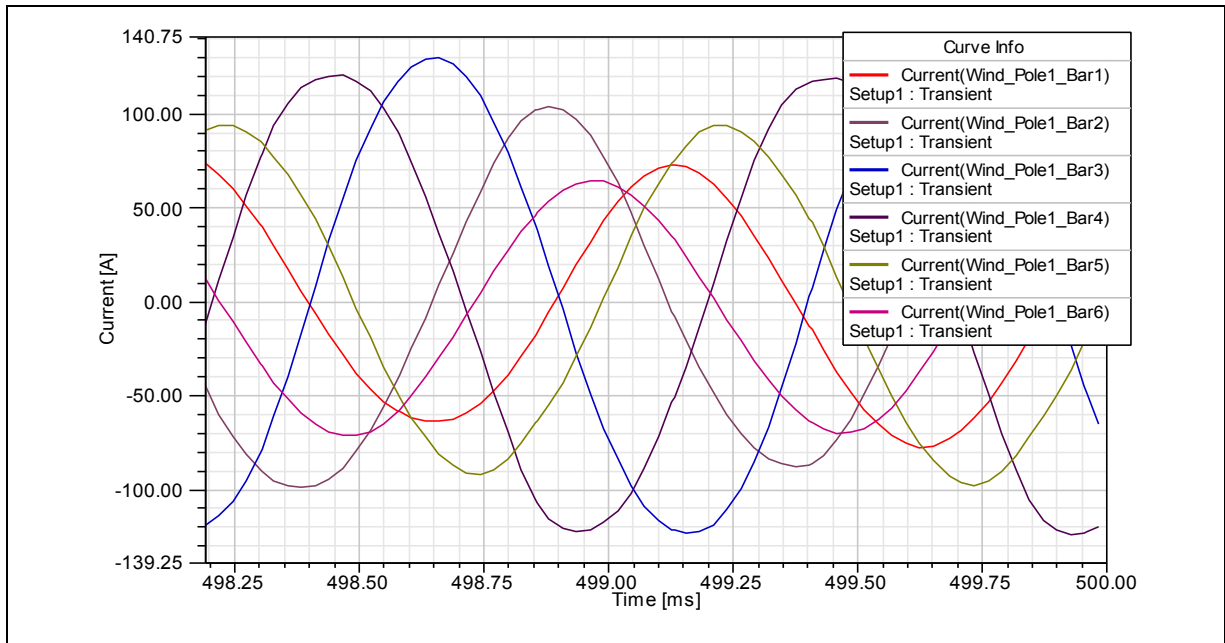


Figure 5.24 Damper bar current

Even though the damper bar currents seem perfectly sinusoidal, the FFT reveals the presence of 1008 Hz (14<sup>th</sup> harmonic of 72 Hz) for all six bars.

The current density and consequently the damper bar losses are uneven in open-circuit condition. The total instantaneous damper bar losses on open-circuit were computed for this generator. These were given as a function of time and they vary around an average of 3.91 kW. Fig. 5.25 shows these losses computed for each damper bar of pole 1, where it can be remarked that bars located in the middle of the pole (bars 3 and 4) present higher solid losses.

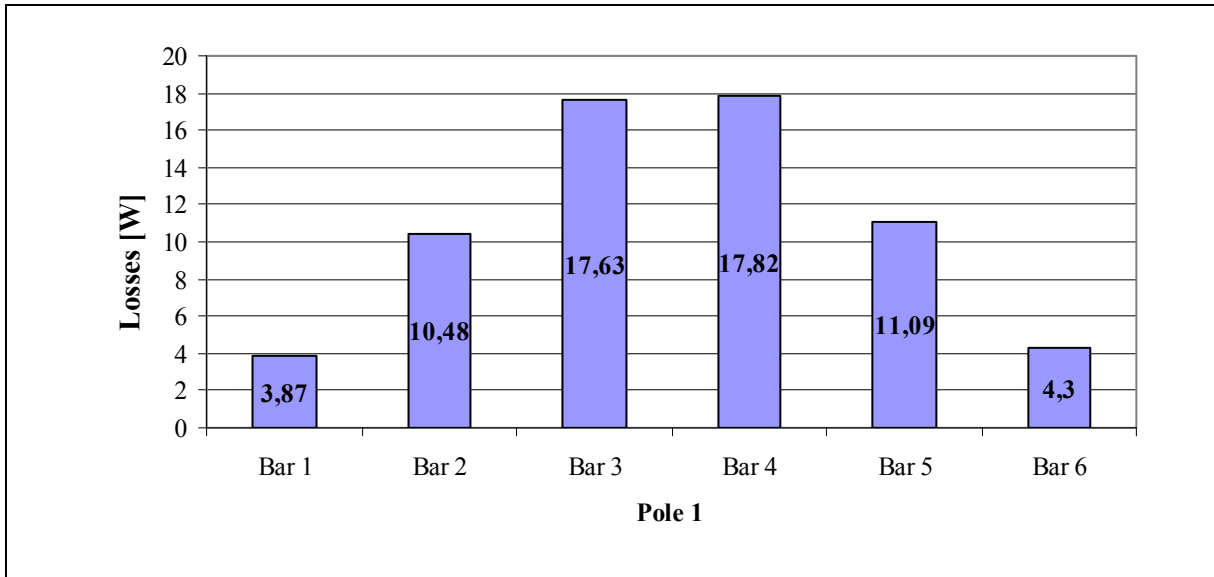


Figure 5.25 Damper bar loss for each bar in pole 1 – open-circuit operation

### 5.3.1.3 Core losses

The magnitude and spatial distribution of the magnetic losses are obtained by simulation for open-circuit. The integration of the loss densities in X, Y and Z (loss matrix) thus obtained in the various components yields a global loss that can be compared to on-site measured values during a standard segregated loss test.

Site measurement can only separate the losses per category (magnetic, Joule, stray and windage) and it does not give the spatial distribution of the magnetic core losses. Validation of localized losses is done by comparing computed local temperatures with those obtained from temperature sensors installed in corresponding locations inside the generator.

Figure 5.26 shows the flux lines distribution and core loss distribution on open-circuit. From the figure, it can be noted that the core loss is higher at the stator teeth and in pole shoes when compared with the other parts of the machine.

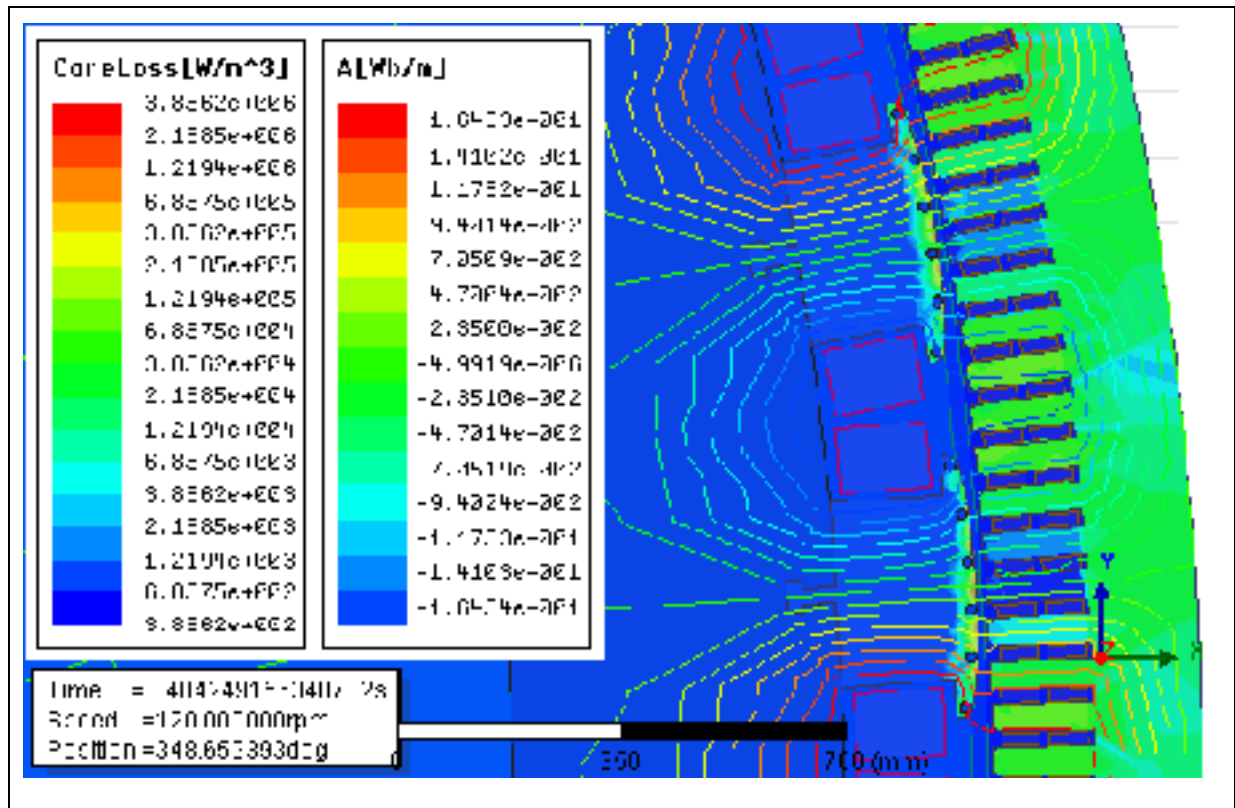


Figure 5.26 Flux lines distribution and core loss distribution at open-circuit

The total computed magnetic core losses including the stator and the rotor on open-circuit for this generator were calculated as 542 kW. A post processing of this was performed to separate the losses into the stator and in the rotor losses that resulted as 391 kW and 151 kW respectively, as shown in Fig. 5.27. It can be concluded from these results that the calculated total core losses at no-load rated voltage (542 kW) are in close agreement with the experimental test value (547.6 kW).

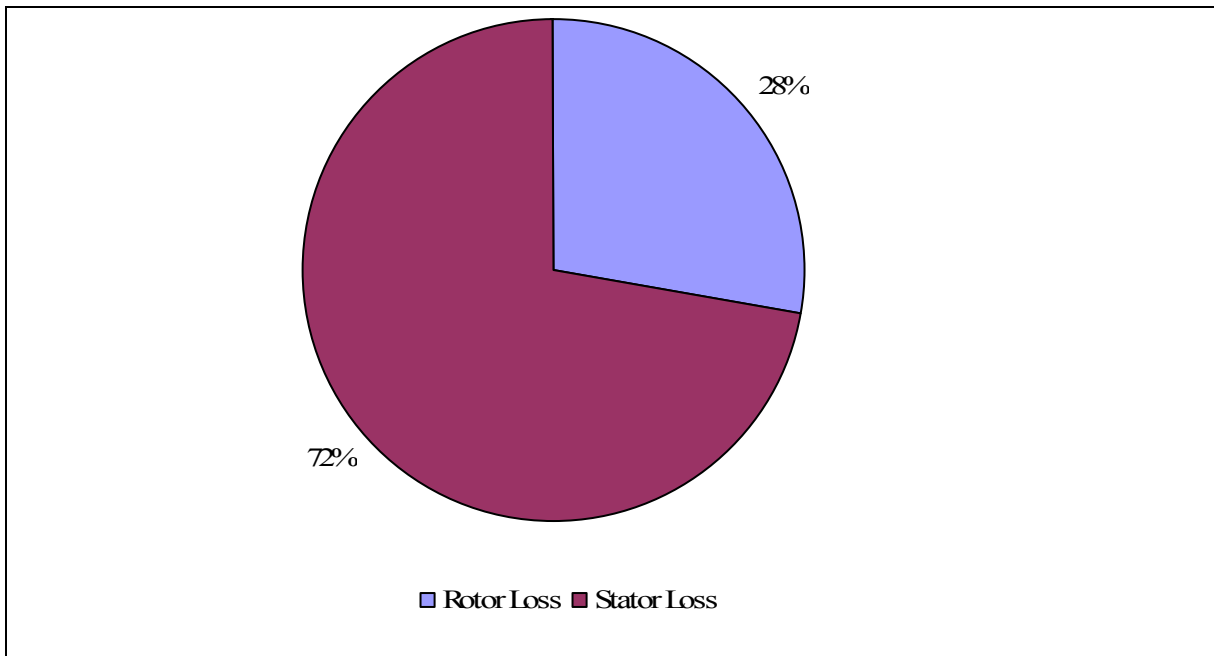


Figure 5.27 Core loss distribution between stator and rotor on open-circuit operation

### 5.3.2 Short-circuit

The machine was also simulated at short circuit and the computed values of the core loss was compared to the measured stray loss obtained during the short-circuit test. The excitation current used is 404 A, the same one as experimentation and the air gap length is 15.875 mm that corresponds to the design air gap.

The simulation results were basically focused on three items, which will be presented in the following subsections:

- magnetic flux density, electromagnetic induction and its harmonics;
- induced damper bar currents its harmonics and losses;
- magnetic losses in the stator and in the rotor.



### 5.3.2.1 Magnetic flux induction and its distribution

The magnetic flux density distribution for short-circuited operating condition was plotted for a specific time step and it is shown in Fig. 5.28. In short-circuited operation, the magnetic field is distorted due to distribution of the windings in the slots and also due to the short-circuit current. The magnetic flux density is lower when compared to the open-circuit simulation. Besides, simulation study shows that there is a different shape for the magnetic flux lines when compared with the open-circuit operation, especially in the back of the stator teeth where some loops are observed.

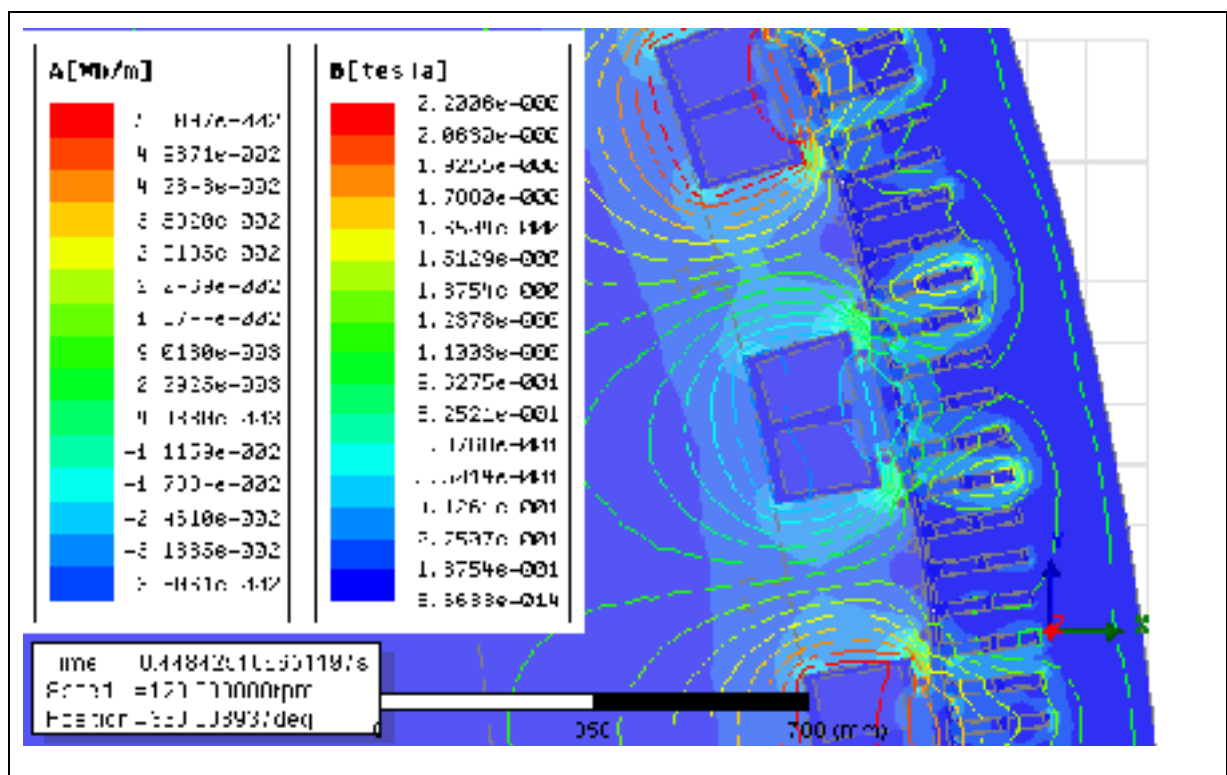


Figure 5.28 Magnetic flux density and flux lines at short-circuit

The computed radial flux density distributions at short-circuit as a function of normalized distance for the airgap (purple curve) and for the rotor arc (red curve) are shown in Fig. 5.29. The magnetic flux density on the rotor arc (middle of the rotor) presents a square waveform

while it has a waveform with a lot of harmonic components in the airgap, more precisely in the middle of the airgap. Further; the flux density is even more disturbed when compared to the magnetic flux density in the airgap on open-circuit.

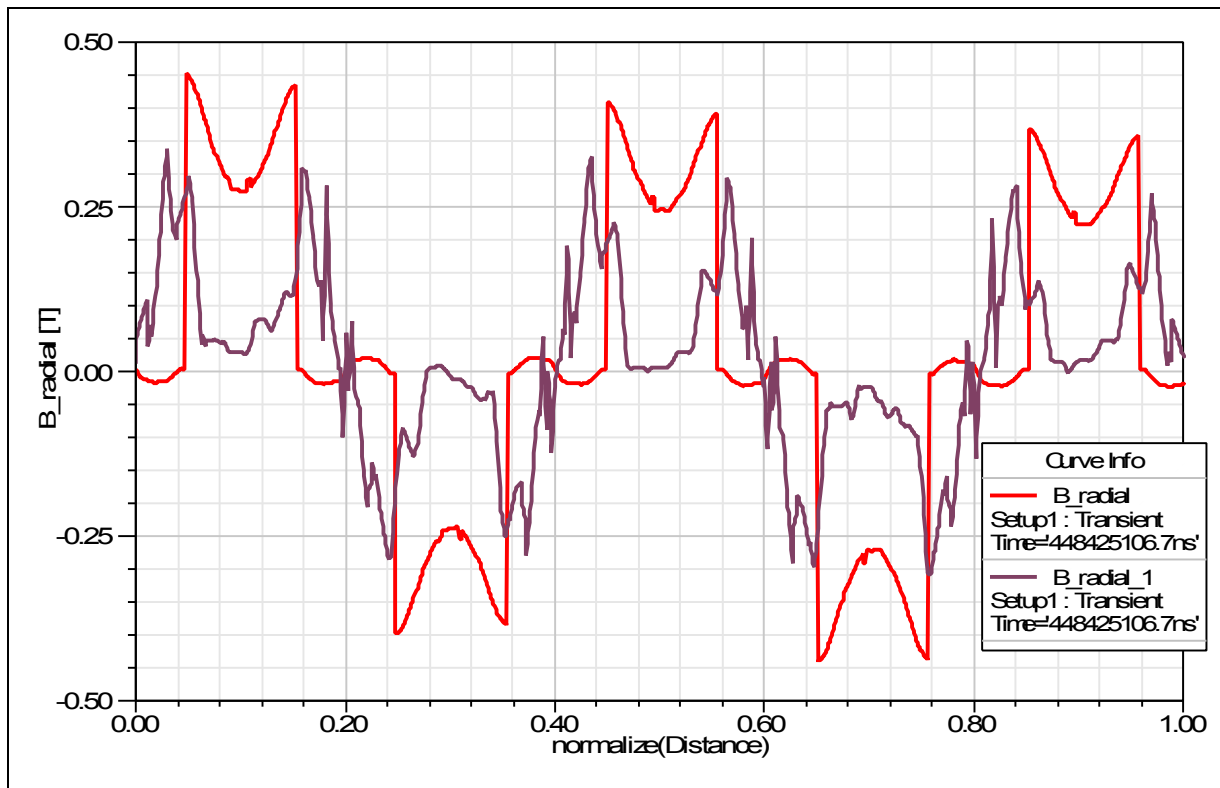


Figure 5.29 Magnetic flux induction B as a function of a normalized distance

The computed radial flux density distribution at short-circuited operation as a function of time for a point placed in the stator teeth (airgap) is shown in Fig. 5.30, where, it can be seen that the peak value of the magnetic flux density is 0.25 T.

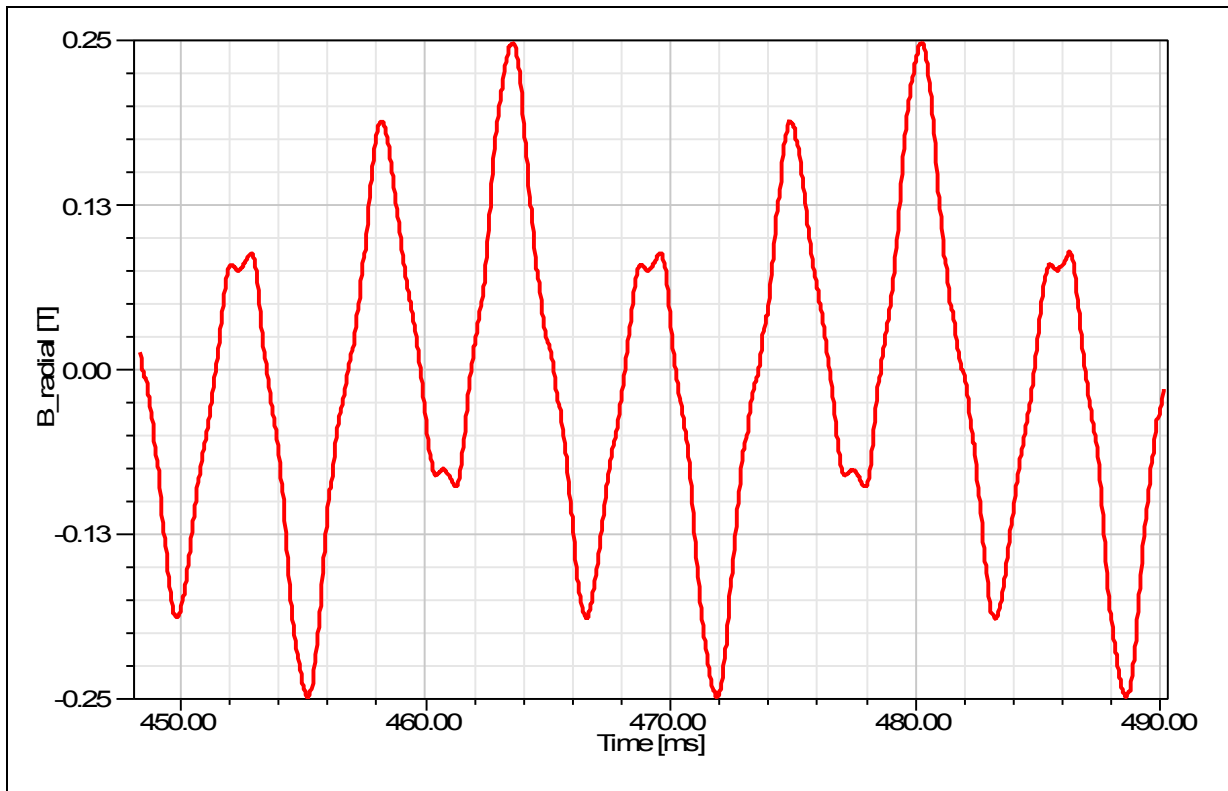


Figure 5.30 Magnetic induction B (airgap) as a function of the time

Moreover, the FFT analysis of the waveform of the magnetic flux density in the airgap for short-circuit operation was performed. This analysis showed the presence of the frequencies 180 Hz, 300 Hz and 420 Hz. It is always important to understand the behaviour of the magnetic flux density in the airgap because the magnetic force and consequently vibration is directly related to the magnetic flux density.

### 5.3.2.2 Damper bar currents

Another important parameter to analyze during a short-circuit simulation is the damper bar losses. Comparing the results obtained on open-circuit (4.2 kW) and those from short-circuit (28 kW) operation, it is clearly seen that the damper bar currents are higher in the second case.

The FFT spectrum analysis was done for the damper bar currents and the presence of multiples of 72 Hz harmonics were found. The amplitudes of the damper bar currents for 72, 144, 216, 288 and 360 Hz are presented in Fig. 5.31 respectively as 202 A, 78 A, 47 A, 64 A and 150 A.

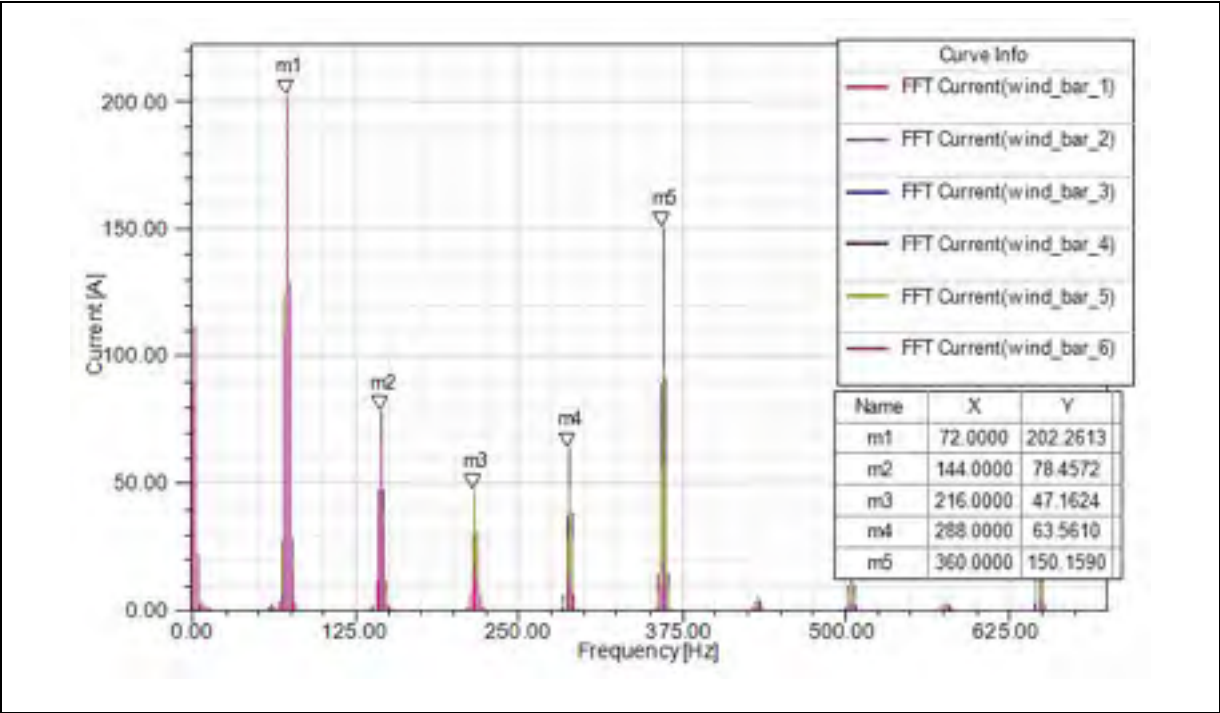


Figure 5.31 FFT analysis of damper bar currents

5.3.2.3 Core losses

For short-circuit simulation, the core loss distribution and the flux lines were plotted for the rotor and the stator of Manic 2 and the results are presented in Fig. 5.32. It can be seen that the core loss is higher at the pole face and also at the stator teeth.

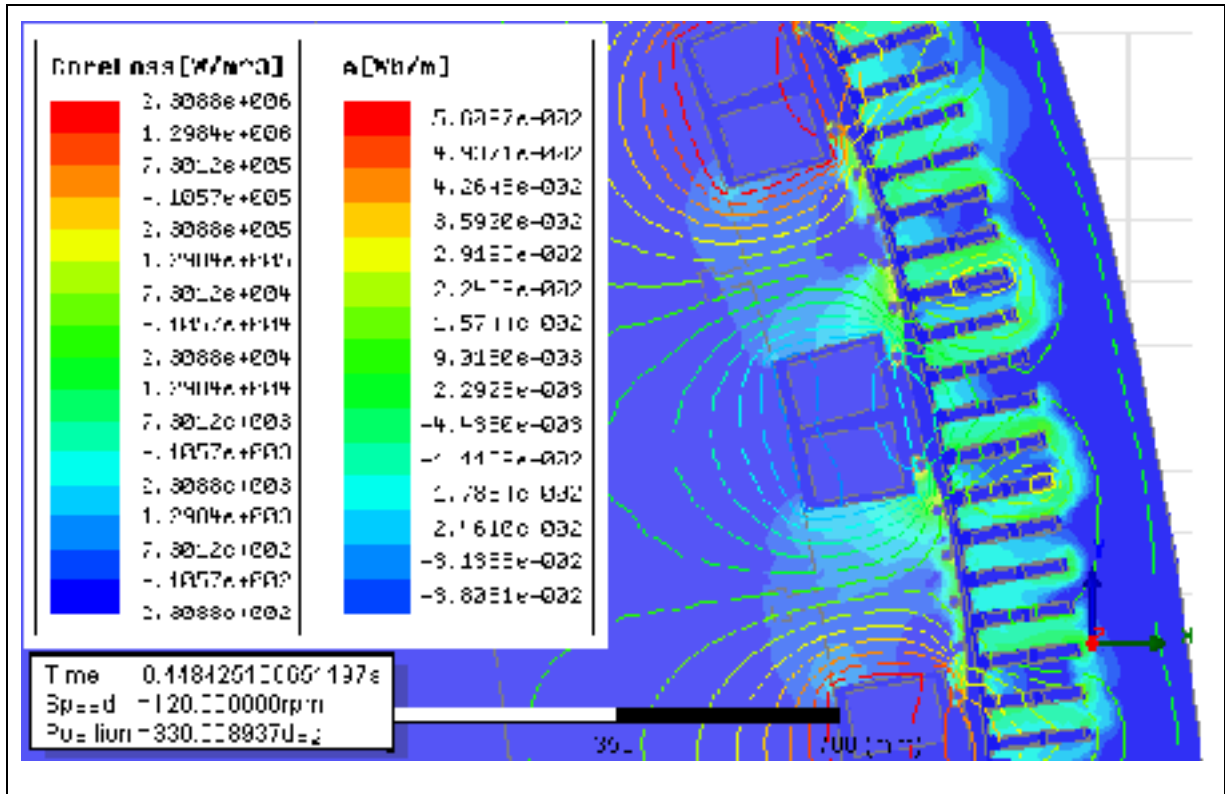


Figure 5.32 Magnetic core loss and flux lines distribution

The total computed stray losses for the machine under study are around 172 kW which include the damper bar losses (28 kW), pole face losses (48 kW), stator eddy current losses (30 kW) and copper stray losses (66 kW), as seen in Table 5.5. It has to be noted that computed stray losses are 21 % lower compared with the measured value (216.3 kW).

Table 5.5 Summarized simulated results

Conditions	Specifications	Core Loss (kW)	Damper Bar Loss (kW)	Copper Stray Losses (kW)
Short-Circuit	If=404 A	78	28	66

The difference in the core loss computation between the simulation and the experimentation can be justified. First, the conditions for the experimental tests and for the simulation were different as detailed below:

- the stator magnetic material is different;
- the thickness of the lamination of the stator material is different;
- the insulation is different;
- the stator stacking factor is also different.

For short-circuit, the stray losses are mostly eddy current losses and the aforementioned items are directly related to this type of loss. Besides, it is a 2D simulation where the end losses are not computed.

Therefore, the 2D model used for the simulation the induced losses in the end connections of the generator are not computed. The losses at end connections are more pronounced at short circuit test and this effect can be only included in a 3D finite element model. Besides, the model depth used for simulations is only an equivalent one and is calculated for both stator and rotor. This equivalent length is smaller than the real stator winding length.

#### **5.4 Core loss computation at different load operating conditions**

Transient electromagnetic simulations were performed for this machine under the following operating conditions: 71%, 100% and 120% of nominal load. These values were chosen because some experimental measurements were done specifically at those load levels. The measured excitation currents were used for each operating condition as inputs to the current driven mode simulation study. Table 5.6 summarizes the results obtained from experimental tests.

Table 5.6 Experimental values of phase current and power factor

<b>Description</b>	<b>If (A)</b>	<b>Stator Voltage (kV)</b>	<b>Stator Current (kA)</b>	<b>Apparent Power (MVA)</b>	<b>Active Power (MW)</b>	<b>PF</b>
71%	628	8,074	3,561	86,25	76,67	0,8889
100%	739	8,102	5,0638	123,08	110,23	0,8956
120%	821	8,358	5,845	146,55	132,72	0,9056

The simulation results were basically focused on three items, which will be presented in the following subsections:

- magnetic flux density, electromagnetic induction and its harmonics;
- induced damper bar currents, their harmonics and losses;
- magnetic losses in the stator and in the rotor.

#### **5.4.1 Magnetic flux density and its distribution**

The flux lines and the magnetic flux density distribution were obtained at an instant of time for the load levels at 71%, 100% and 120% of the nominal value and the results are presented in the figures 5.33 to 5.35. From, the figures, it can be seen that the magnetic flux density is more pronounced in the pole shoes and also in the stator teeth. The scales of the magnetic flux density were set from 0.03 T to 2.5 T for the three cases; in this way, the comparison between the two cases is possible; further, the increase of the load is observed by changing of the magnetic flux density distribution under different load configurations.

Unlike open-circuit simulation, an asymmetry in the distribution of the magnetic flux lines is observed when comparing the leading edge to the trailing edge.

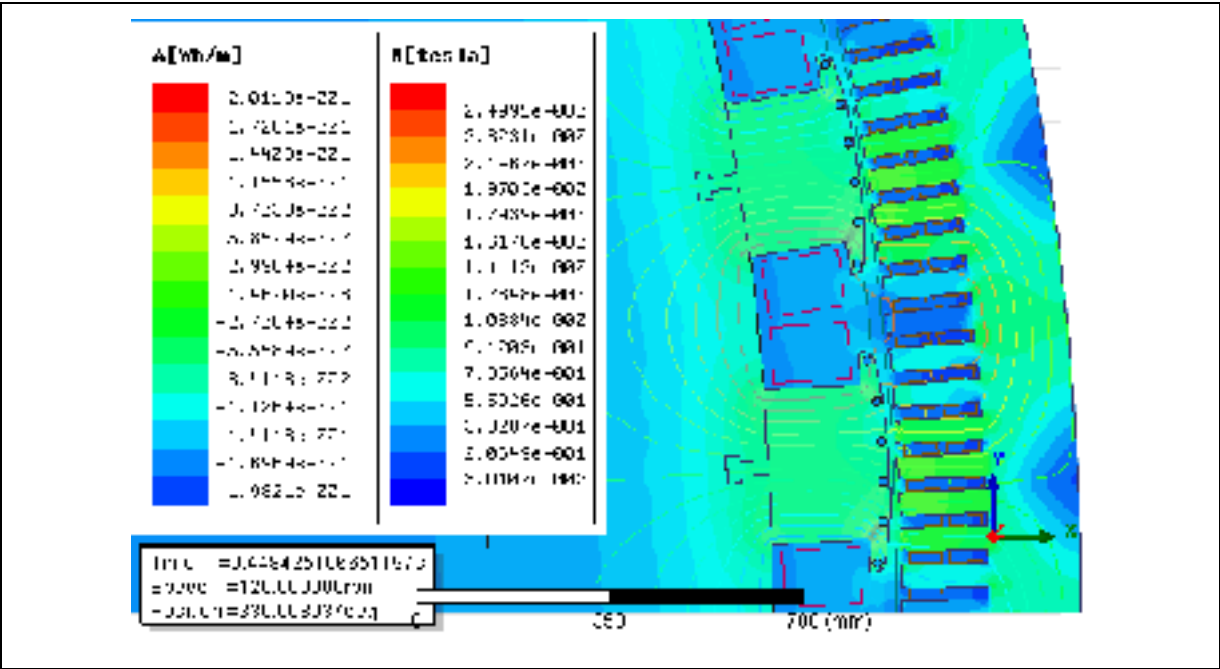


Figure 5.33 Flux lines and magnetic flux density distribution for 71% of nominal load

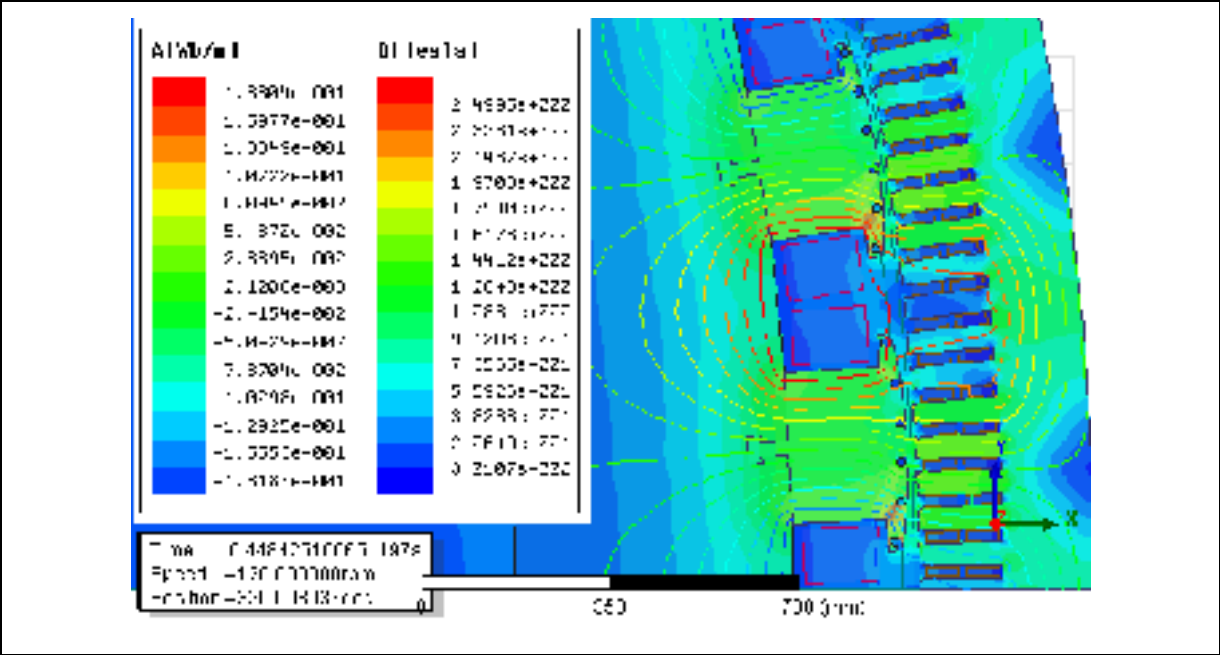


Figure 5.34 Flux lines and magnetic flux density distribution for 100% of nominal load



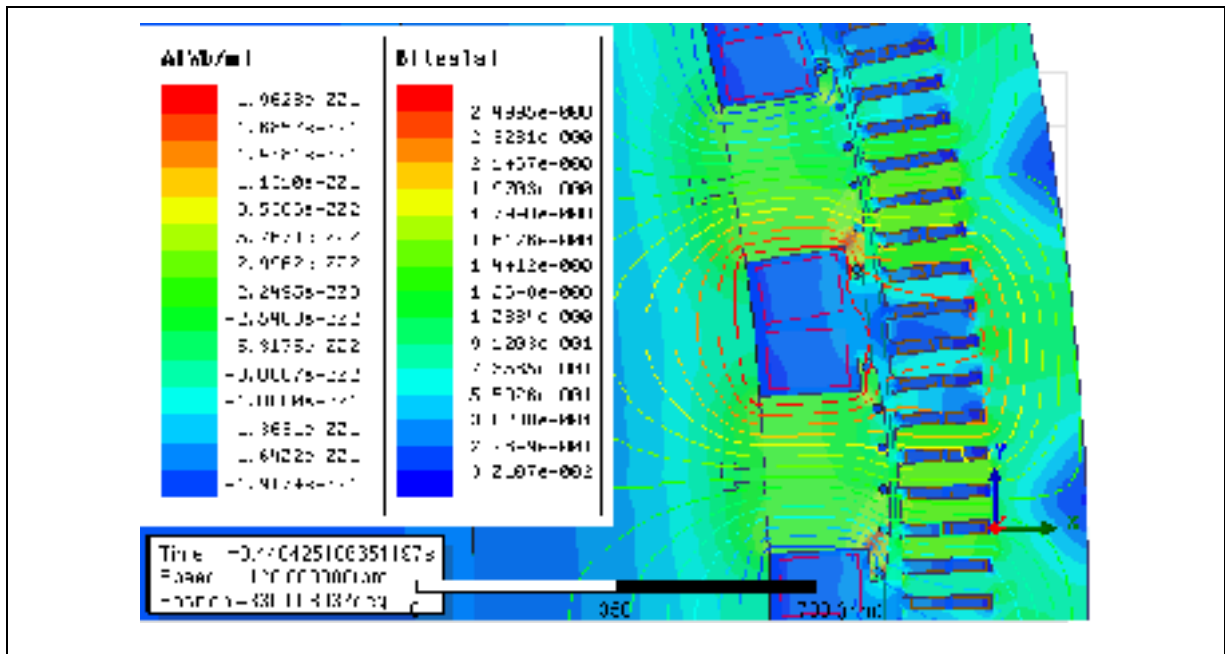


Figure 5.35 Flux lines and magnetic flux density distribution for 120% of nominal load

Besides, the magnetic flux density was analyzed for two arcs, the first one placed in the middle of the airgap and the second one placed in the middle of the salient pole. Both magnetic flux densities were plotted as a function of normalized distance (0-1) for the load conditions of 71%, 100% and 120% of the nominal value and the results are presented in Fig. 5.36 to 5.38. It is observed that the magnetic flux density is higher in the pole shoe arc than at the airgap arc; it presents a rectangular wave shape; moreover, the magnetic flux density in the airgap arc contains a sinusoidal waveform superposed with many harmonics related to the slot pulsating frequency.

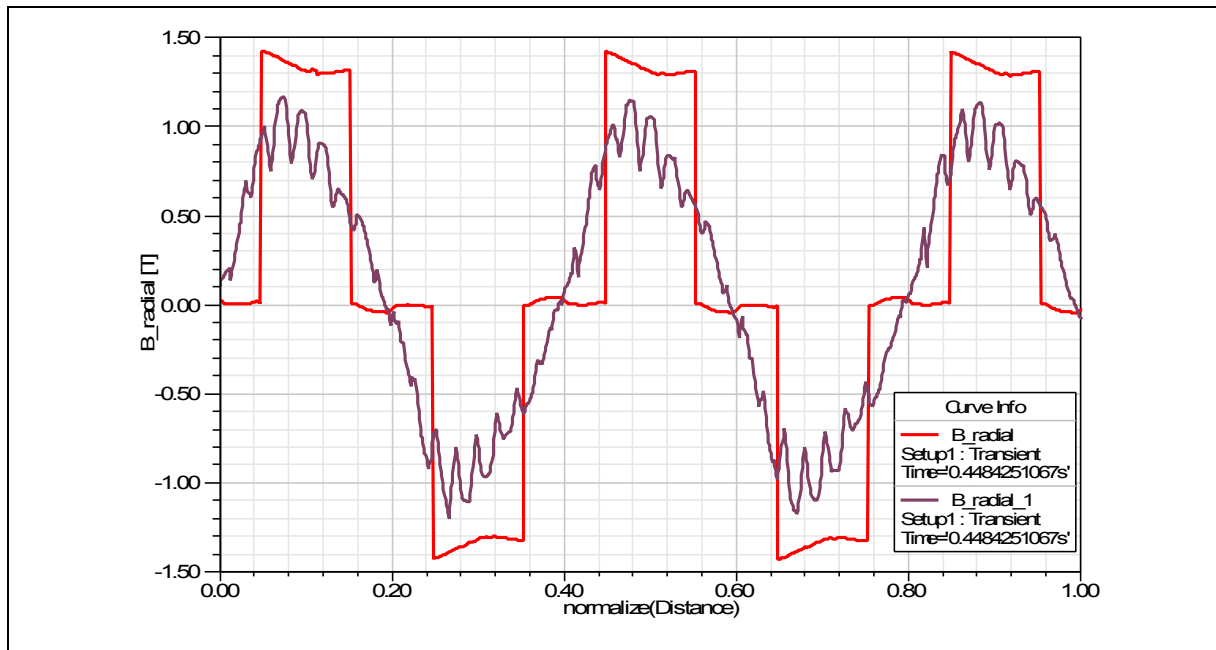


Figure 5.36 Magnetic flux density in the airgap and in the pole face as a function of the normalized distance for 71% of nominal load

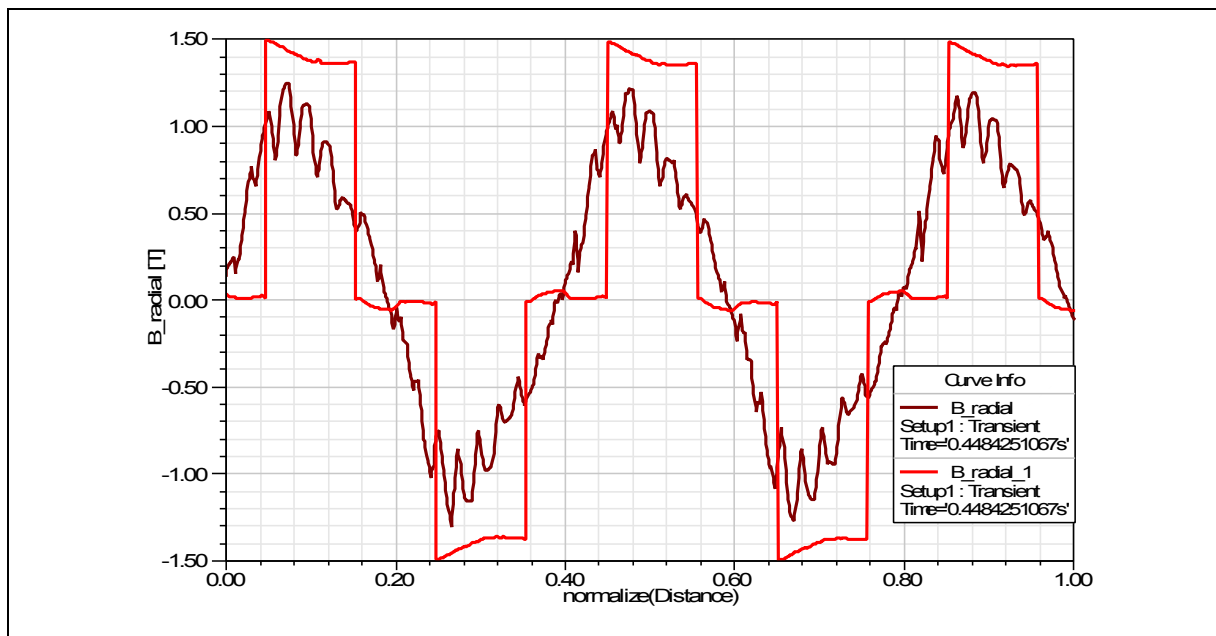


Figure 5.37 Magnetic flux density in the airgap and in the pole face as a function of the normalized distance for 100% of nominal load

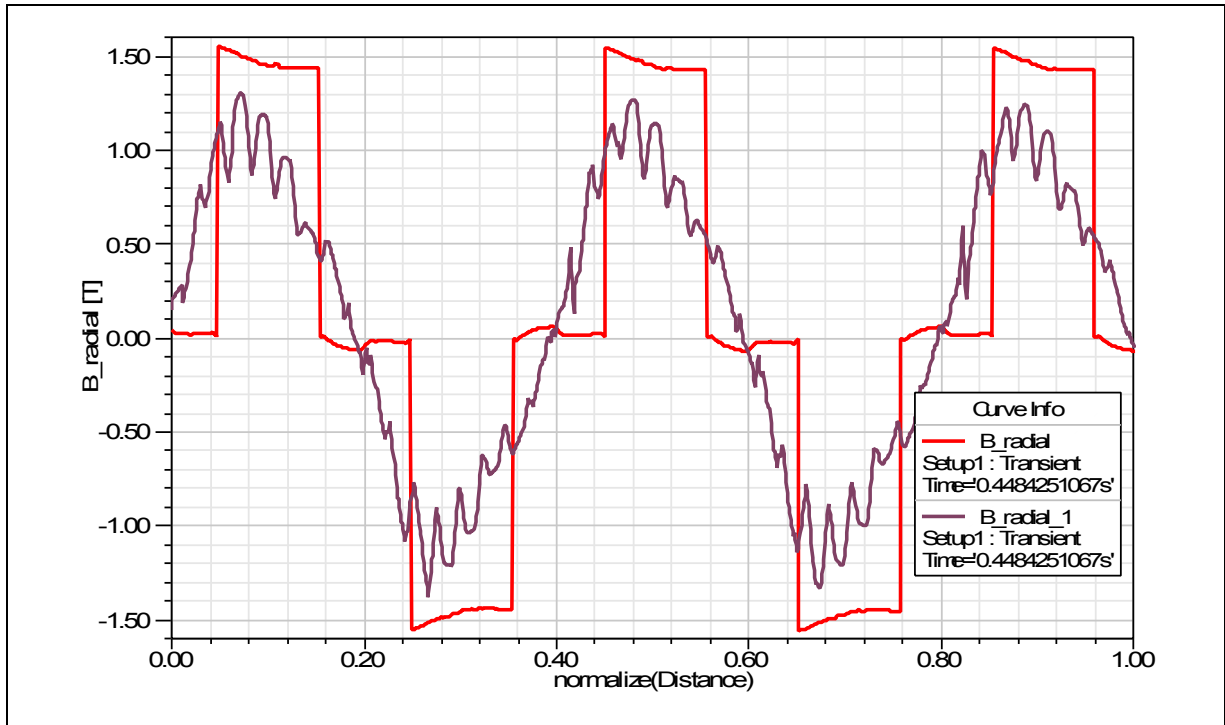


Figure 5.38 Magnetic flux density in the airgap and in the pole face as a function of the normalized distance for 120% of nominal load

The comparison between the simulated and measured magnetic flux density for a specific point of the stator tooth is shown at Fig. 5.39 to 5.41 for the operation conditions of 71%, 100% and 120% of the nominal load. It is observed that the simulation and the experimental magnetic flux density for a single point as a function of the time are in agreement regarding the shape and the amplitude of the signal. The maximum deviation between simulated and measured results was 2.41%, 2.53% and 7.80% respectively for 71%, 100% and 120% of the nominal load.

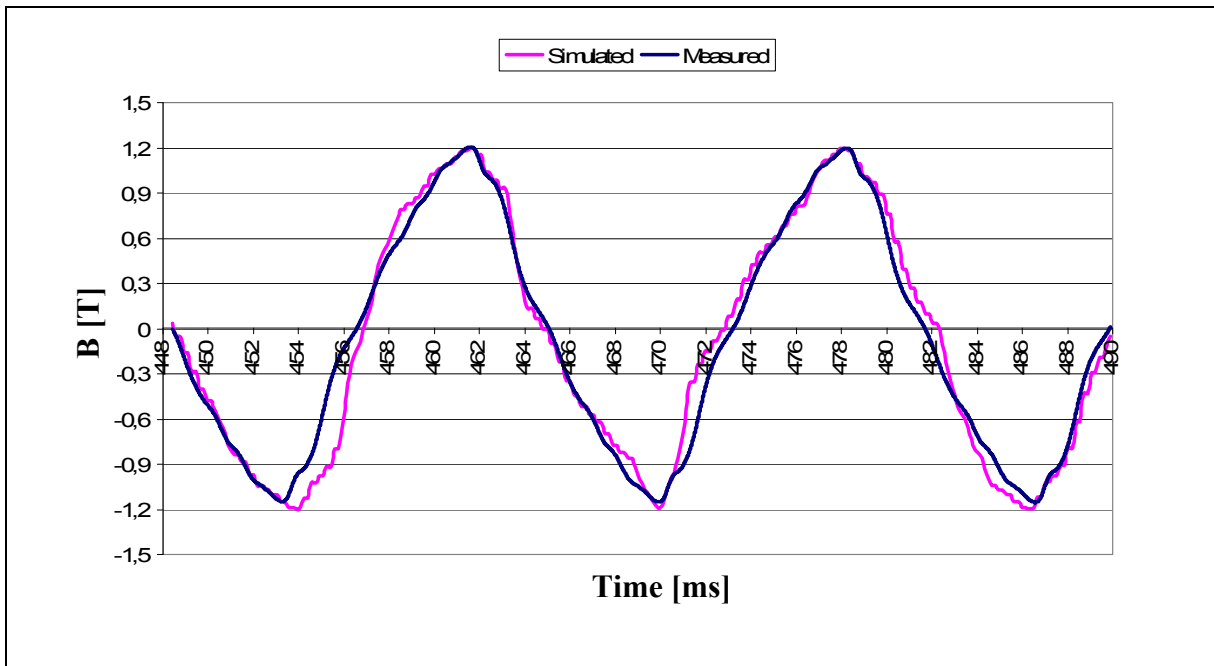


Figure 5.39 Simulated and measured magnetic flux density in the airgap as a function of the time for 71% of nominal load

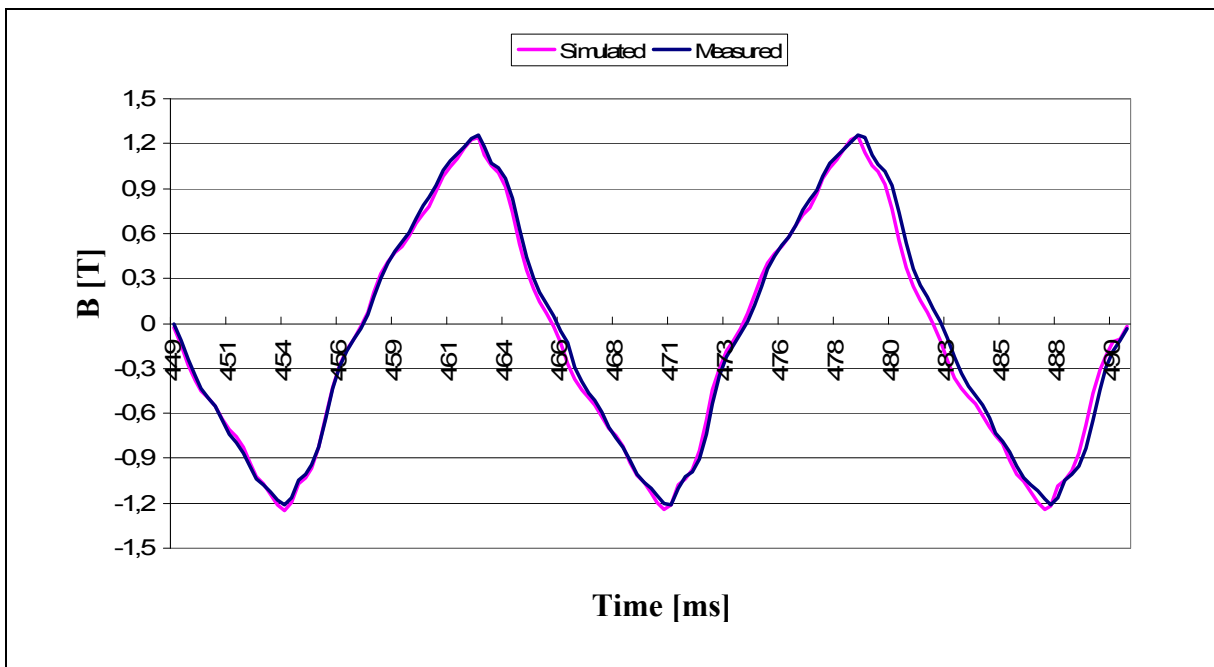


Figure 5.40 Simulated and measured magnetic flux density in the airgap as a function of the time for 100% of nominal load

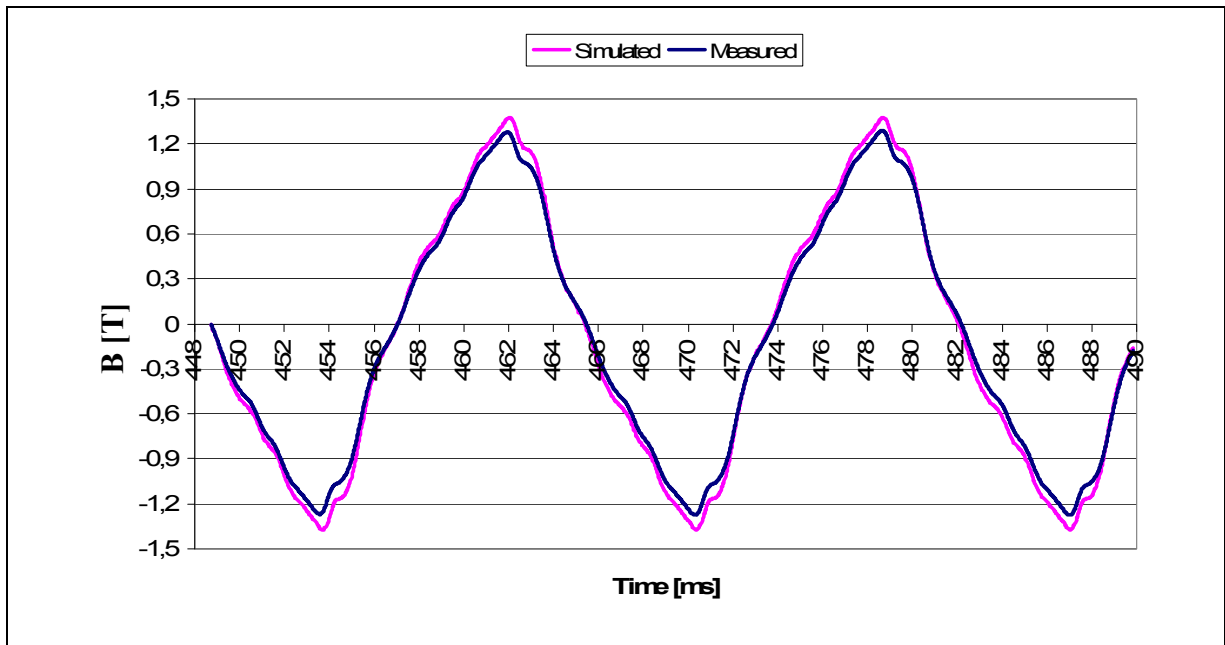


Figure 5.41 Simulated and measured magnetic flux density in the airgap as a function of the time for 120% of nominal load

#### 5.4.2 Damper bar currents and its losses

When the machine is operating on load, the configuration of the damper bar current wave changes; as a result, many harmonics can be found in the waveform when compared to open-circuit condition. The bars 1 (leading) and 6 (trailing) contain the higher currents. For higher loads higher damper bar currents can be seen.

The losses in the damper bars are resulting from the induced currents at fundamental and higher harmonic tooth ripple frequencies. FFT spectral analysis for the damper bar currents in the case of the 6 bars of the pole is done: one for each operating condition in order to detect the ripples present in the damper bar current waveform as well as to detect the presence of multiple frequencies of 72 Hz. The simulation time used for this simulation permitted the presence of a frequency up to 2016 Hz.

From Fig. 5.42 to 5.44, the results of this spectral analysis of the damper bar currents are presented for 71%, 100% and 120% of nominal load respectively. For 71% of nominal load, the bars 1, 2, 5 and 6 present the principal harmonic component of 72 Hz, and for bars 3 and 4, the principal harmonic frequency is 360 Hz.

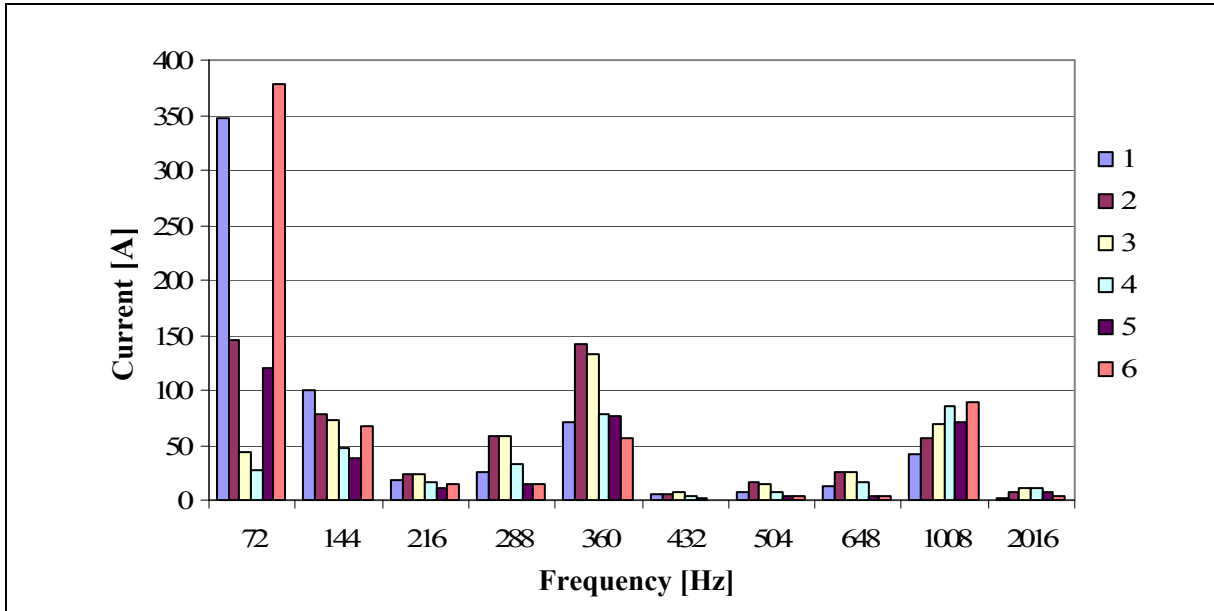


Figure 5.42 FFT of the damper bar currents for 71% of nominal load

For nominal load and 120% of nominal load, the bars 1, 5 and 6 present the principal harmonic component of 72 Hz, and for bars 2, 3 and 4, the principal harmonic frequency is 360 Hz, as seen in Fig. 5.43 and 5.44 respectively.

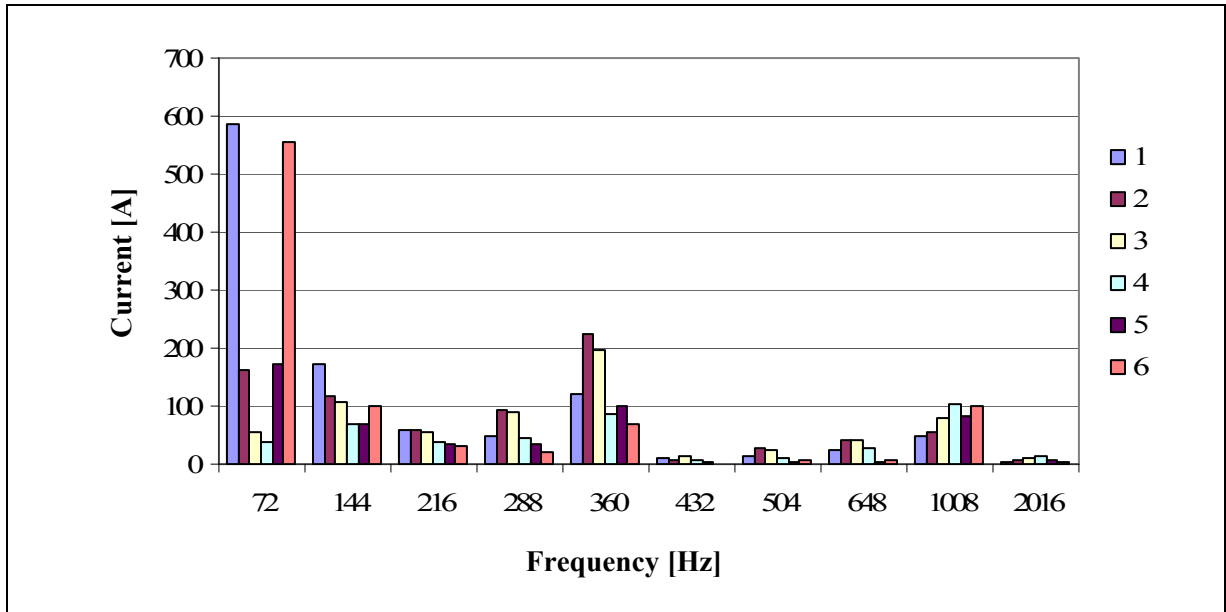


Figure 5.43 FFT of the damper bar currents for nominal load

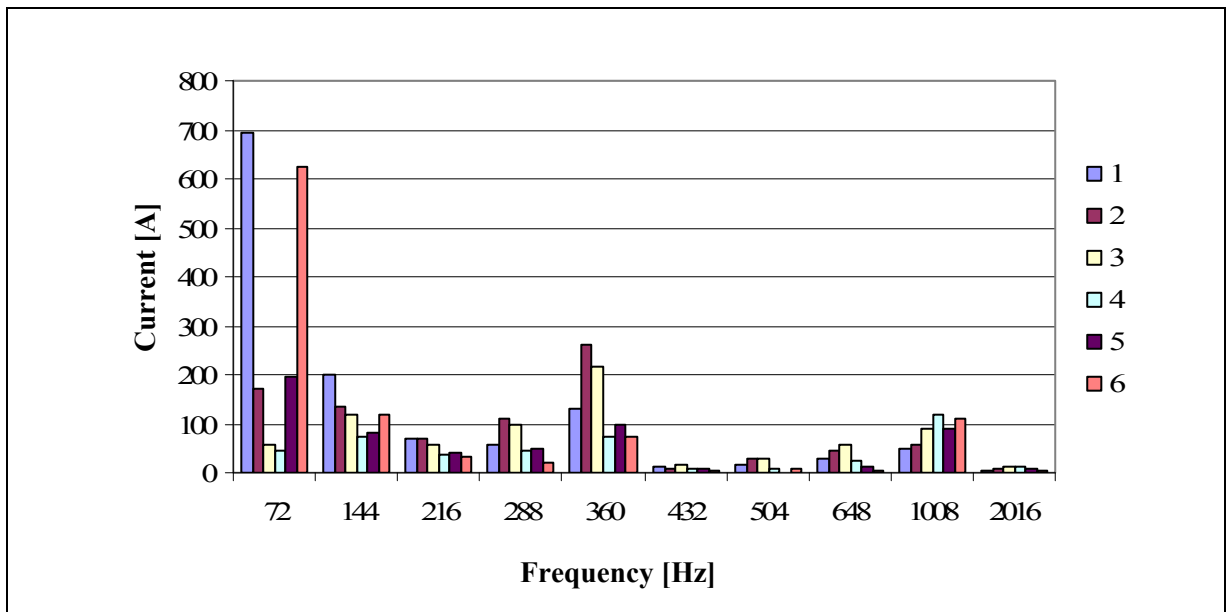


Figure 5.44 FFT of the damper bar currents for 120% of nominal load

In addition, the damper bar losses were computed for 71%, 100% and 120% of the nominal load respectively as 16.71 kW, 32.19 kW and 42.21 kW. Plotting the results of the damper bar loss as a function of the percentage of the nominal load for the three cases, it can be

observed that the curve is not linear. Actually, a second order function is obtained when the three operating points are connected. This conclusion is not surprising because it is well-known that the damper bar losses are proportional to the square of the current.

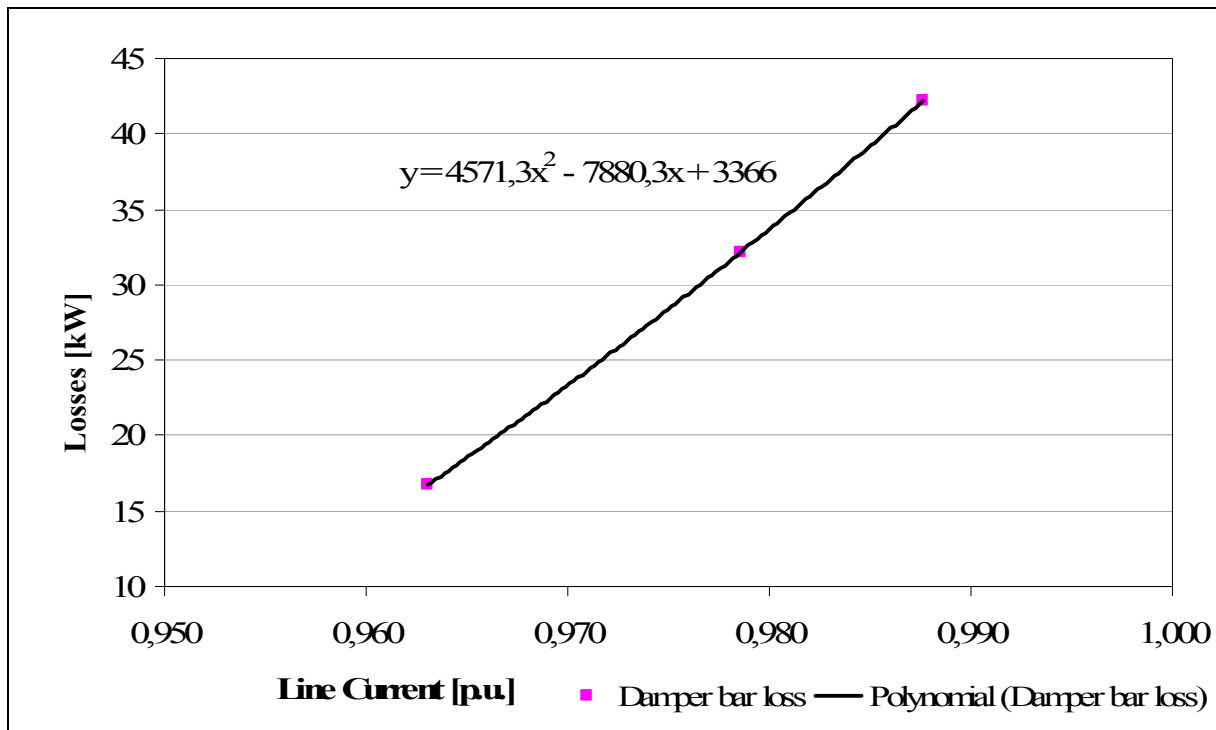


Figure 5.45 Damper bar losses as a function of the line current in p.u.

Another analysis was performed to evaluate the damper bar losses per bar for each of the operating conditions of 71%, 100% and 120% of the nominal load. Fig. 5.46 details the losses for pole 1 for each bar and it is noticed that the bars 1 and 6 have higher losses for all the load conditions studied. Besides, it can be observed that when the machine is operating at a lower than nominal load condition (71% of its nominal value), the losses are almost 50% lower than those when the machine is operating at nominal load condition.



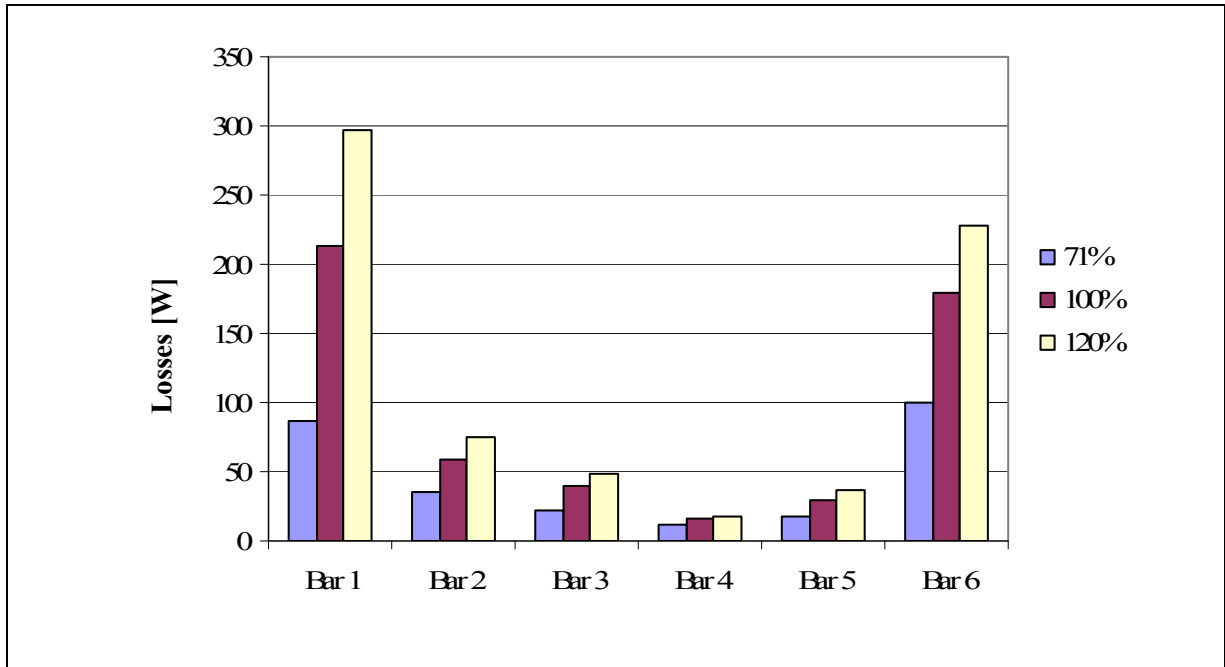


Figure 5.46 Damper bar losses per bar (pole 1)

### 5.4.3 Magnetic losses and its distribution

The simulations were performed under the same loaded conditions as used for experimental tests, namely, 71 % (87.39 MVA; 0.8889 p.f.;  $I_f = 628$  A); 100% (123.08 MVA; 0.8956 p.f.;  $I_f = 739$  A) and 120% (146.55 MVA; 0.9056 p.f.;  $I_f = 821$  A). The core loss distribution and the flux lines at a specific time for each load configuration are shown in Fig. 5.47 to Fig 5.49. It can be noted that the core loss is higher at the stator teeth and in pole shoes when compared with the other parts of the machine. It can also be observed that the flux lines on loaded condition become somewhat distorted when compared to the no-load condition. This distortion is basically related to the presence of the load impedance.

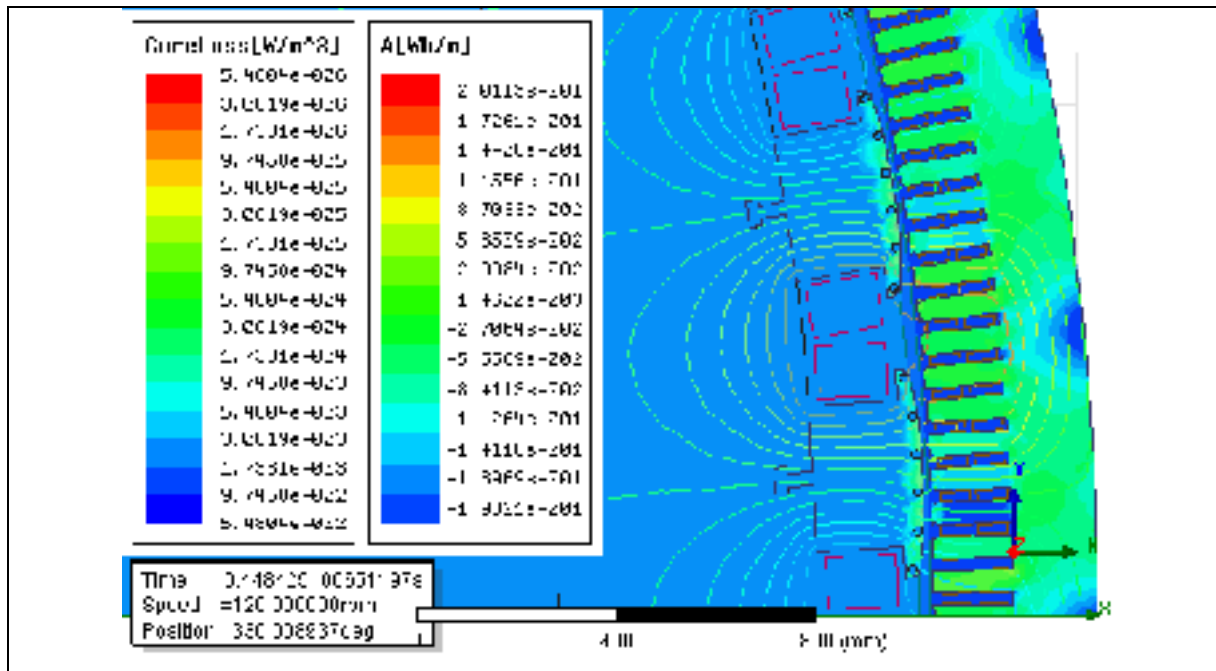


Figure 5.47 Magnetic core loss distribution and flux lines for 71% of nominal load

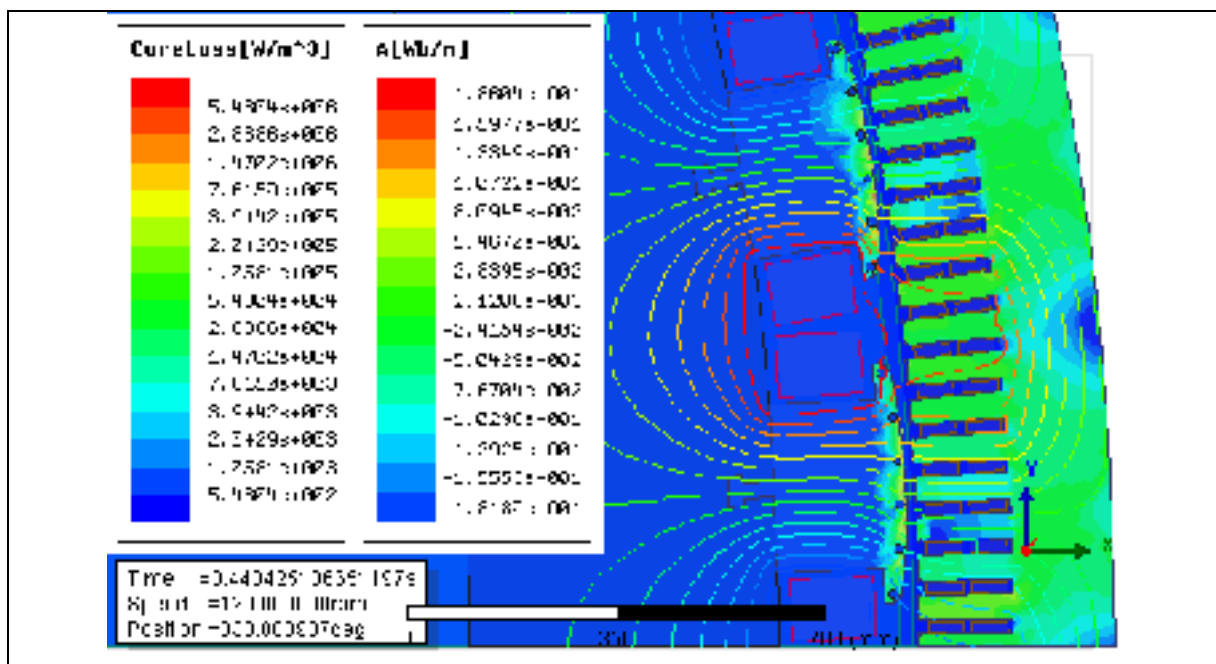


Figure 5.48 Magnetic core loss distribution and flux lines for nominal load



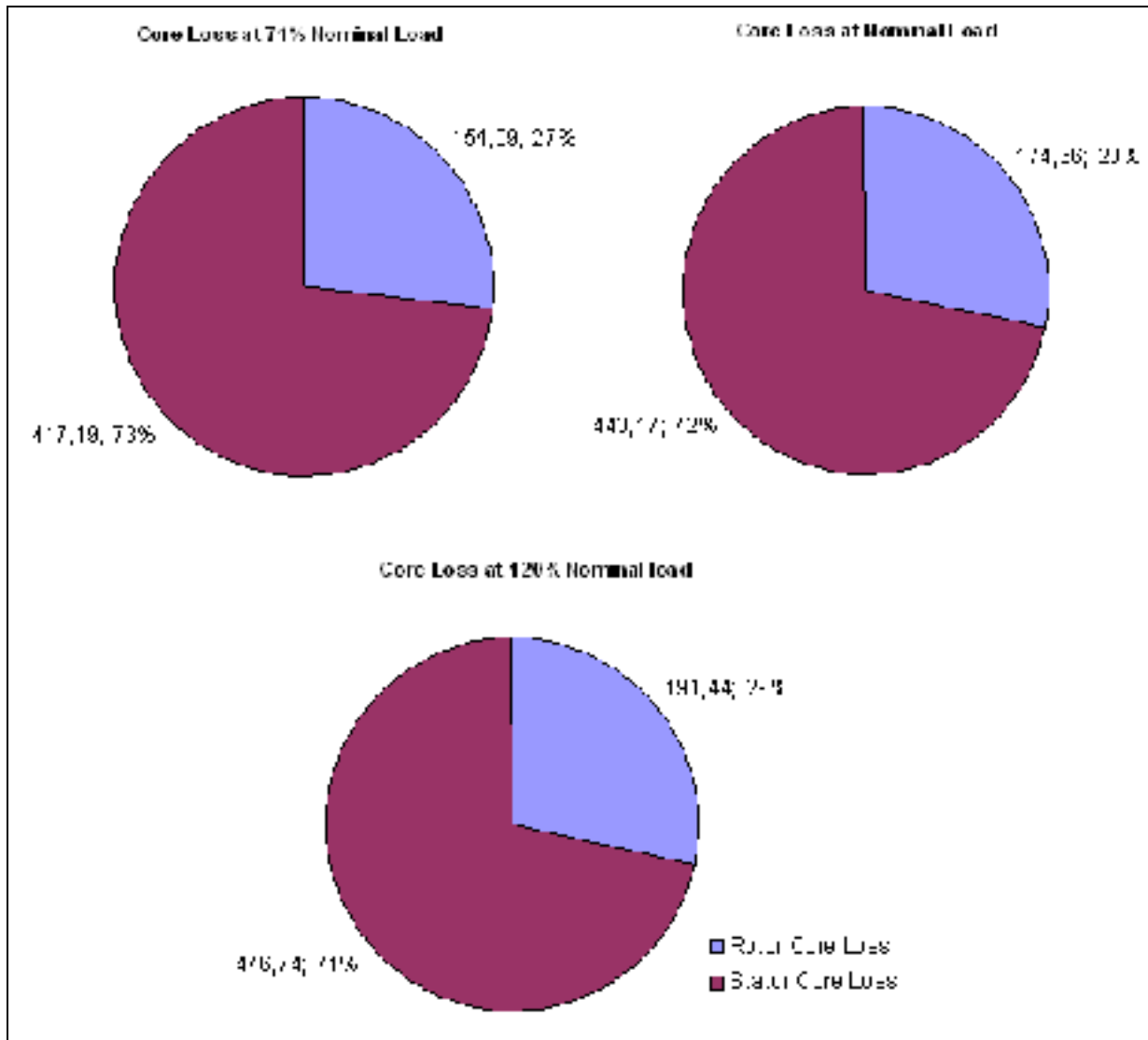


Figure 5.50 Comparison between rotor and stator core loss at 71%, 100% and 120% of nominal load

For 100% nominal load, further simulations were performed to separate the magnetic core loss into hysteresis loss (323 kW) and eddy current loss (295 kW). Figure 5.51 shows the results for the rotor (175 kW) and the stator (443 kW).

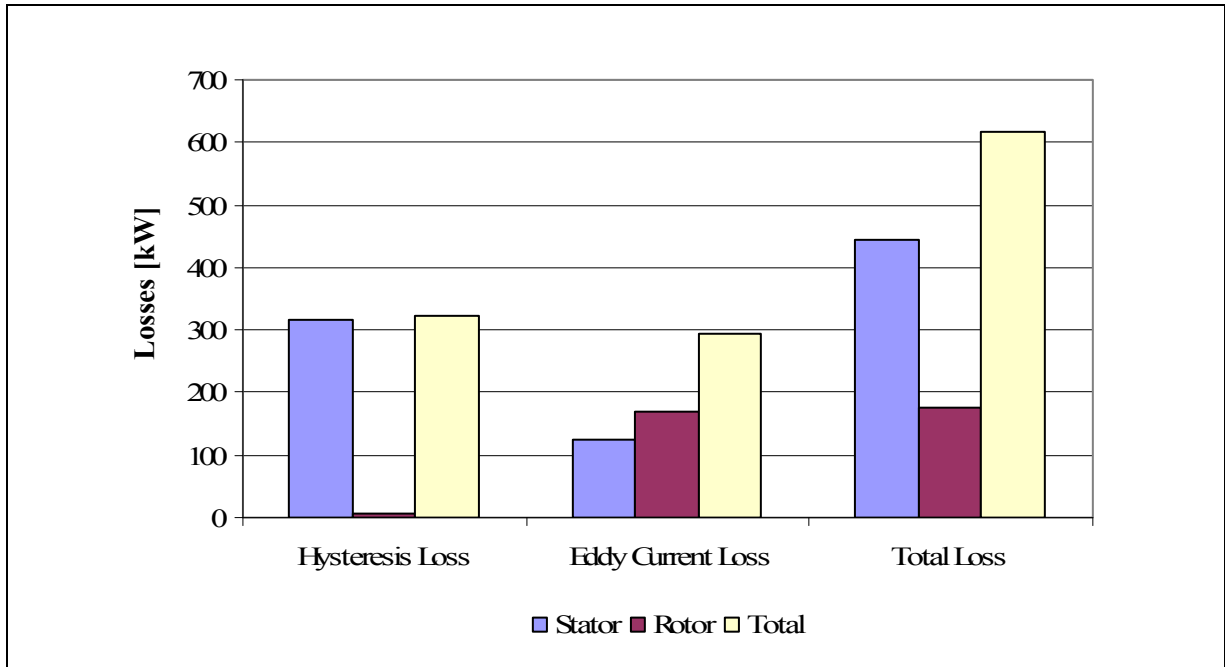


Figure 5.51 Division of the load core loss into hysteresis and eddy current for nominal load

Some authors assumed that the rotor hysteresis core losses are negligible (Rasilo, 2012). The computed value of hysteresis losses for this specific machine is not negligible but they are 2.9% of the total rotor core loss at nominal load.

#### 5.4.3.1 Core losses calculation with the implemented model

Using the proposed approach to compute the core loss, three different load configurations were studied for values at 71%, 100% and 120% of nominal load.

First, the flux density and its spectral analysis were determined for the airgap, rotor pole face, rotor body, stator teeth and stator yoke. Then, these values were used for the proposed model to calculate the stator core losses and the pole face core losses.

Finally, the magnetic core losses are computed based on electromagnetic solutions using three different models: dynamic core loss model given by Eq. (4.94); stator core loss model

calculated by (4.105) and finally, rotor pole surface magnetic losses calculated by (4.107), as showed in Table 5.7.

Table 5.7 Computed magnetic core loss models

Models	Core losses governing equation
Embedded core loss model	Eq. (4.94): $P_v(t) = H_{irr} \left( \frac{dB}{dt} \right) + k_c \left( \frac{dB}{dt} \right)^2 + k_e \left  \frac{dB}{dt} \right ^{\frac{3}{2}}$
Implemented core loss model	Stator core loss (eq. 4.105): $P_v = \sum_{n=1}^N \left( K_h(B_n) ((nf) B_n^2 + K_c(nf, B_n) (nfB)^2) \right)$
	Rotor core loss (eq. 4.107): $P_{fe,p} = k_0 (B \tau_1)^2 (Z_1 n_N)^{1.5}$

The magnetic core losses of the generator are then computed with three different magnetic core loss models for the three operating points, as seen in Table 5.8. Initially the magnetic losses are computed based on the dynamic core loss model in the time domain as given in eq. (4.94). For that, Maxwell 2D software was used to calculate the magnetic flux density and the core losses were computed as 572.07 kW; 617.83 kW and 668.17 kW respectively for 71%, 100% and 120% of nominal load. Later, a post processing was performed to separate the losses into stator losses and rotor losses for the three configurations; all the results are summarized in Table 5.8.

With the magnetic flux density already computed, different core loss models were studied. For the variable coefficient method (eq. 4.105) a good knowledge of the material is needed. That is the reason why this method was only performed for the stator. For the rotor material, the curve of losses vs. magnetic flux is available only at 60 Hz. The stator core losses were

computed as 441.57 kW; 462.86 kW and 502.73 kW respectively for 71%, 100% and 120% of nominal load levels.

Last, a method to compute the rotor loss in large generators was studied. The additional loss at load was computed by eq. (4.107) as 161.43 kW; 178.55 kW and 195.51 kW respectively for 71% ad, 100% and 120% of nominal load.

Table 5.8 Summary of the computed magnetic core loss with different models for the measured load conditions

<b>Model name</b>		<b>Stator losses (kW)</b>	<b>Rotor losses (kW)</b>
71%	Embedded model	417.19	154.09
	Implemented model	441.57	161.43
100%	Embedded model	443.17	174.66
	Implemented model	462.86	178.55
120%	Embedded model	476.74	191.43
	Implemented model	502.73	195.51

Table 5.8 can also be presented in the form of bar charts as shown in Fig. 5.52, where embedded and implemented models are compared for 71%, 100% and 120% of nominal load.

For this machine, it can be noted that the results obtained from frequency domain methods (implemented model) are comparable to those from obtained using time domain methods (embedded model). The embedded model and implemented model in the rotor used constant eddy current and hysteresis coefficients and on the other hand, the implemented model in the stator used variable coefficient.

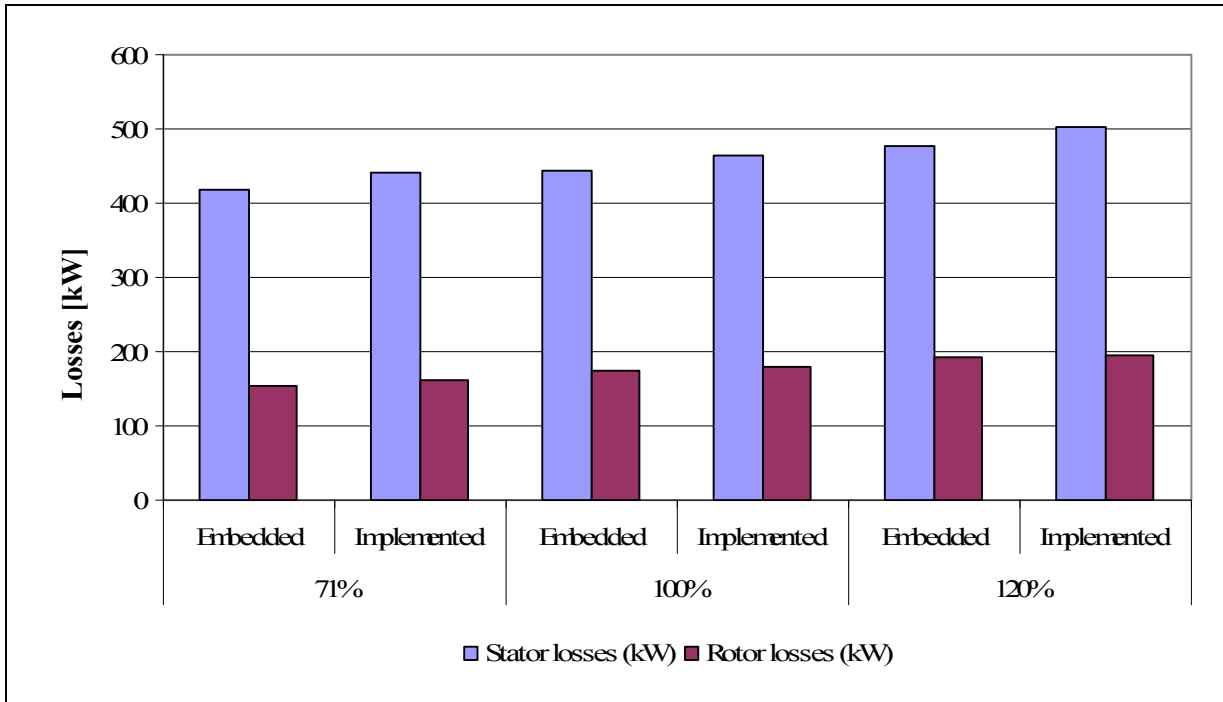


Figure 5.52 Computed magnetic core loss with different models for the measured load conditions

## 5.5 Temperature of the damper bars

One of the goals of Hydro Quebec is to identify units with potential for uprating. With this aspect on mind, Chaaban *et al.* studied the thermal behaviour of a large hydro generator by using analytical equations for the calculation of the heat convection coefficients for a potential power increase (Chaaban *et al.*, 2008). By estimating the excitation current of the generator, the developed software could compute the maximum upper load limit related to the insulation class of the stator winding.

In the same project, Hudon *et al.* considered the electromagnetic core loss distribution to evaluate the hotspot temperature of a machine. Two cases were used to demonstrate the limitation of the resistive temperature detectors sensors for the evaluation of the exact hotspot. The authors highlighted that when a machine is considered for uprating a balance of



an electromagnetic and thermal modeling must be done with detailed on-site measurements (Hudon *et al.*, 2010a).

The comparison between measured and computed temperatures at different load conditions are summarized in Table 5.9 where it can be observed that the predicted results from model are in general in good agreement with the test data. The results were also presented at (Merkhouf *et al.*, 2013). The small discrepancies between measurement and computed temperature values can be attributed to the following:

- in general, the temperatures were underestimated during measurements. In the heat run test for the four load conditions, the experiment ended before reaching complete steady state conditions.
- as a first approximation, the convection heat transfer coefficient, calculated by equation (4.84), was considered constant all around the pole faces and winding. This simplification is not really accurate. For example, the measured coil surface temperature at 146 MVA is equal to 77.5°C on the leading edge of turn #3, while the temperature on the same turn on the trailing edge is much higher reaching 85.9°C. This asymmetry in temperature suggests that the heat transfer coefficient at the trailing edge is lower than on the leading edge.
- another source of discrepancy between the model predictions and measurement comes from the measured pole face temperature facing the airgap, which is believed to be a few degrees off from the actual surface temperature. In fact, it is very difficult to measure accurately the surface temperature of moving hot body at very high speed in a cooler medium. In the present case, the tip velocity is equal to 66.5 m/s (239 km/h). At this speed, a sensor, glued to the hot wall and protected by an external layer of silicon, is surely influenced by the relatively colder air nearby. Measurements and simulation in our laboratory show that the error in similar situations could reach 10°C or more, depending on the attachment configuration and protection of the sensors.

- another important parameter that impacts on the calculation of pole surface temperature is the thermal conductivity of pole's body in radial and circumferential directions. This is because the heat generated by the losses, concentrated on the surface, will diffuse more or less toward the rim where it is carried away by the cooling air. In addition, the conductivity used in the model will have a major impact on how the heat diffuses in the pole body itself to drain the losses to the surrounding air. The heat convection coefficient along the surface is the other main factor that will have an impact on the maximum temperature in the rotor. A theoretical evaluation of this conductivity is difficult due to the stacking of steel plates and the consequent thermal contact resistance between them. In our analysis, the conductivity was taken equal to 20 W/m°C whereas a solid bloc of the same steel has conductivity of 50 W/m°C.

Table 5.9 Comparison between measured and computed damper bar temperature  
Extracted from Merkhouf *et al.* (2013)

Power level	0 MVA		123.08 MVA		146.55 MVA	
Damper Bar	Calc. (°C)	Meas. (°C)	Calc. (°C)	Meas. (°C)	Calc. (°C)	Meas. (°C)
T-damper #1	39.0	--	68.9	--	80.0	--
T-damper #2	43.9	48.8	74.8	80.8	83.6	88.6
T-damper #3	48.6	52.5	78.6	79.3	87.4	85.9
T-damper #4	48.4	51.4	71.1	73.8	80.0	80.0
T-damper #5	43.7	47.5	63.5	68.8	71.8	75.3
T-damper #6	38.9	--	61.2	--	69.9	--

The values presented in Table 5.9 are plotted as bar charts in Fig. 5.53. It can be seen that the values obtained from computation when compared with those obtained from measurement for bars 2, 3, 4 and 5, they are in a good agreement. Besides, by computation, a prediction of the temperature in the bars 1 and 6 was also obtained.

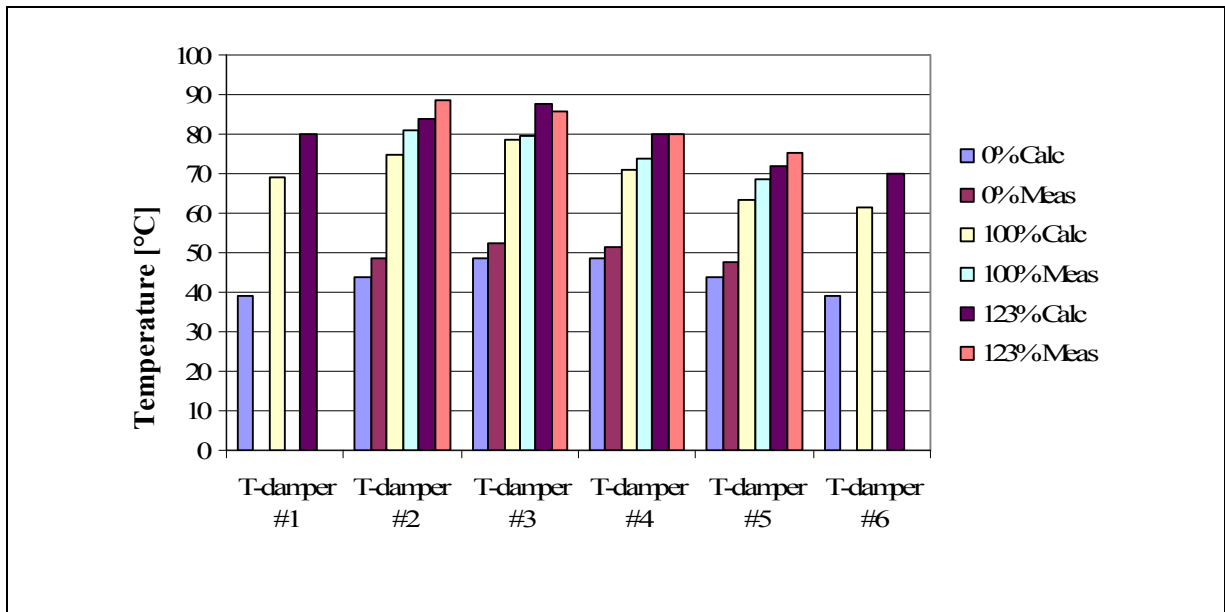


Figure 5.53 Measured and calculated damper bar temperature for 3 different load conditions  
Extracted from Merkhouf *et al.* (2013)

Figure 5.54 shows the 3D model of the computed temperature distribution for the rotor of Manic 21 for nominal load operation. This model was developed by the thermal group of IREQ and the results for other operating conditions are available at the report (IREQ report, 2012).

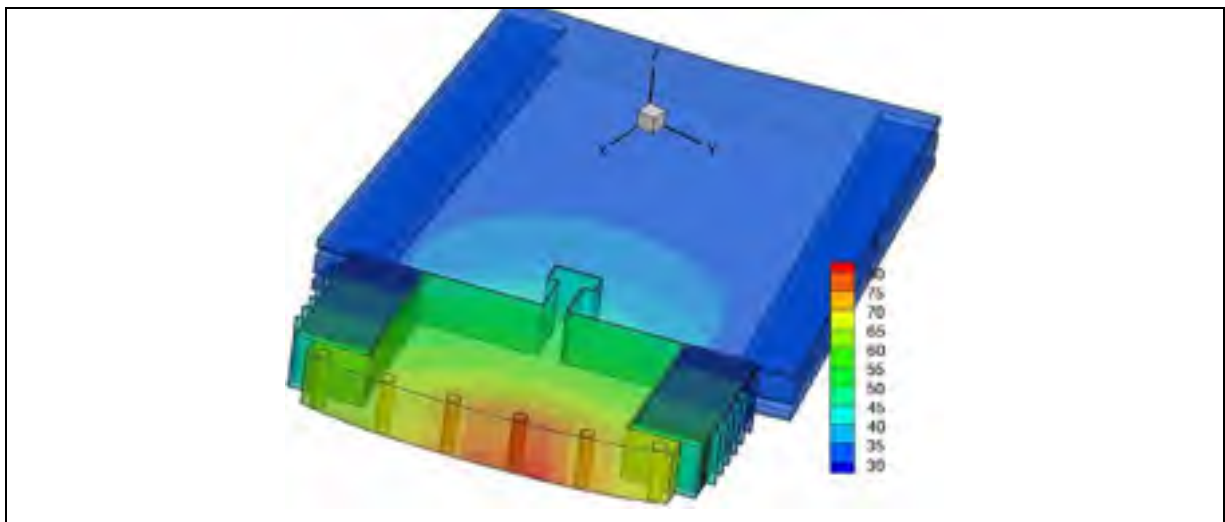


Figure 5.54 Calculated rotor temperature

## 5.6 Conclusions

The quantification of the influence of the mesh, the magnetic material, the excitation current and the size on the airgap helped to arrive at an appropriate model. After the model is validated, the machine was simulated on open-circuit, short-circuit and at three different load conditions (71%, 100% and 120% of nominal load). For the same conditions, experimental measurements were obtained. A comparison between the computed values for core loss and magnetic flux density, with those obtained by experiment, shows that the proposed model is appropriate for further studies that are presented in the next chapter. In it, the machine under study will be analyzed if it can be safely be uprated to work with a higher power output and to determine what would be this new operating point.

Another important aspect of the present chapter considered here was the determination of the losses by different methods. To achieve this, first, an extensive literature review was done; then the dynamic model with constant coefficients (eq. 4.94) was compared with one method for the stator (core loss separation with variable coefficients, eq. 4.105) and another one for the rotor (additional loss at load, eq. 4.107). The approach of a different method for the stator and the rotor was used in the absence of previous knowledge of the magnetic material characteristics. This was due to the fact that the stator magnetic material was changed before we started this study. For the stator, all the characteristic curves regarding the losses as functions of the magnetic flux for multiple of 60 Hz were available. For the rotor magnetic material, this characteristic was obtained only at 60 Hz and this measurement was performed by the manufacturer many years ago. In conclusion all the computed results from simulation are in good agreement with the experimental ones.

The major result of this study reveals that the magnetic core loss distribution and the magnetic field distribution can henceforth be used, as a starting point, by other researchers to perform thermal and mechanical modeling of the machine.

## CHAPTER 6

### INDUSTRIAL APPLICATION OF THE DEVELOPED TECHNIQUE

Environmental barriers always occur when there is need to expand the electric generation capacity. With the ever increase demand for electricity consumption, the uprating of existing generators seems to be an interesting alternative to augment electricity production. However, in order to maximize the electricity production, a preliminary study to analyze the possibility of uprating the capacity of an existing machine without reducing its life time and the reliability of the power system is always preferable.

Two different studies were considered in this thesis. The first study had the aim to uprate an existing machine, and the second one aimed to understand the electromagnetic behaviour of a slightly damaged machine.

In order to analyze the uprated operation of an existing generator, a second set of simulations studies was done on a machine “Manic 21” at Hydro-Quebec generating station. The simulations were necessary to analyze from the electromagnetic point of view, if the machine could operate or not at a higher loaded condition than the one specified by the manufacturer. Also, to study the thermal and mechanic aspects of this increased loaded operation. Finally, a decision would be taken if the machine could be suitable or not for uprating aimed to increase its output power accordingly.

It is well-known that continuous mechanical and thermal stresses in the machine can lead to severe impacts on the stator core and also sometimes in the rotor core. This is the reason why the three aspects, namely, electromagnetic, mechanical and thermal, have to be carefully studied in order to demonstrate if the increase in the power output could interfere with the remaining life expectancy of the machine.

The second application of the developed model was done with the intention to analyze a slightly damaged machine named Rapide-des-Quinze. Here, the aim is not to increase the nameplate power output, but to understand the electromagnetic behaviour of the machine. The damage is on the stator windings and depending on the number of bypassed coils and their positions in the winding; under these conditions, one needs to check if the machine could operate at full load, although a reduction of the power output is usually done.

With the cut stator bars, unbalanced line currents in synchronous generators produce negative sequence current in the stator winding, and consequently this induces a double-frequency (120 Hz) current in the rotor amortisseur winding (DeHaan, 1999). Due to the double frequency current, additional heat losses in the damper bars occur and they are admissible provided the negative sequence line currents are limited to a maximum 5% of rated line current, as designated by IEEE-ANSI C50.12 (IEEE-ANSI C50.12 *apud* DeHaan, 1999). The line current and the damper bars losses are investigated for the studied machine and also for a hypothetical case of a machine with 4 cut coils.

This chapter is divided into two sections. The first section deals with the uprated operation of Manic 21, and the second one presents the electromagnetic analysis of the machine Rapide-des-Quinze.

## **6.1 Extrapolation of Manic 21 (>100% load)**

In this section, an evaluation has been done, if the machine Manic-21 is able to operate with a higher power output. The machine has two operating points, the one determined by the manufacturer that is used during the summer periods and another higher point that is used during the winter. These two operating positions are selected as a function of the water in the river; hence, if the water is colder (in the winter the water is usually 5°C), the machine can operate at higher loads and in the summer when the water temperature average is 15°C, the machine operates at nominal load.

Two new operating points were chosen for the study. These operating conditions were obtained from preliminary extrapolated results of the temperature in the core of the machine. The first operating point is at 170 MVA when the machine operates in the summer season; this value represents an increase of 38.66% of the power output of the machine (170/122.6 MVA). The second one is at 188 MVA when the machine operates during winter season, which represents an increase of 24.75% in the power of the machine (188/150.7 MVA).

The rating of a synchronous generator is specified in terms of the maximum apparent power in MVA load at a specified power factor and voltage for which the generator is designed to operate in steady state. In the case of Manic-2, the rated values are at a power factor of 90% lagging and a stator voltage of 13.8 kV. For the extrapolated conditions, the power factor is 90% lagging and the stator voltage is 14.5 kV.

However, an important input was unknown, namely, the excitation current for each of the extrapolated operating points. For the determination of the excitation current at different load conditions (extrapolated), some parameters must also be considered:

- the type of materials for rotor laminations and stator;
- the impact of the magnetic saturation of the materials across reactances;
- the angle of the internal power generator according to the load (as it is used in solving the vector diagram for determining the internal voltage of the alternator for a given supply voltage at its terminals);
- the variation of the gap function in terms of operating points and its extrapolation;
- the impact of non- uniformities of the air gap and the integration of this information into a simulation of a periodic sector;
- the average air gap dimension changes depending on the load, on the one hand, due to electromagnetic forces acting on all the components of the generator and on the other, due to thermal expansion of the rotor and the stator core.

The result presented in Fig. 6.1 shows the excitation current characteristics obtained from measurements (red curve), simulation with air gap design (black diamonds), with real air gap (blue curve) and with effective air gap (green dots).

It has to be noted that the currents obtained by simulation with the air gap design are higher. This is quite normal; because with a larger air gap there is the need of a higher excitation current to magnetize the magnetic circuit.

On the other side, the currents obtained by simulations with real gap (measured at each operating condition) approach of the currents measured at lower powers (no-load and 71 %), and the current gradually diverges at higher powers (146 MVA, 170 MVA and 188 MVA).

The excitation currents obtained with an average effective gap (green curve in Figure 6.1) illustrate the differences between actual and measured air gap up to a power of 188 MVA. The difference between the actual and effective air gap at every point of operation is only of the order of 1.5 mm.

Note that the two air gap (measured and effective) increases with MVA; and that the point of operation to extrapolate to 188 MVA falls exactly on the air gap design that is 15.875 mm. The operating point 188 MVA (winter conditions) with the air gap (that is predicted by the gap provided by the extrapolation of the curve in Fig. 6.1) is for simulated design with an excitation current of 982 A.



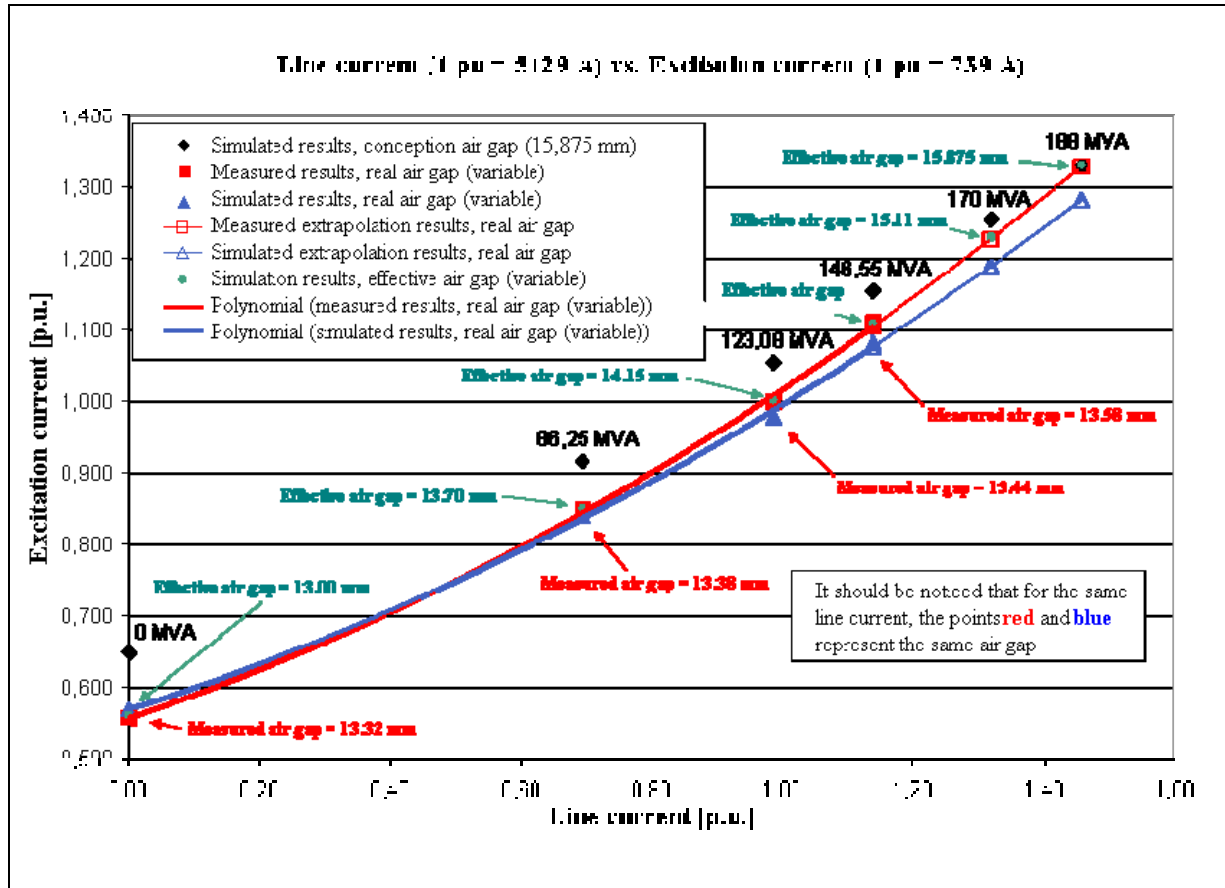


Figure 6.1 Line current versus excitation current for different load conditions  
Extracted from Hudon *et al* (2012)

In summary, the excitation current was determined for two extrapolated load conditions at 170 MVA and 188 MVA as 924 A and 983 A, respectively. For the extrapolated operating points, a stator voltage of 14.5 kV was taken. The phase current was calculated in order to obtain the correct power output.

The open circuit core loss at 14.5 kV can be determined from the tendency curve presented in Fig. 6.2 (simulated results). Using the tendency equation, the open-circuit core loss was computed as 636 kW for 14.5 kV.

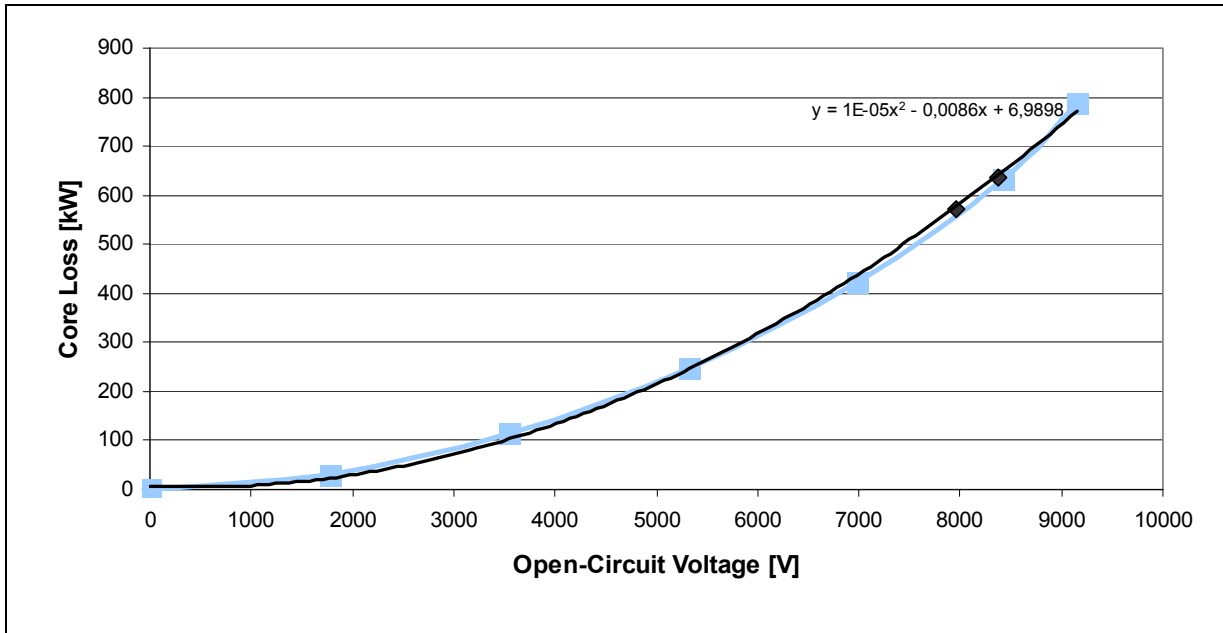


Figure 6.2 Open-circuit core loss curve and tendency curve

The strategy usually applied when the machine is uprated is to increase the stator voltage in order to decrease the stator line current and consequently decrease the joule losses in the stator winding.

The magnetic flux density in the air gap, the magnetic flux distribution and the core loss are analyzed for power levels at 170 MVA and 188 MVA and voltage at 14.5 kV.

#### 6.1.1 Extrapolation condition – 170 MVA at 14.5 kV

The first analysis dealt with the magnetic flux density in the air gap at the 170 MVA operating condition and voltage at 14.5 kV. For that, after post-processing the waveforms of the magnetic flux density as a function of time (for a specific point) and as a function of distance (for an arc placed in the middle of the air gap) were determined as shown in Fig. 6.3.a and 6.3.b.

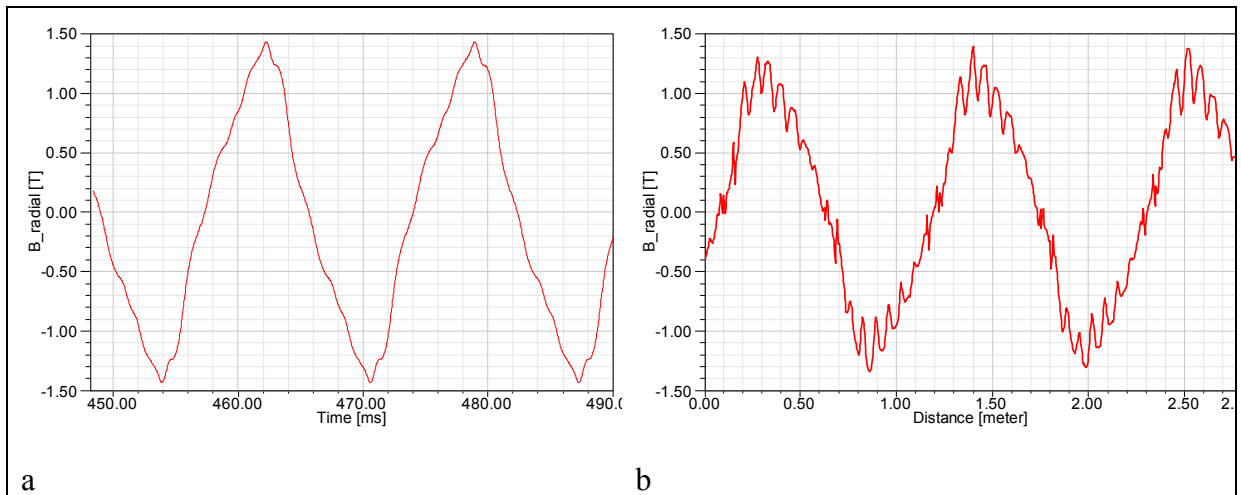


Figure 6.3 Flux distribution in the air gap for 170 MVA: a) as a function of time, b) as a function of the distance

Then, the magnetic flux distribution was plotted and a zoom in the pole and the stator teeth is presented in Fig. 6.4 for 170 MVA. It can be seen that the higher values of the magnetic flux distribution are located at the pole shoes and also in the stator teeth.

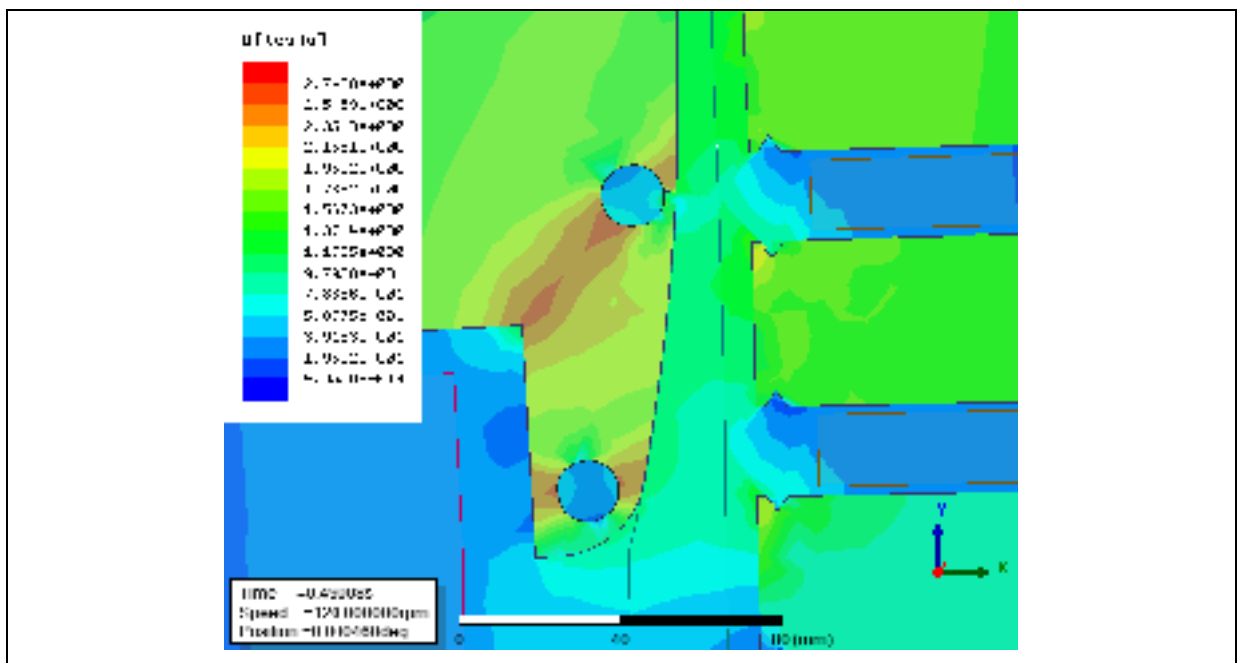


Figure 6.4 Flux distribution for 170 MVA

### 6.1.2 Extrapolation condition – 188 MVA at 14.5 kV

The first analysis is for the magnetic flux density in the air gap at an operating power of 188 MVA. For that, after post-processing, the waveforms of the magnetic flux density as a function of time (for a specific point) and as a function of distance (for an arc placed in the middle of the air gap) were determined, as shown in Fig. 6.5a and b.

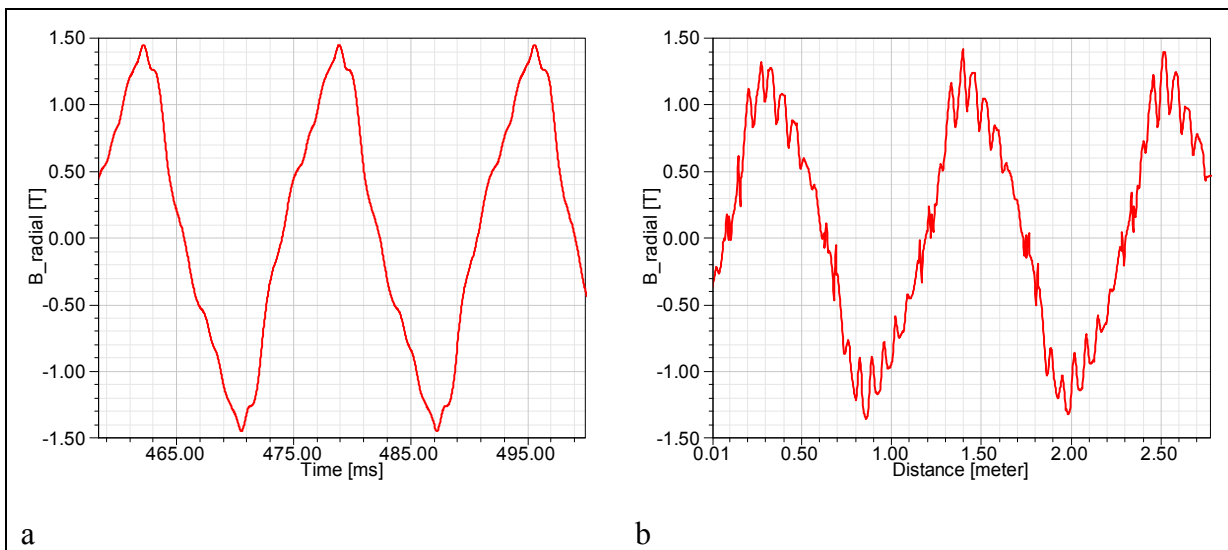


Figure 6.5 Flux distribution in the air gap for 188 MVA: a) as a function of time, b) as a function of the distance

After that, the magnetic flux distribution was plotted and a zoom in the pole and the stator teeth is presented in Fig. 6.6 for 188 MVA. It can be seen that higher values of the magnetic flux distribution are located at the pole shoes and also in the stator teeth.

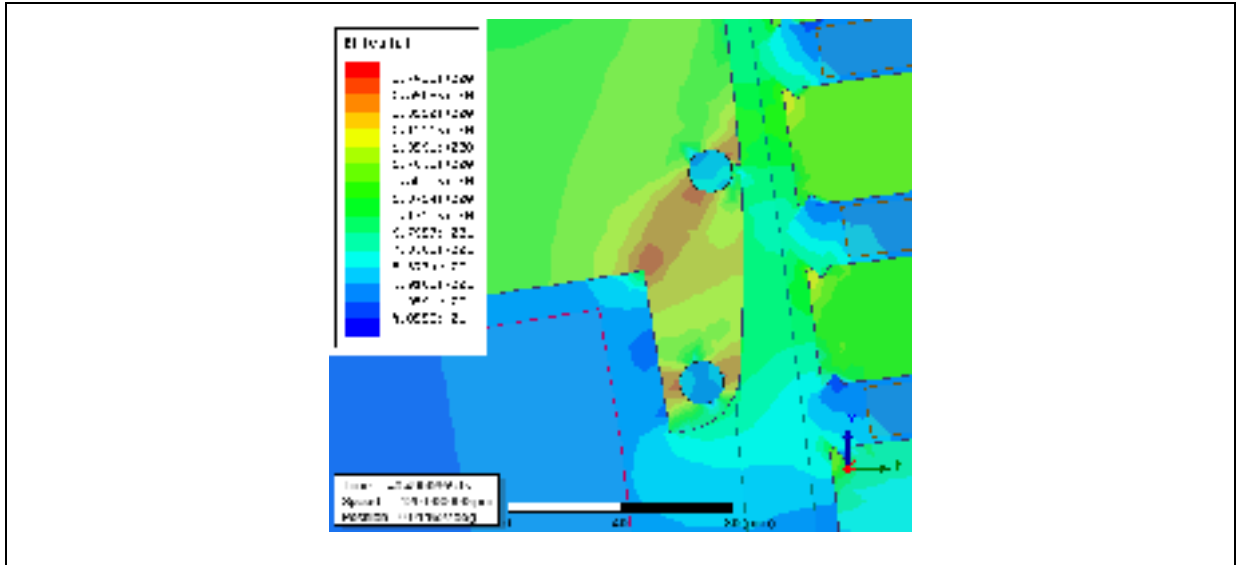


Figure 6.6 Flux distribution for 188 MVA at 14.5 kV

### 6.1.3 Discussions for the extrapolation conditions at 14.5 kV

In Fig. 6.3a and 6.5a are plotted the radial magnetic flux density for 170 MVA and 188 MVA at 14.5 kV. The peak values of 1.428 T and 1.446 T were obtained respectively for each power output as shown in Figure 6.7.

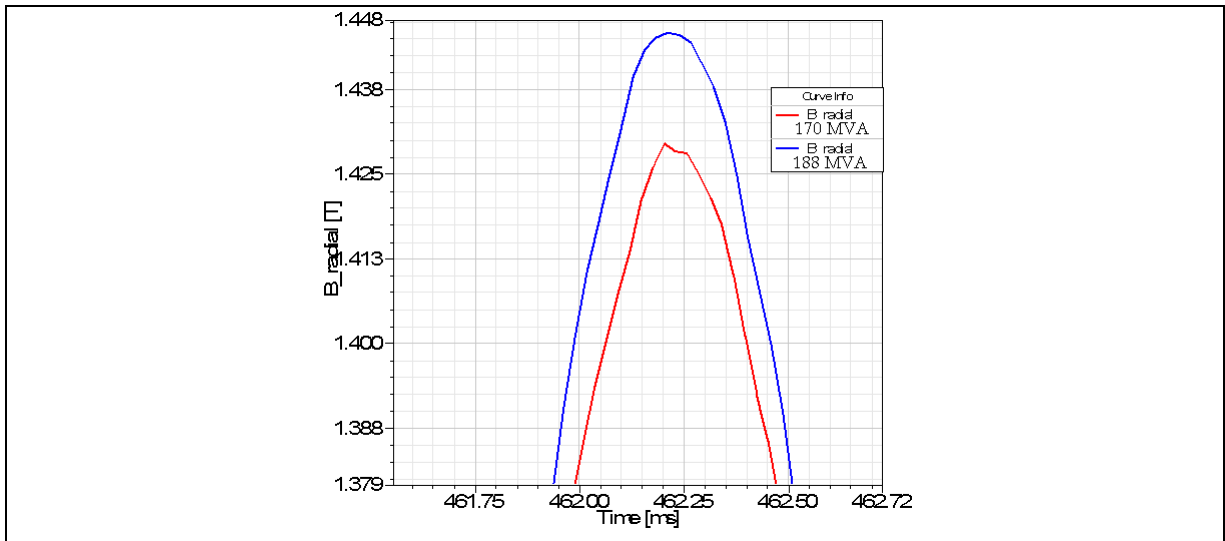


Figure 6.7 Radial flux density for 170 MVA and 188 MVA (14.5 kV)

Comparing the magnetic flux density distribution at 170 MVA and 188 MVA (Fig 6.4 and 6.6) power levels, it can be seen that the magnetic flux density is slightly different, especially at the pole face. These two cases have to be studied to find out how this new magnetic flux distribution would affect the temperature distribution in the machine and if the temperature is going to exceed the insulation limits for the machine.

In Table 6.1, the simulated line current is presented for power levels at 170 MVA and 188 MVA. For 188 MVA, the computed rms value from obtained simulation results of the phase current is found 7552 A.

Table 6.1 Simulated and expected values for stator phase current (14.5 kV)

<b>Power Output (MVA)</b>	<b>I field (A)</b>	<b>Simulated I phase (rms) (A)</b>	<b>Rated I phase (rms) (A)</b>	<b>Variation %</b>
170	924	6827	6769	0.86
188	983	7552	7486	0.89

The total magnetic core loss was also computed for the two new conditions, namely, 170 MVA and 188 MVA which represent 139% and 153% of the nominal load respectively. It can be seen from Table 6.2 that when the power output is increased the core loss also increase in the rotor and in the stator of the machine. For a 9.57% of increase of the power output from 170 MVA to 188 MVA, the losses increased only 1.56%.

Table 6.2 Simulated results for machine operating over the nominal conditions

<b>Power Output (MVA)</b>	<b>Excitation Current (A)</b>	<b>Rotor Loss (kW)</b>	<b>Stator Loss (kW)</b>
170	924	205,90	494,98
188	983	209,57	502,26

As predicted, with the increase in the power output, the increase of the core loss is not linear, as confirmed in Fig. 6.8, where the core loss was plotted as a function of the phase current for the power output of 146.5 MVA, 170 MVA and 188 MVA. The core loss does not increase proportionally as could be expected beyond a certain point when the maximum power output is obtained. After this limit, the magnetic material enters in saturated condition. This results in operating the machine beyond the admissible limit which could lead to hot spots in the magnetic material and hence compromise the insulation of the machine.

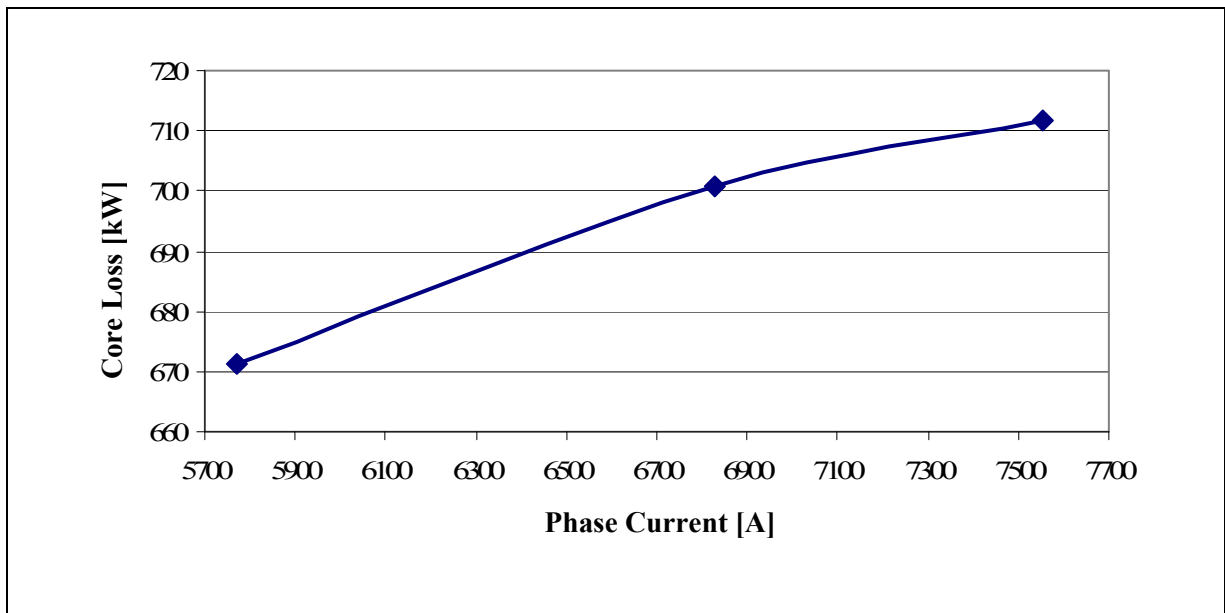


Figure 6.8 Magnetic losses for 146.5 MVA, 170 MVA and 188 MVA

The core loss on open-circuit for 14.5 kV was computed as 636 kW. Deducting this value from the magnetic loss, the stray load loss can be calculated as 35 kW, 65 kW and 76 kW for 146.5 MVA, 170 MVA and 188 MVA power levels respectively. The results of the stray load loss are plotted as a function of the square of the phase current in p.u., Fig. 6.9.

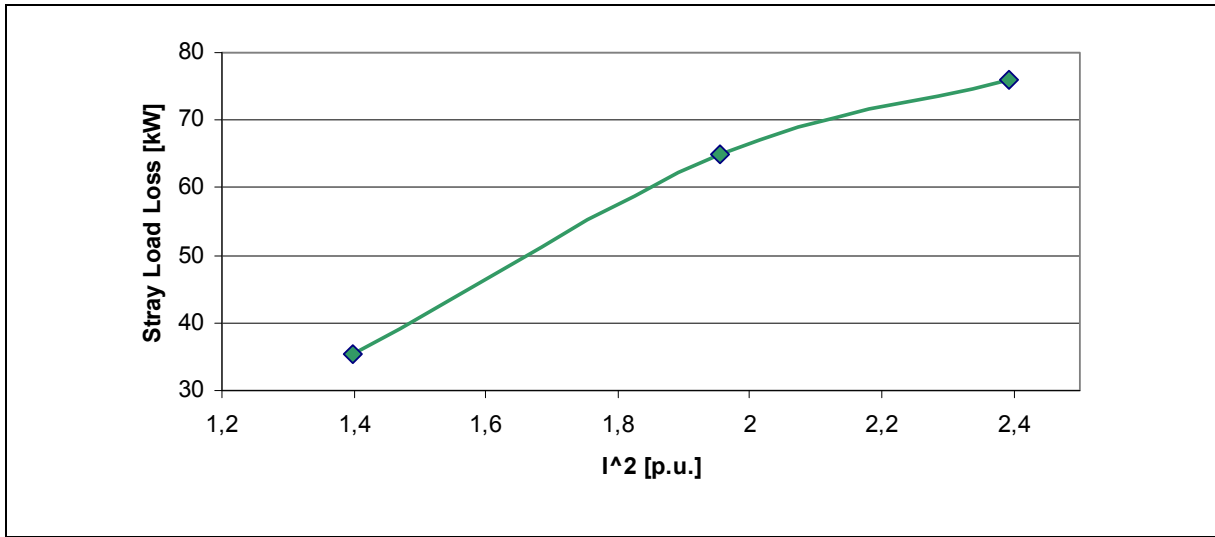


Figure 6.9 Stray load losses for 146.5 MVA, 170 MVA and 188 MVA as a function of the  $I^2$  phase

The proposed method to compute the core loss is done for two different configurations: one, at the extrapolated point at 170 MVA and another at 188 MVA. The procedure and the equations used to obtain the losses are the same as explained in the previous section. The magnetic core losses are computed based on the different electromagnetic solutions obtained using three different models: First, dynamic core loss model given by Eq. (4.94); secondly, stator core loss model calculated by (4.105) and finally, using rotor pole surface magnetic losses as calculated from (4.107).

The magnetic core losses for the generator are then computed for three different magnetic core loss models at the two extrapolated points.

Initially the magnetic losses are computed based on the dynamic core loss mode in the time domain and given in (4.94). For that, Maxwell 2D software was used to calculate the magnetic flux density and the core losses were computed as 700.88 kW and 711.83 kW respectively for 170 MVA and 188 MVA. Later, post processing was performed to separate the losses into stator losses and rotor losses.



With the magnetic flux density already computed, different core loss models were studied. For the variable coefficient method (eq.4.105) a high level of knowledge was needed about the material used. That is the reason why this method was only performed in the stator, as mentioned before, because the characteristics of the losses at 60 Hz were available only for the rotor material. The stator core losses were computed as 528.71 kW and 531.21 kW respectively at power levels of 170 MVA and 188 MVA.

Last, a method to compute the rotor loss in the case of large generators was studied. The additional loss at load was computed by (4.107) as 211.80 kW and 215.96 kW respectively at power levels of 170 MVA and 188 MVA.

The rotor and stator core results obtained from the embedded and implemented models are summarized in Fig. 6.10 for 170 MVA and 188 MVA.

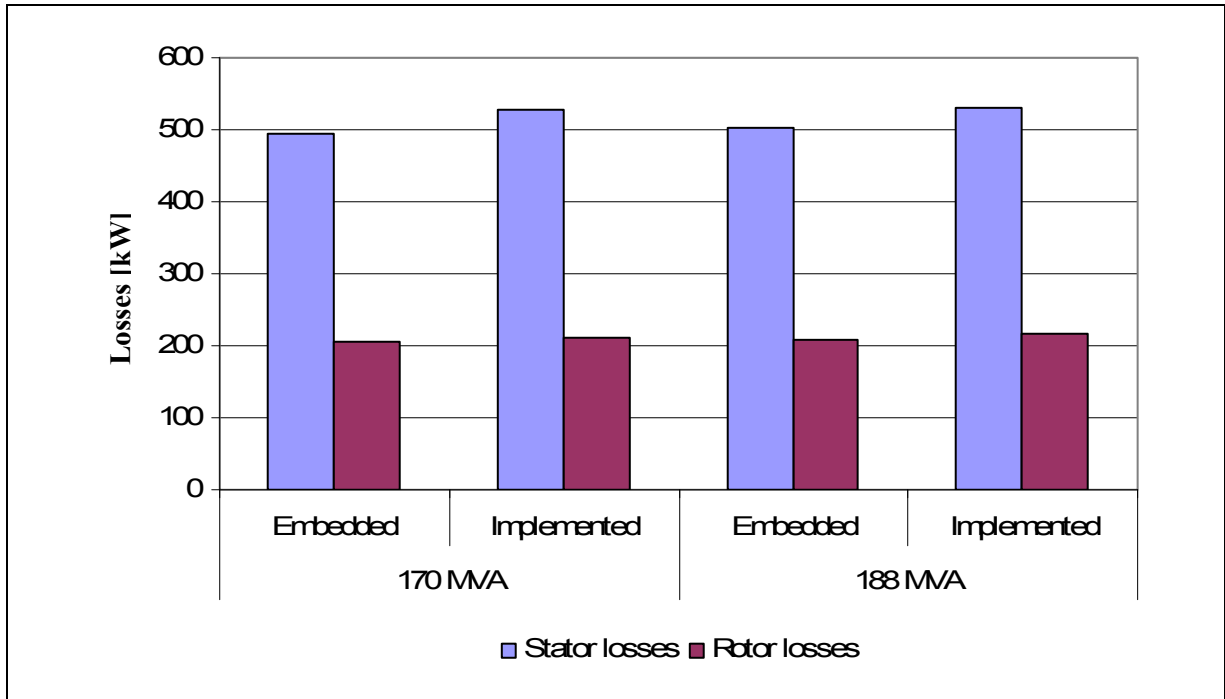


Figure 6.10 Losses for 170 MVA and 188 MVA for different core loss models

After the electromagnetic simulations were done, the magnetic flux distribution and the core loss distribution matrix were transferred to the thermal study in order to decide if the machine could or could not operate over the nameplate values. This study focuses on the determination of the hot spots of the machine, especially in the pole shape, stator teeth, damper bars and stator windings.

Standard C50-12 establishes that the hottest-spot temperature in indirectly cooled salient-pole synchronous generator should not exceed 155°C for class F insulation system. Also that when the machine is operating at output rated conditions and the temperature of the air leaving the coolers is inferior to 40°C, the maximum limit for temperature rise in the stator windings for machines with rated voltage between 12 kV and 24 kV is 105°C and in the rotor windings is 100°C. For instance, if the machine is operating at rated output conditions and the temperature of the air leaving the coolers is 25°C (25°C<40°C), the maximum allowed temperature in the stator and the rotor windings will be 130°C and 125°C respectively. However, for the stator core and rotor core, a value of the maximum temperature is not specified. And only the following statement is made “*not detrimental to the insulation of that part or any adjacent part*”. More details can be found at C50-12, session 7.1 (C50-12, 2005).

Hudon *et al.* computed the rotor core and stator core temperatures for the two extrapolated conditions, 170 MVA and 188 MVA (Hudon *et al.*, 2012). These results are presented in Table 6.3, where it can be observed that the rotor temperature reached 122°C for 188 MVA during operation in the winter season.

Table 6.3 Computed rotor and stator temperatures for 170 MVA and 188 MVA  
Extracted from Hudon *et al.* (2012)

<b>Power Output (MVA)</b>	<b>Condition</b>	<b>Voltage (kV)</b>	<b>T<sub>calc</sub> rotor (°C)</b>	<b>T<sub>calc</sub> stator (°C)</b>
170	Summer (water at 15 °C)	14.5	114	89
188	Winter (water at 5 °C)	14.5	122	93

Assuming that the temperature of the air leaving the coolers is 30°C, the maximum calculated temperatures for the rotor core and the stator core do not exceed the allowable maximum value of the temperature in the rotor and stator windings. However, one of the directives of Hydro-Québec production is that the maximum temperature cannot be more than 100°C anywhere in the machine. Hence, it can be concluded that the machine cannot be operated at the extrapolated point at 170 MVA in the summer and at 188 MVA in the winter due to the reason that the temperature would be the maximum allowable rotor temperature.

More extrapolated points were studied and in the end, new limits for operating conditions were defined by combining electromagnetic, thermal, vibration, fluids simulations. Finally, these new operating points are 150 MVA for the summer and 165 MVA for the winter. The first operating point represents an increase of 22.35% in the power output of the machine (150/122.6 MVA) during summer and an increase of 9.49% in the power output of the machine (150.7/165 MVA) during winter. The computed rotor and stator core temperatures are presented in Table 6.4.

Table 6.4 Computed rotor and stator temperatures for 150 MVA and 165 MVA  
Extracted from Hudon *et al.* (2012)

<b>Power Output (MVA)</b>	<b>Condition</b>	<b>Voltage (kV)</b>	<b>T<sub>calc</sub> rotor (°C)</b>	<b>T<sub>calc</sub> stator (°C)</b>
150	Summer (water at 15 °C)	14.5	101	71
165	Winter (water at 5 °C)	14.5	100	78

For these two operating conditions (150/165 MVA), the same electromagnetic analysis was done. The magnetic flux density distribution and the core loss distribution were also computed. For instance, the magnetic flux density distribution and the core loss distribution for 165 MVA are shown in Fig. 6.11.

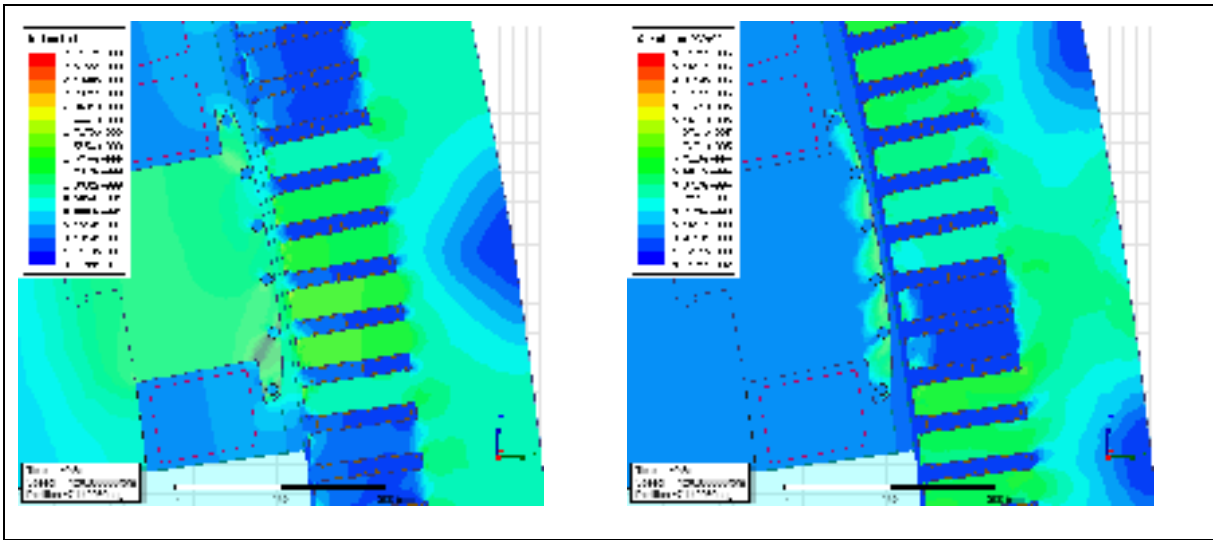


Figure 6.11 Magnetic flux density distribution and the core loss distribution for 165 MVA

## 6.2 Cut coil study of Rapide-des-Quinze

The investigated generator had the nameplate rating of 32.5 MVA, 68 poles, 432 slots, 13.2 kV, 105.9 rpm, 60 Hz with 6 damper bars per pole. This machine presents a stator bar cut and bypassed in the terminal B2 and it is operating at 86% of its rated load.

The armature winding of Rapide-des-Quinze is fractional with  $2+2/17$  slots per pole per phase, which allows 17 poles pitch model to be used for the electromagnetic transient simulation, as shown in Fig.6.12.

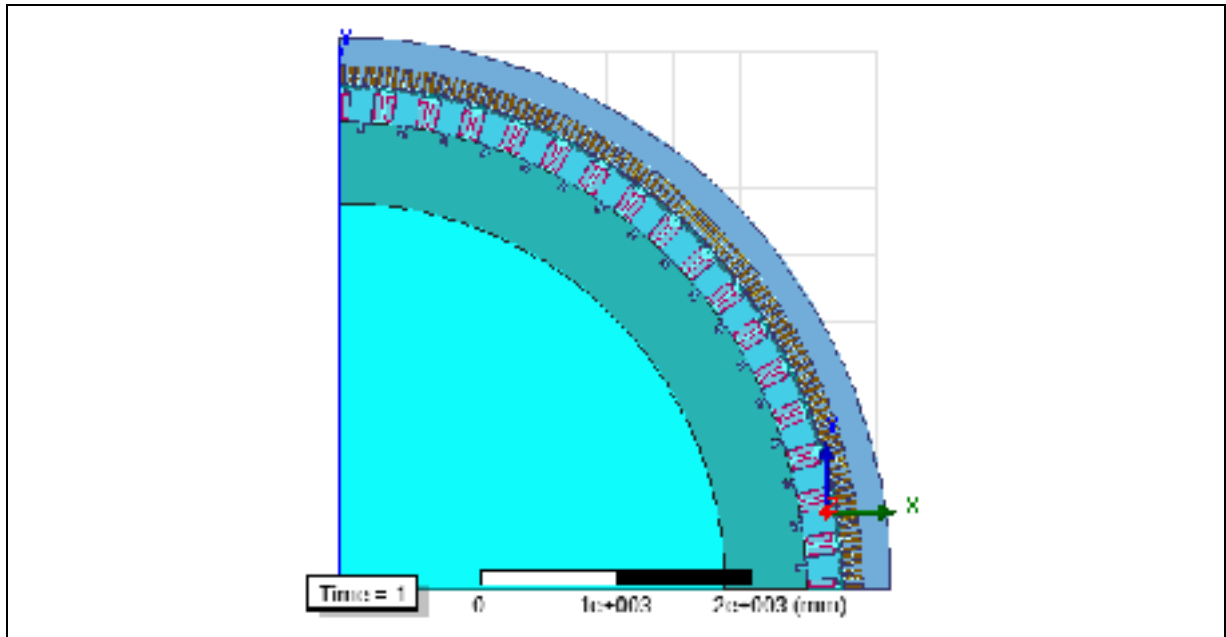


Figure 6.12 17 poles machine model

When any coil is bypassed in the stator windings, the electromagnetic symmetry will not only be determined by the number of slots per pole per phase, but also by the spatial distribution of these bypassed coils. In this case, a complete generator has to be modeled resulting in a large finite element model (68 poles for this generator).

The mesh chosen for the simulation consists of more than 256000 elements. Fig.6.13 presents the meshing 2D model for the specific machine.

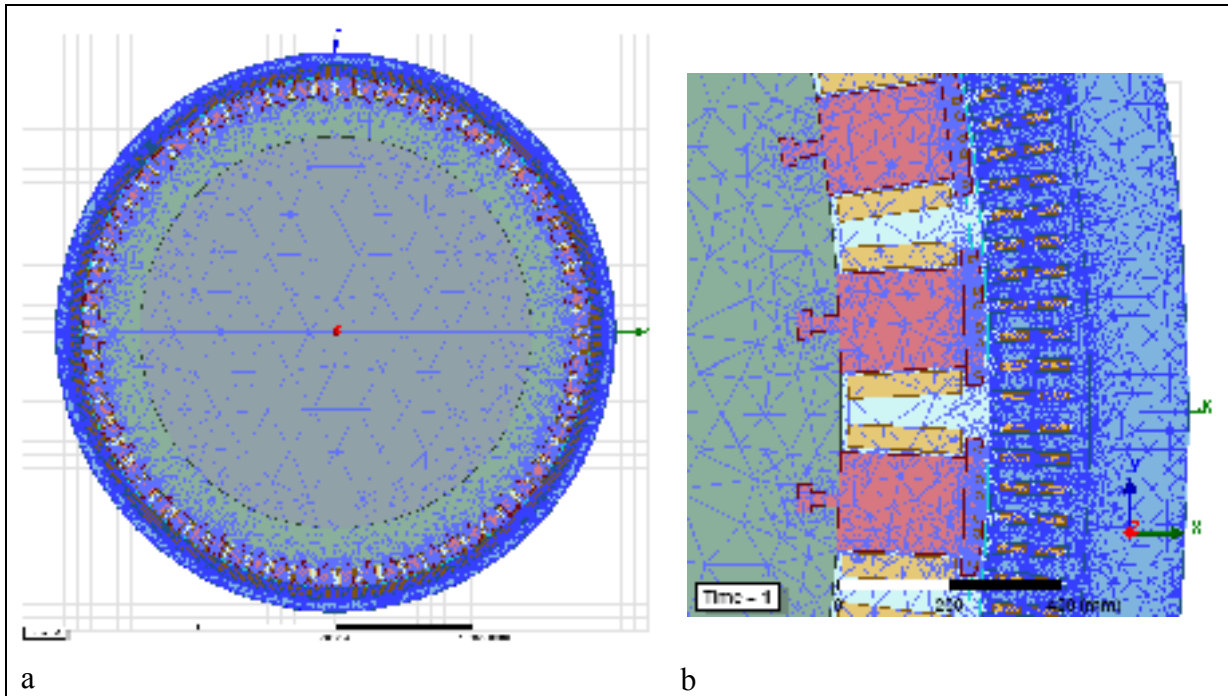


Figure 6.13 Meshing 2D of a 32.5 MVA hydro electrical generator a) entire machine, b) zoom of the 2D mesh

To allow critical analysis, a small time step is required; according to the Nyquist criteria the simulation time-step used was of  $10^{-4}$  seconds; this was computed using eq. 4.87. This permits computing higher harmonics up to the 80th. With this time-step, it is therefore possible to capture most of the existing harmonics in the machine including the slot passing frequencies.

Two variables are used during the process of comparison between experimental tests and simulation results: total magnetic core loss and air gap magnetic flux density.

In the electrical generator with bypassed coils in the stator windings, the electromagnetic symmetry is not only determined by the number of slots per pole per phase, but also for the spatial distribution of these bypassed coils. For FEM simulation, the complete generator has to be modeled resulting in a large number of poles (68 poles in this case) to be simulated.

For this research work, five simulations were performed: open-circuit symmetrical machine; 86% nominal load with one cut bar and 86% nominal load with four cut bars; 100% nominal load with one cut bar and 100% nominal load with four cut bars.

In the open-circuit simulation the computed core losses were approximately 155 kW. It has to be noted that for 2D model simulation does not include the induced losses in the end plates and some additional losses (due to 3D effect). So the computed loss should be higher, even though, the value is close to the measured value of 176 kW.

For loaded condition, the simulation was performed at 86% of the nominal load because of water restrictions at the time of the year when the measurements were done.

#### **6.2.1 Circuit current calculation with one bypassed coil**

This case represents the actual condition of the generator under study (one bypassed coil in one phase of the circuit number 2). Two simulations were performed in this configuration: first, the machine with the present operating condition of 86% of the rated loaded condition and second with nominal load.

It can be seen from Fig. 6-14 that when the machine operates at 86% of its nominal load with one bypassed coil, the currents in each circuit do not exceed the rated value of 0.25 per unit which was already expected due to the low operating condition of this particular case. With the machine operating at 86% of nominal load and with one cut coil, most of the computed current in the different circuits are unbalanced.

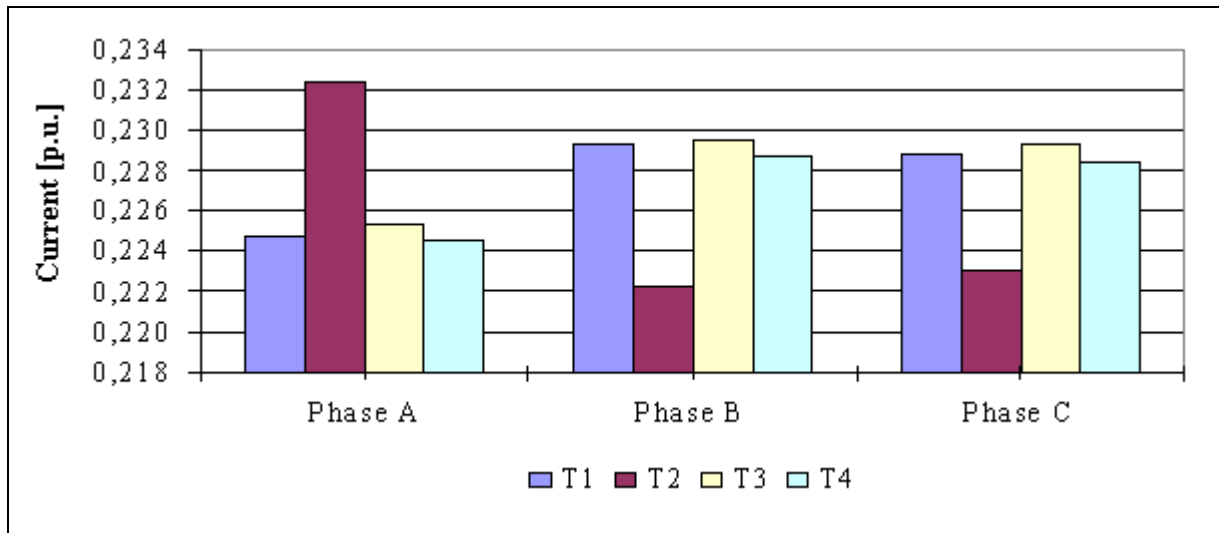


Figure 6.14 Current in p.u. per phase – load operation (86%) - 1 cut coil circuit B2

Fig. 6.15 presents the results for the generator operating at nominal load with one bypassed coil where it can be observed that the currents are unbalanced and also the terminal currents A2, B1, B3, B4, C1, C3 and C4 are higher than the rated phase current. At terminal A2, the phase current exceeds the nominal current by 1.84%. Even with this slightly higher current, the machine can operate at nominal load with 1 cut bar if the winding temperature is within the acceptable range (less than 130° C) (IEEE -ANSI C50.12).

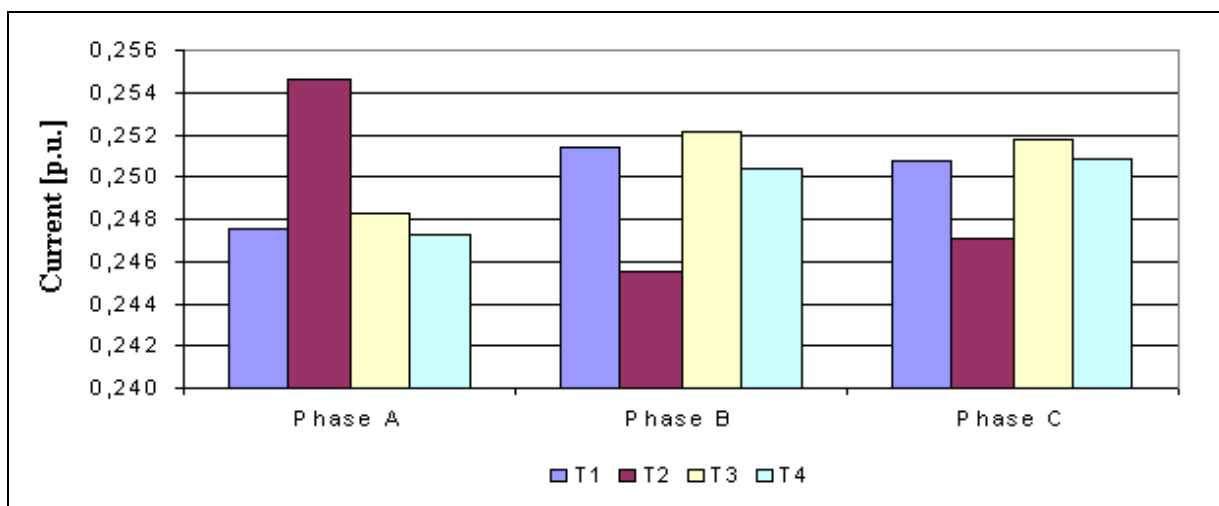


Figure 6.15 Current in p.u. per phase – load operation (100%) - 1 cut coil circuit B2



A comparison between experimental and simulation results of the machine operating at 86% of nominal load and with 1 cut coil is presented in Fig. 6.16. The two results are in good agreement, thus validating the accuracy of the model.

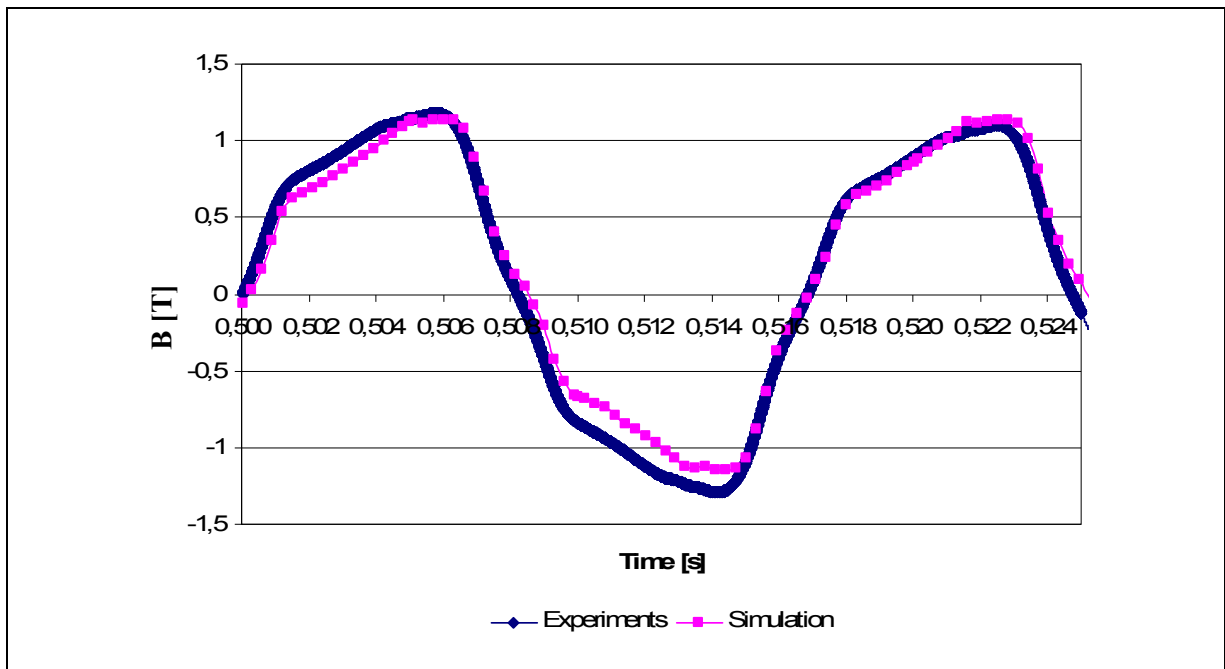


Figure 6.16 Comparison of experimental and simulation results 86% with 1 cut coil

### 6.2.2 Circuit current calculation with four bypassed coils

In this hypothetical case, electromagnetic simulation was carried out with four bypassed coils in the same phase and same circuit (B2). The computed currents in each circuit in this case are summarized in Fig. 6.17 and Fig. 6.18 for nominal load and at 86% of the nominal load respectively.

From Fig. 6.17 it can be observed that the machine cannot operate at rated load with this configuration and the machine needs to be de-rated because the computed currents are higher by 10.90% than the rated value at terminal A2.

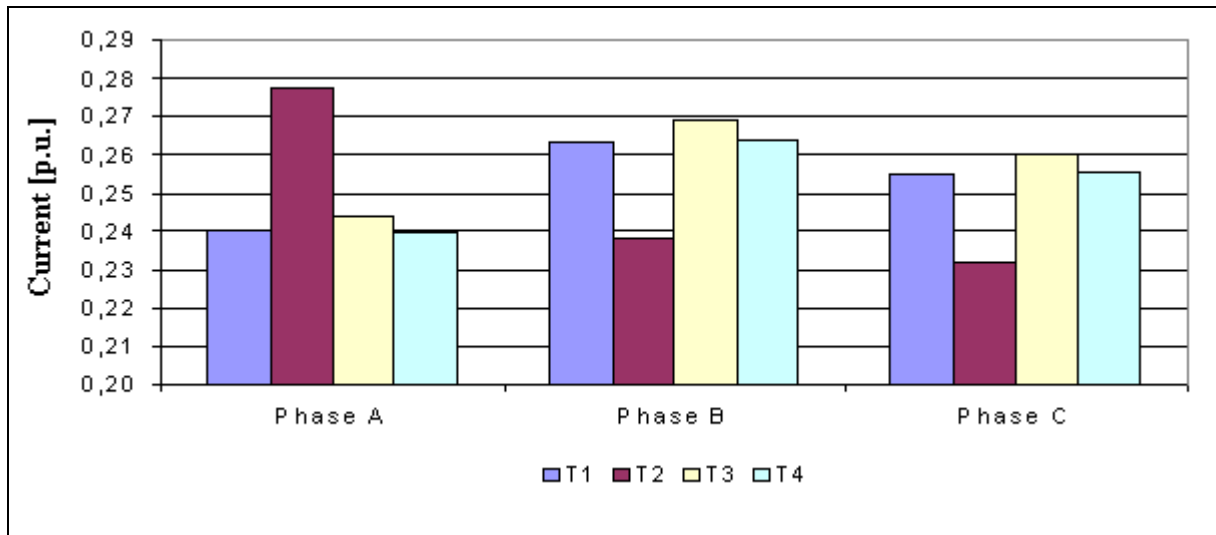


Figure 6.17 Current in p.u. per phase – load operation (100%) - 4 cut coils circuit B2

The simulation was performed at 86% of the nominal load and it can be seen that the current in the circuit A2 is subjected to a 10.11% increase when compared with the rated phase current. For terminal phase B3 and C3, the currents increase also by 13.67% and 4.84% respectively.

It is observed in this hypothetical case, if the machine has 4 bars cut at terminal B2, the machine needs to be further de-rated in order to operate.

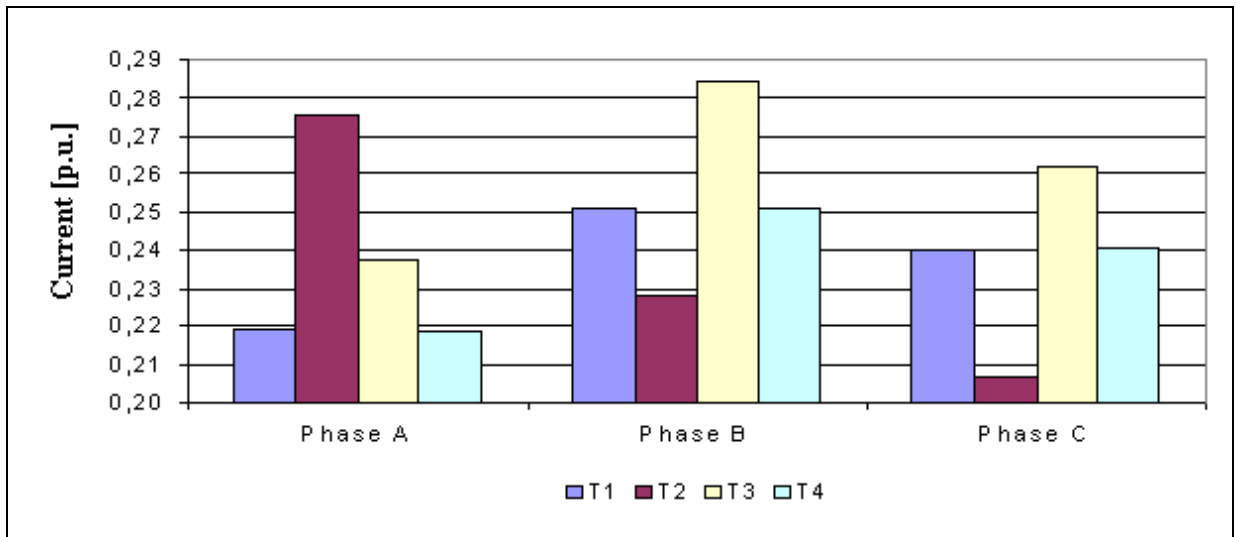


Figure 6.18 Current in p.u. per phase – load operation (86%) - 4 cut coils circuit B2

The computed magnetic flux distribution of the machine with 4 cut out coils in the stator is shown in Fig.6.19.

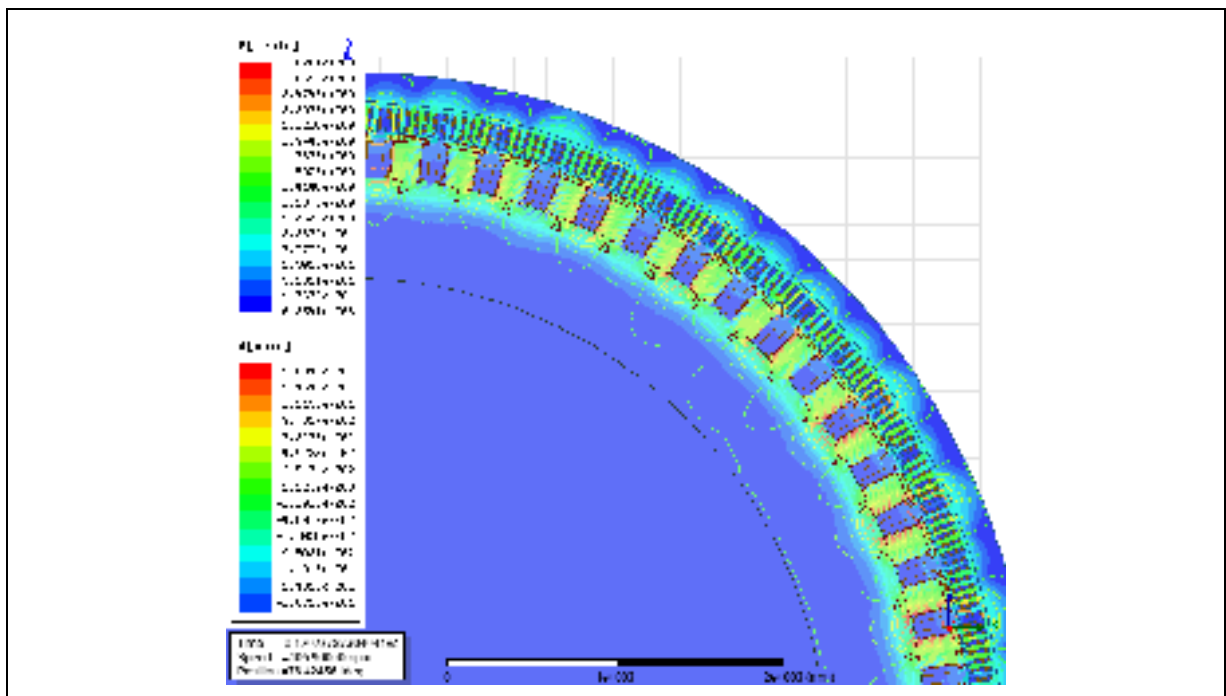


Figure 6.19 Magnetic flux density and flux lines distribution for an asymmetrical machine with 4 cut coils (86% of nominal load)

The computed damper bar losses vary as a function of the load condition and especially as a function of the number of cut bars. When there is an unbalance in the stator currents, one of the reactions is to increase the current in the damper bar and consequently the damper bar losses. The results of the four simulated cases are presented in Table 6.5.

Table 6.5 Damper bar losses – load operation (86% and 100%)

<b>Condition</b>	<b>86%</b>		<b>100%</b>	
	<b>Health</b>	<b>4 cut bar</b>	<b>Health</b>	<b>4 cut bar</b>
Damper bar loss	18	30	22	35

### 6.3 Conclusions

A finite element method was used to study two different machines in actual power under generation plants.

Manic 21 had the uprate study and it was concluded that the machine cannot operate at 170/188 MVA, but it can operate at 150/165 MVA during summer/winter seasons respectively. For that, the magnetic flux density distribution and the core loss distribution were analyzed when the machine operates at 14.5 kV and those results were combined with thermal and mechanical studies to determine the maximum operating conditions of the machine within the safe range.

A second set of finite element studies was done in order to compute the different circuit currents in a large hydro electrical machine with many different cases of bypassed stator coils. From this simulation, the following observations are made:

- for one coil by-passed in one circuit of one phase, the calculated currents at 86 % of rated load are in the acceptable range. In practice, if the temperature of the stator windings

(RTD) is within the acceptable limit of operation and monitored, it is not necessary to de-rate the unit with only one cut coil;

- in the case of 4 coils bypassed in one circuit and when the machine operates at 86% of nominal load, the increased current depends on the position of the removed coils; for this specific case, the increased current varies from -17.26% to 13.64%;
- it was found from this study that, depending on the position of cut out coil, the solution can vary and it should be analyzed carefully case by case;
- in the present study the operation is restricted to rated power factor at 0.8 lagging. Nevertheless, it can also be analysed for other operating points of the machine with leading power factor, if required.



## CONCLUSION

This work is of industrial nature where two studies were investigated: the first one considered the uprating of an existing hydro generator (122.6 MVA during summer season /150.7 MVA for winter) and the second study deals with the analysis of damaged 32.5 MVA hydro generator that operates with one stator cut coil.

Each hydro generator machine is a unique piece of equipment that was constructed according to specific parameters such as: river's water flow and waterfall. The size of the machine, the power output, the number of poles, the number of stator bars, and the winding sequence are different for each machine. Therefore, the results obtained in this work can only be extended to similar units of the same hydro electrical plant.

For the first study, finite element models of a salient pole synchronous generator were constructed and electromagnetic simulations were performed at nominal load. The simulation results were compared with experimental ones and the model was validated under the following considerations: the impact of the magnetic material characteristics on the total core loss; the influence of the changes of the mesh size on the core loss distribution; the effect of excitation current and the impact of the air gap length on the total core losses computation and also in the core loss distribution.

For the investigation on mesh density impact, three different meshes were compared. The first one presented is a refined mesh in the pole shoes and stator teeth; the second and the third were even much more refined. When different mesh densities were compared, the variation of the total computed magnetic core loss becomes negligible. However, if the aim of the simulation is the prediction of the core loss distribution profile or the current in the damper bar or the magnetic flux density on the air gap, the mesh density has to be selected depending on the purpose of the study.

Moreover, it was found that the derived total magnetic core losses at rated load condition varies by at least 25% depending of selected magnetic material in the stator and rotor.

The increase of the measured excitation current during the simulation for this specific machine can be reflected as a linear increase of the magnetic core losses in the stator and the rotor.

When the air gap length influence was studied, four different models were constructed and simulated using the measured excitation current. It was found that for the effective air gap of 14.93 mm, the computed core loss (678 kW) is comparable with the experimental value of 665 kW. In this brief study, it can be concluded that the accurate prediction of the local core loss is really dependent on the operating air gap shape.

The quantification of mesh density, magnetic material, excitation current and size on the air gap influence helped to conceive an appropriate electromagnetic model. The latter can henceforth be used by other researchers to perform thermal and mechanical analysis on the machine.

Later, the developed model was used to analyze open-circuit and short-circuit operation. Basically, three parameters were investigated: the magnetic flux density; induced damper bar currents and damper bar losses and stator and rotor core losses. Most of the obtained simulation results were in good agreement with the available experimental data collected from the field. For instance, the calculated total core losses (542 kW) at no-load rated voltage are comparable 547.6 kW measured during the experimental test.

For the same investigated set of parameters, the studied machine was also used to perform different load operations (71%, 100% and 123%). In addition, the temperature of the damper bars were analytically computed and was successfully compared with experimental results, which enhance the confidence in the developed model.



After the model was validated, it was used to the extrapolation study. Therefore, the generator was considered for uprate and the core loss distribution was carefully studied and new power output (150/165 MVA) was established.

The accurate prediction of the core losses distribution in different parts of the generator allowed determining the temperature limits for each part of the existing generators. Therefore, increasing the electric power production with limited financial investment by uprating existing hydro generators becomes a promising option.

For the second industrial application study, another synchronous salient pole hydro generator was investigated. In this case, this machine operates with one stator cut coil and the intention was not to increase the output power; but to make a diagnostic of the actual condition of the generator. When a damaged machine is modeled, it becomes necessary to simulate the entire machine because there won't be magnetic symmetry. The FE model was constructed for the damaged machine and electromagnetic simulations were performed at load and open-circuit conditions. Simulating the entire machine has a big impact on the simulation time and on the size of the data file to be processed.

The first part of the study was based on the stator current at load operation. Through simulation it was shown that with 86% of nominal load, the stator current doesn't overpass the safety limits so the insulation of the bars won't be compromised.

Besides, the magnetic flux density of the air gap was also investigated as a function of the time by simulation as well as by experimentation. Both results were compared for 86% nominal load and are in a good agreement, thus validating the accuracy of the model.

The third part of the study was based on the core losses at open-circuit. The results obtained by simulation (155 kW) were compared with the measured value of 176 kW. The observed

difference was due to the fact that the 2D model doesn't take into account the induced losses in the end plates and some additional losses that can only be computed in a 3D model.

Finally the stator current of the machine was studied with more than one cut coil only as a hypothetic case. The problem of a machine operating like with one or more cut stator coils is that the life expectancy can be reduced if the suitable operating condition is not considered.

## **FUTURE WORK AND IMPROVEMENT**

In order to improve the developed model further research efforts are necessary such as:

- develop of a complete set of models taking into account the mechanical effects of the air gap shape such as ellipticity and eccentricity and the impact of those on the magnetic losses;
- elaborate a 3D model to take into account the induced losses in the end plates;
- consider the rotational loss in the stator core for more accurate core loss computational results;
- perform an economic analysis that consider the life reduction estimated of the generator caused by the output power increase and taking into account the associated additional revenue produced by the increase of the power output as computed by the proposed model;
- include other faults into the complete 2D model such as: damper bar faults;
- study the influence of the stator coil position when removing one or more and also the impact of removing completely one stator circuit in arbitrary phase of the generator.

## ANNEX I

### Kh and Kc variable coefficients

Table 6.6 Stator  $K_h$  coefficient

<b>B</b>	<b>K<sub>h</sub></b>
0,1	220,06
0,2	176,72
0,3	159,02
0,5	137,19
0,5	135,88
0,6	128,15
0,7	107,03
0,8	105,55
0,9	116,86
1	105,87
1,1	95,26
1,2	99,31
1,3	96,12
1,5	96,7
1,5	106,65
1,6	105,3
1,7	100,33

Table 6.7 Stator  $K_c$  coefficient

		Frequency															
		60	120	180	250	300	360	520	580	550	600	660	720	780	850	900	960
<b>B</b>	<b>0,1</b>	1,70	1,55	1,35	1,25	1,13	1,15	1,15	1,08	1,03	0,99	1,06	1,02	1,12	1,17	1,35	1,60
	<b>0,2</b>	1,70	1,39	1,28	1,20	1,15	1,09	1,09	1,05	1,00	1,00	1,05	1,05	1,11	1,15	1,32	1,55
	<b>0,3</b>	1,32	1,33	1,22	1,15	1,11	1,08	1,07	1,05	0,99	1,05	1,00	1,02	1,09	1,20	1,59	1,55
	<b>0,5</b>	1,27	1,26	1,18	1,13	1,08	1,03	1,05	0,98	0,95	0,98	1,00	1,05	1,07	1,55	1,59	1,51
	<b>0,5</b>	1,25	1,23	1,15	1,10	1,05	1,00	0,99	0,99	0,95	0,95	0,99	1,01	1,59	1,55	1,55	1,55
	<b>0,6</b>	1,20	1,17	1,12	1,07	1,05	0,97	0,96	0,95	0,93	0,91	0,98	1,55	1,59	1,36	1,51	1,52
	<b>0,7</b>	1,16	1,15	1,08	1,05	0,98	0,96	0,95	0,91	0,90	0,93	1,53	1,55	1,39	1,29	1,39	1,59
	<b>0,8</b>	1,13	1,11	1,06	1,02	0,97	0,95	0,95	0,92	0,88	1,59	1,53	1,37	1,28	1,29	1,39	1,55
	<b>0,9</b>	1,15	1,09	1,05	1,00	0,95	0,92	0,90	0,90	1,51	1,59	1,36	1,29	1,31	1,32	1,55	1,69
	<b>1,0</b>	1,08	1,07	1,01	0,97	0,90	0,88	0,87	1,33	1,51	1,53	1,31	1,23	1,23	1,28	1,37	1,57
	<b>1,1</b>	1,02	1,05	0,99	0,93	0,89	0,88	1,56	1,33	1,37	1,38	1,25	1,25	1,22	1,32	1,58	2,05
	<b>1,2</b>	1,00	1,03	0,98	0,92	0,89	1,59	1,56	1,35	1,32	1,28	1,22	1,18	1,17	1,25	1,56	2,02
	<b>1,3</b>	1,00	1,00	0,96	0,89	1,29	1,59	1,51	1,29	1,25	1,19	1,16	1,18	1,25	1,33	1,59	1,99
	<b>1,5</b>	0,97	0,99	0,95	1,29	1,29	1,50	1,35	1,20	1,20	1,20	1,17	1,18	1,20	1,28	1,66	1,87
	<b>1,5</b>	0,95	0,98	1,38	1,29	1,30	1,30	1,25	1,16	1,15	1,13	1,11	1,16	1,21	1,26	1,65	1,73
	<b>1,6</b>	0,93	1,55	1,38	1,25	1,23	1,25	1,20	1,09	1,10	1,12	1,11	1,12	1,20	1,26	1,63	1,82
	<b>1,7</b>	1,55	1,55	1,30	1,18	1,18	1,19	1,13	1,07	1,05	1,07	1,09	1,13	1,19	1,21	1,62	1,82

## BIBLIOGRAPHY

- Aguiar, A.B.M., Merkhoulf, A., Hudon, C., Al-Haddad, K. 2014. Influence of the variation of the input parameters on the simulation results of a large hydrogenerator. IEEE Transactions on Industry Applications, Vol. 50, No. 1, p. 261-268.
- Aguiar, A.B.M., Merkhoulf, A., Al-Haddad, K. 2013a. *A new approach for computation of magnetic core losses in large hydro electrical generator*. 39th Annual Conference on IEEE Industrial Electronics Society - IECON 2013, Vienne, Austria, p. 2506-2511.
- Aguiar, A.B.M., Merkhoulf, A., Al-Haddad, K. 2013b. *Open-circuit and short-circuit core losses computation in a large hydro generator*. 39th Annual Conference on IEEE Industrial Electronics Society - IECON 2013, Vienne, Austria.
- Aguiar, A.B.M., Merkhoulf, A., Al-Haddad, K. 2013c. *Cut out bars fem simulation of large hydro generator*. Nineteenth COMPUMAG Conference on the Computation of Electromagnetic Fields, Budapest, Hungary, Jul. 2013c.
- Aguiar, A.B.M., Merkhoulf, A., Hudon, C., Al-Haddad, K. 2012a. *Investigation of the electromagnetic simulation results variation of a hydro electrical generator*. 38<sup>th</sup> Annual Conference on IEEE Industrial Electronics Society - IECON 2012, Montreal, Canada, p. 5370-5375.
- Aguiar, A.B.M., Merkhoulf, A., Al-Haddad, K. 2012b. *Influence of the airgap length on the magnetic core loss in large hydro generator*. XX<sup>th</sup> International Conference on Electric Machines, ICEM, Marseille, France, p. 328-332.
- Aguiar, A.B.M., Merkhoulf, A., Bélec, M., Hudon, C., Al-Haddad, K. 2011a. *Large hydro electrical generator modeling considering different magnetic materials*. 10<sup>th</sup> International conference on modeling and simulation of electric machines, converters and systems - Electrimacs Conference, Cergy-Pontoise, France, p.1-6.
- Aguiar, A.B.M., Merkhoulf, A., Al-Haddad, K., Hudon, C. 2011b. *Electromagnetic modelling of existing large hydro generator*. International Electric Machines and Drives Conference, IEMDC, Niagara Falls, Canada, p. 389-393.
- Agrawal L.K., Tripathi, S.B.L. 2011. *Study of fault detecting techniques in electrical machines*. VSRD Int. J. Electr. Electron. Commun. Eng., vol. 1, no. 8, p. 478–489.
- Aktik, C. 2010. *Conception et fabrication d'un capteur CMOS à effet-Hall pour la mesure du vecteur de Poynting*. Report IREQ Project – Université de Sherbrooke, 13 p.

- Alger, P. L. 1970. *Induction Machines, Their Behavior and uses*, New York: Gordon and Breach Sciences, 518 p.
- Amaya, M., Costa, A., Palacios, J. and Cadavid, W. 2003. *Identification of the synchronous machine parameters by the simulation of time domain tests using finite-elements method*, IEEE Int. Electr. Mach. Drives Conf. 2003. IEMDC'03, p. 556–560.
- Andersson, U. 2001. *Time-Domain Methods for the Maxwell equations*. PhD Thesis. Royal Institute of Technology, Department of Numerical Analysis and Computer Science, 160 p.
- Andrade Filho, M.G. 1995. *Uma abordagem numérica para problemas de valor de contorno de Dirichlet envolvendo equação de Helmholtz*. Ph.D. Thesis. Universidade Estadual de Campinas, UNICAMP, Campinas, Brazil, 119 p.
- Aoulkadi, M. 2011. *Experimental Determination of stray load losses in cage induction machines*. Ph.D. Thesis, Technischen Universität Darmstadt, 324 p.
- Arshad, W. M., Ryckebusch, T., Magnussen, F., Lendenmann, H., Eriksson, B., Soulard, J. and Malmros, B. 2007. *Incorporating lamination processing and component manufacturing in electrical machine design tools*, Conference Record of the 2007 IEEE 52<sup>nd</sup> IAS Annual Meeting Industry Applications Conference, p. 94-102.
- Awad, M.L. 1999. *Modeling of synchronous machines for systems studies*, PhD Thesis, University of Toronto, 144 p.
- Bastos, J.P., Sadowski, N. 2003. *Electromagnetic modeling by finite element methods*. Marcel Dekker, Inc, 510 p.
- Benderskaya, G. 2007. *Numerical Methods for transient field-circuit coupled simulations based on the finite integration technique and a mixed circuit formulation*. Ph.D Thesis, Universität Darmstadt, 149 p.
- Bertalanic, Z. Pavlica, M., Malijkovic, Z. 2010. *Analysis of hydro-generator's losses determined by calorimetric method*. XIX International Conference on Electrical Machines, ICEM, Rome, p. 1-6.
- Bertalanic, Z., Malijkovic, Z., Pavlica, M. 2008. *Measurement of hydro-generator's end region temperature*, XVIII International Conference on Electrical Machines, p. 1-4.
- Bertotti, G, Fiorillo, F., Soardo, G.P. 1987. *Dependence of power losses on peak magnetization and magnetization frequency in grain-oriented and non-oriented 3% SiFe*. IEEE Transactions on Magnetics, Vol. MAG-23, No.5, p.3520-3522.

- Bertotti, G., Pasquale, M. 1992. *Physical interpretation of induction and frequency dependence of power losses in soft magnetic materials*. IEEE Transactions on Magnetics, Vol.28, No.5, p.2787-2789.
- Bertotti, G., Fiorillo, F., Pasquale, M. 1993. *Measurement and prediction of dynamic loop shapes and power losses in soft magnetic materials*. IEEE Transactions on Magnetics, Vol.29, No.6, p.3596-3598.
- Blecken, W-D. 1997. *Applying new technology in the upgrading or uprating of generators*, Hydropower Dams, no. 5, p. 26–32.
- Boldea, I. 2005. *Synchronous generators*. Taylor & Francis, 448 p.
- Bortoni E. C. and Jardini, J. A. 2005. *A Standstill frequency response method for large salient pole synchronous machines*, IEEE Transactions Energy Conversion., vol. 19, no. 5, p. 687–691.
- Bottauscio, O., Canova, a., Chiampi, M., & Repetto, M. 2002. *Iron losses in electrical machines: influence of different material models*, IEEE Transactions On Magnetics, VOL. 38, NO.2, p. 805–808.
- Bozorth R.M. 1951. *Ferromagnetism*. New York, D. Van Nostrand, 968 p.
- Brighty, W.B., Brown, C.A., Kelch, E.J., Rhudy, R.G., Snively, H.D. 1987. *EPRI EL-5983 - Synchronous machine operation with cutout coils*. Electric Power Research Institute, Research Project 2330-2, Final Report.
- Brune, K., Seinsch, H.O. 2006. *Performance of three-phase motors after disconnecting damaged coils*, Springer-Verlag, Vol. 89, No. 5, p.271-283.
- Calvert, J.F. 1938. *Amplitudes of magnetomotive force harmonics for fractional slot windings – I*. In Transactions of the American Institute of Electrical Engineers, Vol. 57, Issue 12, p. 777-785.
- CERI. 2008. *World energy: the past and possible future*. Canadian Energy Institute, 2008. Available at: [http://www.cna.ca/english/pdf/studies/ceri/CNA\\_CERI07\\_EN.pdf](http://www.cna.ca/english/pdf/studies/ceri/CNA_CERI07_EN.pdf). Accessed in: April 6, 2010.
- Chaaban, M., Leduc, J., Hudon, C., and Nguyen, D.N. 2008. *Thermal behaviour of large hydro-generator*. In International Symposium on Transport Phenomena and Dynamic of Rotating Machinery, p. 1-8.
- Chari M.V.K., Silvester, P.P. 1980. *Finite elements in electrical and magnetic field problems*. John Wiley & Sons, 232 p.

- Chen, Y. and Pillay, P. 2002. *An improved formula for lamination core loss calculations in machines operating with high frequency and high flux density excitation*, Conf. Rec. 37th IAS Annual Meeting, vol. 2, p. 759–766.
- Chmelicek, P. *Synchronous generator reactance prediction using FE analysis*, Master Dissertation, Brno University of Technology, 2010.
- Chow, P., Nobes, R., Kubota, T., and Namiki, T. 2007. *Advanced methods for electromagnetic simulation*. Fujitsu Sci. Tech. Journal, Vol. 53, No. 5, p. 525-531.
- Clyde, V., Maughan, P.E. 2004. *Root cause diagnostics of generator service failures*, Proc IEEE International Symposium on Electrical Insulation, p. 154-162.
- Concordia, C. 1951. *Synchronous machines: Theory and performance*. John Wiley & Sons, 224 p.
- Davat, B., Ren, Z., Lajoie-Mazenc, M. 1985. *The movement in the field modeling*, IEEE Transactions on Magnetics, Vol.. 21, No. 6, p. 2296-2298.
- DeHaan, J., 1999. *Electrical unbalance assessment of a hydroelectric generator with bypassed stator coils*, in International Conference Electric Machines and Drives, p. 803–805.
- Dlala, E. A. 2008. *Magnetodynamic vector hysteresis models for steel laminations of rotating electrical machines*, PhD Thesis, Helsinki University of Technology, 97 p.
- Dlala, E. 2009. *Comparison of models for estimating magnetic core losses in electrical machines using the finite-element method*. IEEE Transactions Magnetics, vol. 55, no. 2, p. 716–725.
- Dunlop, C.J. 2008. *Modeling magnetic core loss for sinusoidal waveforms*. Master of Science, Massachusetts Institute of technology, MIT, 110 p.
- Fam, W.Z. 1971a. *Direct measurement of the fundamental and harmonic tooth-ripple losses in solid poles. part I: theory*. In IEEE Transaction on Power Apparatus and Systems, Vol. PAS-90, No. 2, p. 597-601.
- Fam, W.Z. 1971b. *Direct Measurement of the fundamental and harmonic tooth-ripple losses in solid poles. part II: experimental investigation*. In IEEE Transactions on Power Apparatus and Systems, Vol. PAS-90, No. 2, p. 602-610.
- Fam, W.Z. 1988. *Poynting vector probe for measuring power at extremely low power factor*. In IEE Proceedings, Vol. 135, Pt. A, No. 6, July, p. 385-389.



- Fan, Z., Han, L., Zhou, G., Hou, X., and Liao, Y. 2008. *Loss and heat computations of damper bars in large tubular hydro-generator*, in International Conference Electric Machines and Systems, p. 525–529.
- Feiyang, H., Weili, L., and Yu, Z. 2010. *Calculation of damper winding loss and influence on large hydro-generator temperature*, 2010 International Conference on Computer Application and System Modeling (ICCASM 2010), vol. 5, p. 365–369.
- Fuchs, E., Masoum, M.A.S. 2008. *Power quality in power systems and electrical machines*. Elsevier, 664 p.
- Galbraith, A S G. 2005. *Estimation of synchronous generator parameters using time-domain Responses*. Master of Science, University of Stellenbosch, 170 p.
- Gamblin R. and Solomon, B. 2002. *Experience with hydrogenerator core testing and repair*, in Iris Rotating Machine Conference, p. 1–5.
- Gordon C., and Barton, T.H. 1995. *Reluctance distribution modeling of saturated salient pole synchronous machines*. IEEE Transactions Energy Convers., vol. 9, no. 2, p. 323–329.
- Guedes, M.A.B.V. 1983. *Métodos para análise do campo magnético das máquinas elétricas*. PhD Thesis. Faculdade de Engenharia, Universidade do Porto, 315 p.
- Guedes, M.V. 1996. *O alternador síncrono trifásico – modelização*. Class Notes, 1996. Available in: [http://paginas.fe.up.pt/maquel/AD/AST\\_model.pdf](http://paginas.fe.up.pt/maquel/AD/AST_model.pdf). Accessed on: April 1<sup>st</sup>, 2010.
- Guo, Y., Zhu, J.G., Zhong, J., Lu, H., Jin, J.X. 2008. *Measurement and modeling of rotational core losses of soft magnetic materials used in electrical machines: a review*. IEEE Transactions on Magnetics, Vol.55, No.2, p. 279–291.
- Han S-H, Jahns TM, Zhu ZQ. 2010. *Analysis of rotor core eddy-current losses in interior permanent-magnet synchronous machines*. IEEE Transactions Ind. Appl., vol. 56, no. 1, p. 196–205.
- Hawa, Charbel Al. 2003. *Methods for determination of the excitation current in synchronous generators*. Technical report. Vol. 100, Sweden, 38 p.
- Hill, J. 1996. *Efficient Implementation of mesh generation and FDTD simulation of electromagnetic fields*. Master's Dissertation. Worcester Polytechnic Institute, 324 p.
- Hiramatsu, D., Tokomasu, T. Fujita, M. Kakiuchi, M., Otaka, T., Sato, O., Nagasaka, K. 2007. *Estimation of rotor surface losses in small-to-medium cylindrical synchronous machine*. In IEEE Power Engineering Society General Meeting, p.1–8.

- Hudon C, Bélec M, Lévesque M. 2008. *Study of slot partial discharges in air-cooled generators*, *IEEE Transactions Dielectr. Electr. Insul.*, vol. 15, no. 6, p. 1675–1690.
- Hudon, C., Merkhouf, A., Chaaban., M. 2010a. *Consideration of loss distribution to evaluate the hotspot temperature when up-rating generators*. Conference Record of the 2010 IEEE International Symposium on Electrical Insulation (ISEI), p. 1-5.
- Hudon, C., Merkhouf, A., Chaaban., M., Bélanger, S., Torriano, F., Leduc, J., Lafleur F., Morissette, J. F., Millet, C., Gagné, M. 2010b. *Hydro-generator multi-physic modeling*. *European Journal of Electrical Engineering*, Vol13/5-6 p.563-589.
- Hudon, C., Bélanger, S., Chaaban, M., Merkhouf, A., Leduc, J., Lafleur F., Torriano, F., Morissette, J. F., Bélec, M. 2012. *Augmentation de puissance de l'alternateur 21 de la centrale Manic-2*. Diffusion Hydro-Québec, Report, 263 p.
- Iamamura, B.A.T. 2011. *Contribution a la détection de défauts dans les rotors des turboalternateurs*, PhD Thesis, Université Lille 1, 196 p.
- IEEE Std. 115. 2010. *Guide, Test procedures for synchronous machines*, IEEE Standard 115-2010, 208 p.
- Ionel D.M., Popescu M., Dellinger S.J., Miller T.J.E., Heideman R.J., McGilp M.I. 2006. *On the variation with flux and frequency of the core loss coefficients in electrical machines*, *IEEE Transactions on Industry Applications*, vol. 52, no. 3, p. 658– 667.
- Ionel, D. M., Popescu, M., McGilp, M. I., Miller, T. J. E., Dellinger, S. J., Heideman, R. J. 2007. *Computation of core losses in electrical machines using improved models for laminated steel*, *IEEE Transactions Ind. Appl.*, Vol. 43, no. 6, p. 1554–1564.
- Jiles, D. C., Atherton, D.L. 1983. *Ferromagnetic hysteresis*, *IEEE Transactions Magnetics*, vol. MAG-19, p. 2183–2185.
- Jiles, D.C., Thoeke, J.B., Devine, M.K. 1992. *Numerical determination of hysteresis parameters for the modeling of magnetic properties using the theory of ferromagnetic hysteresis*, *IEEE Transactions Magnetics*, vol. 28, no. 1, p. 27–35.
- Kanerva, S. 2005. *Simulation of electrical machines, circuits and control systems using finite element*. Ph.D. Thesis. Helsinki University, 94 p.
- Karmaker, H.C. 1982. *Open circuit tooth ripple losses in slotted laminated poles of electrical machines with amortisseur windings*. In *IEEE Transactions on Power Apparatus and Systems*, vol. PAS-101, No. 5, p. 1122-1128.

- Karmaker H., Mi, C. 2005. *Improving the starting performance of large salient- pole synchronous machines*, IEEE Transactions on Magnetics, Vol.50, No. 5, p. 1920-1928.
- Karmaker, H.C., Knight, A. M. 2005. *Investigation and simulation of fields in large salient-pole synchronous machines with skewed stator slots*. In IEEE Transactions on Energy Conversion, vol. 20, No. 3, p. 605-610.
- Kaukonen, J. 1999. *Salient pole synchronous machine modelling in an industrial direct torque controlled drive application*, PhD Thesis, Lappeenranta University of Technology, 150 p.
- Keller, S., Xuan, M., Simond, J.J. 2006. *Computation of the no-load voltage waveform of laminated salient-pole synchronous generators*. IEEE Transactions on Industrial Applications, vol. 52, no. 3, p. 681–687.
- Keller, S., Xuan, M., Simond, J.J., Schwery, A. 2007. *Large low-speed hydro-generators – unbalanced magnetic pulls and additional damper losses in eccentricity conditions*, IET Electr. Power Appl., vol. 1, no. 5, p. 657–665.
- Kim, C.E., Sykulski, J.K. 2002. *Harmonic analysis of output voltage in synchronous generator using finite-element method taking account of the movement*, IEEE Transactions on Magnetics, Vol.38, No.2, March, p. 1249-1252.
- Kladas, A., Razek, A. 1988. *Eddy current currents modeling in synchronous machines during starting accounting for the nature of damper en connections*, IEEE Transactions Magnetics, Vol. 25, p. 186-186.
- Knight, A.M., Karmaker, H., Weeber. K. 2011. *Use of a permeance model to predict force harmonic components and damper winding effects in salient pole synchronous machines*. Proceedings of the International Electric Machines and Drives Conference, p.179-185.
- Knight, A.M., Troitskaia, S., Stranges, N., Merkhoulf. A. 2009a. *Analysis of large synchronous machines with axial skew, part 1: flux density and open-circuit voltage harmonics*. IET Electric Power Applications, Vol. 3 Issue 5, p. 389-397.
- Knight, A.M., Troitskaia, S., Stranges, N., Merkhoulf. A. 2009b. *Analysis of large synchronous machines with axial skew, part 2: inter-bar resistance, skew and losses*. IET Electric Power Applications, Vol. 3 Issue 5, p. 398-406.
- Koncar. 2013. *In Hydro power plant refurbishment*. Available at: <http://www.koncar-ket.hr/en/documents/12hydro--power-plant.pdf>. Accessed at: September 1<sup>st</sup>, 2013.

- Krause, P., Wasynczuk, O., Sudhoff, S.D. 2002. *Analysis of electrical machinery and drive systems*. IEEE Press on Power Engineering, Second Edition, 613 p.
- Krings, A., Soulard, J. 2010. *Overview and comparison of iron loss models for electrical machines*. Journal of Electrical Engineering, ISSN 1582-4594, Vol. 10, No. 3, p. 162-169.
- Krings, A., Nategh, S., Stening, A., Grop, H., Wallmark, O., and Soulard, J. 2012. *Measurement and modeling of iron losses in electrical machines*. In 5th International Conference Magnetism and Metallurgy WMM2012, p. 101–119.
- Kuczmann, M. 2009. *Potential formulations in magnetics applying the finite element method*. Lecture Notes, University Győr, Hungary, 2009.
- Lahres, S. 2007. *Automated numerical analyses for the design of electrical machines*. HyPower, no. 15, p. 13–19.
- Laldin, O., Dlala, E., Arkkio, A. 2011. *Circuit models for predicting core losses in the stator and rotor of a caged induction machine with sinusoidal supplies*. IEEE Transaction on Magnetism, Vol.57, No.5.
- Lenz, J. E. 1990. *A Review of magnetic sensors*, Proceedings of the IEEE, vol. 78, no. 6, p. 973–989.
- Lee, P., Kuo, K., Wu, C., Wong, Z., Yen, J., 2011. *Prediction of iron losses using the modified Steinmetz equation under the sinusoidal waveform*. Proceedings of 2011 8<sup>th</sup> Asian Control Conference, p. 579–585.
- Lewin, Walter. 2002. *8.02 Electricity and magnetism*. (Massachusetts Institute of Technology: MIT OpenCourseWare), <http://ocw.mit.edu> (Accessed from March to June, 2013). License: Creative Commons BY-NC-SA, Spring 2002.
- Lin, R. 2010. *Electromagnetic and mechanical finite analysis of eng region of large-sized three-phase squirrel-cage induction machines*. Ph.D Thesis. Aalto University, 74 p.
- Lin, D., Zhou, P., and Cendes, Z.J. 2005. *A dynamic core loss model for soft ferromagnetic and power ferrite materials in transient finite element analysis*, In IEEE Transaction on Magnetic, Vol. 40, NO.2, p. 1318-1321.
- Lin, D., Zhou, P., Chen, Q. M., 2008. *The effects of steel lamination core losses on transient magnetic fields using T-Ω method*. IEEE Vehicle Power and Propulsion Conference, no. 1, p. 1–4.

- Li, J., Abdallah, T., Sullivan, C.R. 2001. *Improved calculation of core loss with nonsinusoidal waveforms*. Thirty-Sixth IAS Annual Meeting - Conference Record IEEE Ind. Appl. Conf., vol. 05, p. 2203–2210.
- Matsuki, J., Katagi, T., Okada, T. 1995. *Slot ripples in the damper windings of a salient-pole synchronous generator*. In IEEE Transactions on Energy Conversion, Vol.9, No.1, pg. 126-135.
- Mayergoyz, I.D. 1986. *Mathematical models of hysteresis (invited)*, IEEE Transactions Magnetics, vol. MAG-22, no. 5, p. 603–608.
- Meunier G. 2010. *The finite element method for electromagnetic modeling*, John Wiley & Sons, 832 p.
- Merkhouf, A., Aguiar, A.B.M., Chaaban, M., Hudon, C., Al-Haddad, K. 2013. *Damper windings performance evaluation in large hydro electrical generators* In: Nineteenth COMPUMAG Conference on the Computation of Electromagnetic Fields, Budapest, Hungary.
- Merkhouf, A., Hudon, C., Guillot, E., Aguiar, A.B.M., Al-Haddad, K. 2012. *Electromagnetic loss computation in large hydroelectrical generator using different existing models*. In: XX<sup>th</sup> International Conference on Electric Machines, ICEM, Marseille, France, p. 238-252.
- Merkhouf, A., Hudon, C., Bélec, M., Guillot, E., Aguiar, A.B.M., Al-Haddad, K. 2011. *Electromagnetic loss computation in existing large hydroelectric generators*. In: International Electric Machines and Drives Conference, IEMDC, Niagara Falls, Canada, p. 113-118.
- Merkhouf, A. 2002. *Prediction of electrical parameter of the hydro-generators with using finite element method*. In 7<sup>th</sup> International Conference on Modeling and Simulation of Electric Machines, Converters and Systems (Electrimacs).
- Merkhouf, A. 2003. *Optimization of the electromagnetic devices using genetic algorithm method*. In Canadian Conference on Electrical and Computer Engineering, IEEE Canada, Vol.1, p.271-274.
- Merkhouf, A., Doyon, P., Upadhyay, S. 2008. *Variable frequency transformer – concept and electromagnetic design evaluation*. In IEEE Transactions on Energy Conversion, Vol.23, No.5, p. 989-996.
- Merkhouf, A., Karmaker, H., McLaren, D., Ferguson, J., Boueri, B., Benchaita, L. Li, Y. 2005. *Modern tools and practices for large hydro generator design*. In Hydropower & Dams, Issue 1, p. 64-67.

- Moore, W.J.M., Love, G., Raftis, F.A. 1975. *Measurement of short circuit load losses in large three phase power transformer using an alternating current comparator bridge*. In IEEE Transaction on Power Apparatus and Systems, Vol. PAS-95, No. 6, p. 2074-2076.
- J. Mühlethaler, J. Biela, J. W. Kolar, and A. Ecklebe, 2012. *Improved core-loss calculation for magnetic components employed in power electronic systems*, IEEE Transactions on Power Electronics, vol. 27, no. 2, p. 965–973.
- Nabeta, S.I., Foggia, A., Coulomb, J.L., Reyne, G. 1995. *A non-linear time-stepped finite-element simulation of a symmetrical short-circuit in synchronous machine*. In IEEE Transaction on Magnetics, Vol. 31, No. 3, p. 2040-2043.
- Nandi, S., Ahmed, S., Toliyat, H.A. 2001. *Detection of rotor slot and other eccentricity related harmonics in a three phase induction motor with different rotor cages*, IEEE Transactions Energy Convers., vol. 16, no. 3, p. 253–260.
- Negrea, M.D. 2006. *Electromagnetic flux monitoring for detecting faults in electrical machines*. Ph.D. Thesis. Helsinki University of Technology, 142 p.
- Païement, B., Vallerand, D., Deguise, E. 2002. *Centrale Manic 2 – Essais de réception de l'alternateur A24 après réfection*. Report Direction Expertise de Centrales – Essais Spéciaux de Production. Hydro Québec, 146 p.
- Petite, P. 2008. *Numerically efficient finite element simulation of voltage driven solid rotor synchronous machines*. Master of Science, Pennsylvania State University, 41 p.
- Petrichenko, D. 2007. *Contribution à la modélisation et à la conception optimale des turbo-alternateurs de faible puissance*. Ph.D Thesis, École Centrale de Lille, 159 p.
- Pirou, F., Tounzi, A., Merkhoul, A. 2014. *Séminaire de recherche : Modélisation élément finis de système électromagnétiques basse fréquence*. Lecture Notes, ÉTS and Université Lille 1.
- Pluta, W. A. 2011. *Core loss models in the electrical steel sheets with different orientation*. Przegląd Elektrotechniczny, ISSN 0033-2097, R.87, Nr 9b, p.37-52.
- Preston, T.W., Reece, A.B. and Sangha P.S. 1988. *Induction motor analysis by time-stepping techniques*, IEEE Transactions on Magnetics, Vol.24, no.1, p.471-474.
- Pyrhönen, J., Jokinen, T., Hrabovcová, V. 2009. *Design of rotational electrical machines*. Wiley-Press, 538 p.
- Rajput, R. K., 2006. *A textbook of electrical machines*. Laximi Publishing, 571 p.

- Ranlöf, M., Wolfbrandt, A., Lindholm, J., Lundin, U. 2009. *Core loss prediction in large hydropower generators: influence of rotational fields*. In IEEE Transaction on Magnetics, Vol. 55, No. 8, p. 3200-3206.
- Ranlöf, M., Perers, R., Lundin, U. 2010. *On permeance modeling of large hydrogenerators with application to voltage harmonics prediction*. In IEEE Transaction on Energy Conversion, Vol. 25, No.5, p. 1179-1186.
- Ranlöf, M. 2011. *Electromagnetic analysis of hydroelectric generators*. Ph.D. Thesis, 120 p.
- Rasilo, P. 2012. *Finite-Element Modeling and calorimetric measurement of core losses in frequency-converter-supplied synchronous machines*. PhD Thesis, Aalto University, 102 p.
- Reinert, J., Brockmeyer, A., De Doncker, R.W.A.A. 2001. *Calculation of losses in ferro- and ferrimagnetic materials based on the modified Steinmetz equation*, IEEE Transactions on Industry Applications, vol. 37, no. 5, p. 1055–1061.
- Rhudy, R.G., Snively, H.D., White, J.C. 1988. *Performance of synchronous machine operating with unbalanced armature windings*. IEEE Transactions on Energy Conversion, Vol.3, No. 2, p. 391-397.
- Roches, G. V. 2011. *Frequency and time simulation of squeal instabilities: application to the design of industrial automotive brakes*. PhD Thesis, École Centrale des Arts et Manufactures, 236 p.
- Rodrigues Filho, B.A. 2007. *Estudo da convergência no método de elementos finitos aplicado a dispositivos eletromagnéticos nao lineares*, Master Dissertation, University of Sao Paulo, 153 p.
- Salminen, P. 2005. *Fractional slot permeance magnet synchronous motors for low speed applications*. Ph.D. Thesis, Lappeenranta University of Technology, 152 p.
- Sawatani, K., Sano, K., Ootake, S. 1986. *Stator frame deformation problem in large diameter hydro-generator*, IEEE Transactions Energy Convers., vol. EC-1, no. 1, p. 33–38.
- Shanel, M., Pickering, S.J., Lampard, D., 2000. *Application of computational fluid dynamics to the cooling of salient pole electrical machines*, ICEM, 2000, pp 338-352.
- Sharma, S. R. 2006. *Feasibility study of options for aging hydro-power generation facility*. Master of Science, University of Texas at Arlington, 211 p.

- Siddiqui, K. M., Sahay, K., Giri, V.K. 2014. *Health monitoring and fault diagnosis in induction motor- a review*, Int. J. Adv. Res. Electr. Electron. Instrum. Eng., vol. 3, no. 1, p. 6549–6565.
- Standard IEC 60034-1. 2010. *Rotating electrical machines –part 1: rating and performance*. IEC 60034-1, 144 p.
- Standard IEC 60034-2-1. 2007. *Rotating electrical machines - methods for determining losses and efficiency from tests (excluding machines for traction vehicles)*, IEC 60034-2-1, 154 p.
- Standard IEC 60034-2-1. 2010. *Rotating electrical machines –Part 2-2: Specific methods for determining separate losses of large machines from tests*, IEC 60034-2-1, 56 p.
- Standard IEEE C50.12. 2005. *IEEE standard for salient-pole 50 Hz and 60 Hz synchronous generators and generator/motors for hydraulic turbine applications rated 5 MVA and above*, IEEE Std. C50.12, 45 p.
- Standard IEEE C50.13. 2005. *IEEE Standard for Cylindrical-Rotor 50 Hz and 60 Hz Synchronous Generators Rated 10 MVA and Above*. IEEE Std. C50.13, 60 p.
- Steinmetz, C.P. 1983. *On the law of hysteresis*. Proceedings of the IEEE, no 2, p. 197 - 221 (originally published in AIEE Transactions, No 9 (1892), p. 3-65).
- Stone, G.C., Boulter, E.A., Culbert, I., Dhirani, H. 2005. *Electrical Insulation for rotating machines – design, evaluation, aging, testing and repair*. IEEE Press Series on Power Engineering, 135 p.
- Stone, G.C., Sasic, M., Dunn, D., Culbert, I. 2009. *Recent problems experienced with motor and generator windings*, Rec. Conf. Pap. - Ind. Appl. Soc. 56th Annu. Pet. Chem. Ind. Conf. PCIC 2009., p. 1–9.
- Sen, P.K. 1971. *Direct Measurement of the fundamental and harmonic tooth ripple losses in laminated poles*. Master Thesis, Nova Scotia Technical College, 170 p.
- Szabados, B. 2014. *Lecture Notes – Chapter 3- Synchronous generator modeling*. Available at: <http://power.mcmaster.ca/szabados/courses/esigelec/notes/>. Accessed on August 12<sup>th</sup> 2014.
- Testoni, P. 2003. *Implementation in the ANSYS finite element code of the electric vector potential  $\vec{T} - \Omega, \Omega$  formulation and its validation with the magnetic vector potential  $A - V$ ,  $A$  formulation*. Ph.D thesis, Università Degli Studi di Cagliari, 68 p.



- Thivierge, J. P., Gauthier, G. A., Doucet, Y. 2010. *Centrale Manic 2 – Essais de réception de l'alternateur A21 après réfection*. Report Direction Expertise de Centrales – Essais Spéciaux de Production. Hydro Québec, 30 p.
- Traxler-Samek, G., Schwery, A., Zickermann, R., Ramirez, C. 2006. *Optimized calculation of losses in large hydro-generators using statistical methods*. In Recent Developments of Electrical Drives, Ed. Springer, vol. I-2, p. 13-23.
- Traxler-Samek, G., Lugand T., Schwery, A. 2010a. *Additional losses in the damper windings of large hydrogenerators at open-circuit and load conditions*. In IEEE Transactions on Industrial Electronics, Vol.57 No. 1, p.155-160.
- Traxler-Samek, G., Zickermann, R., Schwery, A. 2010b. *Cooling airflow, losses, and temperatures in large air-cooled synchronous machines*. In IEEE Transactions on Industrial Electronics, Vol. 57, No. 1, p. 172–180.
- Traxler-Samek, G., Zickermann, R., Schwery, A. 2008a. *Advanced calculations of temperature rises in large air-cooled hydro-generators*. In 18<sup>th</sup> International Conference on Electrical Machines, ICEM 2008, p. 1-6.
- Traxler-Samek, G., Lugand, T., Schwery, A. 2008b. *Calculation of power losses in the damper winding of large hydrogenerators at open-circuit and load conditions*. In 18<sup>th</sup> International Conference on Electrical Machines, ICEM 2008, p. 1-6.
- Troitskaia, S.G. 2008. *Prediction of the performance of large synchronous machines with skewed stators*. PhD Thesis, University of Alberta, 110 p.
- Tsukerman, I. A., Konrad, A., Lavers, J.D. 1992. *A Method for circuit connections in time-dependent eddy current problems*. In IEEE Transactions on Magnetics, Vol. 28, No. 2, p.1299-1302.
- Tsukerman, I.A. 1995. *Accurate computation of ripple solutions on moving finite element meshes*. In IEEE Transactions on Magnetics, Vol. 31, No. 3, p.1472-1475.
- Tumanski, S. 2007. *Induction coil sensors – a review*. In Institute of Physics Publishing, Measurement Science and Technology, Vol. 18, p. 31-56.
- Ueda, Y., Ohta, H., Uenosono, C. 1987. *Instrument for real- time measurement of airgap flux distribution of on load synchronous generators*. In IEE Proceedings, Vol. 135, Pt. A, No. 5, p. 331-334.
- Van Den Bossche, A., Vaichev, V.C., Georgiev, G.B. 2005. *Measurement and loss model of ferrites with non-sinusoidal waveforms*. 35th Annual IEEE Power Electronics Specialists Conference, no. 1, p. 5815-5818.

- Van der Vorst, H. A. 2003. *Iterative Krylov Methods for large linear systems*. Cambridge University Press, 223 p.
- Vas, P., *Parameter estimation, condition monitoring, and diagnosis of electrical machines*. Oxford, U.K, Clarendon, 1993.
- Venkatachalam, K., Sullivan, C.R., Abdallah, T. and Tacca, H. 2002. *Accurate prediction of ferrite core loss with nonsinusoidal waveforms using only Steinmetz parameters*. In 8<sup>th</sup> IEEE Workshop on Computer in Power Electronics, p. 36-42.
- Vögele, H., Xuan, M., Simond, J., 1998. *Modelling of a single-phase generator equipped with a damper winding having solid lateral bars*. Proceedings ICEM 1998, Vol. 3, p. 266-271.
- Zarko, D., Maljkovic, Z., Pavlica, M. 2008. *Estimating magnetic properties of synchronous generator's materials*. Przegląd Elektrotechniczny, ISSN 0033-2097, R.85, Nr 12, p. 267-269.
- Zhan, Y. 2010. *Stray analysis of ac machines using time-stepped finite elements*. Ph.D. Thesis – University of Alberta, 147 p.
- Zhang Dong, L., Feng, Z., Yunpeng, H. 2002. *Numerical calculation of airgap magnetic field of a salient synchronous generator with the consideration of the effect of turn insulation*, Proceedings of International Conference on Power System Technology, vol. 2, p. 775-778.
- Zhou, P., Fu, W. N., Lin, D., Stanton, S., Cendes, Z. J. and Xu, L. 2002. *Numerical modeling of electrical machines and its application*, In IEEE Industrial Applications, 37<sup>th</sup> Annual Meeting, No. 1, p. 1936-1942.
- Zhu, J.G. 1994. *Numerical Modelling of magnetic materials for computer aided design on electromagnetic devices*, PhD Thesis, University of Technology, Sydney, 301 p.
- Zhu, J.G., Ramsden, V.S. 1998. *Improved formulations for rotational core losses in rotating electrical machines*. IEEE Transactions on Magnetics, Vol. 35, No.5, p.2235–2252.
- Zienkiewicz O.C. and Taylor, R. L. 2005. *The finite element method: its basis and fundamentals*, Butterworth-Heinemann, 6<sup>th</sup> edition, 749 p.
- Znidarich, M.M. 2008a. *Hydro generator stator cores. Part 1 – Constructional features and core losses*. In Australasian Universities Power Engineering Conference, AUPEC 08, p. 1-8.

- Znidarich, M.M. 2008b. *Hydro generator stator cores. Part 2 – core losses, degradation mechanisms, testing and specification*. In Australasian Universities Power Engineering Conference, AUPEC 08., p. 1-9.
- Wakileh, G.J. 2003. *Review: harmonic in rotating machines*. In Science Direct, Electric Power System Research 66, Elsevier, p.31-37.
- Wallin, M., Ranlöf, M., Lundin, U. 2010. *Design and construction of a synchronous generator test setup*, XIX International Conference on Electrical Machines, ICEM 2010, p. 1-5.
- Walker, J.H. 1947. *Parasitic losses in synchronous-machine damper winding*. In Journal of the Institution of Electrical Engineers, Part II: Power Engineering, Vol. 95. Issue: 37, p. 13-25.
- Walker, J.H, Kerruish, M.A. 1960. *Open-circuit noise in synchronous machines*. In Proceedings of the Institution of Electrical Engineers, Vol. 107, Part A, No. 36, p. 505-512.
- Walker, J.H. 1981. *Large synchronous machines design, manufacture and operation*. In Clarendon Press Oxford, 288 p.
- Wang, L., Jatskevich, J., Dommel, H.W. 2007. *Re-examination of synchronous machine modeling techniques for electromagnetic transient simulations*. IEEE Transactions on Power Systems, Vol.22, No.3, August, p. 1221-1230.
- Wang, L., Jatskevich, J., Dinavahi, V., Dommel, H.W., Martinez, J. A., Strunz, K., Rioual, M., Chang, G. W. and Iravani, R. 2010. *Methods of interfacing rotating machine models in transient simulation programs*, IEEE Transactions on Power Delivery, vol. 25, no. 2, p. 891-903.
- Wang, X. H., Sun, Y. G., Ouyang, B., Wang, W. J., Zhu, Z. Q. and Howe, D. 2002. *Transient behaviour of salient-pole synchronous machines with internal stator winding faults*, IEE Proc. Electr. Power Appl., vol. 159, no. 2, p. 153-151.
- Weeber, K. 1997. *Determination of dynamic parameters of large hydro-generators by finite-element simulation of three-phase sudden short circuit tests*. IEMDC Conference, p. 13-15.
- Weeber, K. 1998. *Design of amortisseur windings of single-phase synchronous generators using time-stepping finite element simulations*, Proceedings ICEM 98, p. 1042-1047.

- Weili, L., Yu, Z., Yuhong, C. 2011. *Calculation and analysis of heat transfer coefficients and temperature fields of air-cooled large hydro-generator rotor excitation windings*, IEEE Transactions on Energy Conversion, vol. 26, no. 3, p. 956-952.
- Weili, L., Dawei, L., Yu, Z. 2012. *Calculation of iron loss in large hydro-generator under-load*, Adv. Mater. Res., vol. 533–550, p. 6096-6102.
- Yamazaki, K., Watanabe, Y. 2006. *Interbar current analysis of induction motors using 3-d finite element method considering lamination of the rotor core*. In IEEE Transactions on Magnetics, Vol. 52, No. 5, p. 1287-1290.
- Yamazaki K., Watari, S. 2005. *Comparison of methods to calculate iron losses caused by harmonic fields in rotating machines*. In Progress in Electromagnetic Research Symposium, p. 329-332.
- Yicheng C., Pragsen, P. 2002. *An improved formula for lamination core loss calculations in machines operating with high frequency and high flux density excitation*. Conference Record of the 2002 IEEE Industry Applications Conference (37th IAS Annual Meeting), Vol.2, p.759-766.